Numerical analysis of the performance of flapping foil power generators

Author:
Liu, Zhengliang

Publication Date:
2018

DOI:
https://doi.org/10.26190/unsworks/20569

Numerical Analysis of the Performance of Flapping Foil Power Generators

Zhengliang Liu

A thesis submitted in fulfilment

of the requirements for the degree of

Doctor of Philosophy

The University of New South Wales

School of Engineering and Information Technology

Feb 2018

PLEASE TYPE

The University of New South Wales
Thesis/Dissertation Sheet

Surname or Family name: Liu	
First name: Zhengliang	Other name/s:
Abbreviation for degree as given in the University calendar: PhD	
School: School of Engineering and Information Technology	Faculty: UNSW, Canberra @ ADFA
Title: Numerical analysis of the performance of flapping foil power generators.	

Abstract 350 words maximum: (PLEASE TYPE)

An innovative concept of wind turbines, the flapping foil power generator that exploits dynamic stall, is numerically studied at Reynolds number of 1100. The combination of the kinematic parameters and the coupling between the foil deformation and aerodynamic loads are investigated to uncover the physical mechanism for high performance.

Firstly, the discrete vortex method (DVM) is improved to capture flow separations at the leading and trailing edges of the foil. Its results compare well with those of immersed boundary-lattice Boltzmann method (IB-LBM) and experiments. Its computational cost is at least two orders of magnitude less than that of the IB-LBM.

Then, kinematic parameters are optimized using a multi-fidelity evolutionary algorithm implemented with a dynamic stall model and the improved DVM. The results show that despite the use of low fidelity models and limited budget of computational resources, the multi-fidelity strategy is capable of finding kinematic conditions suitable for high performance. In addition, detailed flow analysis using IB-LBM has revealed that high efficiency and power output are associated with the detachment of the leading edge vortex (LEV) near stroke reversal, resulting in a horseshoe-shaped vorticity wake with a width approximating the swept distance of foil behind the turbine plane. When the LEV detaches from the foil near mid stroke, both efficiency and power output suffer.

Finally, a flexible system consisting of a rigid foil and a passively actuated flat plate tail connected through a torsional spring to the trailing edge of the rigid foil is studied numerically using the IB-LBM for different mass densities and natural frequencies under different kinematic conditions. The results show that a tail with appropriate mass density and resonant frequency can improve the maximum efficiency by 7.24% compared to the rigid system. This is because the deflection of the tail reduces the low pressure region on the pressure surface caused by the LEV after the stroke reversal, resulting in a higher efficiency. In addition, a spring-connected tail with a low resonant frequency improves the performance significantly at high flapping frequencies.

Originality Statement

I, Zhengliang Liu, hereby declare that this submission is my own work and to the best of my knowledge it contains no materials previously published or written by another person, or substantial proportions of material which have been accepted for the award of any other degree or diploma at UNSW or any other educational institution, except where due acknowledgement is made in the thesis. Any contribution made to the research by others, with whom I have worked at UNSW or elsewhere, is explicitly acknowledged in the thesis. I also declare that the intellectual content of this thesis is the product of my own work, except to the extent that assistance from others in the projects design and conception in style, presentation and linguistic expression is acknowledged.

Signed ....

Date ....

Copyright Statement

I hereby grant the University of New South Wales or its agents the right to archive and to make available my thesis or dissertation in whole or part in the University libraries in all forms of media, now or here after known, subject to the provisions of the Copyright Act 1968. I retain all proprietary rights, such as patent rights. I also retain the right to use in future works (such as articles or books) all or part of this thesis or dissertation. I also authorise University Microfilms to use the 350 word abstract of my thesis in Dissertation Abstract International (this is applicable to doctoral theses only). I have either used no substantial portions of copyright material in my thesis or I have obtained permission to use copyright material; where permission has not been granted I have applied/will apply for a partial restriction of the digital copy of my thesis or dissertation.

Signed ....

Authenticity Statement

I certify that the Library deposit digital copy is a direct equivalent of the final officially approved version of my thesis. No emendation of content has occurred and if there are any minor variations in formatting, they are the result of the conversion to digital format.

Signed ....

Abstract

An innovative concept of wind turbines, the flapping foil power generator that exploits dynamic stall, is numerically studied at Reynolds number of 1100. The combination of the kinematic parameters and the coupling between the foil deformation and aerodynamic loads are investigated to uncover the physical mechanism for high performance.

Firstly, the discrete vortex method (DVM) is improved to capture flow separations at the leading and trailing edges of the foil. Its results compare well with those of immersed boundary-lattice Boltzmann method (IB-LBM) and experiments. Its computational cost is at least two orders of magnitude less than that of the IB-LBM.

Then, kinematic parameters are optimized using a multi-fidelity evolutionary algorithm implemented with a dynamic stall model and the improved DVM. The results show that despite the use of low fidelity models and limited budget of computational resources, the multi-fidelity strategy is capable of finding kinematic conditions suitable for high performance. In addition, detailed flow analysis using IB-LBM has revealed that high power extraction performance is associated with the detachment of the leading edge vortex (LEV) near stroke reversal, resulting in a horseshoe-shaped vorticity wake with a width approximating the swept distance of foil behind the turbine plane. When the LEV detaches from the foil near mid stroke, both efficiency and power output

suffer.

Finally, a flexible system consisting of a rigid foil and a passively actuated flat plate tail connected through a torsional spring to the trailing edge of the rigid foil is studied numerically using the IB-LBM for different mass densities and natural frequencies under different kinematic conditions. The results show that a tail with appropriate mass density and resonant frequency can improve the maximum efficiency by 7.24% compared to the rigid system. This is because the deflection of the tail reduces the low pressure region on the pressure surface caused by the LEV after the stroke reversal, resulting in a higher efficiency. In addition, a spring-connected tail with a low resonant frequency improves the performance significantly at high flapping frequencies.

Acknowledgements

The completion of my doctoral thesis is not only a milestone in the scientific arena, but also a period of intense learning on a personal level. I wish to express my sincere gratitude to the people who have supported and helped me so much throughout this period.

First and foremost, I would like to express my great appreciation to my supervisors, Prof Joseph C.S. Lai, Dr Fang-Bao Tian and A/Prof John Young, for giving me the opportunity to study at UNSW Canberra. Their continuous support, precious suggestions and constant encouragement throughout my research are highly appreciated. I could not have imagined having better support and guidance for my PhD study.

I would also like to thank my colleagues and officemates Zongjun Li, Ern Ong, Wang Li, Lincheng Xu, Jingtao Ma, Qiuxiang Huang, Yi Zhu, Xin Li, Yifei Cui, Rongkang Gao, Dan Meng, Chenman Wang, Biruk Hailu Tekle, Shameem Ahmed, Vishal Naidu, Rakib Imtiaz Zaman, Abdul Kader, Shayani Mendis and Mohammad Anwar-Us-Saadat for their support, encouragement and friendship.

I would also like to acknowledge the support of the University of New South Wales International Postgraduate Award for the pursuit of this study.

I am grateful for Yue Chen, my girlfriend, and my families for their encouragement, continuous support and help during this study.

List of Publications Based on this Thesis

Journal Papers

[1] Zhengliang Liu, Joseph C.S. Lai, John Young, and Fang-Bao Tian. Discrete vortex method with flow separation corrections for flapping-foil power generators. *AIAA Journal*, 55(2):410-418, 2017, (based on Chapter 4).

[2] Zhengliang Liu, Fang-Bao Tian, John Young, and Joseph C.S. Lai. Flapping foil power generator performance enhanced with a spring-connected tail. *Physics of Fluids*, 29(12):123601, 2017 (editor's pick), (based on Chapter 6).

[3] Zhengliang Liu, Kalyan Shankar Bhattacharjee, Fang-Bao Tian, John Young, Tapabrata Ray, and Joseph C.S. Lai. Kinematic optimization of a flapping foil power generator using multi-fidelity evolutionary algorithm. *Renewable Energy*, submitted, (based on Chapter 5).

Conference Papers

[1] Zhengliang Liu, Joseph C.S. Lai, John Young, and Fang-Bao Tian. A discrete vortex method for flapping foil power generator modeling at low Reynolds numbers. In *24th International Congress of Theoretical and*

Applied Mechanics, Montreal, Canada, August 2016, (based on Chapter 4).

[2] Zhengliang Liu, Joseph C.S. Lai, John Young, and Fang-Bao Tian. Numerical study on the performance of a flapping foil power generator with a passively flapping flat plate. In *20th Australasian Fluid Mechanics Conference*, Perth, Australia, December 2016, (based on Chapter 6).

Contents

List of Figures

List of Tables

List of Abbreviations

AR	aspect ratio
2D	two-dimensional
3D	three-dimensional
CFD	computational fluid dynamics
DVM	discrete vortex method
DOF	degree of freedom
EA	evolution algorithm
FSI	fluid-structure-interaction
IB-LBM	immersed boundary-lattice Boltzmann method
LESP	leading edge suction parameter
LEV	leading edge vortex
MFEA	multi-fidelity evolution algorithm
NS	Navier-Stokes
RMS	root mean square
SFEA	single-fidelity evolution algorithm
SST	Menters shear stress transport
TEV	trailing edge vortex
UPM	unsteady panel method

URANS unsteady Reynolds averaged Navier-Stokes

Nomenclature

A_0, A_n	Fourier coefficients in Eq. 4.4 and Eq. 4.5 respectively
B_{EA}	computational time budget in Fig. 3.11, Fig. 3.12, Section 3.4 and Chapter 5
C_C	chord force coefficient, $F_C/(1/2\rho U^2 c)$
C_D	static drag coefficient, $F_D/(1/2\rho U^2 c)$
C_{EA}	child population in Fig. 3.11, Fig. 3.12 and Section 3.4
C_L	lift coefficient, $L/(1/2\rho U^2 c)$
C_{Ld}	dynamic lift coefficient given by Eq. 3.13
C_{Ls}	static lift coefficient given by Eq. 3.12
C_M	moment coefficient, $M/(1/2\rho U^2 c^2)$
C_N	normal force coefficient, $F_N/(1/2\rho U^2 c)$
C_P	power coefficient, $P/(1/2\rho U^3 c)$
C_{Ph}	power coefficient due to plunge motion, $P_h/(1/2\rho U^3 c)$
$C_{P\theta}$	power coefficient due to pitch motion, $P_\theta/(1/2\rho U^3 c)$
C_R	rotational circulation coefficient, $\pi\,(0.75 - x_{piv})$
D_{EA}	status of an individual is sure for discarding in Fig. 3.11, Fig. 3.12 and Section 3.4
F_C	chord force, N

F_D	drag, N
F_{EA}	fidelity level in multi-fidelity evolutionary algorithm in Fig. 3.11, Fig. 3.12, Section 3.4 and Chapter 5
F_N	normal force, N
G_{EA}	generation in Fig. 3.11, Fig. 3.12, Section 3.4 and Chapter 5
H	instantaneous vertical position of the foil pitching axis, m
H_0	plunge amplitude, m
H_s	thickness of the tail, m
I	non-dimensional moment of inertia, $I = J/\left(\rho c^4\right)$
J	moment of inertia, kg·m^2
J_a	added moment of inertia, kg·m^2
K_{EA}	status of an individual is sure for keeping in Fig. 3.11, Fig. 3.12 and Section 3.4
K_p	stiffness in the plunge direction, N/m
K_t	torsional stiffness in the pitch direction, N·m/rad
K_s	torsional stiffness of the spring connected tail, N·m/rad
L	lift, N
L_{tail}	length of the tail, m
M	pitch moment about the pivot point, N·m
$\boldsymbol{M_{LB}}$	transformation matrix in Section 3.3
P	instantaneous total power, W
P_{EA}	parent population in Fig. 3.11, Fig. 3.12 and Section 3.4
P_h	instantaneous power due to plunge motion, W
P_r	reference power available in the flow, W

P_θ	instantaneous power due to pitch motion, W
Re	Reynolds number, Uc/v
R_{fly}	damping of the flywheel, J·s
R_h	damping in the plunge direction, N·s/m
R_θ	torsional damping in the pitch direction, J·s
S_1, S_2	coefficients of separation point curve fit in Eq. 4.12
$\boldsymbol{\hat{S}_{LB}}$	diagonal matrix of the relaxation rates in Section 3.3
S_{EA}	total population in Fig. 3.11, Fig. 3.12 and Section 3.4, $S_{EA} = P_{EA} + C_{EA}$
T	time period of one flapping cycle, s
T_{EA}	selection threshold in Fig. 3.11, Fig. 3.12 and Section 3.4
U	freestream velocity, m/s
U_{EA}	status of an individual is not evaluated in Fig. 3.11, Fig. 3.12 and Section 3.4
U_{eff}	effective incident velocity, $\sqrt{\dot{H}^2 + U^2}$, m/s
W	local velocity normal to the foil, m/s
X	chordwise position measured from the leading edge, m
X_m	chordwise position of the mass center measured from the leading edge, m
X_{piv}	chordwise position of the pivot point measured from the leading edge, m
X_{shift}	chordwise distance between the pivot points of two foils in multiple foil configuration, m
Z	position perpendicular to the foil chord, m
b	span, m

c	chord length, m
c_i	particle velocity in Section 3.3, m/s
d	maximum distance swept by the foil, m
e	thickness of the foil, m
f	flapping frequency, Hz
f_0	natural frequency of the spring connected tail in Chapter 6, Hz
f_i	distribution function of velocity c_i in Section 3.3
f^{sep}	effective separation point in Eq. 4.13
f_0^{sep}	steady-state separation point in Eq. 4.12
f^*	non-dimensional flapping frequency, fc/U
f_0^*	non-dimensional natural frequency of the spring connected tail in Chapter 6, f_0c/U
f_r^*	resonant frequency defined in Eq. 6.1
h	non-dimensional instantaneous vertical position of the foil pivot point, H/c
h_0	non-dimensional plunge amplitude, H_0/c
k_1, k_2	coefficients of the Leishman-Beddoes model in Chapter 4
k	reduced flapping frequency, $2\pi fc/U$
k_h	non-dimensional stiffness in the plunge direction, $K_p/\left(\rho U^2\right)$
k_θ	non-dimensional torsional stiffness in the pitch direction, $K_t/\left(\rho U^2 c^2\right)$
m_{foil}	mass of the foil, kg
m_h	mass of all the parts in the system undergoing the plunge motion, kg
$\boldsymbol{m_{LB}}$	vector of momentum in Section 3.3

p	pressure, Pa
p_∞	freestreem pressure, Pa
r	position of the particles in Section 3.3, m
r_h	non-dimensional damping in the plunge direction, $R_p/\left(\rho U c\right)$
r_θ	non-dimensional damping in the pitch direction, $R_\theta/\left(\rho U^3 c\right)$
s_{im}	static imbalance parameter, $\mu_m\left(x_m - x_{piv}\right)$
t	time, s
u	velocity in the x direction, m/s
v	velocity in the y direction, m/s
x	streamwise coordinate in Cartesian coordinates, m
x_m	non-dimensional chordwise position of the mass center measured from the leading edge, X_m/c
x_{piv}	non-dimensional chordwise position of the pivot point measured from the leading edge, X_{piv}/c
x_{shift}	non-dimensional chordwise distance between the pivot points of two foils in multiple foil configuration, X_{shift}/c
y	transverse coordinate in Cartesian coordinates, m
z	spanwise coordinate in Cartesian coordinates, m
Γ	circulation bounded on the foil, m^2/s
Γ_V	circulation of leading and trailing edge vortices, m^2/s
Δt^*	non-dimensional time step, $\Delta t^* = \Delta t U/c$
Φ	velocity potential
α	angle of attack defined in Eq. 2.2, $^\circ$
α_0	amplitude of the angle of attack, $^\circ$

$\alpha_{T/4}$	quarter-period value of effective angle of attack, $^\circ$
α_1	break point of separation point curve, $^\circ$
α_{eff}	effective angle of attack, $^\circ$
α_{max}	maximum angle of attack in one flapping cycle, $^\circ$
β	flywheel angle, $^\circ$
β_p	structure damping coefficient in the plunge direction
γ	vorticity distribution over the foil, m/s
η	efficiency defined in Eq. 2.6, $\overline{C}_P c/d$
η_c	crossover distribution index in Section 3.4 and Chapter 5
η_m	mutation distribution index in Section 3.4 and Chapter 5
θ	instantaneous angular position of the foil, rad
ϑ	chordwise coordinate transformation variable, rad
θ_0	pitch amplitude, $^\circ$
λ_{EA}	size of recombination pool in Section 3.4 and Chapter 5
μ_{EA}	population size in Fig. 3.11, Fig. 3.12, Section 3.4 and Chapter 5
μ	linear density ratio of the tail in Chapter 6, $\rho_l/(\rho c)$
μ_m	mass ratio of the foil, $m_{foil}/(\rho c^2)$
ν	kinematic viscosity, m^2/s
ρ	freestream density, kg/m^3
ρ_l	linear density of the tail in Chapter 6, $\rho_l = \rho_{tail} H_s$, kg/m^2
ρ_{foil}	density of the foil, kg/m^3
ρ_{tail}	density of the tail, kg/m^3
τ_1, τ_2	characteristic time coefficients in Eq. 4.13
τ_{LB}	relaxation time in Section 3.3

φ	phase angle between the pitch and plunge motion, $^\circ$
χ	feathering parameter defined in Eq. 2.1
ψ	phase difference between the pitch motions of the front and rear foils in multiple foil configuration, $^\circ$
ω	angular velocity, rad/s
ω_p	natural angular frequency of the system in the plunge direction, rad/s, $\sqrt{K_P/m_h}$
ω_z	spanwise vorticity, Hz

List of Superscripts

^{cir}	circulatory term of the discrete vortex method in Chapter 4
^{eq}	equilibrium of a variable in Section 3.3
^{non}	non-circulatory term of the discrete vortex method in Chapter 4
^{sep}	(force/moment) considering the flow separations in Chapter 4
^{suc}	(force) corresponding to the pressure suction peak at the leading edge in Chapter 4
^{vis}	viscous component of (force/moment) in Section 3.2
$'$	a variable in the foil coordinate system
$\dot{}$	time derivative of a variable
$\ddot{}$	second derivative with respect to time of a variable
$\bar{}$	time averaged value of a variable

Chapter 1

Introduction

1.1 General introduction

With the increase of pollution emitted into the atmosphere due to human activities, air pollution and global warming threaten human and animal health and intensify natural disasters. Among human activities, energy consumption is the primary source of emission, producing 68% of global greenhouse gas in 2010 (IEA 2016). Fossil fuels including petroleum, coal, and natural gas are commonly used to generate power. In 2014, 82% of world energy was supplied by fossil fuels (IEA 2016). Besides greenhouse gases, a number of harmful air pollutants, such as sulfur oxides and nitrogen oxides, are emitted during energy production using fossil fuels. In order to address the problem associated with the use of fossil fuels, it is crucial to move towards finding alternative sustainable energy sources (Panwar et al. 2011). Renewable energy sources, such as wind power, hydropower, solar power and geothermal power, create a much less harmful impact on human health and the climate change (Jacobson 2009). In terms of the global installed capacity in 2016, wind power (487 GW) ranks the second of the technologies applied to generate renewable electric power (2,017 GW in total), after hydropower (1,096 GW) (REN21 2017). Due to its relatively competitive price and worldwide resource base, the commercial and technical investment in wind energy increases rapidly in the power sector (Pryor & Barthelmie 2010). By 2020 the growth rate of global cumulative wind energy capacity will remain more than 10% (GWEC 2014) and the installed capacity in the European Union is expected to increase to 149% of that in 2014 (Giorgio et al. 2015). Besides wind energy, tidal energy offers a reliable energy source with a technical potential capacity of 500-1000 TW h/yr (Pelc & Fujita 2002). Since tidal power generators share many similarities to wind turbines, technology of harvesting energy from water currents can benefit from the advances in wind turbine designs (Rourke et al. 2010).

Although the use of wind energy can be traced back to 3,000 years ago, the first wind turbine with rotating blades to generate electricity was built by Poul la Cour in 1981 (Ackermann & Söder 2000) because of the complexity of the wind energy technique. Since then rotary turbines have been commonly used to harvest energy from air and water currents. In general, a high tip speed ratio is desirable in rotary turbine design for high efficiency. However, the high speed at the tip of the blade can result in considerable noise (Ragheb & Ragheb 2011) and large centrifugal forces which may cause blade failure (Schubel & Crossley 2012), especially for large scale wind turbines. To resolve these issues, some efforts have been made on utilizing other mechanisms to harvest energy, e.g. bladeless turbines (El-Shahat 2016) and flapping foil turbines (Young et al. 2014). Also in 1981, the capability of harvesting energy from the motion of a flapping foil was first demonstrated by McKinney & DeLaurier (1981). The applications of flapping foil are inspired by aquatic creatures as well as birds and insects, involving complex unsteady flows. Thanks to the rapid development of flapping foil propulsive systems (Platzer et al. 2008, Triantafyllou et al. 2004), power generators harvesting energy from the motion of flapping foils as an alternative to rotary turbines have been under active investigation in the last 10 years (Young et al. 2014, Xiao & Zhu 2014).

In the concept of a flapping foil power generator, the foil generally undergoes pitch and plunge motions. The performance is measured as the percentage of power extracted from the fluid passing through the turbine plane, as for rotary turbines. In contrast to rotary turbines which rely on attached flows for high efficiencies, flapping foil turbines can benefit from exploiting flow separations for high aerodynamic loads, especially in laminar flows. Compared to conventional turbines, the flapping power generator has several prominent features:

- It gives promising performance under low speed environment, potentially expanding the applications in different flow regimes. The efficiency of conventional turbines falls rapidly at low speeds (below 2 m/s for tidal turbines (Lewis et al. 2015) and 5 m/s for wind turbines (Wright & Wood 2004, Akpinar & Akpinar 2005)), while the flapping power generator operated as a tidal turbine can provide relatively high efficiency (around 30% Abiru & Yoshitake (2011*a*)) even at the cut-in speed (1 m/s) of conventional turbines where little power is extracted (Lewis et al. 2015). Since the estimation of available wind and tidal power is based on the flow speed limits of rotary turbines (6.9 m/s for wind energy Jacobson (2009) and 2 m/s for tidal energy Pelc & Fujita (2002)), decreases in flow speed limits by employing flapping foil power generators imply the increase of usable energy resources. For instance, when the wind speed of commercial applications decreases to 5.9 m/s, the global wind power potential doubles (Archer & Jacobson 2005).

- As the velocity of a flapping foil is approximately the same along the span, it operates at low tip speeds. This is beneficial to the environment by reducing both noise and impact on aquatic creatures (Masters 2013). Further more, centrifugal forces which may lead to structure failure of rotational blades are negligible on flapping blades.

- Untwisted flapping foil has a robust structure and low manufacturing cost. In addition, the flapping foil power generator can be installed in shallow water since the it sweeps a rectangular area (Xiao & Zhu 2014).

Thus, the flapping foil power generator is attractive as a supplement or alternative to conventional turbines. Several international companies have developed prototypes to harvest energy from flapping motions, including Engineering Business Ltd (UK) (Rostami & Armandei 2017), Pulse Tidal Company (UK) (Marsh 2009), BioPower System (Australia) (Kloos et al. 2009) and Festo AG (Germany) (Send 2016).

1.2 Research objectives

The aim of this study is to explore the high performance of the flapping foil power generator and uncover the associated flow physics by numerical modelling and simulations. Compared to conventional turbines which rely on attached flow for high efficiencies, a flapping foil turbine can exploit the flow separation near the nose of the foil to form leading edge vortices, resulting in high efficiency, particularly at low flow velocities. Due to the sensitivity of the leading edge vortex (LEV) dynamics to the kinematics of flapping foil generators, the performance of flapping foil turbines is affected by many parameters including kinematics, foil geometry, material properties and environmental effects. For example, the kinematics of a flapping foil undergoing sinusoidal pitch and plunge motions is governed by five parameters, which will be discussed in Section 2.2.1. However, previous studies on kinematic parameters generally focused on two variables with others fixed. To compete against rotational turbines, it is necessary to search for the optimal combination of kinematic parameters since the trial and error approach is far from ideal. However, it is computationally expensive to optimise kinematic parameters using Computational Fluid Dynamics (CFD) methods because of their high computational cost. Moreover, analytical models based on the quasi-steady assumption and potential flow theory are insufficient for flapping foil analysis under some circumstances (e.g. slow flow speeds) where the flow can be highly separated. In addition, studies on propulsion systems based on flapping locomotion including fish, rays and insect wings indicate that an appropriate degree of structural flexibility can improve the propulsive performance. Considering the similarity of locomotion in thrust and power generation applications, it is hypothesised that an appropriate coupling between the foil deformation and the aerodynamic load acting on the foil can improve the performance of a flapping foil power generator.

Within the overall aim, the specific objectives are to:

- develop a low order model for the simulation of a flapping foil experiencing deep dynamic stall, which takes into account of flow separations at low flow speeds and consumes much less time than CFD methods;
- validate the low order model and determine the utility of approximate models for prediction of the energy harvesting performance and aerodynamic loads acting on the flapping foil;
- search for optimal kinematic parameters for high energy extraction per-

formance using a generic population-based metaheuristic optimization algorithm (evolutionary algorithm) with the validated low order models;

- investigate impacts of the flexibility on the aerodynamic loads and energy harvesting performance of a flapping foil power generator; and
- explore the relationships between energy harvesting performance, kinematic and structure parameters and formation and convection of the vortices.

1.3 Thesis outline

The structure of the remainder of this thesis is briefly outlined below.

In Chapter 2, the mechanisms and advantages of harvesting energy from a fluid flow using a flapping foil are discussed. The recent progress in analytical, numerical and lab-based experimental studies as well as prototype tests is reviewed. In addition, the influence of kinematic parameters, foil geometry and deformation and environmental effects is examined.

In Chapter 3, various methods employed in the thesis are presented and validated against the data in the literature. Firstly, a reduced order model developed by Bryant et al. (2013) for flapping foil simulations is described. This model is reproduced with Matlab and compared with the results of Bryant et al. (2013). The model is further validated by matching its results with the CFD results of Kinsey & Dumas (2008), to serve as a baseline. Then, an innovative numerical method to simulate the fluid, the immersed boundary-lattice Boltzmann method (IB-LBM), is presented. The space and time refinement and validation of the in-house code using IB-LBM with multi-block technique are conducted. Finally, the optimization solver of evolutionary algorithm using single and multi fidelity strategies is presented and compared with a classical non-gradient optimisation method, the complex method (Krus & Andersson 2003), for artificial non-linear functions.

In Chapter 4, the discrete vortex method (DVM) for flapping foil simulations with large leading and trailing edge flow separations is developed. The DVM is based on the potential flow theory and introduces a leading edge suction force to incorporate the leading edge flow separation. In addition, corrections using semi-empirical functions are employed to account for the effects of trailing edge flow separation. To examine the time cost, the computational time of the DVM is compared with that of IB-LBM under different kinematic conditions. Then, instantaneous lift and power coefficient as well as the mean power coefficient and efficiency predicted by the DVM with flow separation corrections are compared with those given by the Bryant model (Bryant et al. 2013) reproduced in Chapter 3. The results are also validated against the CFD simulations and experimental data in the literature as well as results given by the IB-LBM code.

In Chapter 5, the multi-fidelity evolutionary algorithm (MFEA) is used to search for high energy extraction performance solutions of a flapping foil power generator. Solutions of different fidelity levels are evaluated by the Bryant model reproduced in Chapter 3 and the DVM developed in Chapter 4. A single objective problem with two variables is first used to illustrate the benefits of the multi fidelity optimization strategy. Then, single-objective and bi-objective optimization problems of five design variables are considered and compared with the singe-objective problem of two variables. The best solutions obtained by the bi-objective problem are evaluated with IB-LBM in order to provide insight into the physics underpinning the performance of a flapping foil power generator. The influence of the kinematic parameters on the performance of the flapping foil power generator is discussed through analysis of the non-dominated solutions. Finally, specified cases are investigated through aerodynamic loads as well as the averaged flow fields to examine the relationship between the kinematics and the performance of the flapping foil.

In Chapter 6, the influence of the flexibility on the performance of a flapping foil power generator is examined at a Reynolds number of 1100. The flexibility is modelled by a torsional spring connecting a passively actuated plate to the trailing edge of the rigid foil, as described in Section 3.1. A parametric study on mass density and natural frequency is conducted under the optimum kinematic condition of the rigid system identified from the literature and numerical simulations using IB-LBM. Then the influence of passive deformation of the tail under different kinematic conditions is examined through comparison of the rigid system and the flexible system with different resonant frequencies.

In Chapter 7 major conclusions from the research and recommendations for further research are made.

Chapter 2

Background

As mentioned in Chapter 1, the concept of harvesting energy from flapping motions has been under active investigation in the last 10 years, and possesses several advantages compared to rotary turbines. In this chapter, the fundamentals of harvesting energy from flapping motions and factors affecting the performance of flapping foil turbines are examined. To clarify the difference of flapping foil turbines from the rotary turbines, the mechanical behaviour and classification of flapping foil systems are introduced in Section 2.1. Then, parameters governing the kinematics of the flapping foil power generator with different activation mechanisms are compared and discussed in Section 2.2. In Section 2.3, geometries of the foil and system including deformation are examined. Finally, environmental effects are briefly discussed in Section 2.4.

2.1 Flapping foil fundamentals

Flapping motions are commonly utilized by animals like the tuna and the dragonfly to achieve effective propulsion (Lentink & Dickinson 2009). Furthermore, flexible structures such as fish fins are able to absorb energy from incoming vortices through flapping motions to develop thrust (Beal et al. 2006). The concept of using a flapping foil to harvest energy from the incoming flow was pioneered by McKinney & DeLaurier (1981). A later study by Jones & Platzer (1997) showed that a dual-mode (combined pitch and plunge motions) flapping wing could extract power from the incoming flow when the pitch amplitude exceeded the induced angle of attack due to plunge motion. Thus depending on kinematics, a flapping foil undergoing pitch and plunge motions can operate in two modes: propulsion and power extraction. When energy is extracted from the incoming flow, power output is defined as positive. Kinsey & Dumas (2008) suggested a "feathering criterion" χ to estimate the threshold:

$$\chi = \frac{\theta_0}{\arctan(H_0 c\omega/U)}, \tag{2.1}$$

where U is the freestream velocity; H_0 and θ_0 are respectively the plunge and pitch amplitudes; and ω is the angular frequency of the flapping motion. When χ is above 1, the flapping foil operates in power extraction mode and the pitch amplitude is larger than the maximum angle of attack induced by the plunge motion (Kinsey & Dumas 2008). This parameter can be used to estimate the threshold of the pitch amplitudes for given frequencies and plunge amplitudes, above which power is extracted (Young et al. 2014). Comparison between contours of efficiency predicted by inviscid methods (the Theodorsen's theory and the unsteady panel method) and viscous methods by solving Navier-Stokes (NS) equations indicates that the flow stays attached near the threshold (Young et al. 2014).

Since a high level of the flow separation reduces the efficiency of rotary turbines (Make & Vaz 2015), a number of studies on rotary turbines were performed focusing on active control to alleviate the flow separations (Mal-

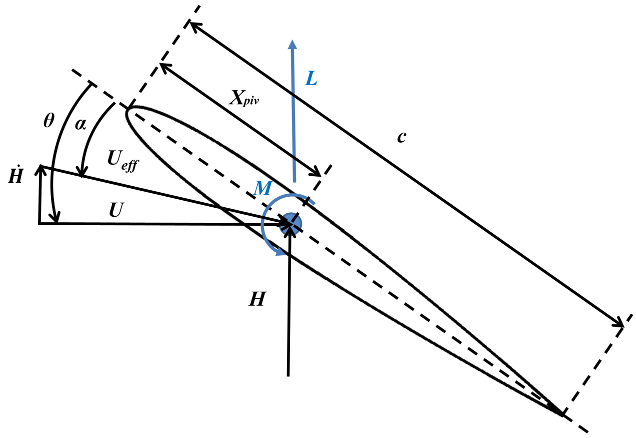

Fig. 2.1: Plunge motion H, pitch motion θ, angle of attack α, hydrodynamic lift L and moment M about the pivot location, which is X_{piv} from the leading edge of the foil with a chord length of c. $U_{eff} = \sqrt{\dot{H}^2 + U^2}$ is the effective velocity.

donado et al. 2010, Wang et al. 2013, Yen & Ahmed 2013). However, studies on flapping foil power generators show that the formation and evolution of the leading edge vortex (LEV) resulting from the leading edge flow separation play a significant role on the performance at least for low Reynolds number when χ is far above the threshold. Specifically, high performance occurs under defined conditions governed by appropriate synchronization of the LEV shedding and the foil motions (Kinsey & Dumas 2008, Zhu 2011). Thus, controlling the formation of LEV may be a possible approach to improve the performance of a flapping foil power generator (Kim et al. 2017). Since it is related to the onset of flow separation, the angle of attack α, due to combined pitch and plunge motions (Fig. 2.2), is frequently adopted in flapping foil studies:

$$\alpha = \theta - \tan^{-1}(\dot{H}/U), \tag{2.2}$$

where $\dot{H}$ is the plunge velocity.

Despite the fact that propulsive and energy harvesting systems using flapping foils exploit a mechanism akin to that in the locomotion of insects and ocean creatures, the energy flux of the two systems are in the opposite directions. In the propulsive system, energy is consumed to generate thrust. Thus its performance is characterized by the force generated in the travelling direction and it creates a jet-like flow (reverse Kármán vortex street). On the other hand, the energy harvesting system extracts power from the incoming flow and creates a wake-like flow (Kármán vortex street). Analogous to rotary turbines, the performance of energy harvesting systems using flapping foils is quantified by two non-dimensional parameters: the mean power coefficient $\overline{C}_P$ and efficiency η, defined as the ratio of the power P extracted to a reference power P_r available from the flow.

The cycle-averaged power coefficient $\overline{C}_P$ is expressed as:

$$\overline{C}_P = \frac{1}{T}\int_{t_0}^{t_0+T} C_P\left(t\right)dt, \tag{2.3}$$

where T is the period; and $C_P\left(t\right)$ is the instantaneous power coefficient C_P defined by

$$C_P\left(t\right) = \frac{P}{\frac{1}{2}\rho U^3 c} = \frac{P_h\left(t\right) + P_\theta\left(t\right)}{\frac{1}{2}\rho U^3 c}, \tag{2.4}$$

where ρ is the freestream density ; c is the chord length; P is the instantaneous total power, $P_h\left(t\right) = L\dot{H}\left(t\right)$ is the instantaneous power component due to the plunge motion and $P_\theta\left(t\right) = M\dot{\theta}\left(t\right)$ is the instantaneous power component due to the pitch motion; and L and M are respectively the lift and moment as shown in Fig. 2.1

As noted by Kinsey & Dumas (2014), there are 4 definitions for reference power P_r which is used to compute η. In the first one, the reference power available in the flow is measured as the kinetic energy of the flow passing through the overall maximum distance d swept by any part of the foil during one flapping cycle. Then P_r and η are expressed as:

$$P_r = \frac{1}{2}\rho U^3 d, \tag{2.5}$$
$$\eta = \frac{P}{P_r} = \overline{C}_P \frac{c}{d}. \tag{2.6}$$

In the second definition (Lu et al. 2014), P_r is measured as the flux of kinetic energy through the distance swept by the pivot point, which is twice of the plunge amplitude H_0:

$$P_{r2} = \frac{1}{2}\rho U^3 (2H_0), \tag{2.7}$$
$$\eta_2 = \frac{P}{P_r} = \overline{C}_P \frac{c}{2H_0}. \tag{2.8}$$

In the other two definitions, the Betz limit (Betz 1919), which states that the maximum extractable power is 16/27 the available power in the flow, is introduced:

$$P_{r3} = \frac{16}{27}\left(\frac{1}{2}\rho U^3 d\right), \tag{2.9}$$
$$\eta_3 = \frac{27}{16}\overline{C}_P \frac{c}{d} \tag{2.10}$$
$$P_{r4} = \frac{16}{27}\left(\rho U^3 H_0\right), \tag{2.11}$$
$$\eta_4 = \frac{27}{16}\overline{C}_P \frac{c}{2H_0}. \tag{2.12}$$

The first definition of η in Eq. 2.6 is recommended by Kinsey & Dumas (2014) and is commonly used in studies of the flapping foil power generators.

With respect to the activating mechanism of the device, flapping foil pow-

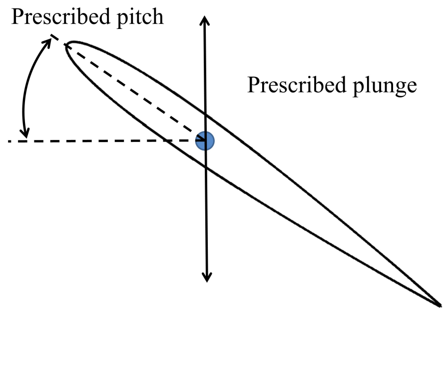

(a) System with prescribed pitch and plunge motion.

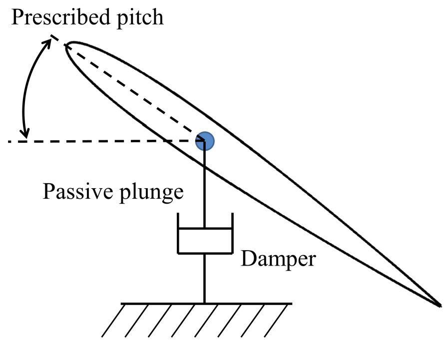

(b) System with prescribed pitch and passive plunge motion.

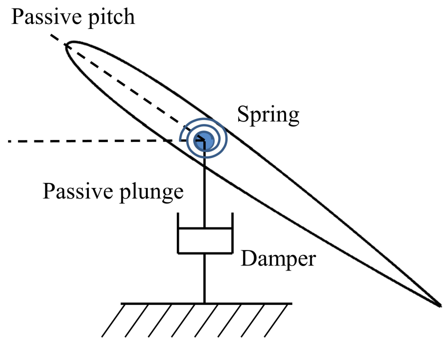

(c) System with passive pitch and plunge motion

.

Fig. 2.2: Schematics of a flapping foil power generator with prescribed, semi-passive and fully passive motions, after Young et al. (2014) and Xiao & Zhu (2014).

er generators can be classified into three categories (Fig. 2.2): systems with prescribed pitch and plunge motions, one motion prescribed and the other flow-induced and fully flow induced pitch and plunge motions. In the fully prescribed system (Fig. 2.2a), if the time averaged input power to drive the foil is negative in one flapping cycle, the system is considered as extracting power. Due to the specified pitch and plunge motions, models based on this activation type are easy to implement and favoured in theoretical and numerical studies. Generally, in the semi-passive system (Fig. 2.2b), the pitch motion is imposed and the foil responses to the hydrodynamic force by undergoing a plunge motion on which power is extracted via a electric generator. Because of the requirement of power input to drive the pitch motion, the net power extracted from the flow is the power extracted from the plunge motion minus the power required for the pitch motion. The semi-prescribed system is commonly implemented by a motor driving pitch motion in experimental studies. Prototypes Stingray, bioStream and DualWingGenerator developed respectively by Pulse Tidal Company (Marsh 2009), BioPower System (Kloos et al. 2009) and Festo AG (Send 2016) employ the semi-passive system. In the fully passive system (Fig. 2.2c), no device is required to drive the motion of the foil. In some studies (Jones et al. 1999, Young et al. 2013), a linkage mechanism is employed to ensure a constant phase between pitch and plunge motions during operation. The prototype tested by Kinsey et al. (2011) is a single degree of freedom system with the constrained passive pitch and plunge motions. A detailed list of representative studies on the fully prescribed system, semi passive system and fully passive system is respectively summarized in Table A.1, A.2 and A.3.

2.2 Governing kinematics

Table 2.1: Summary of optimal kinematic parameters ($f^*, \theta_0, h_0, \varphi$ and x_{piv}) at which the highest efficiency using the definition in Eq. 2.6 was achieved in studies on flapping foil power generators with prescribed pitch and plunge motions. η_m is the maximum efficiency achieved by the corresponding method in the **Method** column and $\overline{C}_{Pm}$ is the power coefficient corresponding to the maximum efficiency. If α_0 was not given in the literature, it is calculated from other parameters using Eq. 2.2. NA stands for not available, NST stands for not stated, TT stands for Theodorsen's theory (Theodorsen 1979), UPM stands for the unsteady panel method, NS stands for Navier-Stokes solver, URANS stands for unsteady Reynolds averaged Navier-Stokes and EXP stands for experiment.

Authors	**Year**	**Method**	**Re**	**Geometry**	f^*	$\theta_0(^\circ)$	h_0	$\varphi(^\circ)$	x_{piv}	$\alpha_0(^\circ)$	$\overline{C}_{Pm}$	η_m
				Fully prescribed system								
Jones & Platzer	1999	UPM	∞	NACA0012	0.287[a]	71.3[b]	0.83[c]	90	0.5	15	0.52	25.7%
Davids	1999	UPM	∞	NACA0012	0.238[a]T	76.3[b]	1	90	0.5	20	0.82	34.9%[d]

[a]Original reduced frequency was defined as $k = 2\pi fc/U$. The non-dimensional frequency f^* is calculated using $f^* = fc/U$.

[b]Calculated according to the amplitude of the angle of attack α_0, plunge amplitude h_0 and non-dimensional frequency f^*.

[c]Calculated according to the maximum non-dimensional plunge velocity kh_0 and reduced frequency k.

[d]The study by Davids (1999) stated a peak efficiency of 30.0% in Table 1 on page 41. Here the efficiency of 34.9% listed in Appendix 2 on page 78 is considered.

Authors	**Year**	**Method**	**Re**	**Geometry**	f^*	$\theta_0(^\circ)$	h_0	$\varphi(^\circ)$	x_{piv}	$\alpha_0(^\circ)$	$\overline{C}_{Pm}$	η_m
Lindsey	2002	UPM	∞	NACA0014	0.270[a]	76.8[b]	0.9	90	0.55	20	>0.6[e]	>30%[e]
		NS	2.0×10^4		0.159[a]	NST	1.3	NST	NST	NA	0.53	17.2%
		URANS	1.0×10^6		0.207[a]	NST	1.3	NST	NST	NA	1.00	31.5%
Jones et al.	2003	UPM	∞	NACA0014	0.223[a]	75.3[b]	1.25	110	0.25	15	0.74	21.5%[f]
		NS	2.0×10^4		0.135[a]	73	1.3	90	0.25	25	0.91	28.9%[f]
		URANS	1.0×10^6		0.104[a]	73	1.3	90	0.25	32.4	1.25	39.8%[f]
Kinsey & Dumas	2008	NS	1100	NACA0015	0.14	76.3	1.0	90	0.333	35.0	0.86	33.7%
Simpson et al.	2008	EXP	1.3×10^4	NACA0012	0.16	85.9	1.23	90	NST	34.4	1.06	<43%[g]
Ashraf et al.	2011	NS	2.0×10^4	NACA0014	0.127	73	1.05	90	0.5	73.0	0.89	34%
					0.127	73	1.05	90	0.5	73.0	1.44[h]	54%[i]

[e] Extracted from the contours given by Lindsey (2002).

[f] Calculated according to the power coefficient and swept distance computed from Eq. 2.13 and 2.14.

[g] Original efficiency was given by Eq. 2.8. Cannot recalculate the efficiency using the definition in Eq. 2.6 without pivot location x_{piv}.

[h] Total power coefficient of multiple foils.

[i] Total efficiency of multiple foils.

Authors	**Year**	**Method**	**Re**	**Geometry**	f^*	$\theta_0(^\circ)$	h_0	$\varphi(^\circ)$	x_{piv}	$\alpha_0(^\circ)$	$\overline{C}_{Pm}$	η_m
Zhu	2011	NS	1000	Joukowski	0.14	90	1.0	90	0.35	48.7	0.81[j]	31%
Kinsey & Dumas	2012*b*	URANS	5.0×10^5	NACA0015	0.14	75	1.0	90	0.333	33.7	1.64[h]	64%[i]
Xiao et al.	2012	NS	1.0×10^4	NACA0012	0.15[k]	63.3	1.0	90	0.333	20	0.98	39%[l]
Kinsey & Dumas	2014	URANS	5.0×10^5	NACA0015	0.16	85	1.5	90	0.333	28.6	1.56	44.6%
Lu et al.	2014	NS	1.0×10^4	NACA0012	0.125[k]	47[b]	0.8	90	0.333	15	0.46	21%[m]
Xu et al.	2016	URANS	4.4×10^4	NACA0015	0.11	70	1.0	90	NST	73.0	NST	35%
					0.14	70	1.0	90	NST	73.0	NST	54%[i]
Kim et al.	2017	EXP	5.0×10^4	Elliptical	0.13	70	0.8	90	0.50	36.8	0.74[f]	38%

[j] Calculated according to the efficiency and swept distance computed from Eq. 2.13 and 2.14.

[k] Original frequency is given by the Strouhal number $St = 2fh_0/U$. The non-dimensional frequency f^* is calculated using $f^* = fc/U$

[l] The definition of efficiency in the study by Xiao et al. (2012) was the same as Eq. 2.8. Since the curve of power coefficient (Fig.5) and that of efficiency (Fig. 6) is different, definition in Eq. 2.6 is considered here.

[m] Original efficiency was given by Eq. 2.8. Recalculated the efficiency using the definition in Eq. 2.6.

Authors	Year	Method	Re	Geometry	f^*	$\theta_0(^\circ)$	h_0	$\varphi(^\circ)$	x_{piv}	$\alpha_0(^\circ)$	$\overline{C}_{Pm}$	η_m
Sun et al.	2017	URANS	6.0×10^5	NACA0015	0.12	85	1.0	90	0.333	48.0	1.03[f]	39.2%
				NACA0025	0.14	100	1.0	90	0.333	58.7	1.49[f]	54.0%
Wang et al.	2017	NS	1.3×10^4	NACA0012	0.18	82.9	1.0	90	0.333	34.4	1.05	35.5%
Semi passive system												
Shimizu	2004	TT	∞	NACA0012	0.09[a]	50	NST	NST	0.49	NA	0.34[n]	29%[o]
Shimizu	2008	TT	∞	NACA0012	0.09[a]	50	0.9	109	0.446	NA	0.34[n]	28.8%[o]
		URANS	4.6×10^5		0.09[a]	50	1.4	108	0.465	NA	0.60[n]	35.3%[o]
Zhu & Peng	2009	NS	1000	Joukowski	0.20[a]	60	NST	NST	0.333	NA	0.31	27%
Abiru & Yoshitake	2011*a*	EXP	1.2×10^5	NACA0015	0.10[a]	50	0.49	90	0.5	NA	0.30[p]	22%[o]

[n]The power coefficient is computed from the dimensional power given by Shimizu (2004) with an assumed air density of 1.225 kg/m^3.

[o]Original efficiency was given by Eq. 2.10. Recalculated the efficiency using the definition in Eq. 2.6.

[p]The power coefficient is computed from the dimensional power given in Abiru & Yoshitake (2011*a*) with an assumed water density of 998 kg/m^3.

Authors	**Year**	**Method**	**Re**	**Geometry**	f^*	$\theta_0(^\circ)$	h_0	$\varphi(^\circ)$	x_{piv}	$\alpha_0(^\circ)$	$\overline{C}_{Pm}$	η_m
Huxham et al.	2012	EXP	4.5×10^4	NACA0012	0.10	58	0.45	NST	0.25	46	0.29[q]	24%
Deng et al.	2015	NS	1000	NACA0015	0.16	75	NST	82	0.333	NA	0.57[r]	33.4%
Teng et al.	2016	NS	NACA0015	1000	0.16	75	NST	NST	NST	NA	NST	32%
Fully passive system												
McKinney & DeLaurier	1981	EXP	8.5×10^4	NACA0012	0.10	25	0.3	90	0.5[s]	14.3	0.13[n]	16%
			1.1×10^5		0.12	30	0.3	90	0.5[s]	16.9	0.17[n]	17%[o]
Davids	1999	EXP	NST	NACA0012	NST	49	0.53	92.5	0.51	NA	0.19	15.5%
Lindsey	2002	EXP	2.2×10^4	NACA0014	0.122[a]	73	1.05	NST	NST	34.0	0.25	<12%[t]

[q]Calculated from the input and output power coefficient and non-dimensionalized by $1/2\rho U^3 c$.

[r]In the study by Deng et al. (2015), $\overline{C}_{Pm}$ is 0.42. Here $\overline{C}_{Pm} = 0.57$ is considered since the original one is incorrect after communication with the authors.

[s]Deducing from Eq. 16 in the study by McKinney & DeLaurier (1981)

[t]The original efficiency in the study by Lindsey (2002) was 23%. However, according to the plunge amplitude of 1.05 and power coefficient of 0.25, the

Authors	Year	Method	Re	Geometry	f^*	$\theta_0(^\circ)$	h_0	$\varphi(^\circ)$	x_{piv}	$\alpha_0(^\circ)$	$\overline{C}_{Pm}$	η_m
Jones et al.	2003	EXP	2.2×10^4	NACA0014	0.104[a]	73[u]	1.3[u]	90	0.25[u]	32.4	0.23	8.0%[f]
Peng & Zhu	2009	NS	1000	Joukowski	0.12	40	NST	NST	0.5	NA	0.14	20%
Kinsey et al.	2011	EXP	4.8×10^5	NACA0015	0.14	75	1	90	0.333	33.7	0.77[v]	30%
					0.12	75	1	90	0.333	38.0	1.02[v,h]	40%[i]
Young et al.	2013	NS	1100	NACA0012	0.19	90	1	90	0.5	40	NST	37.9%
		URANS	1.1×10^6		0.19	90	1	90	0.5	40	NST	41.4%
Veilleux & Dumas	2017	URANS	5.0×10^5	NACA0015	0.096	83	1.26	300[w]	0.333	58[x]	1.08	33.6%

efficiency should be less than 12%

[u]Deducing from Section 2.2 in the study by Jones et al. (2003).

[v]Calculated according to the efficiency and swept distance of 2.55 chord length mentioned in the study by Kinsey et al. (2011).

[w]Peak-to-peak phase angle between the pitch and plunge motions extracted form Fig.15 in the study by Veilleux & Dumas (2017).

[x]Extracted form Fig.15 in the study by Veilleux & Dumas (2017).

Generally, the flapping foil power generator undergoes simple pitch and plunge motions, while the surge motion (parallel to the oncoming flow) was also considered in several studies (Wu et al. 2016, Jiang et al. 2016). These motions are governed by a large number of parameters which have a significant impact on the performance of the flapping foil power generator. Depending on the model used to describe the flapping motion, parameters affecting the kinematics of the flapping foil can be different between studies, especially those in the fully passive system. For comparison of the optimal operating condition achieved in parametric studies on different activation modes, five optimal kinematic parameters (non-dimensional flapping frequency f^*, pitch amplitude θ_0, non-dimensional plunge amplitude h_0, phase angle φ between the pitch and plunge motions, non-dimensional pivot location x_{piv}) which are commonly used in the literature are listed in Table 2.1. As the mean power output $\overline{C}_P$ increases linearly with h_0 when other parameters are fixed (Xiao & Zhu 2014), the optimal condition in Table 2.1 is considered as that under which the highest efficiency η defined in Eq. 2.6 is achieved.

2.2.1 Fully prescribed system

The fully prescribed system is an ideal model for theoretical analysis of the mechanisms for high energy harvesting performance since it does not take into account structural dynamics in response to the aerodynamic loads, reducing the complexity in a fluid-structure-interaction (FSI) system. The vertical position of the leading and trailing edge of the foil can be obtained simply from the motion via:

$$H_{LE}(t) = H(t) - x_{piv} c \sin\theta(t), \tag{2.13}$$

$$H_{TE}(t) = H(t) + (1 - x_{piv}) c \sin\theta(t), \tag{2.14}$$

where H_{LE} and H_{TE} are the vertical position of the leading and trailing edge respectively; $x_{piv} = X_{piv}/c$ and X_{piv} is the distance from the leading edge of the foil to the pivot point along the chord as shown in Fig. 2.1. Then the swept distance d is computed as the peak to peak value of H_{LE} or H_{TE} whichever is larger. As summarized in Table A.1, this system is commonly used in numerical studies.

In the fully prescribed system, the pitch and plunge motions are completely imposed via several kinematic parameters: the non-dimensional flapping frequency $f^* = fc/U$, the pitch amplitude θ_0, the non-dimensional plunge amplitude $h_0 = H_0/c$, the phase angle φ between the pitch and plunge motions, the non-dimensional pivot location x_{piv} and other adjustable parameters used to alter the motion profiles (Xiao et al. 2012, Lu et al. 2014). Since the pioneering study on the fully prescribed system conduced by Jones et al. (1999), many efforts have been made to identify the optimal combination of kinematic parameters to achieve high performance.

In the early parametric studies on the fully prescribed system (Jones et al. 1999, Davids 1999, Lindsey 2002, Jones et al. 2003), sinusoidal pitch and plunge motions were imposed. The kinematics of the system were governed by only 5 parameters: f^*, θ_0, h_0, φ and x_{piv}. In their study, an unsteady panel method (UPM) based on the potential flow theory was used to search optimal combinations of the kinematic parameters in the range of $f^* = 0.01 - 0.8$, $\theta_0 = 8° - 105°$, $h_0 = 0 - 5$, $\varphi = 65° - 125°$ and $x_{piv} = -0.3 - 1.3$. Since the

UPM would fail when flow separations occurred, the amplitude of the angle of attack α_0 was limited up to 20° (Davids 1999). Thus the formation of LEVs was not taken into account in the UPM simulations. Due to the limitation of computational resources, only around 15 specified cases were evaluated using a NS solver at Reynolds numbers $Re = 2 \times 10^4$ and 1×10^6, giving the highest efficiency of 39.8% at $Re = 1 \times 10^6$, $f^* = 0.104$, $\theta_0 = 73°$, $h_0 = 1.3$, $\varphi = 90°$ and $x_{piv} = 0.25$ (Lindsey 2002, Jones et al. 2003).

Kinsey & Dumas (2008) presented contours of efficiency in the range of $f^* = 0.01 - 0.25$, $\theta_0 = 0° - 90°$ at $Re = 1100$, $h_0 = 1.0$, $\varphi = 90°$ and $x_{piv} = 0.333$, giving the highest efficiency of 33.7% at $f^* = 0.14$ and $\theta_0 = 76.3°$. In addition, they tested three pivot locations $x_{piv} = 0.25, 0.333$ and 0.5 under the optimal ($f^* = 0.14$ and $\theta_0 = 76.3°$) and non-optimal ($f^* = 0.18$ and $\theta_0 = 60.0°$) conditions and concluded that the pivot location was important to the force evolutions and power extraction performance. The important role of LEV in synchronization between the plunge velocity and the lift was first proposed in this study. Zhu (2011) extended the parametric study conducted by Kinsey & Dumas (2008) in the range of $f^* = 0.05 - 0.25$, $\theta_0 = 30° - 90°$, $h_0 = 0.3 - 2.0$, $\varphi = 60° - 130°$ and $x_{piv} = 0.2 - 0.5$ at $Re = 1100$ and analysed the stability of the wake behind the turbine plane by solving the inviscid Orr-Sommerfeld equation. In this study, he mapped the influence of f^* and θ_0 on the efficiency with constant h_0 and x_{piv} and found that the peak efficiency was achieved around $f^* = 0.15$ regardless of other parameters. The analysis of wake stability indicated that the most unstable frequency in the wake coincided with the flapping frequency under the optimal operating condition.

Prescribed pitch and plunge motions of non-sinusoidal profiles have also drawn some attention in recent years. In these studies (Ashraf et al. 2011, Xiao et al. 2012, Deng et al. 2014, Fenercioglu et al. 2015, Lu et al. 2015), adjustable parameters were introduced to alter the motion profiles. To achieve high performance, these parameters need to be adjusted under given conditions since the optimal motion profiles are dependent on the pitch and plunge amplitudes (Xiao et al. 2012, Deng et al. 2014) and the phase angle between the pitch and plunge motions (Ashraf et al. 2011). In addition, the experiment conducted by Fenercioglu et al. (2015) suggested an optimal pivot point location x_{piv} of 0.25 for sinusoidal motions and of 0.5 for non-sinusoidal motions. Adopting non-sinusoidal motion makes it possible to harvest energy via the pitch motion (i.e. $C_{P\theta}$ is positive Lu et al. (2015)) and improves the performance of the flapping foil power generator(Ashraf et al. 2011, Deng et al. 2014).

Despite differences in motion profiles, parametric studies on the fully prescribed system with sinusoidal and non-sinusoidal motions suggest a similar range of optimal kinematic parameters $f^* = 0.11 - 0.18$, $\theta_0 = 60° - 100°$, $h_0 = 0.8 - 1.5$, $\varphi = 90° - 110°$ and $x_{piv} = 0.25 - 0.5$ for high efficiency (η) (Table 2.1). In addition, the contribution of the power extracted via the plunge motion ($\overline{C}_{Ph}$) dominates the overall power output ($\overline{C}_P$) under the optimal kinematic conditions.

2.2.2 Semi passive system

In the semi passive system, it is intuitive to impose the pitch motion and harvest energy via the flow induced plunge motion since studies on the fully prescribed system indicate power generated from the plunge motion is much higher than that from the pitch motion. As shown in Fig. 2.3, the foil responds in the plunge direction to the lift generated by the pitch motion. The plunge amplitude is constrained by the spring and the damper in the plunge direction

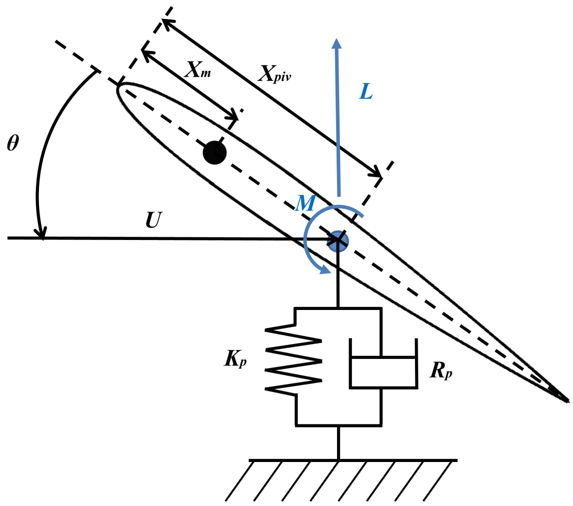

Fig. 2.3: Schematic of a power generator with semi-passive motions, after Zhu et al. (2009).

with a stiffness of K_h and R_h respectively. The equation of the oscillation in the plunge direction is expressed as (Shimizu et al. 2008, Zhu et al. 2009):

$$m_h\ddot{H} + R_h\dot{H} + K_hH = L + m_{foil}\left(X_m - X_{piv}\right)\left(\ddot{\theta}\cos\theta - \dot{\theta}^2\sin\theta\right), \quad (2.15)$$

where m_h is the mass of all the parts in the system undergoing the plunge motion; m_{foil} is the mass of the foil; K_h is the spring stiffness in the plunge direction; R_h is the viscous damping in the plunge direction and X_m is the distance between the leading edge of the foil and the foil mass center. To simplify the problem, it is assumed $m_h = m_{foil}$ and the system is governed by seven non-dimensional parameters: the flapping frequency of the imposed pitch motion (f^*), the pitch amplitude (θ_0), the pivot location (x_{piv}), the location of the foil mass center ($x_m = X_m/c$), the mass ratio ($\mu_m = m_{foil}/\left(\rho c^2\right)$), the stiffness in the plunge direction ($k_h = K_h/\left(\rho U^2\right)$) and the damping in the plunge direction ($r_h = R_h/\left(\rho Uc\right)$). In this system, the power is extracted from the plunge motion via the damper. The net mean power output over one flapping cycle ($\overline{P}$) is defined as the mean power output generated via the plunge motion ($\overline{P}_h$) minus the mean power consumed to maintain the pitch motion ($-\overline{P}_\theta$).

To achieve high performance, Shimizu (2004) and Shimizu et al. (2008) solved an optimization problem of 2 objectives ($\overline{C}_P$ and η) using an evolutionary algorithm (EA). They assumed that the center of the foil mass coincided with the the pivot point $x_m = x_{piv}$ and the pitch amplitude $\theta_0 = 50°$. Thus the design variables reduced from seven to five: $f^* = 0 - 0.09$[a], $x_{piv} = 0 - 1$, $\mu_m = 4m_p/\left(\pi\rho c^2\right) = 5 - 200$, the frequency ratio $\omega_p/\omega = 0.5 - 1.5$, where ω_p is the natural angular velocity of the plunge motion and $\omega = 2\pi f$ is the angular velocity of the imposed pitch motion, and the structure damping coefficient in the plunge direction $\beta_p = 0 - 2$ (the term $R_h\dot{H}$ in Eq. 2.15 was replaced by $iK_h\beta_p H$, where $i = \sqrt{-1}$). In their study (Shimizu et al. 2008), 110,000 solutions were evaluated using the Theodorsen's theory (Theodorsen 1979) and 386 non-dominated solutions were obtained. Then 8 non-dominated solutions were evaluated using an unsteady Reynolds averaged Navier-Stokes (URANS) solver with Baldwin and Lomax turbulence model at $Re = 4.6 \times 10^5$. The peak efficiency given by the simulations using the URANS solver was 35.3%[b], while the Theodorsen's theory with planar wake assumption underestimated the efficiency of the 8 non-dominated solutions with the peak efficiency of 28.8%[b] under a different condition from that given by the UNRANS simulation. This demonstrated the important role of flow separation in performance improvement since the Theodorsen's theory did not account for LEV formation. Their results (Shimizu 2004, Shimizu et al. 2008) indicated that when the

[a]Orginal reduced frequency was defined as $k = \pi f c/U$.

[b]Original efficiency was given by Eq. 2.8. Recalculated the efficiency using the definition in Eq. 2.6.

power output was emphasized, the system underwent large plunge amplitudes ($h_0 \geq 0.9$). In addition, Abiru & Yoshitake (2011*b*) experimentally studied the influence of f^*, θ_0 and β_p using the same structure model as Shimizu (2004) and Shimizu et al. (2008) and achieved a highest efficiency of 22%.

Zhu et al. (2009) investigated the influence of θ_0, x_{piv}, k_h and r_h on the performance of the semi passive system given by Eq. 2.15 using the Theodorsen's theory and a 3-dimensional (3D) solver based on the potential flow theory, suggesting the optimal parameters of $x_{piv} = 0.5$, $k_h = 0$ and $r_h = \pi$. Due to the limitation of the numerical methods, the pitch amplitude was limited up to 30° to avoid flow separations. Zhu & Peng (2009) extended the work with $\mu_m = 0$, $k_h = 0$, $r_h = \pi$ and $Re = 1000$ using a NS solver. The influence of $x_{piv} = 0 - 1$ and $f^* = 0.03 - 0.41$ on the performance was first examined at $\theta_0 = 15°$, where $\eta < 8\%$. They suggested the optimal range of $f^* = 0.13 - 0.22$[a] and $x_{piv} = 0.2 - 0.5$. Then $\theta_0 = 5° - 60°$ with $f^* = 0.2$, $x_{piv} = 0.333$ was investigated and the peak efficiency of 27% was achieved at $\theta_0 = 60°$. The role of the interaction between the LEV and the foil motions in the energy harvesting performance at large pitch amplitudes was emphasized. Following the work conducted by Zhu & Peng (2009), Deng et al. (2015) mapped contours of efficiency in the range of $f^* = 0.08 - 0.22$ and $\theta_0 = 60° - 90°$, giving the highest efficiency of 33.4% at $f^* = 0.16, \theta_0 = 75°$ and $\varphi = 81.8°$. In addition, they found that the efficiency decreased monotonically with the increase of the mass ratio. The study conduced by Teng et al. (2016) verified the optimal $f^* = 0.16, \theta_0 = 75°$ suggested by Deng et al. (2015), and showed that the non-sinusoidal pitch motion could not increase the upper boundary of the energy harvesting performance, while it improved the performance under the non-optimal condition ($f^* = 0.12$ or $\theta_0 = 45°$).

Compared to the fully prescribed system, additional parameters x_m, μ_m,

k_h and r_h are introduced in the semi passive system. Power is extracted via the plunge motion while the pitch motion consumes power to maintain the periodical flapping motion. In addition, h_0 and φ are determined by the plunge response to the loads acting on the foil. However, it is noted that the optimal parameters in the semi passive system ($f^* = 0.09 - 0.22$, $\theta_0 = 50 - 75°$, $h_0 = 0.4 - 1.4$, $\varphi = 80 - 110°$ and $x_{piv} = 0.2 - 0.5$ in Table 2.1) are similar to those in the fully prescribed system (Section 2.2.1).

2.2.3 Fully passive system

According to the constraints applied on the pitch and plunge motions, the fully passive system can operate as one degree of freedom (DOF) system or two DOF system. Fig. 2.4a shows a typical one DOF system considered by Young et al. (2013). The pitch and plunge motions were modelled as functions of the flywheel angle β: $H = f(\beta)$ and $\theta = g(\beta)$. In the two DOF system, there is no mechanical linkage between the DOFs and both DOFs (in the pitch and plunge directions) freely respond to the aerodynamic loads (the lift and moment) acting on the foil, as shown in Fig. 2.4b.

One degree of freedom system

The one DOF system is favoured in experimental studies (McKinney & DeLaurier 1981, Jones et al. 1999, Davids 1999, Lindsey 2002, Jones et al. 2003, Kinsey et al. 2011, Young et al. 2013) since the parameters are convenient to compare with the optimal ones obtained from numerical studies on the fully prescribed system, especially the phase difference between the pitch and plunge motions. It is verified by several studies (Ashraf et al. 2011, Zhu 2011) that the optimal phase angle φ for high performance of the fully prescribed

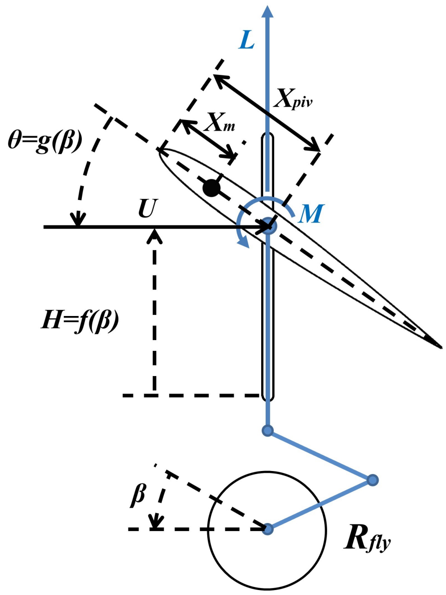

(a) One degree of freedom system.

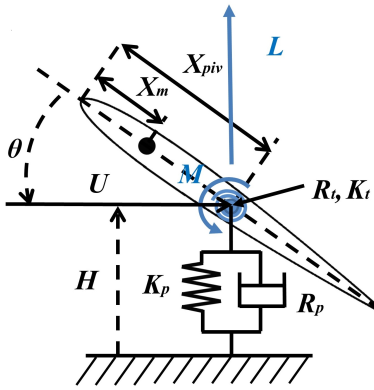

(b) Two degree of freedom system.

Fig. 2.4: Schmatics of a flapping foil power generator with flully passive motions, after Young et al. (2013) and Veilleux & Dumas (2017).

system is around 90° (Section 2.2.1). Thus, it is intuitive to impose $\varphi = 90°$ via the coupling of the pitch and plunge motions.

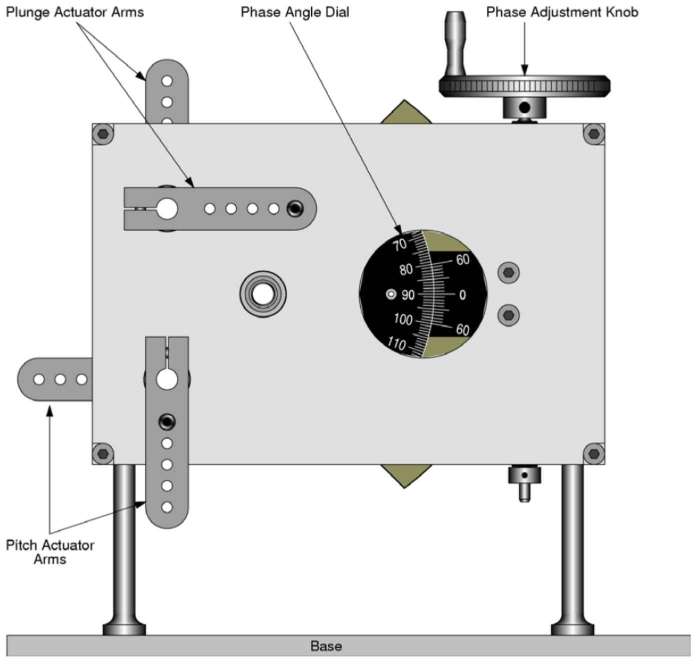

Fig. 2.5: Schematic of actuator arms and phase adjuster used in the experiment of Lindsey (2002).

In the experimental study conducted by McKinney & DeLaurier (1981), the pitch and plunge motions were linked via a Scotch yoke. They focused on the influence of flapping frequency $f^* = 0.08 - 0.20$ and phase angle $\varphi = 60° - 135°$, giving the highest efficiency of 17% at $f^* = 0.12$ and $\varphi = 90°$. Because of the small pitch and plunge amplitudes ($\theta_0 < 30°$ and $h_0 = 0.3$), the performance of this device did not show advantage over other types of wind turbines (McKinney & DeLaurier 1981). Around 20 years later, Jones et al. (1999), Davids (1999), Lindsey (2002) and Jones et al. (2003) conducted successive experimental studies for comparison with their parametric studies using the UPM and NS solver. The phase angle φ was controlled by a phase adjuster through pitch and plunge actuator arms (Lindsey 2002), as shown in Fig. 2.5. They verified the optimal φ was around 90° and increased θ_0 up to

73° and h_0 up to 1.3. However, the peak efficiency experimentally achieved by this lab-scale device was lower than 20%, which was much lower than that of 39.8% given by the URANS solver. The significant performance reduction in the experiment was attributed to the limitations of the apparatus such as high mechanical friction and defects of the aerofoil surface resulting from absorbed water into the wood (Jones et al. 2003).

Kinsey et al. (2011) tested a prototype mounted on a pontoon boat with f^* up to 0.2. Other kinematic parameters were chosen with respect to the optimal condition at $\theta_0 = 75°$, $h_0 = 1$, $\varphi = 90°$ and $x_{piv} = 0.333$ given by their previous parametric study on the fully prescribed system (Kinsey & Dumas 2008). The pitch motion was linked to the plunge motion through a four-link mechanism. An energy harvesting efficiency of 30% for a single foil was demonstrated. Young et al. (2013) considered a similar one DOF system (Fig. 2.4a) where the pitch and plunge motions were functions of the flywheel angle: $H = f(\beta + \varphi)$ and $\theta = g(\beta)$, with $\varphi = 90°$. They examined the influence of $\theta_0 = 30° - 90°$, x_{piv}, the damping coefficient of the flywheel $16R_{fly}/(\pi\rho c^3 U) = 0 - 10$ and the foil and flywheel masses on η. In addition, instead of linking the pitch angle to the flywheel angle, it was found that by linking the angle of attack to the flywheel angle ($\alpha = g(\beta)$), the peak efficiency of the one DOF system increased from 29.6% to 41.4%.

Two degree of freedom system

In the 2 DOF system, the response in the plunge direction to the lift is given by Eq. 2.15, the same as that in the semi passive system (Section 2.2.2). The response in the pitch direction to the moment is expressed as (Veilleux &

Dumas 2017):

$$J\ddot{\theta} + R_\theta\dot{\theta} + K_\theta\theta = M + m_{foil}\left(X_m - X_{piv}\right)\ddot{H}\cos\theta, \quad (2.16)$$

where J is the moment of the inertia, R_θ is the viscous damping in the pitch direction and K_θ is the spring stiffness in the pitch direction. If it is assumed $m_h = m_{foil}$ in Eq. 2.15, the system is governed by eight non-dimensional parameters: the pivot location (x_{piv}), the location of the foil mass center (x_m), the mass ratio (μ_m), the stiffness in the plunge direction ($k_h = K_h/\left(\rho U^2\right)$), the damping in the plunge direction ($r_h = R_h/\left(\rho U c\right)$), the moment of the inertia ($I = J/\left(\rho c^4\right)$) the stiffness in the pitch direction ($k_\theta = K_\theta/\left(\rho U^2 c^2\right)$) and the damping in the pitch direction ($r_\theta = R_\theta/\left(\rho U c^3\right)$). In this system, the averaged power due to the inertia from the plunge motion balances that from the pitch motion (Veilleux & Dumas 2017). Thus the contribution of the inertia to the mean power output $\overline{C}_P$ is zero.

Peng & Zhu (2009) analysed the stability of a 2 DOF system using the Theodorsen's theory in the range of $x_{piv} = 0-1$ and $k_\theta = 0-1$ with $m_{foil} = 0$, $I = 0$, $k_h = 0$, $r_h = \pi$ and $r_\theta = 0$. They concluded that when $x_{piv} \geq 0.25$ and k_θ was sufficiently small (depending on x_{piv}), the system was unstable. In addition, results given by a NS solver at $Re = 1000$ showed that when $x_{piv} = 0.4, 0.5$ and 0.6, the peak η was achieved around 20% at different $k_\theta = 0.022$, 0.054, and 0.078 respectively. Zhu (2012) extended their work by considering $k_h = 1$, 2 and 3 and the density ratio $\rho_{foil}/\rho = 0, 1$ and 10, where ρ_{foil} is the density of the foil, in the shear flow. It was found that k_h had impact on the performance (e.g. the maximum efficiency increased from around 16% at $k_h = 1$ to around 18% at $k_h = 2$). In addition, when the mass was concentrated at the leading edge with $\rho_{foil}/\rho = 10$, the maximum efficiency increased from

16% to 31% compared to the case with $\rho_{foil}/\rho = 0$. This was attributed to the increase of the moment of inertia. Compared to the case with negligible ρ_{foil}/ρ, the case with high ρ_{foil}/ρ showed decreases in f^* from $0.29 - 0.31$ to $0.16 - 0.25$ and increases in θ_0 from $25° - 50°$ to $32° - 100°$, approaching the optimal parameters in the fully prescribed system (Section 2.2.1). However, when $x_m = x_{piv}$, increasing μ_m resulted in performance reduction, which was also verified by Jiang et al. (2017).

Veilleux & Dumas (2017) performed a gradient-like optimization to maximize η and/or $\overline{C}_P$ where the trade off was not considered. A single parameter called static imbalance $s_{im} = \mu_m (x_m - x_{piv})$ with $x_{piv} = 1/3$ was introduced in their study and the number of design variables reduced to seven (s_{im}, μ_m, k_h, r_h, I, k_θ and r_θ). 71 solutions were evaluated using URANS at $Re = 5 \times 10^5$, giving an optimal solution with $\eta = 33.6\%$ and $\overline{C}_P$ at $s_{im} = -0.03$, $\mu_m = 3.0$, $k_h = 1.2$, $r_h = 1.5$, $I = 0.10$, $k_\theta = 0.03$ and $r_\theta = 0.12$. Under the optimal condition, the parameters determined by the structure responses were $f^* = 0.096$, $\theta = 83°$, $h_0 = 1.26$ and $\varphi = 300°$[c]. It was found that $\varphi = 300°$ under the optimal condition was quite different from that of 90° in the fully prescribed system. Wang, Du, Zhao & Sun (2017) gave similar $\varphi = 296°$ under the optimal condition ($\eta = 30\%$), while the non-optimal case with $\eta = 8\%$ gave $\varphi = 352°$. Moreover, the study conducted by Wang, Du, Zhao & Sun (2017) demonstrated that the performance was sensitive to x_{piv}, as was the structure response region (also found by Peng & Zhu (2009)). For instance, the peak $\overline{C}_P$ in the range of $r_h = 0 - 6$ increased from 0.06 to 0.92 when x_{piv} increased slightly from 0.33 to 0.35 at similar k_h and k_θ (i.e. k_h and k_θ were proportional to $(f_p c/U)^2$ which is $(1/2.9)^2$ at $x_{piv} = 0.33$ and $(1/3.0)^2$ at $x_{piv} = 0.35$, where

[c]Peak-to-peak phase angle between the pitch and plunge motions extracted form Fig.15 in Veilleux & Dumas (2017)

f_p is the natural frequency of the system in the plunge direction) and the same x_m, μ_m, I and r_θ.

2.3 Geometry of the foil and the system

2.3.1 Foil shape, aspect ratio and end plates

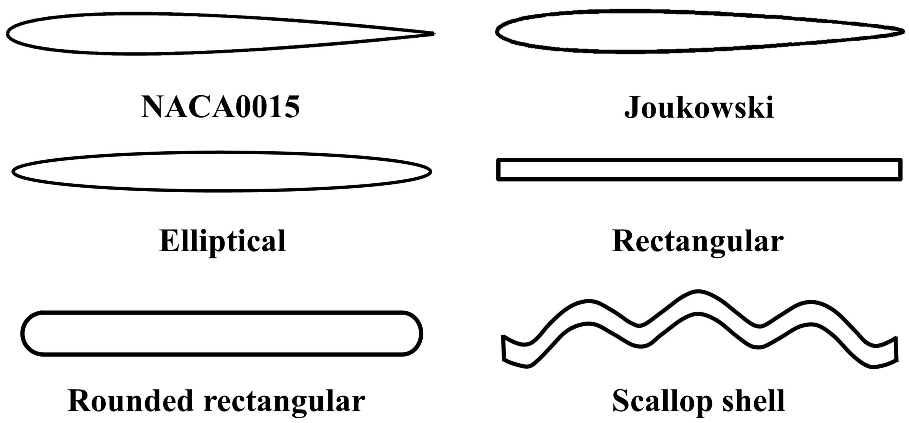

Fig. 2.6: Foil with different shapes of the cross section.

There have been several investigations on the cross section shape of the foil. Besides aerofoils such as the NACA series and Joukowski foil, some other cross sections considered in the studies of the flapping foil power generator are shown in Fig. 2.6. Kinsey & Dumas (2008) considered three NACA 4 digit aerofoils with a thickness of 2%, 15% and 20% under two conditions ($Re = 1100$): the non-optimal condition without LEVs and the optimal with LEV. They concluded that the influence of aerofoil thickness on the performance was insignificant. Kim et al. (2017) experimentally examined an elliptical foil and rectangular foil with different thickness and edge shapes in the range of $f^* = 0.09 - 0.17$ at $Re = 5 \times 10^4$, drawing the same conclusion as Kinsey & Dumas (2008). Le et al. (2013) investigated scallop shell shaped (Fig. 2.6), NACA0008 and cambered NACA0012 foils in the range of $f^* = 0.1-0.15, \theta_0 = 55° - 65°$ and $h_0 = 0.7-1.1$ at $Re = 9\times10^4$. They found that the scallop shell shaped foils did not give any advantage over NACA0008 foil in the performance and concluded that the performance of the flapping foil power generator was primarily dependent on the kinematics. However, Sun et al. (2017) found that the situation was different at high Reynolds numbers $Re = 6 \times 10^5$. They mapped the contours of efficiency in the range of $f^* = 0.08 - 0.26$ and $\theta_0 = 50° - 110°$ using a UNRANS solver with the Spalart Allmaras turbulence model, considering NACA 4 digit aerofoils with different thickness. It was found that the peak efficiency of 39.2% was achieved at $f^* = 0.12$ and $\theta_0 = 85°$ with the NACA0015 foil while that of 54.0% was achieved at $f^* = 0.14$ and $\theta_0 = 100°$ with the NACA0025 foil.

Studies on a finite span wing with the aspect ratio (AR=b/c, where b is the span) from 1 to 10 showed that the efficiency decreased with decreasing AR due to three-dimensional (3D) effects (Simpson et al. 2008, Kinsey & Dumas 2012*c*, Drofelnik & Campobasso 2015, 2016, Kim et al. 2017). Specifically, Deng et al. (2014) found that when finite AR was considered, the fully prescribed system undergoing sinusoidal pitch motion gave lower efficiency than that undergoing non-sinusoidal pitch motion even if the system undergoing non-sinusoidal pitch motion gave better efficiency when the span was infinite. This is because the enhanced LEV observed in the system undergoing non-sinusoidal pitch motion for 2D flows was susceptible to 3D instabilities due to the spanwise flow reducing the streamwise velocity. In addition, the reduction in energy harvesting performance due to 3D effects (e.g. lift reduction near the tip due to the downwash associated with the tip vortex and variation in the vortex structure across the span) was alleviated when end plates were mounted (Abiru & Yoshitake 2011*b*, Kinsey & Dumas 2012*c*, Drofelnik & Campobasso 2015, 2016, Kim et al. 2017). Kim et al. (2017) examined different sizes of the end plates and found that when the distance from the foil to the edge of the end plate was $0.75c$, the efficiency of the flapping wing with AR=2.5, 3.5 and 4.5 was the highest. Even though the end plates were beneficial to the suppression of the tip vortex effects, the increase of friction and interactions between the end plates and the flow may balance this benefit. Thus there existed an optimal size of end plates for performance improvement.

2.3.2 Active and passive deformation

In flapping foil propulsion, it has been demonstrated by a number of studies that the deformation of the foil has beneficial effects on the force generation (Shyy et al. 2010). However, studies on the effects of the foil deformation on the energy harvesting performance are limited (Young et al. 2014, Xiao & Zhu 2014).

Liu et al. (2013) controlled the deformation of the leading and trailing edges of a NACA0012 foil in the fully prescribed system, as shown in Fig. 2.7a. In their study, α_0 was in the range of $0° - 10°$, which was much lower than the optimal $\alpha_0 = 30° - 40°$ given by the experimental study of Kim et al. (2017). A peak efficiency of 32% was achieved by controlling the deformation of the trailing edge at $f^* = 0.2$, compared to that of 13% for a rigid foil at $f^* = 0.16$ with other kinematic parameters remaining the same, specifically $\alpha_0 = 10°$.

Tian et al. (2014) examined the influence of the active deformation of a flat plate under the optimal condition of the fully prescribed system suggested by Kinsey & Dumas (2008) ($f^* = 0.14$, $\theta_0 = 76.3°$, $h_0 = 1.0$, $\varphi = 90°$ and $x_{piv} = 0.333$, resulting in $\alpha_0 = 35°$). An efficiency of 38.2% was achieved via controlling the leading segment, 11.3% higher than that of 33.4% given by

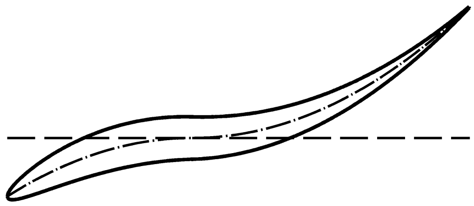

(a) Control of camberline deformation at the leading and trailing edges.

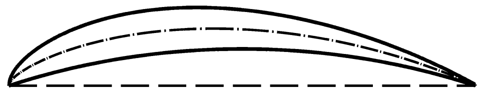

(b) Control of camberline deformation at the mid chord.

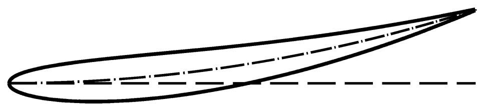

(c) Control of camberline deformation at the trailing edge.

Fig. 2.7: Active deformation via controlling the camberline at different chordwise location, after Liu et al. (2013), Hoke et al. (2015) and Zhu et al. (2015). The dashed line represents the camberline of the rigid foil and dash-dot line is the camberline of the deformable foil.

Table 2.2: Comparison of deformation enhanced performance in the literature. If α_0 was not given in the literature, it is calculated from other parameters using Eq. 2.2. η_r and η_d are the maximum efficiency achieved by employing the rigid foil and deformable foil, respectively. $\overline{C}_{P\mathrm{r}}$ and $\overline{C}_{P\mathrm{d}}$ are respectively the power coefficient corresponding to the efficiency η_r and η_d. NA stands for not available and NST stands for not stated.

Authors	Year	α_0 (°)	η_r (%)	η_d (%)	$\frac{\eta_\mathrm{d}-\eta_\mathrm{r}}{\eta_\mathrm{r}}$	$\overline{C}_{P\mathrm{r}}$	$\overline{C}_{P\mathrm{d}}$	$\frac{\overline{C}_{P\mathrm{d}}-\overline{C}_{P\mathrm{r}}}{\overline{C}_{P\mathrm{r}}}$
Active deformation								
Liu et al.	2013	10	12	32	1.67	0.14	0.75	4.36
Tian et al.	2014	35	33.4	38.2	0.14	0.86	0.98	0.14
Hoke et al.	2015	35	32.9	37.9	0.16	0.84	0.97	0.15
Zhu et al.	2015	35	35.4	41.1	0.16	0.91	1.05	0.15
Passive deformation								
Tian et al.	2014	35	32.4	30.2	−0.09	0.86	0.82	−0.04
Wu et al.	2015	20	23.1	33	0.44	0.33	0.56	0.70
Wu et al.	2015	NST	15	20	0.33	0.22	0.41	0.86
Jeanmonod & Olivier	2017	35	31.6	NST	NA	0.81	0.83	0.02

the rigid plate under the same kinematic condition. Hoke et al. (2015) and Zhu et al. (2015) performed the active control of the camberline deformation at the mid chord (Fig. 2.7b) and the trailing edge (Fig. 2.7c) respectively under the same optimal condition of the fully prescribed system, giving similar increases in the efficiency by 15.8% and 16.1% to 37.9% ($Re = 1100$) and 41.1% ($Re = 10^4$), respectively (see Table 2.2). In addition, Hoke et al. (2015) noted that the power consumption for active deformation was significant (e.g. the efficiency decreased from 37.9% to around 34.5%), which was generally neglected in the studies of the active deformation.

The performance of the flexible system containing a rigid foil of $0.7c$ and a flexible flat plate of $0.3c$ pinned to the trailing edge of the rigid foil under non-optimal conditions was investigated by Wu, Shu, Zhao & Tian (2015) in the fully prescribed system and Wu, Wu, Tian, Zhao & Li (2015) in the semi passive system. In the fully prescribed system, the peak efficiency of $\eta = 33\%$ was achieved at $\alpha_0 = 20°$ and $f^* = 0.2$, 44% higher than that of 23% achieved by the rigid system at $f^* = 0.15$ with other parameters remaining the same. In the semi passive system, the peak efficiency of around 20% was achieved at $\theta_0 = 40°$ (optimal $\theta_0 = 50° - 75°$ in Section 2.2.2), compared to that of around 15% given by the rigid system under the same kinematic condition.

Tian et al. (2014) and Jeanmonod & Olivier (2017) discussed the influence of the flexibility on the performance of the fully prescribed system under the optimal kinematic condition suggested by Kinsey & Dumas (2008). Flat plates with similar flexibility distributions were employed in their studies: a uniformly flexible plate, a plate with a flexible leading segment and a plate with a flexible trailing segment. In their studies, the flexible cases did not show significant performance improvement under the optimal condition. In contrast, Jeanmonod & Olivier (2017) demonstrated the capability of the flexibility to improvement the performance under non-optimal conditions, which was similar to Wu, Shu, Zhao & Tian (2015).

In Table 2.2, it is noted that the improvement in the power output $\overline{C}_P$ by employing deformable foils is greater than that in the efficiency η when $\alpha_0 \leq 20°$ since the swept distance increases significantly due to the foil deformation. On the other hand, improvements in $\overline{C}_P$ and η are similar under the optimal kinematic condition of the rigid foil where $\alpha_0 = 35°$.

2.3.3 Multiple foil configurations

Interactions between flapping foil turbines may have significant impact on the performance in the application of wind farms. Thus, the arrangement of the turbines, such as the distance between the turbines X_{shift} and the phase difference ψ between the flapping motions needs to be considered. In the tandem foil configurations, the foils generally undergoing pitch and plunge motions with the same neutral position and different phase angles; thus the swept distance used to compute the efficiency in Eq. 2.6 is the same as the single foil system. In the parallel foil configurations, the swept distance is measured as the overall area swept by all the foils.

The system with two foils in tandem was first employed by Lindsey (2002) and Jones et al. (2003) in their experimental studies with a constant non-dimensional distance $x_{shift} = X_{shift}/c = 9.6$ and $\psi = 90°$. Ashraf et al. (2011) conducted simulations of a tandem configuration with sinusoidal and non-sinusoidal pitch and plunge motions in the range of $x_{shift} = 2{-}6, \psi = 0°{-}180°$. In their study, the peak efficiency of 50% for the system with sinusoidal motions was achieved at $x_{shift} = 2$ and $\psi = 180$, while that of 54% for the system with non-sinusoidal motions was achieved at $x_{shift} = 6$ and $\psi = 135$. Due to the interactions between the two foils, the front foil undergoing non-sinusoidal motions gave higher $\overline{C}_P$ of 1.00 than that of 0.89 given by the single foil under the same optimal kinematic condition. Moreover, the peak efficiency of the tandem configuration with sinusoidal motions was achieved at $\varphi = 110°$, larger than that of 90° in the single foil system.

Xu et al. (2016) found that the arrangement of the two foils also influenced the optimal value of f^* when the system undergoing sinusoidal pitch and plunge motions. In their work, the peak efficiency of 54%, 54% and 50% given by the tandem system with different $x_{shift} = 4.5$, 5.4 and 6.3 and the same $\psi = 180°$ was achieved at $f^* = 0.16$, 0.15 and 0.12 respectively. In addition, the fully passive system of 1 DOF experimentally tested by Kinsey et al. (2011) achieved the highest efficiency of 30% at $f^* = 0.14$ for a single foil and that of 40% at $f^* = 0.12$ for two foils in tandem with $x_{shift} = 5.4$ and $\psi = 180°$. A similar shift in the optimal f^* was found in their numerical study using 2D RANS (Kinsey & Dumas 2012*b*) where a peak efficiency of 64% was achieved at $f^* = 0.16$ for two foils in tandem with $x_{shift} = 5.4$ and $\psi = 180°$ while that of 40% was achieved at $f^* = 0.14$ for a single foil.

In the experiment conducted by Abiru & Yoshitake (2011*a*), a semi passive system containing two foils in tandem was tested in the range of $x_{shift} = 0.6-5$, $\psi = 0°$ and 180°. They found that the amplitude of the imposed pitch motion θ_0 had little impact on the performance when $x_{shift} > 2$. In the range of $x_{shift} = 4 - 5$, the influence of the interactions between the two foils on the performance was negligible. In contrast to the optimal $\theta_0 = 50°$ of the single foil system given by their previous experimental study (Abiru & Yoshitake 2011*b*), the peak efficiency ($\eta_{max} = 46\%$) of the tandem system was achieved at low $\theta_0 = 30°$ with $x_{shift} = 1.5$ and $\psi = 180°$.

Wu, Zhan, Wang & Zhao (2015) and Wu, Chen & Zhao (2015) numerically investigated multiple foils in parallel configurations with auxiliary foils of $0.5c$ undergoing the pitch motion in the fully prescribed and semi passive systems. The phase difference and distance between the flapping foil turbine and the auxiliary foils were adjusted to achieve high performance. In the fully prescribed system, an auxiliary foil was placed below the flapping foil turbine. With the auxiliary foil placed $0.85c$ from the neutral position of the flapping foil and a phase angle of 135°, a highest efficiency of 34.7% was found at $f^* = 0.18$, while the single flapping foil achieved a peak efficiency of 29.1% at $f^* = 0.16$. In the semi passive system, two auxiliary foils were respectively placed above and below the flapping foil, giving a highest efficiency of 43.1%. In these studies, the contribution of the flapping foil and the auxiliary foils to power output P was considered, while the available power in the flow P_r only contained the kinetic energy of the flow passing through the distance swept by the flapping foil, neglecting that swept by the auxiliary foils. When the swept distance is measured as the overall area swept by all the foils, the peak efficiency given by the parallel configuration in the fully prescribed system is 27.6%.

2.4 Environmental effects

2.4.1 Reynolds number

The importance of the timing of the LEV formation, convection and interaction with the flapping foil was numerically and experimentally demonstrated by several studies in the laminar flow region ($Re \leq 10^4$) (Kinsey & Dumas 2008, Young et al. 2014, Fenercioglu et al. 2015). In addition, studies in the range of $Re = 100 - 10,000$ indicated that the efficiency increases with the increase of Re (Kinsey & Dumas 2008, Zhu 2011, Wu, Yang, Shu, Zhao & Yan 2015). In the transitional flow region ($10^4 < Re \leq 10^5$), the LEV dynamics was little affected and the LEV dominated performance improvement observed in the laminar flow region carried over to the transitional flow region (Ashraf et al. 2011, Young et al. 2014). The numerical study on a self-sustained pitch-plunge flapping foil in the range of $Re = 4 \times 10^4 - 12 \times 10^4$ indicated that laminar calculations agreed well with the experimental data while predictions of the natural frequency and angle of attack made by URANS simulations were not as good as those given by the laminar calculations when the aerodynamic forces dominated the foil dynamics (Veilleux & Dumas 2013). In addition, predictions given by URANS with the SA (Spalart-Allmaras) and $k - \omega$ SST (Menters shear stress transport) turbulence model showed significant differences when $Re > 8 \times 10^4$.

When the turbulent flow was considered ($Re > 10^5$), the synchronization of the LEV formation and foil motions was lost for high performance cases (Campobasso et al. 2013, Kinsey & Dumas 2014). Numerical study of Kinsey & Dumas (2014) showed that high energy extraction performance was achieved when α_0 was around 33° and the maximum non-dimensional rate of change of the angle of attack $\dot{\alpha}c/U$ was around 0.55, where no LEV was observed in some cases. Sun et al. (2017) numerically studied NACA 4 digit foils with different thickness at $Re = 6 \times 10^5$ (Section 2.3.1). They found that without the LEV formation, the thick foil (NACA0025) generated more power via the plunge motion due to higher C_L, resulting in better performance ($\eta = 54\%$) compared to the case using NACA0015 where LEV was observed ($\eta = 39\%$). The performance of a single foil predicted by 2D and 3D URANS simulations conducted by Kinsey & Dumas (2012*a*) showed reasonable agreement with that given by the prototype test conducted by Kinsey et al. (2011). However, both

2D and 3D URANS simulations considering the tandem foil configuration over-predicted the peak efficiency ($\eta = 65\%$ at $f^* = 0.14$ for 2D and $\eta = 55\%$ at $f^* = 0.14$ for 3D) compared to the experiment (Kinsey et al. 2011) ($\eta = 40\%$ at $f^* = 0.12$). In addition, Kinsey & Dumas (2012*a*) found that different turbulence models (SA, $k-\omega$ standard, $k-\omega$ SST) predicted different timing and position of flow separations, which was also verified by Young et al. (2013).

2.4.2 Boundary effects

Besides flow conditions such as the velocity and viscosity of the flow, interactions between the flapping foil and the surrounding environment also have impact on the energy harvesting performance. The influence of constrained flow, where the foil was confined in a channel as shown in Fig. 2.8a, was investigated by Karakas et al. (2016) and Gauthier et al. (2016). In the experiment conducted by Karakas et al. (2016), two side walls were placed at various distances from a flat plate undergoing pitch and plunge motions. Two end plates were mounted at the top and bottom of the channel to eliminate 3D effects. It was found that the wall effect reduced the efficiency of the flapping foil turbine undergoing prescribed non-sinusoidal motions, while it improved the efficiency of the turbine undergoing sinusoidal motions from around 13% to 17%, compared to the turbine in the free flow. Gauthier et al. (2016) numerically investigated a NACA0025 foil with AR=10 undergoing sinusoidal pitch and plunge motions. The flow was constrained in a rectangular channel consisting of horizontal planes. With the optimal distances between the solid walls and the flapping foil (i.e. solid walls were placed 1.27 c above and below the neutral position of the plunge motion), a considerable efficiency of 77% [d]

[d]Calculated from the swept distance and the power ratio defined in Gauthier et al. (2016).

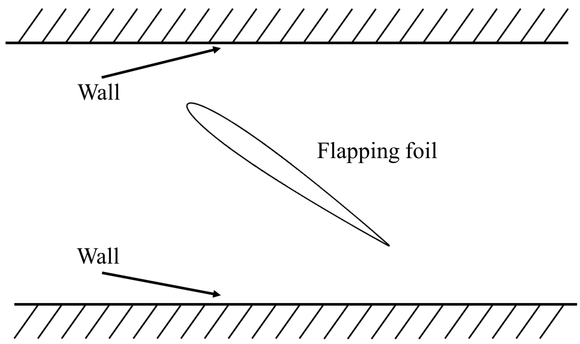

(a) A flapping foil placed in the constrained flow.

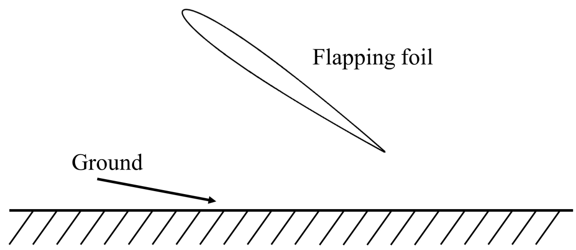

(b) A flapping foil placed near the ground.

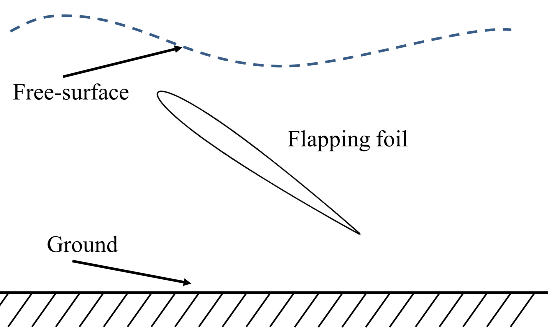

(c) A flapping foil placed in the shallow water.

Fig. 2.8: Schematic of a flapping foil placed in the domain with different boundary conditions, after Karakas et al. (2016), Wu, Yang, Shu, Zhao & Yan (2015) and Liu (2017).

was achieved. Similar to studies on rotary turbines installed in channels, the efficiency can exceed the Betz limit of 59.3% with the increase of the blockage ratio (Vennell 2013).

Wu, Yang, Shu, Zhao & Yan (2015) numerically examined a 2D NACA0015 foil undergoing sinusoidal pitch and plunge motions placed near the ground, leaving the flow above the flapping foil unconstrained (Fig. 2.8b). By adjusting the distance between the flapping foil and the ground, an efficiency of 24% was achieved at $f^* = 0.2$, $\alpha_0 = 20°$ when the flapping foil was placed $1.5c$ above the ground ($\eta = 20\%$ in the fully free flow). The influence of the shear flow on the performance of the 2 DOF fully passive system given by Eq. 2.15 and 2.16 was numerically studied by Zhu (2012). The results showed that with the small shear (i.e. shear layer rate $\beta_U = 0.05$, where the inflow velocity $U(y) = U + \beta_U y$), the response region for energy harvesting was enlarged. In addition, the fully passive system achieved comparable efficiency of around 20% in the linear shear flow ($\beta_U = 0.05$) as that of 20% in the uniform flow performed by Peng & Zhu (2009).

Liu (2017) considered a fully prescribed system of the tandem configuration in the shallow water, as shown in Fig. 2.8c. Different from efficiency improvement achieved by Wu, Yang, Shu, Zhao & Yan (2015) through the ground effect, the interactions between the boundary layer of the ground and the foil resulted in performance reduction under the near-optimal condition $f^* = 0.14$, $\alpha_0 = 28.7°$. In addition, the convection of the vortices generated by the foils in the shallow water was slower than that in the free flow.

2.5 Summary

2.5.1 Key findings in the literature

In this chapter, major numerical and experimental studies on the flapping foil power generator have been reviewed with regard to kinematics, geometry and environmental effects.

Even though parameters governing the kinematics of the flapping foil were dependent on the model used to described the flapping motion, majority of studies on semi passive and fully passive (one degree of freedom) systems found that high energy extraction performance was achieved when the kinematic parameters approximated the optimal parameters found in the the fully prescribed system. In addition, the importance of the leading edge vortex (LEV) dynamics to the energy harvesting performance was verified in systems with different activating mechanisms, specifically in the laminar flow regime. Considering the simplicity to implement prescribed motions, the fully prescribed system is commonly used for parametric studies to uncover the physical mechanism for high energy extraction performance. Studies on the fully prescribed system suggested a range of optimal values: non-dimensional frequency $f^* = 0.11 - 0.18$, pitch amplitude $\theta_0 = 60° - 100°$, plunge amplitude $h_0 = 0.8 - 1.5$, phase difference between the pitch and plunge motions $\varphi = 90° - 110°$ and non-dimensional pivot point location $x_{piv} = 0.25 - 0.5$.

In the laminar flow regime, the influence of the foil geometry on the energy extraction performance is insignificant. On the contrary, the thickness of the foil affects the energy extraction performance significantly when the turbulent flow is considered. Studies on active deformation indicated that the local angle of attack was increased by the foil deformation and the improvement in energy extraction performance was achieved under different conditions, especially at low angles of attack (non-optimal condition of the rigid system). In these studies, the power consumption for active deformation was generally neglected. Performance improvement was also achieved by employing passive deformation at low angles of attack, while the improvement under the optimal condition of the rigid system was insignificant. In addition, the interactions between multiple foils influence the energy extraction performance as well as the optimal values of kinematic parameters.

When the flapping foil power generator operates in the laminar flow and transitional flow regimes, good synchronization between the plunge motion and LEV formation results in high power extraction performance. When it operates in the turbulent flow regime, high performance can be associated with either attached flow or separated flow involving LEVs. In addition, the uncertainty over the prediction of flow separations by different turbulence models was found in several studies using unsteady Reynolds averaged Navier Stokes (URANS) methods. In constrained flows, the efficiency can exceed the Betz limit of 59.3% and the interaction between the boundary layer and the foil may have either positive or negative effects on the power extraction performance, depending on the kinematics of the flapping foil.

2.5.2 Motivation and major work of this study

Because of the substantial computational resources required in 3D simulations (Kinsey & Dumas 2012*c*, Xiao et al. 2014) and uncertainties associated with turbulence modelling, this study is focused on two-dimensional (2D) laminar flow at the Reynolds number of 1100. Details of the physical problem will be described in Section 3.1.

As mentioned in Section 1.2, one of the prerequisites for industrial application of the flapping foil power generator is to search for the optimal combination of kinematic parameters. However, due to the high computational cost of computational fluid dynamics (CFD) simulations (Kinsey & Dumas 2008), it is computationally prohibitive to use CFD method in parametric studies and optimization involving multiple design variables (e.g. 5 kinematic parameters in the prescribed system with sinusoidal pitch and plunge motions). To reduce the time cost, potential flow based methods (e.g. unsteady panel method and Theodorsen's model) were employed to solve the flapping foil problem with constraints to ensure that the flow is fully attached in several studies. To take advantages of low computational cost and remove the constraints associated with the attached flow resulting from potential flow based methods, a dynamic stall model and an improved discrete vortex method for 2D simulations will be described in Section 3.2 and Section 4.1 respectively. The advantages and disadvantages of these two methods will be discussed in Chapter 4. Considering the non-linearity of the flapping foil problem, an evolutionary algorithm (EA) is used to search for the optimal values of the kinematic parameters in Chapter 5. A comparison of a traditional optimization method (complex method) and the EA on solving a non-linear problem will be conducted in Section 3.4.

As discussed in Section 2.3.2, performance improvement by employing the passive deformation of the foil was only achieved under the non-optimal conditions of the rigid system (e.g. $\alpha_0 = 20°$ compared to the optimal $\alpha_0 > 30°$ given by parametric studies on a rigid system). In addition, the role of flexibility in enhancing energy harvesting performance and the associated with physics are still not well understood, especially under the near optimal conditions of the rigid system. This is the motivation of the work presented in Chapter 6. An immersed boundary-lattice Boltzmann method (IB-LBM) is used to solve the fluid-structure-interaction problem and provide flow fields for detailed analysis. The IB-LBM is efficient for simulations involving moving boundaries and deformations since it avoids mesh regeneration. In addition, it is well suited for computations on a parallel architecture. Details of the IB-LBM will be discussed in Section 3.3.

Chapter 3

Validation of Methods Used

In this chapter, the physical models and computational methodologies used to solve the flapping foil energy harvesting problem are introduced. The main objective of this chapter is to validate the methods used in Chapters 4-5. In Section 3.1, the modelling of a fully prescribed system (as mentioned in Chapter 2) with a rigid aerofoil considered in Chapters 4 and 5 is described. Then, the aero-elastic model of a tail pinned to the rigid foil by a torsional spring considered in Chapter 5 is presented. In Section 3.2, a reduced order model developed by Bryant et al. (2013) used in Chapters 4 and 5 is described and reproduced with Matlab. In Section 3.3, the immersed boundary-lattice Boltzmann method (IB-LBM) with the multi-block technique (Tian, Luo, Zhu, Liao & Lu 2011, Tian, Luo, Zhu & Lu 2011) is presented and validated against data in the literature. In Section 3.4, the process of the multi-fidelity evolutionary algorithm (MFEA) (Branke et al. 2017) used in Chapter 5 is introduced and compared with a classical non-gradient optimization method.

3.1 Physical problem and mathematical formulation

In the flapping foil turbine problem of interest, a rigid system with a rigid NACA0015 foil (Fig. 3.1) and a flexible system with a rigid NACA0015 foil and a spring connected tail (Fig. 3.2) in a uniform flow with velocity U are considered. The mean power output $\overline{C}_P$ and efficiency η of the flapping foil power generator are defined in Eq. 2.3 and 2.6.

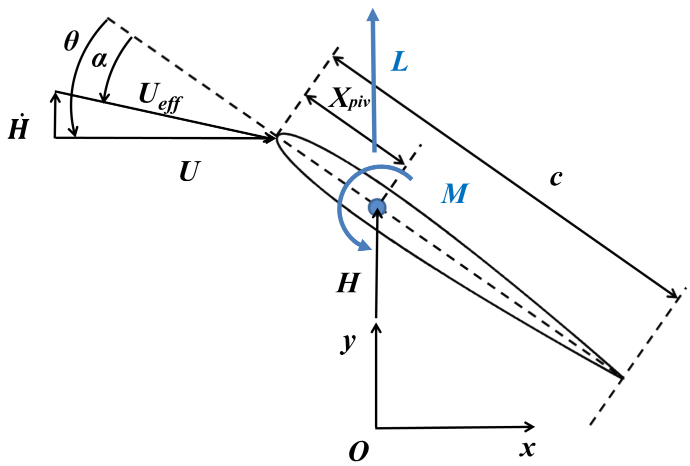

Fig. 3.1: Kinematic parameters and aerodynamic loads for a NACA0015 foil.

The rigid foil with a chord length of c considered in Chapters 4 and 5 undergoes simple sinusoidal pitch and plunge motions given by:

$$\theta(t) = \theta_0 \sin(2\pi f t), \tag{3.1}$$

$$H(t) = H_0 \sin(2\pi f t + \varphi). \tag{3.2}$$

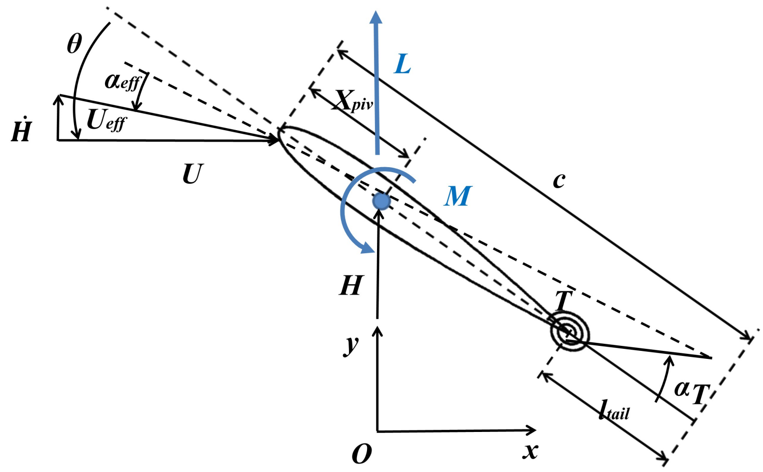

Fig. 3.2: Kinematic parameters and aerodynamic loads for a NACA0015 foil with a tail pinned to the trailing edge (T) by a torsional spring. The angular position of the tail α_T is passively determined by the fluid structure interactions.

The kinematics of this system is governed by 5 parameters: f^*, θ_0, h_0, φ and x_{piv}. In Fig. 3.1, the origin of the coordinates O is at the pivot location when the foil is at its neutral position. The coordinates correspond to a right-hand Cartesian coordinate system with x-axis rightward positive, y-axis upward positive and the angle counter clockwise positive. α defined in Eq. 2.2 is the angle of attack.

In the flexible system, the rigid foil undergoes sinusoidal pitch and plunge motions given by Eq. 3.1 and 3.2 while the motion of the tail is passively determined by the fluid-structure interactions. According to the study on the propulsive system using flapping foils, the flexibility appears to be more important in the chordwise direction than in the spanwise direction (Gursul et al. 2014). Thus a 2D aero-elastic problem modelled by a torsional spring at the trailing edge of the rigid foil (point T) is considered, as shown in Fig. 3.2.

The motion of the tail is then governed by

$$\begin{aligned} J\ddot{\alpha}_T + R\dot{\alpha}_T + K_s\alpha_T =& M_f - \frac{ml_{tail}}{2}\cos\left(\theta + \alpha_T\right)\ddot{y}_T \\ &+ \frac{ml_{tail}}{2}\sin\left(\theta + \alpha_T\right)\ddot{x}_T - J\ddot{\theta}, \end{aligned} \tag{3.3}$$

where $J = \frac{1}{3}ml_{tail}^2$, K_s and R are the moment inertia of the tail about the axis through point T normal to the x-y plane, spring stiffness and damping, respectively; M_f is the fluid moment about the axis through the point T normal to the x-y plane; $m = \rho_l l_{tail}$ is the mass of the tail, $\rho_l = \rho_{tail}h_s$ and l_{tail} are the linear density and the length of the tail respectively; ρ_{tail} and h_s are the density and the thickness of the tail respectively; $\ddot{y}_T$ and $\ddot{x}_T$ are respectively the vertical and horizontal accelerations of point T; and α_T, $\dot{\alpha}_T$ and $\ddot{\alpha}_T$ are respectively the angular position, velocity and acceleration of the tail with respect to the foil at point T, determined by the fluid-structure interactions. In Fig. 3.2, the system of coordinates is the same as that in Fig. 3.1. Notice that the chord length c is the total length of the foil and the tail. α_{eff} is the angle between the line passing through the end of the tail and the leading edge of the foil and the relative velocity $U_{eff} = \sqrt{\dot{H}^2 + U^2}$. In Eq. 3.3, M_f is the moment acting on the tail computed by the fluid solver and coupled with the structure solver, and the last three terms on the right hand side represent the moment due to inertia effects resulting from the prescribed plunge and pitch motions. This torsional spring model reduces the structural complexity and converges to the non-linear Euler-Bernoulli beam with the increase of the number of linked flat plates (Eldredge et al. 2010).

3.2 Reduced order model

In numerical studies on the flapping foil power generator, computational fluid dynamics (CFD) methods are commonly used to predict the performance of the flapping foil turbine and detailed information of the flow field on the LEV formation and evolution. However, they require substantial computational resources, for example, a simulation of the flapping foil takes 100 hours on a single P4/3.2-GHz processor (Kinsey & Dumas 2008). Thus it is computationally prohibitive in studies exploring a wide range of parameters. On the other hand, reduced order models could reduce the computational time to minutes, which provide an alternative way to remove the impediment in optimization and engineering design because of their low computational costs. As summarized in Chapter 2, several studies have employed methods based on the potential flow theory to predict the performance of the flapping foil power generator, assuming the flow is fully attached. However, these methods neglect the formation of LEVs resulting from flow separations, which have significant impacts on the energy harvesting performance.

Studies on reduced order aerodynamic modelling when LEVs form are motivated by helicopter studies in which the phenomenon of dynamic stall is observed (McCroskey 1981). In recent decades, several semi-empirical models, for instance, Office National D'Etudes et de Recherches Aerospatiales (ONERA) model (McAlister et al. 1984) and Leishman-Beddoes model (Leishman & Beddoes 1989) have been developed and modified for dynamic stall modelling in subsonic flows. Considering the similarity of helicopter blades and flapping foils, methods used in dynamic stall studies provide valuable references for reduced-order-model development for flapping foil power generators.

The non-dimensional frequency f^* and the pitch amplitude θ_0 in dynamic stall studies ($0 < f^* < 0.016$, $0° < \theta_0 < 10°$) (Dyachuk et al. 2013) are generally smaller than those in studies on flapping foil power generators ($0 < f^* < 0.25$, $0° < \theta_0 < 90°$) (Kinsey & Dumas 2008). The large amplitude oscillations of the flapping foil characterized by strong leading and trailing edge flow separations present challenges for reduced order modelling. In order to model flapping foil motions at low Reynolds numbers, Bryant et al. (2013) have modified a quasi-steady model using a method analogous to the ONERA model. In this study, the Bryant model is employed in the optimization process as a surrogate model to search the parameter space. The calculation procedure using the Bryant model is summarised as follows.

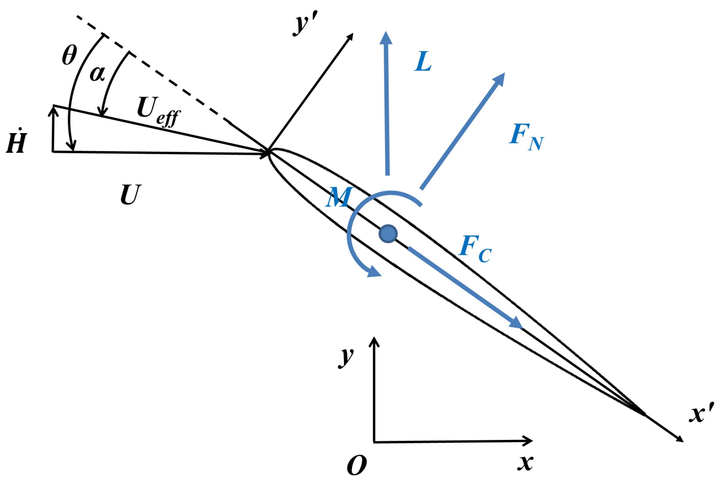

Fig. 3.3: Aerodynamic loads for a NACA0015 foil with the fixed coordinate system (x, y) and the foil coordinate system (x', y') where the origin of the coordinates is at the leading edge of the foil.

As shown in Fig. 3.3, in terms of the inflow velocity U and the motions of the foil, the velocity components (u', v') in the foil coordinate system (x', y')

are given by

$$u' = -U\cos\theta - \dot{H}\sin\theta, \tag{3.4}$$

$$v' = -U\sin\theta + \dot{H}\cos\theta. \tag{3.5}$$

Notice that the coordinate system used in Bryant et al. (2013) corresponds to the system with x-axis leftward positive, y-axis upward positive and the angle clockwise positive. Here, the coordinate system corresponds to one with x-axis rightward positive, y-axis upward positive and the angle counter clockwise positive, as defined in Section 3.1. The lift L in the fixed coordinate system (x, y) is computed from the the normal force F_N and the chord force F_C in the foil coordinate system (x', y'):

$$L = F_N\cos\theta - F_C\sin\theta. \tag{3.6}$$

The model expressed F_N, F_C and the moment M in a similar way to the quasi-steady model used by Andersen et al. (2005) as:

$$F_N = \frac{\pi}{4}\rho e^2\dot{\theta}u' + \rho\Gamma u' - \frac{\pi}{4}\rho c^2\dot{v}' - F_N^{vis}, \tag{3.7}$$

$$F_C = -\frac{\pi}{4}\rho c^2\dot{\theta}v' - \rho\Gamma v' - \frac{\pi}{4}\rho e^2\dot{u}' - F_C^{vis}, \tag{3.8}$$

$$M = J_a\ddot{\theta} + \rho\Gamma u' L_\Gamma - \frac{\pi}{4}\rho c^3\left(x_{piv} - \frac{1}{2}\right)\dot{v}' - M^{vis}, \tag{3.9}$$

where e is the thickness of the foil; F_N^{vis}, F_N^{vis} and M^{vis} are respectively the normal force, chord force and moment due to the fluid viscosity; Γ is the circulation; L_Γ is the moment arm considering changes in the pressure center and J_a is the added mass moment of inertia given by Brennen (1982):

$$J_a = \frac{\pi\rho}{4}\left(\frac{1}{8} + (2x_{piv} - 1)^2\right)\left(c^2 - e^2\right)^2 \tag{3.10}$$

The circulation Γ results from the translational velocity and rotational velocity is:

$$\Gamma = \frac{1}{2}C_L c U_{eff} + C_R c^2 \dot{\theta}, \tag{3.11}$$

where C_L is the lift coefficient, $U_{eff} = \sqrt{\dot{H}^2 + U^2}$ is the effective incident velocity and $C_R = \pi\left(0.75 - x_{piv}\right)$ is the rotational circulation coefficient, assuming that the contribution of the pitch motion to the circulation is zero at 3/4 chord length from the leading edge of the foil (Sane & Dickinson 2002). When the flow separations are taken into consideration, $C_L = C_{Ls} + C_{Ld}$ contains the static lift coefficient C_{Ls} and dynamic coefficient C_{Ld} given by Bryant et al. (2013):

$$C_{Ls} = 1.2\sin\left(2\alpha\right), \tag{3.12}$$

$$\ddot{C}_{Ld} + \frac{2U}{c}s_{b1}\dot{C}_{Ld} + \frac{4U^2}{b^2}s_{b1}C_{Ld} = \frac{U}{c}\dot{C}_{Ls}, \tag{3.13}$$

where s_{b1} and s_{b2} are empirical constants. The viscous forces (F_N^{vis} in Eq. 3.7 and F_C^{vis} in Eq. 3.8) and viscous moment (M^{vis} in Eq. 3.9) are expressed by Bryant et al. (2013):

$$\begin{Bmatrix} F_N^{vis} \\ F_C^{vis} \end{Bmatrix} = \frac{1}{2}\rho c\left(C_D|_{\alpha=0}\cos^2\alpha + C_D|_{\alpha=\pi/2}\sin^2\alpha\right)U_{eff}\begin{Bmatrix} v' \\ u' \end{Bmatrix} \tag{3.14}$$

$$M^{vis} = \frac{1}{2}\rho C_D|_{\alpha=\pi/2}\int_0^c |v' + r\dot{\theta}|\left(v' + r\dot{\theta}\right)r\mathrm{d}r \tag{3.15}$$

Table 3.1: Comparison of mean power coefficient and efficiency predicted by current code, Bryant et al. (2013) and CFD simulations conducted by Kinsey & Dumas (2008) at different f^*, θ_0 and constant $h_0 = 1, \varphi = 90°, x_{piv} = 0.333$.

Kinematic condition	$f^* = 0.14$, $\theta_0 = 76.3°$		$f^* = 0.18$, $\theta_0 = 60°$		$f^* = 0.12$, $\theta_0 = 60°$		$f^* = 0.06$, $\theta_0 = 76.3°$	
Method	$\overline{C}_P$	η	$\overline{C}_P$	η	$\overline{C}_P$	η	$\overline{C}_P$	η
Current code	0.87	34.2%	0.24	10.1%	0.59	24.6%	0.28	11.8%
Bryant et al. (2013)	0.87	34.1%	0.24	10.0%	0.59	24.4%	0.28	11.5%
CFD Kinsey & Dumas (2008)	0.86	33.7%	0.27	11.4%	0.59	24.5%	–	12.3%

where C_D is the static drag coefficient of the foil. The influence of the LEV convection on the pressure center is introduced via two empirical constants in the moment arm term L_Γ. By considering the the changes in the pressure center resulting from the static and dynamic contributions L_Γ is expressed by Bryant et al. (2013) as:

$$L_\Gamma = \frac{c}{2}\left[2x_{piv} - \frac{1}{2} - s_{b3}\left(1 - \cos\left(\frac{\pi\tau_{bv}}{T_{bv}}\right)\right)\right] \tag{3.16}$$

where τ_{bv} is the time variable to track the location of the LEV, T_{bv} is the empirical constant corresponding to the instant at which the LEV is at the trailing edge of the foil and s_{b3} is the empirical coefficient controlling the amplitude of the dynamic pressure center migration. In the Bryant model (Bryant et al. 2013), the empirical constants with respect to the dynamic stall effects have been tuned using the CFD results of Kinsey & Dumas (2008).

The Bryant model is reproduced with Matlab R2013b using the empirical constants ($s_{b1} = 0.57$, $s_{b2} = 0.19$, $s_{b3} = 0.75$ and $T_{bv} = 1.8$) suggested by Bryant et al. (2013). The performance of the flapping foil power generator predicted by the current code compares well with those of Bryant et al. (2013) and CFD simulations conducted by Kinsey & Dumas (2008) in Table 3.1. The

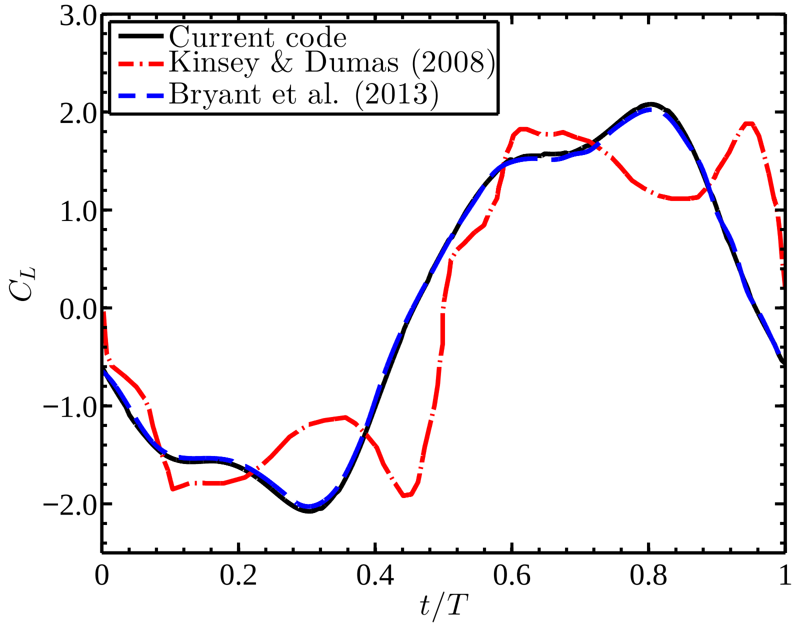

(a) Time history of C_L in one flapping cycle.

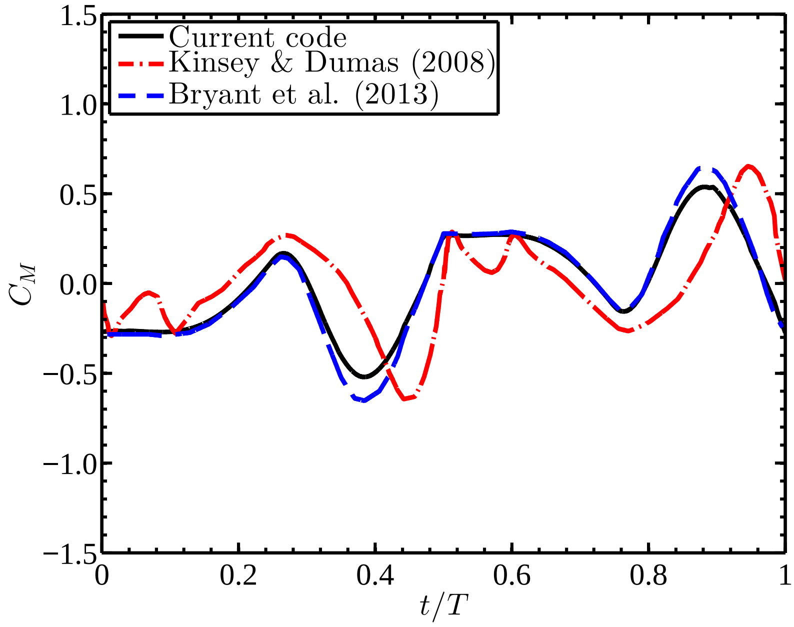

(b) Time history of C_M in one flapping cycle.

Fig. 3.4: Comparison of (a) lift and (b) moment coefficient given by current code with those of Bryant et al. (2013) and CFD results of Kinsey & Dumas (2008) at $f^* = 0.14, \theta_0 = 76.3°, h_0 = 1.0, \varphi = 90°$ and $x_{piv} = 0.333$.

small difference between the results of the current code and those of Bryant et al. (2013) may be due to the method used to solve the differential equation (Eq. 3.13) and the values of the constants $C_D|_{\alpha=0}$ and $C_D|_{\alpha=\pi/2}$. The time histories of $C_L = L/(1/2\rho U^2 c)$ and $C_M = M/(1/2\rho U^2 c^2)$ in Fig. 3.4 given by the current code show reasonable agreement with those in Kinsey & Dumas (2008). The amplitude of C_M given by the current code is a little smaller than that given by Bryant et al. (2013) since $C_D|_{\alpha=0}$ and $C_D|_{\alpha=\pi/2}$ were not given by Bryant et al. (2013). Here $C_D|_{\alpha=0} = 0.13$ and $C_D|_{\alpha=\pi/2} = 2.3$ are chosen according to the drag coefficient C_D of the NACA0015 foil presented in Daniele (2013). When $C_D|_{\alpha=0} = 0.5$ and $C_D|_{\alpha=\pi/2} = 1.8$, C_M predicted by the current code agrees well with that of Bryant et al. (2013), but $\overline{C}_P$ increases from 0.87 to 0.89.

3.3 Immesrsed boundary-lattice Boltzmann method

In this study, the incompressible flow is solved by a relatively new technique: the lattice Boltzmann method (LBM) (Tian, Luo, Zhu, Liao & Lu 2011, Tian et al. 2013). In addition, a multi-block technique is implemented to balance the numerical accuracy and time cost. To couple the fluid and structure solvers, the immersed boundary (IB) method is used to distribute the force to the grids in the vicinity of the solid boundary.

3.3.1 Lattice Boltzmann method

Unlike conventional computational fluid dynamics (CFD) methods, which solve the Navier-Stokes equation, the LBM simulates averaged macroscopic be-

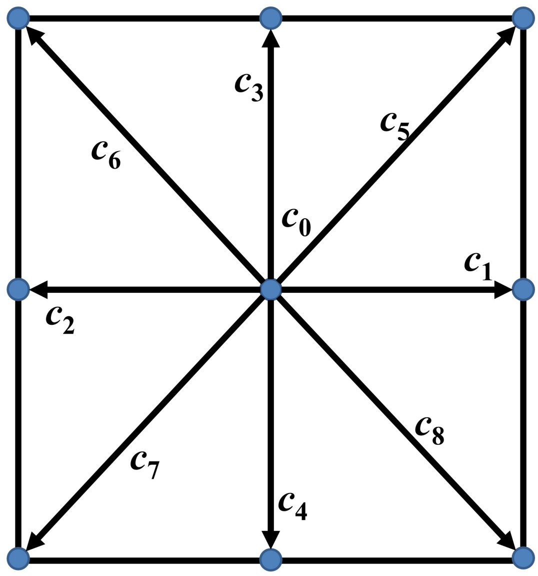

Fig. 3.5: Lattice arrangement for D2Q9 model.

haviour of the flow through the collision and propagation of fictive particles over a discrete lattice mesh (Bösch & Karlin 2013). In the LBM, the statistical behaviour of the particles is described by the distribution function $f_i\left(r,t\right)$ of velocity c_i, referring to the number of the particles positioned between r and $r+dr$ with the velocity from c_i to $c_i+\mathrm{d}c_i$ at instant t (Mohamad 2011), where $_i$ indicates the direction of the velocity, as shown in Fig. 3.5. The difference in $f_i\left(r,t\right)$ between the initial and final states after the collision is given by the lattice Boltzmann equation:

$$\underbrace{f_i\left(r+c_i\mathrm{d}t,t+\mathrm{d}t\right)-f_i\left(r,t\right)}_{\text{streaming}}=\underbrace{\Omega_i\left(r,t\right)}_{\text{collision}}+\boldsymbol{f}\mathrm{d}t. \tag{3.17}$$

where $\Omega_i\left(r,t\right)$ is the collision operator and $\boldsymbol{f}$ is the external force. To increase the numerical stability of the LBM, the collision process is transformed from the velocity space to the momentum space (Lallemand & Luo 2000):

$$f_i\left(r+c_i\mathrm{d}t,t+\mathrm{d}t\right)-f_i\left(r,t\right)=-\boldsymbol{M}_{\boldsymbol{LB}}^{-1}\hat{\boldsymbol{S}}_{\boldsymbol{LB}}\left[\boldsymbol{m}_{\boldsymbol{LB}}\left(r,t\right)-\boldsymbol{m}_{\boldsymbol{LB}}^{eq}\left(r,t\right)\right]+\boldsymbol{f}\mathrm{d}t, \tag{3.18}$$

where $\boldsymbol{M}_{\boldsymbol{LB}}$ is the transformation matrix, $\hat{\boldsymbol{S}}_{\boldsymbol{LB}}$ is the diagonal matrix of the relaxation rates, $\boldsymbol{m}_{\boldsymbol{LB}}$ is the vector of momentum and $\boldsymbol{m}_{\boldsymbol{LB}}^{eq}$ is the vector of equilibrium momentum. For the D2Q9 model, where D2 represents the two dimensional flow and Q9 represents the number of particle speeds as shown in Fig. 3.5, the matrix $\boldsymbol{M}_{\boldsymbol{LB}}$ is given by Liu et al. (2012):

$$\begin{pmatrix} 1 & 1 & 1 & 1 & 1 & 1 & 1 & 1 & 1 \\ -4 & -1 & -1 & -1 & -1 & 2 & 2 & 2 & 2 \\ 4 & -2 & -2 & -2 & -2 & 1 & 1 & 1 & 1 \\ 0 & 1 & 0 & -1 & 0 & 1 & -1 & -1 & 1 \\ 0 & -2 & 0 & 2 & 0 & 1 & -1 & -1 & 1 \\ 0 & 0 & 1 & 0 & -1 & 1 & 1 & -1 & -1 \\ 0 & 0 & -2 & 0 & 2 & 1 & 1 & -1 & -1 \\ 0 & 1 & -1 & 1 & -1 & 0 & 0 & 0 & 0 \\ 0 & 0 & 0 & 0 & 0 & 1 & -1 & 1 & -1 \end{pmatrix},$$

The diagonal matrix $\hat{\boldsymbol{S}}_{\boldsymbol{LB}}$ is given by Jami et al. (2007) and Mohamad (2011) as:

$$\hat{\boldsymbol{S}}_{\boldsymbol{LB}}=\mathrm{diag}\left(0,1.4,1.4,0,1.2,0,1.2,2/\left(1+6\nu\right),2/\left(1+6\nu\right)\right), \tag{3.19}$$

where ν is the kinematic viscosity. The vector of equilibrium momentum $\boldsymbol{m}_{\boldsymbol{LB}}^{eq}$ is given by Mohamad (2011):

$$\boldsymbol{m}_{\boldsymbol{LB}}^{eq} = \left(\mathrm{d}\rho, m_{LB1}^{eq}, m_{LB2}^{eq}, \rho u, -\rho u, \rho v, -\rho v, m_{LB7}^{eq}, \rho uv\right)^{\mathrm{T}},$$

where ρ is the density, $\boldsymbol{u}$ (u, v) are velocities in the fixed coordinate system (x, y), $m_{LB1}^{eq} = -2\mathrm{d}\rho + 3\rho\left(u^2 + v^2\right)$, $m_{LB2}^{eq} = \mathrm{d}\rho - 3\rho\left(u^2 + v^2\right)$ and $m_{LB7}^{eq} = \rho\left(u^2 - v^2\right)$. In the numerical simulations, the process for solving Eq. 3.17 is split into the streaming and collision processes. Generally, these two steps are computed separately.

At the nodes on the boundary of the computational domain, the velocity is imposed as the inflow velocity; the pressure is obtained from the nearest inner nodes; and the distribution function f_i is computed through the non-equilibrium extrapolation method (Guo et al. 2002). When the flow is incompressible, the pressure p and velocity $\boldsymbol{u}$ of the flow are given by

$$p = \frac{1}{3}\sum_{i=0}^{8} f_i, \tag{3.20}$$

$$\boldsymbol{u} = \frac{1}{\rho}\sum_{i=0}^{8} f_i \boldsymbol{c}_i. \tag{3.21}$$

The process of LBM simulations is briefly summarized as: (a) initialize the distribution function f_i from macroscopic initial variables (ρ_0, u_0 and v_0); (b) compute the streaming process on the left hand in Eq. 3.17; (c) compute the collision process in Eq. 3.17; and (d) calculate macroscopic variables p, u and v through Eq. 3.20 and 3.21.

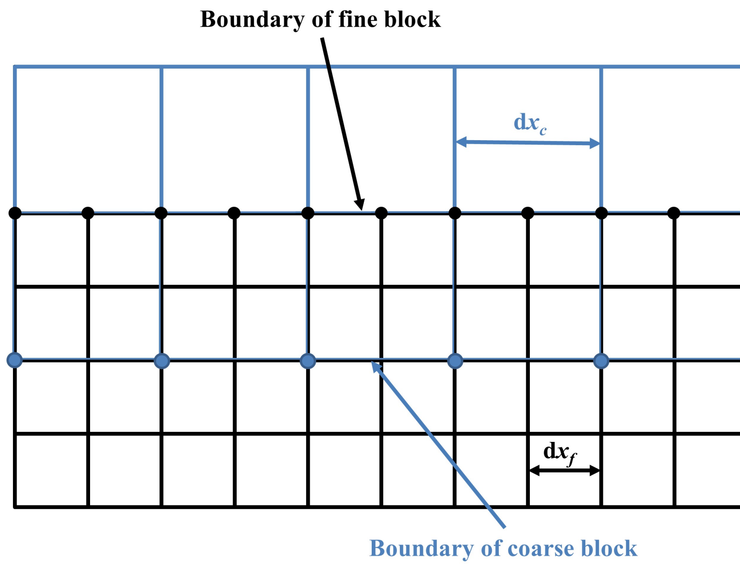

Fig. 3.6: Interface structure between two blocks of different grid sizes.

3.3.2 Multi-block technique

In this study, the multi-block technique proposed by Yu et al. (2002) is implemented into the LBM solver. The adjacent boundary of neighbouring blocks with different time steps and grid spacings overlap and the information exchanged on the interface is implemented to ensure the mass conservation and the continuity of stresses between blocks (Liu et al. 2012). As shown in Fig. 3.6, the nodes of grid spacing $\mathrm{d}x_f$ in the fine block overlap those of grid spacing $\mathrm{d}x_c$ in the coarse block in the vicinity of the interface. The distribution function f_i at the nodes on the boundary of the fine block is exchanged with that of the coarse block through interpolation using three-point Lagrangian formulation. The streaming and collision processes of the LBM are firstly computed in the coarse block. According to Eq. 3.19, the viscosity of the fluid is

$$\nu = (2\tau_{LB} - 1)\,\mathrm{d}x/6, \tag{3.22}$$

where τ_{LB} is the relaxation time. The relationship between the relaxation times in the fine block τ_{LB}^{f} and in the coarse block τ_{LB}^{c} are described by Yu et al. (2002) as:

$$\tau_{LB}^{f} = \frac{1}{2} + \frac{\mathrm{d}x_c}{\mathrm{d}x_f}\left(\tau_{LB}^{c} - \frac{1}{2}\right). \tag{3.23}$$

In this study, the computational domain of $42c \times 24c$ with the outer boundary at $30c$ from the pivot location in Fig. 3.7a is employed in the LBM to predict energy harvesting performance, while that of $70c \times 40c$ with the outer boundary at $50c$ from the pivot location in Fig. 3.7b is used to investigate the vortices in the far downstream flow. As shown in Fig. 3.7, the computational domain containing 17 blocks have 5 grid levels. Grid level 1 is the coarsest grid in blocks I, II, III, IV; gird level 2 is in blocks VI, VII, VIII, IX; gird level 3 is in the 4 blocks surrounded by blocks VI, VII, VIII, IX; gird level 4 is in the 4 blocks adjacent to block V; and gird level 5 is in block V. The time step and grid spacing in the inner block are half of those in the adjacent outer block, e.g. time step and grid spacing in block I, II, III, IV are half of those in block VI, VII, VIII, IX.

3.3.3 Immersed boundary method

The fluid-structure interaction problem is simulated using the immersed boundary (IB) method. Instead of adapting the grid to follow the movement of the interface in body-conformed mesh methods, the IB method distributes the stress exerted by the structure on the fluid to the stationary Cartesian gird in the vicinity of the solid boundary. In the IB method, the velocity on the Lagrangian boundary must satisfy the incompressible Navier-Stokes equation:

$$\rho\frac{\partial \boldsymbol{u}}{\partial t} + \rho\boldsymbol{u}\cdot\nabla\boldsymbol{u} = -\nabla p + \rho\nu\nabla^2\boldsymbol{u} + \boldsymbol{f}, \tag{3.24}$$

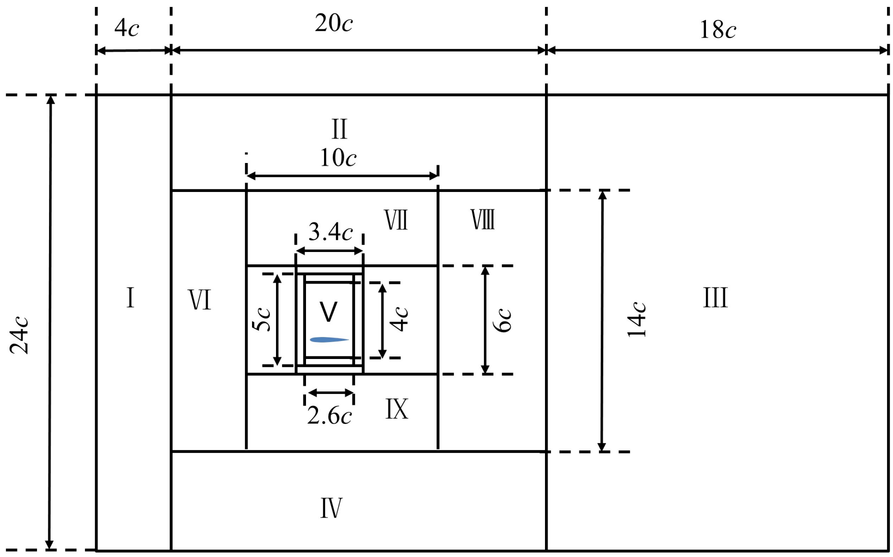

(a) Computational domain with a size of $42c \times 24c$.

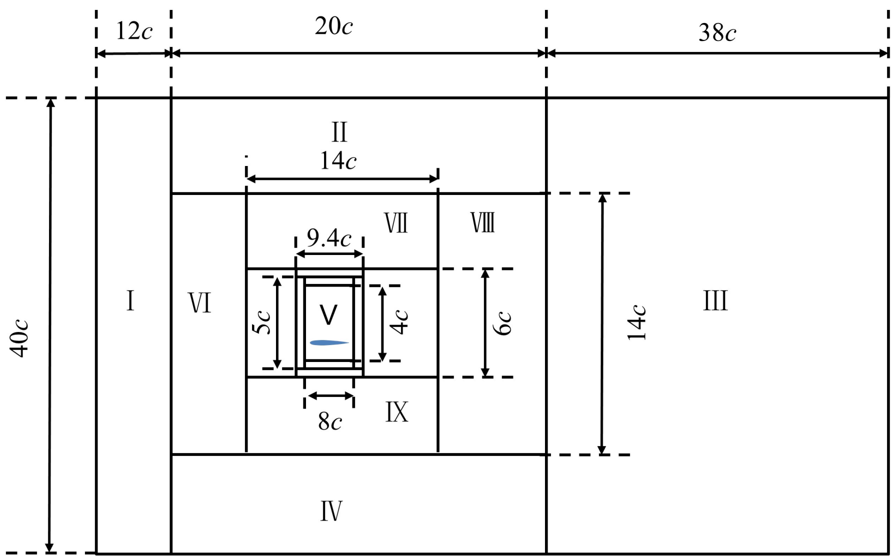

(b) Computational domain with a size of $70c \times 40c$.

Fig. 3.7: Computational domain with 17 blocks and 5 grid levels used in the LBM simulations.

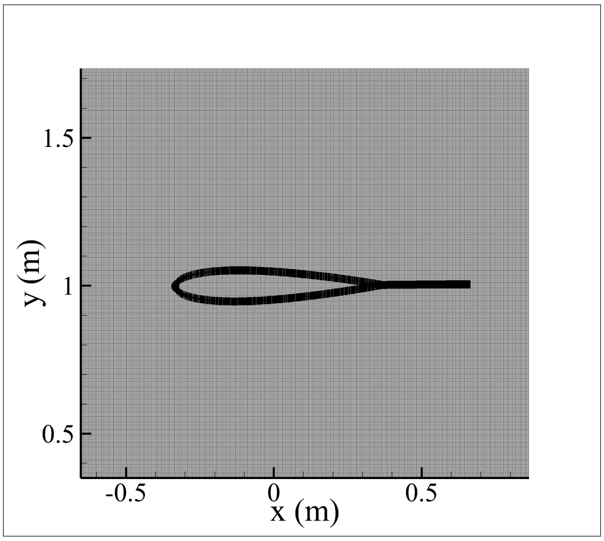

Fig. 3.8: The computational mesh near the foil.

where t is the time, $\boldsymbol{u}$ is the fluid velocity, $\boldsymbol{f}$ is the body force as a source term. $\boldsymbol{f}$ on the Eulerian coordinate $\boldsymbol{x}$ (x, y) is related to the boundary force $\boldsymbol{f}'$ exerted by the structure on the Lagrangian coordinate $\boldsymbol{x}'$ (x', y'). The connection between the Eulerian mesh for the fluid solver and the Lagrangian boundary for the solid solver is approximated by the Dirac δ function (Liu et al. 2012):

$$\boldsymbol{f}(\boldsymbol{x}, t) = \int_S \boldsymbol{f}'(s, t)\, \delta(\boldsymbol{x} - \boldsymbol{x}'(s, t))\, ds, \tag{3.25}$$

where S is the enclosed solid boundary and $0 < s < 1$ is the parameter tracking the point on the Lagrangian boundary. This IB-LBM is efficient for solving FSI problems involving large deformations (Peng & Luo 2008, Sotiropoulos & Yang 2014). The uniform orthogonal grid with immersed boundary is shown in Fig. 3.8. In Chapter 4 and 5, 2000 grid points are distributed over the foil surface, while in Chapter 6, the same number of points is distributed over the foil surface and 200 grid points are distributed over the tail.

Table 3.2: Courant number N_{cour} and efficiency η with respect to the number of grid points and Δt^* at $Re = 1100$, $f^* = 0.14$, $\theta_0 = 76.3°, h_0 = 1, \varphi = 90°, x_{piv} = 0.333$.

Δt^*\Total number of grid points	2.1×10^6	3.3×10^6	8.3×10^6
Courant number N_{cour}			
0.0020	0.040	0.050	0.080
0.0016	0.032	0.040	0.064
0.0010	0.020	0.025	0.040
efficiency η			
0.0020	35.5%	35.1%	33.3%
0.0016	35.6%	35.5%	34.1%
0.0010	36.1%	36.1%	35.6%

Table 3.3: $\overline{|C_L|}$ and $\overline{|C_M|}$ with respect to the number of grid points and Δt^* at $Re = 1100$, $f^* = 0.14$, $\theta_0 = 76.3°, h_0 = 1, \varphi = 90°, x_{piv} = 0.333$.

Δt^*\Total number of grid points	2.1×10^6	3.3×10^6	8.3×10^6
$\overline{\lvert C_L \rvert}$			
0.0020	1.3954	1.3861	1.3192
0.0016	1.4060	1.3955	1.3593
0.0010	1.4127	1.4050	1.3955
$\overline{\lvert C_M \rvert}$			
0.0020	0.2126	0.2045	0.1823
0.0016	0.2146	0.2146	0.1941
0.0010	0.2207	0.2205	0.2179

Table 3.4: $\sqrt{\overline{C_L^2}}$ and $\sqrt{\overline{C_M^2}}$ with respect to the number of grid points and Δt^* at $Re = 1100$, $f^* = 0.14$, $\theta_0 = 76.3°, h_0 = 1, \varphi = 90°, x_{piv} = 0.333$.

Δt^*\Total number of grid points	2.1×10^6	3.3×10^6	8.3×10^6
$\sqrt{\overline{C_L^2}}$			
0.0020	1.4674	1.4619	1.3925
0.0016	1.4777	1.4675	1.4275
0.0010	1.4882	1.4830	1.4679
$\sqrt{\overline{C_M^2}}$			
0.0020	0.2783	0.2609	0.2270
0.0016	0.2819	0.2817	0.2470
0.0010	0.2886	0.2883	0.2874

Table 3.5: Computational results using different grid spacings in the outer blocks at $Re = 1100$, $f^* = 0.14$, $\theta_0 = 76.3°, h_0 = 1, \varphi = 90°, x_{piv} = 0.333$.

Case	η	$\overline{\lvert C_L \rvert}$	$\overline{\lvert C_M \rvert}$	RMS of C_L	RMS of C_M
i	35.5%	1.3955	0.2146	1.4675	0.2817
ii	35.2%	1.4159	0.2043	1.4921	0.2606
iii	35.2%	1.4161	0.2045	1.4920	0.2609

3.3.4 Validations

The grid and time refinement is performed on a rigid foil with the computational domain size of $42c \times 24c$ at $Re = 1100$, $f^* = 0.14$, $h_0 = 1$, $\theta_0 = 76.3°$, $\varphi = 90°$ and $x_{piv} = 0.333$. The convergence of hydrodynamic loads and η with respect to the number of grid points and time steps is demonstrated respectively in Table 3.2-Table 3.4 where $\Delta t^* = \Delta t/Uc$ is the non-dimensional time step size in the outermost blocks (I, II, III and IV). In the context of the multi block technique, the non-dimensional time step size at the finest grid level in the innermost block (block V in Fig. 3.7) is $\Delta t^*/16$. To justify the convergence condition with respect to the Courant Friedrichs Lewy (CFL) condition, Courant number $N_{cour} = U\Delta t/\Delta x$ is listed in Table 3.2, where Δx is the grid spacing in the outermost block. For all the cases, N_{cour} is much less than 1. The results in Table 3.2 - 3.4 indicate that when $N_{cour} = 0.04$, the efficiency and hydrodynamic loads given by cases with different time and grid spacings are almost identical. Hereafter a total number of 3.3×10^6 grid points and a non-dimensional time step $\Delta t^* = \Delta t/Uc = 0.0016$ are utilized. Simulations with smaller grid spacing in the outer blocks are conducted to justify the influence of grid refinement. In Table 3.5, the blocks of case i are the same as those in the grid and time-step independence study; blocks I, II, III and IV of case ii use half the grid spacing of that used in the same blocks of case i; and blocks VI, VII, VIII and IX of case iii use half the grid spacing of that used in the same blocks of case i. The differences in η of the 3 cases are less than 1%. The code using LBM is compiled with Intel Fortran on Linux system and operated on a single Xeon/2.67-GHz processor. It takes 120 hours to compute 12 flapping cycles at $f^* = 0.14$.

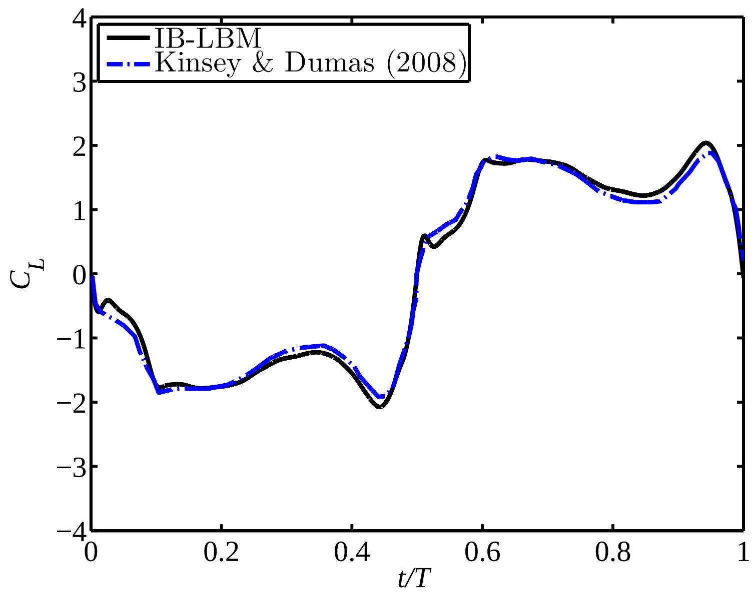

Fig. 3.9: Comparison of lift coefficient with that of Kinsey & Dumas (2008).

The fluid solver is validated in predicting energy harvesting performance against Kinsey & Dumas (2008) under the same condition as that in the previous grid and time refinement analyses. As shown in Fig. 3.9, the instantaneous lift coefficient C_L given by the IB-LBM solver shows good agreement with that of Kinsey & Dumas (2008). The simulation is converged after 12 flapping cycles with the difference in efficiency of less than 1% between the last 5 cycles. Compared with $\eta = 33.7\%$ and $\overline{C_p} = 0.860$ computed by Kinsey & Dumas (2008) using a Navier-Stokes solver provided in ANSYS Fluent 6.1, the LBM predicts a little higher $\eta = 35.5\%$ and $\overline{C_p} = 0.911$. For validation of the IB-LBM solver in solving fluid-structure interaction problems, a propulsion system of two rigid elliptical foils linked through a torsional spring with non-dimensional

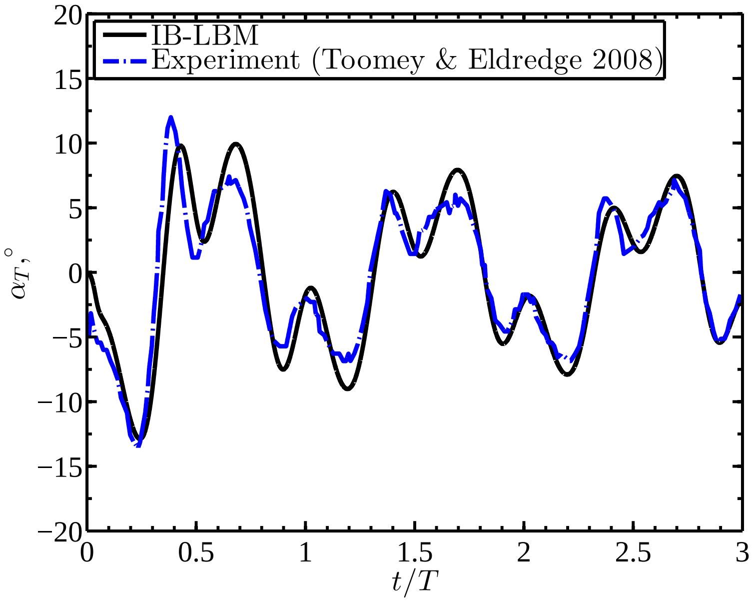

Fig. 3.10: Comparison of the tail angle with that of Toomey & Eldredge (2008).

stiffness $K_s/\left(\rho f^2 c^4\right) = 456$ and non-dimensional damping $R/\left(\rho f c^4\right) = 3.95$ at $Re_t = U_{t,max}c/\nu = 1300$ ($U_{t,max}$ is the maximum translational velocity) investigated by Toomey & Eldredge (2008) is considered. One of the foils undergoes prescribed motion driven by a two-axis motion stage with $x_{piv} = 0.5$. The motion of the other foil is determined by FSI and the solid-to-fluid density ratio of the passive foil is 5. The gap distance between the driven and the passive foils is $0.049c$. The deflection of the passive foil was measured by an HP HEDS-5540 encoder and 100 data points were recorded in each flapping cycle. In this case, the mass and moment of inertia in Eq. 3.3 are values per unit span. As shown in Fig. 3.10, the displacement of the trailing foil agrees well with the experiment data for a torsional flexibility model of Toomey & Eldredge (2008).

3.4 Multi-fidelity evolutionary algorithm

Evolutionary algorithms (EAs) are intelligent methods incorporating random variation and selection inspired by biological evolution. They are commonly used in various fields of science and engineering because they are applicable for a wide range of problems and do not need assumptions on the mathematical properties of the underlying functions (Fogel 1997). In addition, EAs perform well in multi-objective problems since they evaluate several solutions of the Pareto optimal set in a single run (Coello 2006). Due to the complex influence of kinematic parameters on the performance of a flapping foil, native use of evolutionary algorithms would require thousands of function evaluations to achieve near optimal solutions. The high computational expense associated with repeated simulations, such as the Navier-Stokes equations, poses an impediment to the application of evolutionary algorithms for the purpose of design optimization. To reduce the computational expense, Shimizu et al. (2008) implemented an EA with a low fidelity method with the assumptions of planar wake and small amplitude given by Theodorsen (1979). The term fidelity refers to the amount of physics or details implemented within the model. Generally, higher fidelity simulations are more accurate and require more computational resources. For example, a simulation of a flapping foil power generator using FLUENT by solving Navier-Stokes equations takes 100 hours on a single P4/3.2-GHz processor (Kinsey & Dumas 2008), while the Bryant model using semi-empirical functions takes less than 1 second on a single Xeon/2.67-GHz processor (Liu et al. 2016). One promising way to reduce the computational cost of such an optimization exercise is to use evaluation models of different fidelities during the optimization process (Zhou et al. 2007, Ong et al. 2003, Loshchilov 2013). Typically, the low fidelity solution can be obtained from data fitting, a physics based model and a simulation with coarser mesh or relaxed criteria (Leifsson & Koziel 2015).

In this study, the fully prescribed system governed by Eq. 3.1 and 3.2 is optimized using a probabilistic dominance based multi-fidelity optimization algorithm. This multi-fidelity EA is implemented with physics based reduced order models (the Bryant model reproduced in Section 3.2 and the discrete vortex method modified in Chapter 4). Compared to the function approximation model constructed by data fitting where substantial amount of data samples is required to ensure the accuracy of the model, the physics based low fidelity model requires less high fidelity solutions to obtain good accuracy.

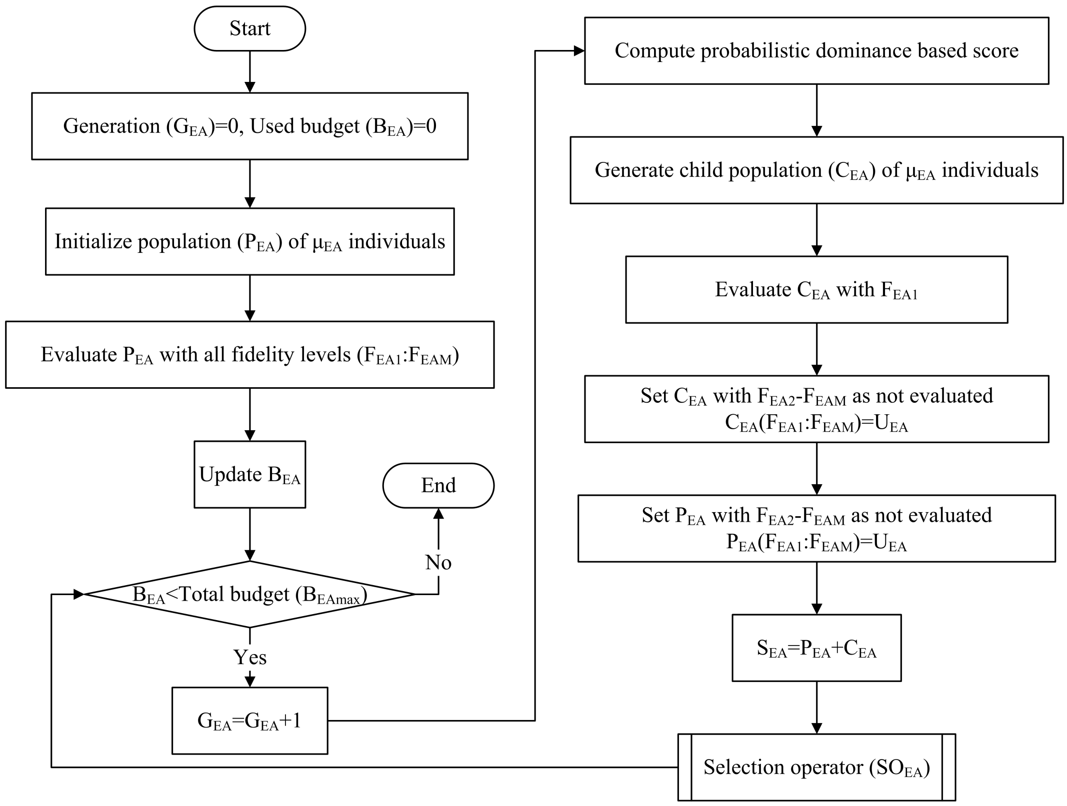

Fig. 3.11: Flowchart of evolutionary algorithm with multi fidelity method (main progress). μ_{EA} is the population size and F_{EA} is the fidelity level from 1 to M where M is the highest fidelity level.

The flowchart of the multi-fidelity evolutionary algorithm is shown in Figs.

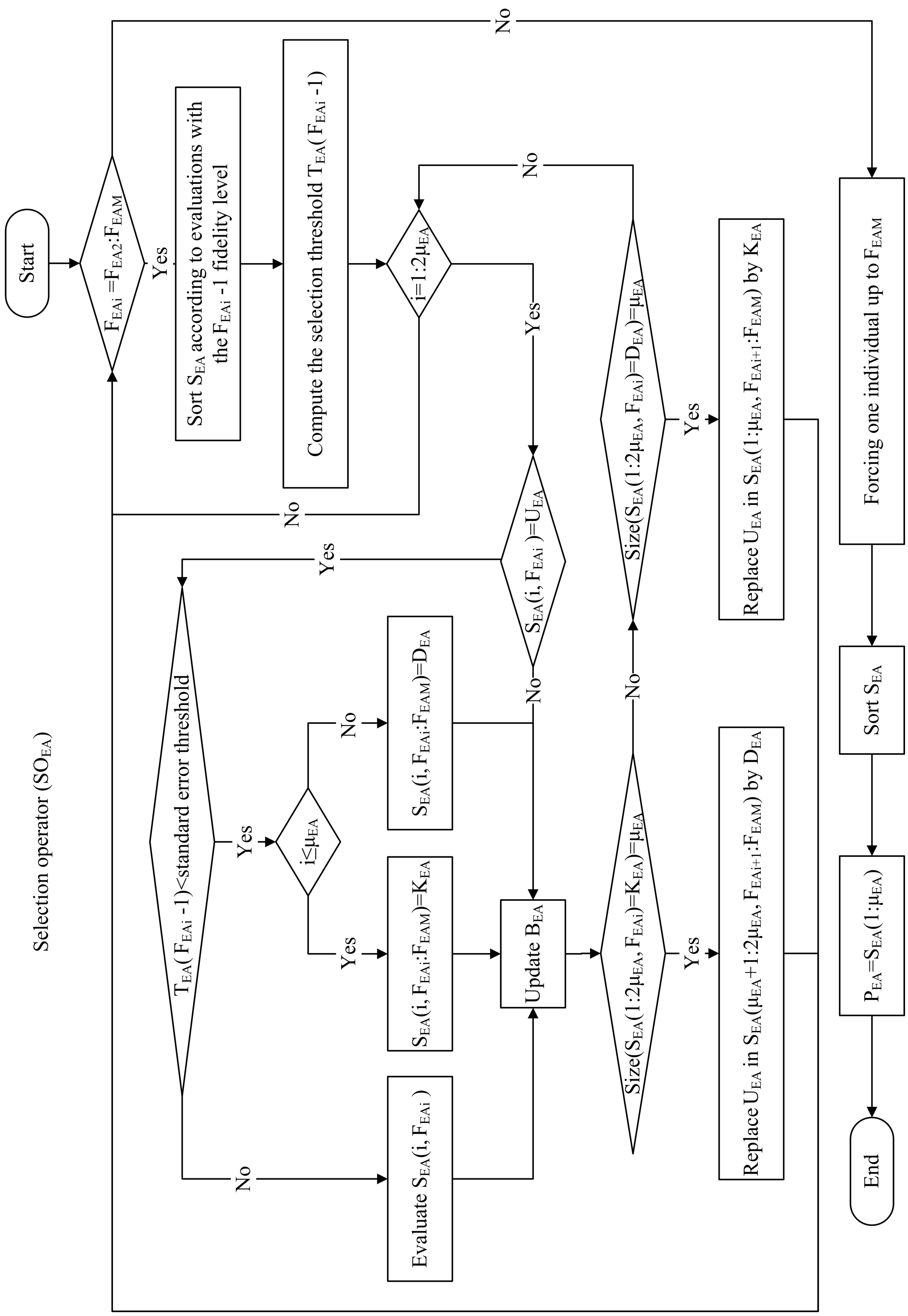

Fig. 3.12: Flowchart of evolutionary algorithm with multi fidelity method (selection operator). μ_{EA} is population size and F_{EA} is the fidelity level from 1 to M where M is the highest fidelity level.

3.11 and 3.12. The proposed approach is an extension of the work described in Branke et al. (2017). The probabilistic score is derived based on the principles discussed in Hughes (2001) rather than from a logistic regression model in Branke et al. (2017). This method is based on ($\mu + \lambda$) evolutionary approach which has a population of size μ_{EA} and a recombination pool of size λ_{EA}. As shown in Fig. 3.11, the fitness values of all solutions (P_{EA} containing μ_{EA} individuals) are evaluated using all the fidelity levels ($F_{EA1} - F_{EAM}$, where $_M$ is the highest fidelity level) during initialization. The probabilistic score and the standard error of the score computation involves prediction of highest fidelity objective values of all solutions using the values of actually evaluated neighbouring solutions at the highest fidelity level (F_{EAM}). Crossover and mutation operators are used to generate offspring solutions (C_{EA}) of size μ_{EA} from parent individuals (P_{EA}) for the next generation G_{EA}. Then, the status of parent and child individuals from the second to the highest fidelity levels (F_{EA2}-F_{EAM}) is marked as not evaluated (U_{EA}). In the selection operator SO_{EA} (Fig. 3.12), the appropriate fidelity levels are selected in an iterative manner based on the probabilistic dominance score. Based on the score, the solutions of the parent and child populations (S_{EA}=P_{EA}+C_{EA}) of $2\mu_{EA}$ individuals are sorted based on evaluations at $F_{EAi} - 1$. Then the selection threshold (T_{EA}) is computed based on the score. If the status of an individual is not evaluated (U_{EA}), the process to determine whether it needs to be evaluated at F_{EAi} will be conducted. The solutions with the selection threshold (T_{EA}) within the standard error threshold are identified to keep or discard: when the rank i is less than or equal to the population size μ_{EA}, the status of the individual is marked as sure for keeping (K_{EA}); otherwise it is marked as sure for discarding (D_{EA}). On the other hand, when T_{EA} is greater than the standard error threshold, the individual is identified for evaluation at the next higher fidelity level (F_{EAi}). If the number of individuals marked as K_{EA} or D_{EA} is sufficient (equals to μ_{EA}), individuals marked as U_{EA} will be selected for evaluation at the next higher fidelity level. This process continues till no solution is selected for evaluation at the next higher fidelity level. A forcing method (Branke et al. 2017) is employed to reduce the risk that solutions based on their low fidelity evaluations are approaching the optimum which is not truly optimum if evaluated at the highest fidelity level. It updates the probabilistic score by evaluating the solution with the smallest probabilistic score at the highest fidelity level in each generation. Solutions (S_{EA}) of $2\mu_{EA}$ individuals are sorted and the parent population (P_{EA}) for the next generation is the top ranked 1-μ_{EA} individuals. Even though the usage of time budget (B_{EA}) is updated in the selection operator (SO_{EA} in Fig. 3.12), the termination criterion ($B_{EA} > B_{EAmax}$) is at the end of each generation (Fig. 3.11). This indicates that the actual time used B_{EAa} with the MFEA is larger than the estimated time budget B_{EAmax}. For comparison with SFEA, the best value of the single objective function given by the MFEA when the estimated time budget B_{EAmax} is used up is the interpolated value of the best objective values at specified used time units (B_{EA} at the end of each generation).

For comparison of the evolutionary algorithm with the classical optimization method, a non-gradient based classical method, the complex method with a randomization factor (Krus & Andersson 2003), is reproduced with Matlab R2013b. Non-linear functions of 3 fidelity levels (f_1, f_2 and f_3) proposed by Branke et al. (2017) are introduced to test the convergence of the optimization

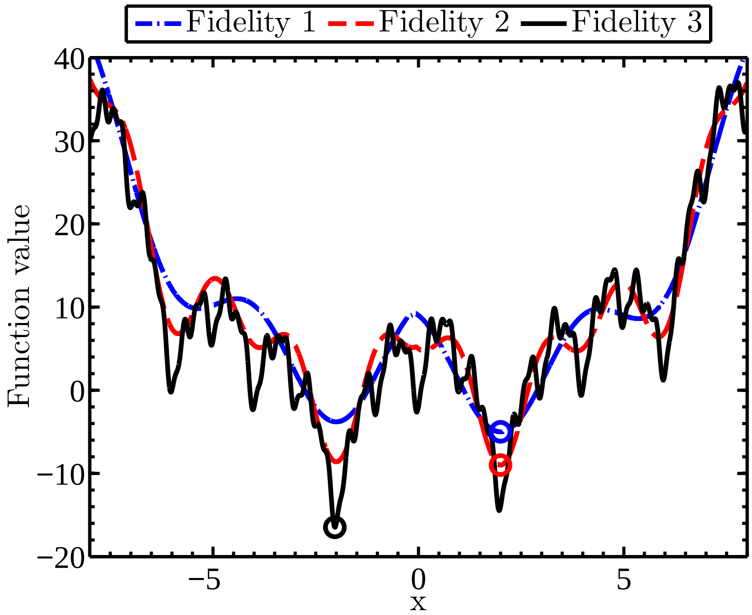

Fig. 3.13: Plot of the artificial functions of fidelity level 1-3, used to test the optimization method. The global optima of the functions are marked with circles.

methods:

$$
\begin{aligned}
f_1 &= \min\left\{ (x-2)^2 + 5\sin\left(\frac{\pi}{2}(x+1)\right), (x+2)^2 + 5\sin\left(\frac{\pi}{2}(x+1)\right) + \frac{6}{5} \right\}, \\
f_2 &= \min\left\{ (x-2)^2 + 5\sin\left(\frac{\pi}{2}(x+1)\right) + 4\sin\left(\pi\left(x+\frac{3}{2}\right)\right), \right. \\
&\qquad \left. (x+2)^2 + 5\sin\left(\frac{\pi}{2}(x+1)\right) + 4\sin\left(\pi\left(x+\frac{3}{2}\right)\right) + \frac{2}{5} \right\}, \\
f_3 &= \min\left\{ (x-2)^2 + 5\sin\left(\frac{\pi}{2}(x+1)\right) + 4\sin\left(\pi\left(x+\frac{3}{2}\right)\right) \right. \\
&\qquad + 3\sin\left(2\pi\left(x+\frac{7}{4}\right)\right) + 2\sin\left(4\pi\left(x+\frac{15}{8}\right)\right) + \sin\left(8\pi\left(x+2\right)\right), \\
&\qquad (x+2)^2 + 5\sin\left(\frac{\pi}{2}(x+1)\right) + 4\sin\left(\pi\left(x+\frac{3}{2}\right)\right) \\
&\qquad \left. + 3\sin\left(2\pi\left(x+\frac{7}{4}\right)\right) + 2\sin\left(4\pi\left(x+\frac{15}{8}\right)\right) + \sin\left(8\pi\left(x+2\right)\right) - 2 \right\}.
\end{aligned}
$$

The artificial functions of fidelity level 1 and 2 (f_1 and f_2) provide coarse approximation to the function of the highest fidelity level (f_3). In addition, the position of the global optimum of f_3 is different from that of f_1 and f_2 , as shown in Fig. 3.13. It is assumed that solving f_1 and f_2 consumes respectively 1/3 and 2/3 computational time of solving f_3.

In the complex method, the reflection coefficient determining the distance between the reflection and the centroid points is 1.3 suggested by Box (1965), and the randomization factor used to generate random noise and repeat factor used to prevent the complex from collapse are respectively 0.3 and 4 suggested by Andersson (2001). Following Branke et al. (2017) and Deb et al. (2002), the probability of crossover and mutation is set to 1 and 0.2, respectively in the EA. The distribution indices for crossover (η_c) and mutation (η_m) are set as 20 and 30, respectively. The number of neighbours is set to three times the number of design variables and the population size is 20 times the number of objectives. The computational time budget is estimated based on the number of simulations at the highest fidelity level, which is at least 100 times the number of design variables.

Function values in the single-fidelity evolutionary algorithm (SFEA) and the complex method are only given by f_3, while function values of fidelity levels 1, 2 and 3 in the multi-fidelity evolutionary algorithm (MFEA) are respectively given by f_1, f_2 and f_3. The number of vertices in the complex method and the population size of the single-fidelity evolutionary algorithm (SFEA) and multi-fidelity evolutionary algorithm (MFEA) are set to 20. A pre-defined time budget equivalent to 3400 runs of f_3 is employed in the single-objective optimization problem solved by the three methods. The results in Fig. 3.14 are based on the average of 30 independent optimization runs with random initial values. The convergence history shows that the starting points of the optimization process using the complex method, SFEA and MFEA are the same. Compared to the complex method where only one reflection point is

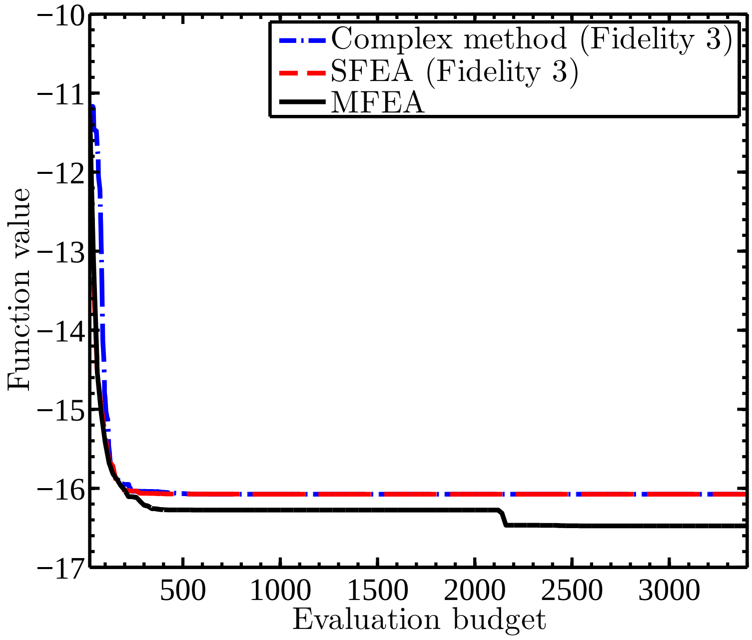

(a)

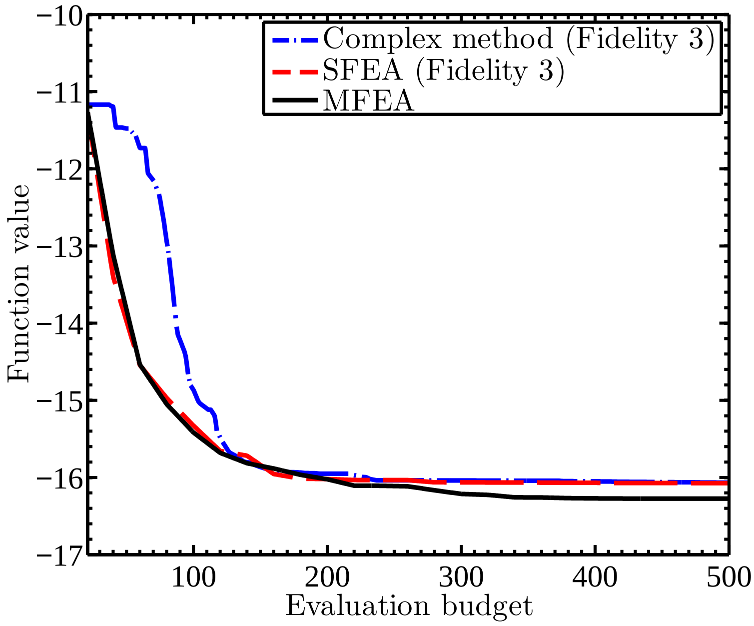

(b)

Fig. 3.14: Convergence history of the singe-objective problem using the complex method, single-fidelity evolutionary algorithm (SFEA) and multi-fidelity evolutionary algorithm (MFEA).

employed in each step, both the SFEA and MFEA provide better results at the early stage of the optimization process (e.g. usage of budget less than 200, Fig. 3.14b) due to the diversity of the individuals in each generation. Although the rate of convergence of the SFEA and MFEA is similar, the MFEA is more likely to converge to the global optimum of -16.5(Fig. 3.14a).

3.5 Summary

In this chapter, the physical problems investigated in Chapters 4-6 were first described. Then, the Bryant model (Bryant et al. 2013) was reproduced and compared with results given by computational fluid dynamics (CFD) method (Kinsey & Dumas 2008). Thirdly, an immersed boundary-lattice Boltzmann method (IB-LBM) was presented and validated after grid and time step refinement against results given by the Navier-Stokes solver (Kinsey & Dumas 2008) and the experiment (Toomey & Eldredge 2008). Finally, multi-fidelity evolutionary algorithm (MFEA) was presented and a study on the convergence of the complex method and the evolutionary algorithm using multi and single fidelity strategies was conducted.

As mentioned in Chapter 2, it is computationally prohibitive to use computational fluid dynamics (CFD) methods for optimizing the energy extraction performance of a flapping foil power generator. To reduce the time costs and take into account the influence of the formation of leading edge vortices (LEV-s), the the Bryant model which introduces dynamics stall effects was reproduced with Matlab. The Bryant model only took several seconds and agreed well with CFD results of Kinsey & Dumas (2008) under specified conditions when the constants are tuned appropriately. The Bryant model reproduced in this chapter and an improved discrete vortex method in which empirical constants are independent of kinematics of the flapping foil developed in Chapter 4 will be implemented into the MFEA to optimize the energy extraction performance.

To obtain details of the flow field and solve fluid-structure interaction (FSI) problems, IB-LBM is used in this study. The IB-LBM is efficient to simulate a flapping foil undergoing large displacement (i.e. the order of the amplitude of the plunge motion is the same as that of the chord length) and large deformation (i.e. the order of the amplitude of the tail angle is the same as that of the pitch motion) since it avoids mesh movement and regeneration. In addition, a multi-block technique and parallelization using OpenMP were employed to reduce time costs. The results of the IB-LBM showed good agreement with those of the Navier-Stokes solver (Kinsey & Dumas 2008) and the experiment (Toomey & Eldredge 2008).

Considering the non-linearity of the flapping foil problem, an evolutionary algorithm is used to optimize the kinematic parameters of the flapping foil power generator. A multi fidelity strategy is employed to reduce the number of evaluations for optimization. The converge of the optimization problem implemented with artificial functions showed that the MFEA converged faster than the traditional optimization method, the complex method, and was more likely to converge to the global optimum compared to the evolutionary algorithm using single fidelity strategy. Further discussions on the convergence of the evolutionary algorithm using multi and single fidelity strategies to solve the flapping foil problem will be presented in Chapter 5.

Chapter 4

Discrete Vortex Method with Flow Separation Corrections

The Bryant model (Bryant et al. 2013) reproduced in Section 3.2 shows reasonable agreement with the CFD results. However, the empirical constants with respect to dynamic stall effects were tuned using the CFD results of Kinsey & Dumas (2008). These constants which are tied to both geometries and kinematics effectively limit the application of the Bryant model to a range of parameters validated by the CFD results. In this chapter, a physics-based model which is only Reynolds number and foil geometry dependent for aerodynamic modelling is developed to reduce the computational cost for flapping foil analysis and to pave the way to engineering design and optimization with higher fidelity and range of applicability than provided by the Bryant or similar methods, but still with dramatically reduced computational cost compared

The following papers have been published from this chapter:
[1]. Zhengliang Liu, Joseph C.S. Lai, John Young, and Fang-Bao Tian. A discrete vortex method for flapping foil power generator modeling at low Reynolds numbers. In *24th International Congress of Theoretical and Applied Mechanics*, Montreal, Canada, August 2016.
[2]. Zhengliang Liu, Joseph C.S. Lai, John Young, and Fang-Bao Tian. Discrete vortex method with flow separation corrections for flapping-foil power generators. *AIAA Journal*, 55(2):410-418, 2017.

to the CFD methods. In Section 4.1, the model based on the discrete vortex method (DVM) is described, which incorporates the formation and evolution of LEVs and empirical functions analogous to the Leishman-Beddoes model (1989) to account for the trailing edge flow separation. In Section 4.2, the computational time of the DVM with flow separation corrections is compared with that of the immersed boundary-lattice Boltzmann method (IB-LBM). Then results given by the modified DVM and the Bryant model reproduced in Section 3.2 are quantitatively compared against IB-LBM simulations and numerical and experimental results in the literature under different flow conditions.

4.1 Code development

The discrete vortex method is a potential flow approach to model unsteady flows. In this method, the foil is discretized by consecutive flat panels. Reduced order models based on this method were modified to model LEVs in unsteady flows by introducing some criteria for the onset of vortex shedding, for example, critical angle of attack (Hammer et al. 2014) and leading edge suction parameter (Ramesh et al. 2014). Although with these criteria, reasonable flow patterns can be obtained, aerodynamic loads acting on the foil are generally over predicted (Pan et al. 2012). Since these models typically assume only flow separation at the leading edge, neglecting the influence of the trailing edge flow separation is not always physically realistic. In this section, the fundamentals of the DVM and corrections in terms of the leading edge flow separation are described and empirical functions proposed by Leishman & Beddoes (1989) are introduced to take into account the reduction in aerodynamic loads corresponding to the trailing edge flow separation.

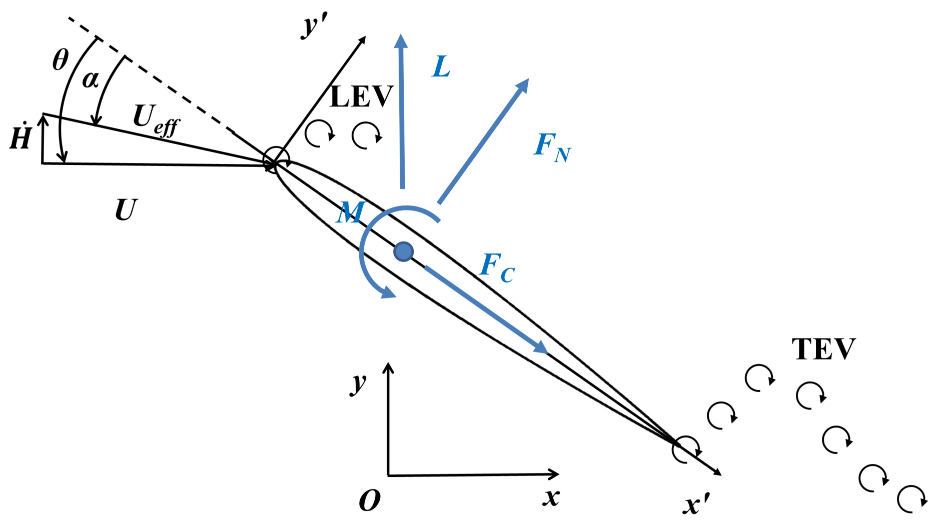

Fig. 4.1: Aerodynamic loads for a NACA0015 foil with fixed coordinate system (x, y) and foil coordinate system (x', y') where its origin is at the leading edge of the foil. Vortex shed from the trailing edge of the foil.

4.1.1 Large amplitude thin aerofoil theory

The Leishman-Beddoes model (Leishman & Beddoes 1989) has been developed for helicopter blade analysis with a maximum angle of attack of 10° in the majority of studies. In this model, the lift and moment coefficients of unsteady attached flow are predicted by the Theodorsen's theory (Theodorsen 1979). However, the application of this classical method is limited by the assumptions of planar wake and small amplitude and is unsuitable for simulations of a flapping foil power generator. To obtain unsteady attached flow solutions at high angles of attack, the DVM outlined by Katz & Plotkin (2001) and extended to non-planar wake and large amplitude simulations is used here.

The DVM attempts to model unsteady flows by discretization of the distributed vorticity by a finite number of small discrete vortex elements. The flapping foil and its wake are respectively modelled by bounded and free vortices. According to the discrete vortex method, trailing edge vortices start to shed from the trailing edge at each time step from time $t > 0$. The free vortices move downstream with the flow particles and their strength remains constant. The velocity induced by each vortex element is obtained using the Bio-Savart Law. Then the velocity field is computed as the sum of the velocities induced by the bounded and free vortex elements.

The local velocity normal to the foil $v'(x,t)$ in the foil coordinate system (x', y') in Fig. 4.1 can be computed according to the boundary condition (Katz & Plotkin 2001):

$$v'(x',t) = \dot{H}\cos\theta - U\sin\theta + \dot{\theta}(x' - x_{piv}c) - \frac{\partial\Phi_L}{\partial y'} - \frac{\partial\Phi_T}{\partial y'}, \tag{4.1}$$

where Φ_L and Φ_T are the velocity potentials with respect to leading and trailing edge vortices. The chordwise position x' is transformed using the chordwise coordinate transformation variable ϑ as (Katz & Plotkin 2001):

$$x' = \frac{c}{2}(1 - \cos\vartheta). \tag{4.2}$$

Based on this transformation, a solution to the vorticity distributions $\gamma(\vartheta, t)$ over the foil is proposed for the time dependent problem (Katz & Plotkin 2001):

$$\gamma(\vartheta,t) = 2U\left[A_0(t)\frac{1+\cos\vartheta}{\sin\vartheta} + \sum_{n=1}^{\infty} A_n(t)\sin(n\vartheta)\right], \tag{4.3}$$

where the coefficients $A_n(t)$ which implicitly satisfy the Kutta condition (zero vorticity at the trailing edge) are computed by (Katz & Plotkin 2001)

$$A_0\left(t\right) = -\frac{1}{\pi}\int_0^\pi \frac{W\left(\vartheta,t\right)}{U}\mathrm{d}\vartheta, \tag{4.4}$$

$$A_n\left(t\right) = \frac{2}{\pi}\int_0^\pi \frac{W\left(\vartheta,t\right)}{U}\cos n\vartheta\mathrm{d}\vartheta, n = 1,2,3,... \tag{4.5}$$

The strength of the latest leading and trailing edge vortices can be calculated using Kelvin's condition (i.e. the total circulation which must be zero for a converged solution, Katz & Plotkin 2001):

$$\Gamma\left(t\right) + \Gamma_{Vi}\left(t\right) + \sum_{k=1}^{i-1}\Gamma_{Vk} = 0, \tag{4.6}$$

where $\Gamma\left(t\right)$ is the circulation bounded on the foil, $\Gamma_{Vi}\left(t\right)$ is the circulation of leading and trailing edge vortices at the current time step t_i, and the last term is the circulation of all the vortices Γ_{Vk} shed in the previous time steps. The circulation of the foil can be obtained by integrating $\gamma\left(\vartheta,t\right)$ along the chordwise coordinate (Katz & Plotkin 2001)

$$\Gamma\left(t\right) = \int_0^\pi \gamma\left(\vartheta,t\right)\mathrm{d}\vartheta = Uc\pi\left[A_0\left(t\right) + \frac{A_1\left(t\right)}{2}\right]. \tag{4.7}$$

4.1.2 Criterion for LEV formation

Experiments (McCroskey 1981, Lee & Gerontakos 2004) have shown that the leading edge separation is correlated to the reversed flow which develops downstream of the suction peak around the leading edge. Inspired by studies on the separation at the leading edge, a criterion referring to the leading edge suction force is introduced by Ramesh et al. (2014) to predict the formation of the LEV. This criterion, named the leading edge suction parameter (LESP), is a non-dimensional measure of the suction at the leading edge

$$\mathrm{LESP}\,(t) = A_0\,(t)\,. \tag{4.8}$$

A critical value of the leading edge suction parameter, named LESP_0, is set such that discrete vortices start to shed from the leading edge when the instantaneous $|\mathrm{LESP}\,(t)\,|$ is higher than LESP_0 and terminate when $|\mathrm{LESP}\,(t)\,|$ falls below LESP_0. LESP_0 is empirically determined by the aerofoil profile and Reynolds number (Re) regardless of kinematic parameters (such as θ_0, h_0 and f^*) and the pivot location. When LEV forms, the strengths of vortices shedding from the leading and trailing edge are determined by solving Eq. 4.6 and $|\mathrm{LESP}\,(t)\,| = \mathrm{LESP}_0$. Here, $\mathrm{LESP}_0 = 0.19$ (NACA0015 foil, $Re = 1100$) suggested by Ramesh et al. (2014) is used. It should be noted that the leading edge separation point is enforced exactly at the leading edge in this study. The effect of this assumption on the accuracy of the DVM calculations may be explored in a future study by determining the separation point based on experimental data (see Katz (1981) and Antonini et al. (2014)).

4.1.3 Trailing edge flow separation

In the DVM with LESP, the influence of the flow separation point movement starting from the trailing edge is neglected because vortex shedding is enforced at the leading and trailing edge. Here, the Kirchhoff flow approximation modified by Leishman & Beddoes (1989) is used for trailing edge flow separation corrections (TEFSC). This simple method using semi-empirical functions to account for unsteady flow separations gives the following expressions for normal force coefficient C_N^{sep}, chord force coefficient C_C^{sep} and moment coefficient

C_M^{sep} (Bauchau 2007):

$$C_N^{sep} = C_N^{cir} \left(\frac{1 + \sqrt{f^{sep}}}{2} \right)^2 , \tag{4.9}$$

$$C_C^{sep} = C_C \sqrt{f^{sep}}, \tag{4.10}$$

$$C_M^{sep} = \left[x_{piv} + k_1 \left(1 - f^{sep}\right) + k_2 \sin\left(\pi \left(f^{sep}\right)^2\right)\right] C_N^{sep}, \tag{4.11}$$

where f^{sep} is the separation point, C_N^{cir} is the circulatory normal coefficient and C_C is the leading edge suction force coefficient. Empirical constants $k_1 = -0.135$ and $k_2 = 0.04$ (only data of NACA0012 is available in Bauchau 2007, independent of Re) represent the direct effect on the center of pressure due to the growth of the separated flow region and the shape of the moment break due to the stall effects respectively (Bauchau 2007).

The position of steady-state separation point f_0^{sep} is generally a nonlinear function of the angle of attack α. In principle, the function f_0^{sep} could be obtained from wind tunnel tests. In the Leishman-Beddoes model (1989), the relationship between f_0^{sep} and α is generalized empirically as a piecewise function (Dyachuk et al. 2013):

$$f_0^{sep} = \begin{cases} 1 - 0.3\exp\left(\frac{|\alpha| - \alpha_1}{S_1}\right) & |\alpha| < \alpha_1 \\ 0.04 - 0.66\exp\left(\frac{\alpha_1 - |\alpha|}{S_2}\right) & |\alpha| \geqslant \alpha_1 \end{cases} , \tag{4.12}$$

where constant $S_1 = 3.0$, $S_2 = 2.3$, $\alpha_1 = 15.25°$ (only data of NACA0012 is available in Bauchau 2007, independent of Re) are determined from static experimental data (Bauchau 2007).

For unsteady flow conditions, the effective separation point f^{sep} differs from the stationary value due to the boundary-layer convection lag. To capture the transient dynamic effects, the movement of f^{sep} can be described using a first order differential equation (Goman & Khrabrov 1994, Fan & Lutze 1996):

$$\tau_1 \frac{df^{sep}}{dt} + f^{sep} = f_0^{sep} \left(\alpha - \tau_2 \dot{\alpha} \right), \tag{4.13}$$

where $\tau_1 = 0.52c/U$ and $\tau_2 = 4.5c/U$ (NACA0015, independent of Re) are relaxation time constants (Goman & Khrabrov 1994).

4.1.4 Integration of hydrodynamic loads

The pressure distributions on the foil can be computed from the unsteady Bernoulli equation (Katz & Plotkin 2001):

$$\begin{aligned} \Delta p \left(x' \right) = & \rho \left(-\dot{H} \sin\theta + U \cos\theta + \frac{\partial \Phi_L}{\partial x'} + \frac{\partial \Phi_T}{\partial x'} \right) \gamma \left(x' \right) \\ & + \rho \frac{\partial}{\partial t} \int^{x'} \gamma \left(x' \right) \mathrm{d}x'. \end{aligned} \tag{4.14}$$

The circulatory normal force coefficient C_N^{cir} due to the instantaneous circulation and the non-circulatory normal force coefficient C_N^{non} including the contribution of the time dependency are obtained by integrating the pressure over the foil and normalising with $(1/2)\,\rho U^2 c$,

$$\begin{aligned} C_N^{cir} = & \frac{2\pi}{U} \left(-\dot{H} \sin\theta + U \cos\theta \right) \left(A_0 \left(t \right) + \frac{1}{2} A_1 \left(t \right) \right) \\ & + \frac{2}{U^2 c} \int_0^{x'} \left(\frac{\partial \Phi_L}{\partial x'} + \frac{\partial \Phi_T}{\partial x'} \right) \gamma \left(x', t \right) \mathrm{d}x', \end{aligned} \tag{4.15}$$

$$C_N^{non} = \frac{2\pi c}{U} \left(\frac{3}{4} \dot{A}_0 \left(t \right) + \frac{1}{4} \dot{A}_1 \left(t \right) + \frac{1}{8} \dot{A}_2 \left(t \right) \right). \tag{4.16}$$

The leading edge suction force coefficient C_C is calculated by the Blasius formula (Garrick 1937):

$$C_C = 2\pi A_0 \left(t \right)^2. \tag{4.17}$$

Using Eqs. 4.9, 4.10 and 4.16, the lift coefficient C_L is given by

$$C_L = (C_N^{sep} + C_N^{non})\cos\theta - C_C^{sep}\sin\theta. \tag{4.18}$$

When the effect of the trailing edge flow separation is introduced through Eq. 4.11, the moment coefficient about x_{piv} can be expressed as

$$\begin{aligned} C_M = &\left[\left(x_{piv} + k_1\left(1 - f^{sep}\right) + k_2 \sin\left(\pi\left(f^{sep}\right)^2\right)\right) C_N^{sep} + C_N^{non} x_{piv}\right] \\ &- \frac{2\pi}{U}\left(1+\sqrt{f^{sep}}\right)^2 \left[\left(-\dot{H}\sin\theta + U\cos\theta\right)\left(\frac{1}{4}A_0(t) + \frac{1}{4}A_1(t) - \frac{1}{8}A_2(t)\right)\right] \\ &- \frac{2}{U^2c^2}\left(1+\sqrt{f^{sep}}\right)^2 \left[\int_0^{x'} \left(\frac{\partial \Phi_L}{\partial x'} + \frac{\partial \Phi_T}{\partial x'}\right)\gamma(x', t)\, x' \mathrm{d}x'\right] \\ &+ \frac{2\pi c}{U}\left[\frac{7}{16}\dot{A}_0(t) + \frac{3}{16}\dot{A}_1(t) + \frac{1}{16}\dot{A}_2(t) - \frac{1}{64}\dot{A}_3(t)\right]. \end{aligned} \tag{4.19}$$

4.2 Code validation and discussion

4.2.1 Computational time

In the runtime test, the Bryant model, DVM and IB-LBM are all compiled with Intel Fortran on Linux system and operated on a single Xeon/2.67-GHz processor. As shown in Fig. 4.2, when the non-dimensional time step $\Delta t^* = \Delta t U/c = 0.010$ and 0.015, the differences in η of the three cases after seven flapping cycles is less than 3% at $Re = 1100$, $f^* = 0.14, \theta_0 = 76.3°, h_0 = 1, \varphi = 90°$ and $x_{piv} = 0.333$. Thus $\Delta t^* = 0.015$ is used for simulations of the DVM. In the Bryant model, the same $\Delta t^* = 0.015$ is used for comparison with the DVM; and $\Delta t^* = 0.0015$ is utilized in the IB-LBM to ensure the convergence of the simulations. $\varphi = 90°$, $x_{piv} = 0.333$ and $h_0 = 1$ are fixed here.

The results of the Bryant model do not change with the increase of the

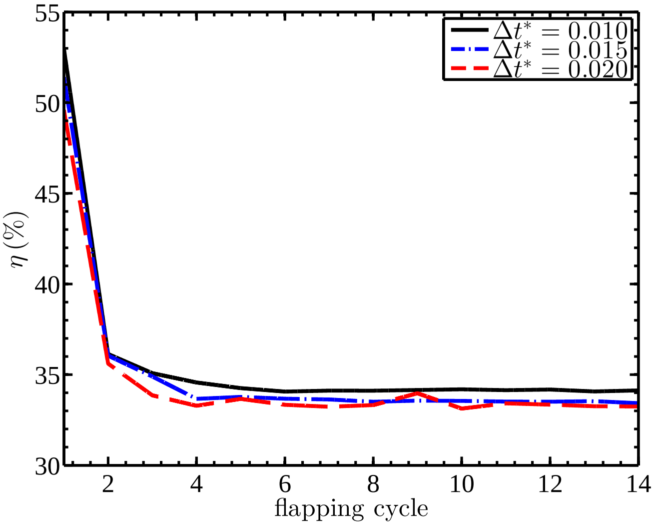

Fig. 4.2: Cycle-to-cycle convergence of the efficiency predicted by the discrete vortex method at $Re = 1100$, $f^* = 0.14, \theta_0 = 76.3°, h_0 = 1, \varphi = 90°$ and $x_{piv} = 0.333$.

Table 4.1: Computational time of the DVM with TEFSC and the IB-LBM for various number of simulated flapping cycles. LBM .vs. DVM stands for the ratio of the computational time of the LBM to the computational time of the DVM.

Kinematics	Cycles	DVM	LBM	LBM .vs. DVM
$f^* = 0.18$	1	2.6 (s)	28665.6 (s)	10831.1
$\theta_0 = 60°$	2	18.9 (s)	54948.7 (s)	2903.3
	4	129.5 (s)	110994.8 (s)	857.0
	8	418.0 (s)	226006.3 (s)	540.6
	12	708.3 (s)	337389.2 (s)	476.3
$f^* = 0.14$	1	8.1 (s)	33274.1 (s)	4121.3
$\theta_0 = 76.3°$	2	53.9 (s)	66586.0 (s)	1235.7
	4	334.2 (s)	139745.8 (s)	418.2
	8	1062.4 (s)	284028.5 (s)	267.4
	12	1813.8 (s)	433331.3 (s)	238.9
$f^* = 0.12$	1	10.0 (s)	42524.6 (s)	4244.6
$\theta_0 = 60°$	2	71.1 (s)	84443.2 (s)	1188.1
	4	334.0 (s)	170784.7 (s)	511.3
	8	882.5 (s)	352264.3 (s)	399.2
	12	1456.8 (s)	511074.5 (s)	350.8

number of flapping cycles simulated. Thus, only the first cycle of the Bryant model is computed, which takes less than 1 second. 12 flapping cycles of DVM and IB-LBM are computed here because IB-LBM converges after 12 cycles as discussed in Section 3.3. Since the time step is fixed, the computational time of the IB-LBM increases monotonically with decreasing f^*, as shown in Table 4.1 for three different kinematics conditions, because the total number of time steps per flapping cycle increases with decreasing f^*. Table 4.1 illustrates that for the calculations of DVM with TEFSC, the computational time required depends not only on the total number of time steps per cycle but also on the number of leading edge vortices shed due to increasing resources required to compute every vortex element shed from the leading edge and the trailing edge. According to Kinsey & Dumas (2008), when $f^* = 0.14$ and $\theta_0 = 76.3°$, strong vortices form at the leading edge of the foil while no obvious LEV is observed in the other two cases. Hence, for $f^* = 0.14$ where there is a large number of vortices, the computational time after 4 cycles is higher than that for $f^* = 0.12$ and $f^* = 0.18$ where there are a very small number of vortices. Nevertheless, as shown in Table 4.1, the computational time required for DVM with TEFSC with three different kinematic conditions spanning a range of very few LEVs to many LEVs is at least two orders of magnitude less than that of the IB-LBM. In addition, the rate of increase in computational time of the DVM is greater than that of the IB-LBM when more cycles are simulated. However, the DVM converges after 7 flapping cycles (Fig. 4.2) while the IB-LBM converges after 12 flapping cycles. Thus in real applications, the time consumption of the DVM is much less than that of the IB-LBM.

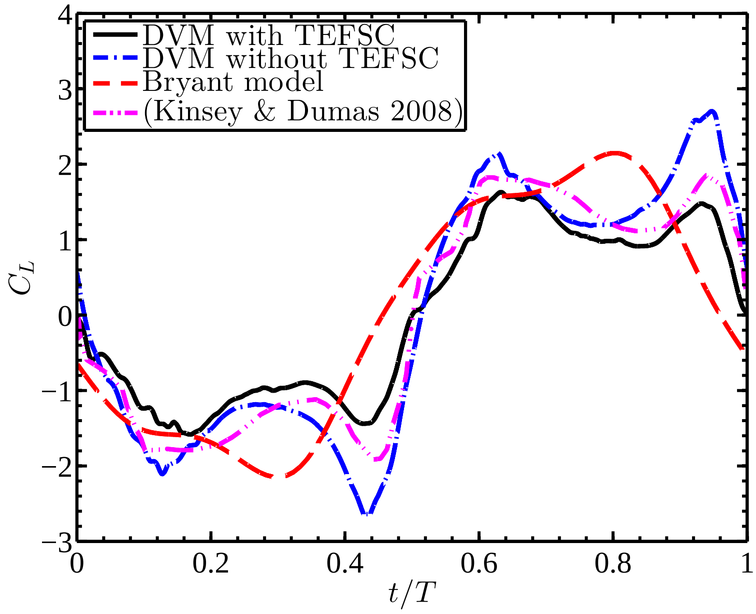

(a) Time histories of C_L.

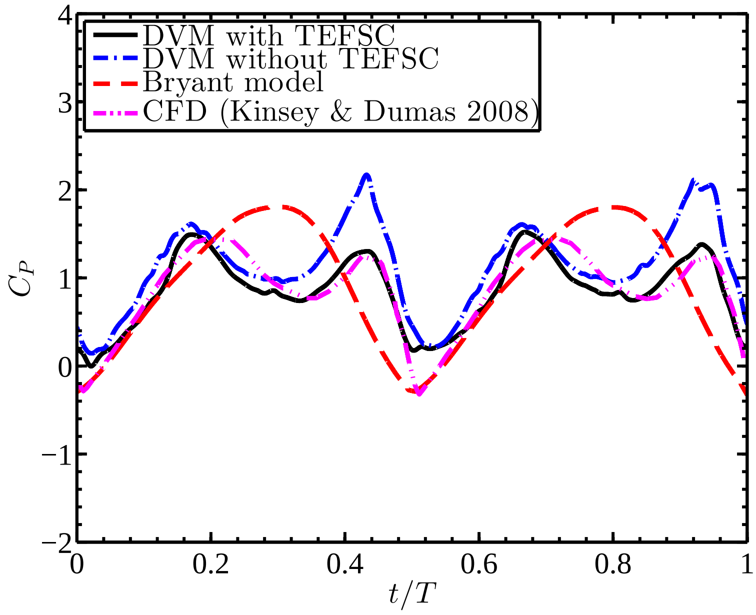

(b) Time histories of C_P.

Fig. 4.3: Comparison of (a) lift coefficient C_L and (b) power coefficient C_P at $f^* = 0.14$, $\theta_0 = 76.3°$, $h_0 = 1$, $\varphi = 90°$ and $x_{piv} = 0.333$ given by the DVM with and without TEFSC, Bryant model (Bryant et al. 2013) reproduced in Section 3.2 and CFD simulations conducted by Kinsey & Dumas (2008).

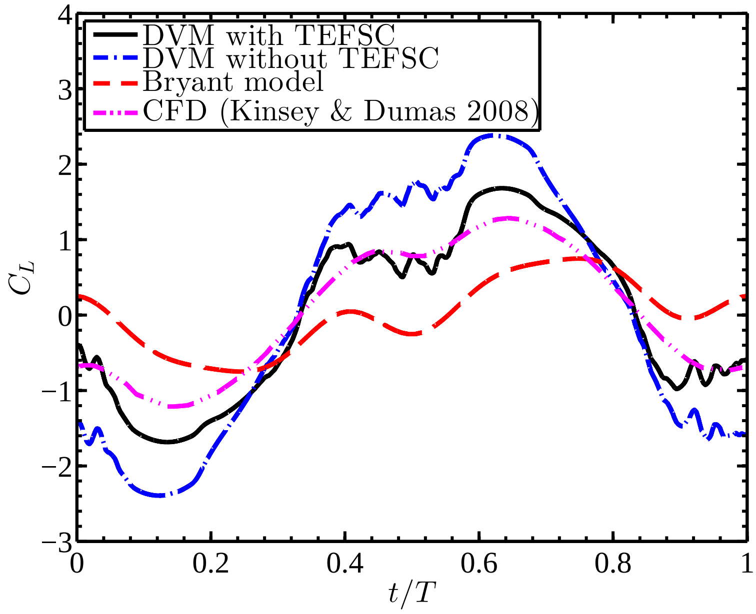

(a) Time histories of C_L.

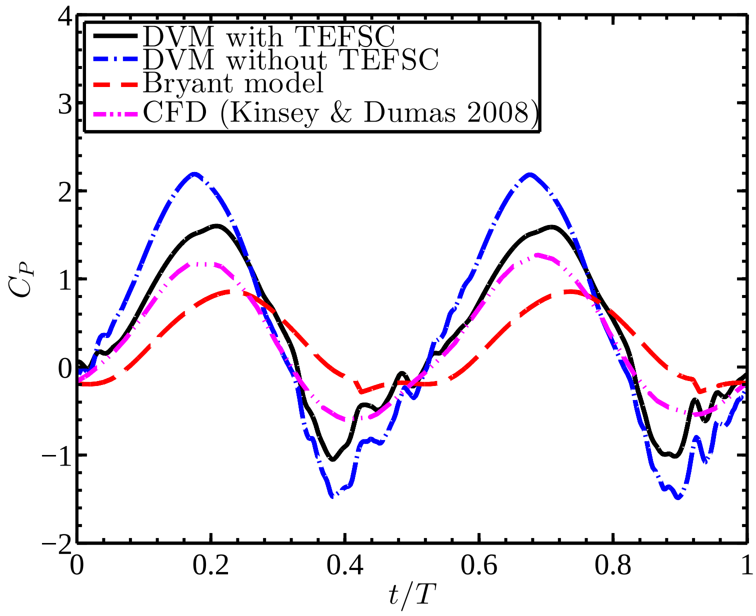

(b) Time histories of C_P.

Fig. 4.4: Comparison of (a) lift coefficient C_L and (b) power coefficient C_P at $f^* = 0.14$, $\theta_0 = 76.3°$, $h_0 = 1$, $\varphi = 90°$ and $x_{piv} = 0.333$ given by the DVM with and without TEFSC, Bryant model (Bryant et al. 2013) reproduced in Section 3.2 and CFD simulations conducted by Kinsey & Dumas (2008).

Table 4.2: Comparison of mean power coefficient $\overline{C}_P$, efficiency η and root mean square (RMS) error of the instantaneous power coefficient C_P given by the DVM with TEFSC (DVM1), DVM without TEFSC (DVM2) and Bryant model (Bryant et al. 2013) reproduced in Section 3.2 against CFD results of Kinsey & Dumas (2008).

Kinematics	Parameter	Bryant	DVM1	DVM2	CFD(Kinsey & Dumas 2008)
$f^* = 0.14$	$\overline{C}_P$	0.87	0.86	1.12	0.86
$\theta_0 = 76.3°$	η	34.1%	33.4%	43.8%	33.7%
	RMS	0.55	0.19	0.45	-
$f^* = 0.18$	$\overline{C}_P$	0.24	0.37	0.41	0.27
$\theta_0 = 60°$	η	10.1%	15.6%	17.3%	11.4%
	RMS	0.37	0.24	0.52	-

4.2.2 Averaged and instantaneous coefficients

To evaluate predictions provided by the DVM and Bryant model, two cases are selected for comparison because strong LEVs are predicted in the first case ($f^* = 0.14$, $\theta_0 = 76.3°$) and no LEV is observed in the second case ($f^* = 0.18$, $\theta_0 = 60°$) with $\varphi = 90°$, $x_{piv} = 0.333$ and $h_0 = 1$. Both the DVM with TEFSC and Bryant model (Bryant et al. 2013) give reasonable $\overline{C}_P$ and η while the DVM without TEFSC gives higher $\overline{C}_P$ and η compared with those of Kinsey & Dumas (2008) (Table 4.2). Since a good synchronization of lift force with the plunge and pitch rate gives a good performance of a flapping foil power generator, it is worthwhile to examine the phase and amplitude of instantaneous C_L. In both cases, the instantaneous C_L and C_P predicted by the DVM with TEFSC (solid line) give better approximations to the CFD results (Kinsey & Dumas 2008) compared to the DVM without TEFSC and the Bryant model (Bryant et al. 2013). In addition, root mean square (RMS) errors of instantaneous C_P in Table 4.2 also demonstrates that the DVM with TEFSC is superior to the Bryant model even if the Bryant model gives a better $\overline{C}_P$ at $f^* = 0.18$, $\theta_0 = 60°$. In the first case (Fig. 4.3), the non-dimensional time at which the peaks of C_L and C_P appear obtained by the Bryant model (Bryant et al. 2013) is significantly different from those of the DVM and Kinsey & Dumas (2008). In the second case (Fig. 4.4), the instantaneous C_L and C_P predicted by the DVM without TEFSC are nearly doubled in half of one stroke compared with those of Kinsey & Dumas (2008). This is attributed to two factors: (a) although no LEV is observed in CFD simulations, C_L is over predicted because the leading edge suction parameter exceeds the critical value LESP_0, resulting in some LEVs for the DVM calculations; and (b) the influence of the trailing edge flow separation resulting in lower aerodynamic loads is neglected. When TEFSC is incorporated into the DVM, the overprediction of C_L and C_P has been significantly reduced by taking into account of the trailing edge flow separation, but C_L and C_P are still higher than those of Kinsey & Dumas (2008) because the leading suction parameter exceeds the critical value LESP_0 resulting in some LEVs even though there are no LEVs observed in CFD simulations. As shown in Fig. 4.4, results of the Bryant model (Bryant et al. 2013) give underestimated amplitudes of C_L and C_P and phase differences of the coefficient curves compared to results of Kinsey & Dumas (2008).

Since time histories of C_M and C_P for different pivot locations are not available in Kinsey & Dumas (2008), the IB-LBM code is used here for validations. The instantaneous C_L obtained by the Bryant model (Bryant et al. 2013) is the same at the same t/T even though the pivot location is different when $x_{piv} = 0.25$ (Fig. 4.5), $x_{piv} = 0.333$ (Fig. 4.3a) and $x_{piv} = 0.75$ (Fig. 4.6) because the influence of the pivot location on the angle of attack has not been taken into account in the Bryant model (Bryant et al. 2013). On the other hand, the DVM with TEFSC shows two obvious peaks near $t/T = 0.1$ and $t/T = 0.4$ with $x_{piv} = 0.25$ (Fig. 4.5), $x_{piv} = 0.333$ (Fig. 4.3a) and one peak

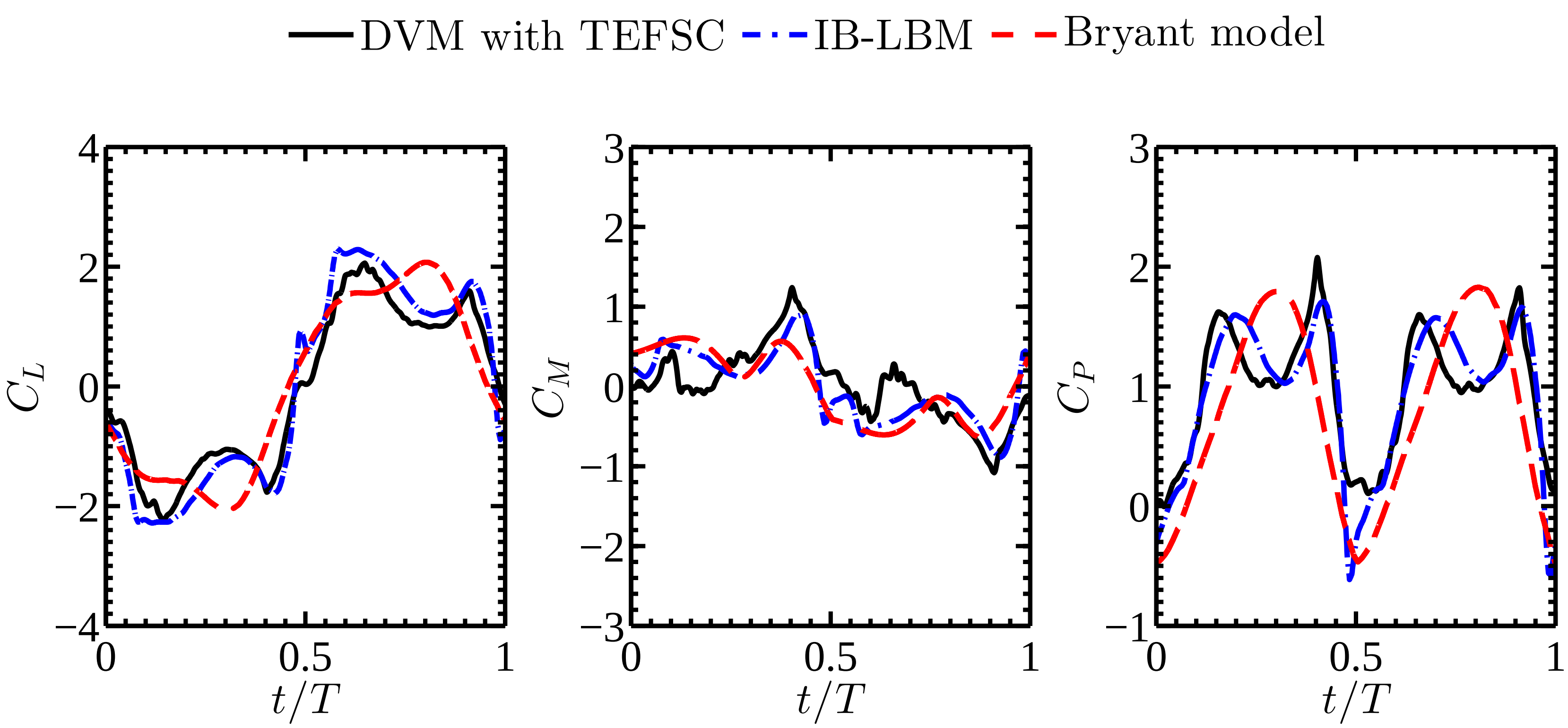

Fig. 4.5: Time histories of C_L, C_M and C_P predicted by the DVM with TEFSC, IB-LBM and Bryant model (Bryant et al. 2013) when $x_{piv} = 0.25$ at $f^* = 0.14$, $\theta_0 = 76.3°$, $h_0 = 1$ and $\varphi = 90°$.

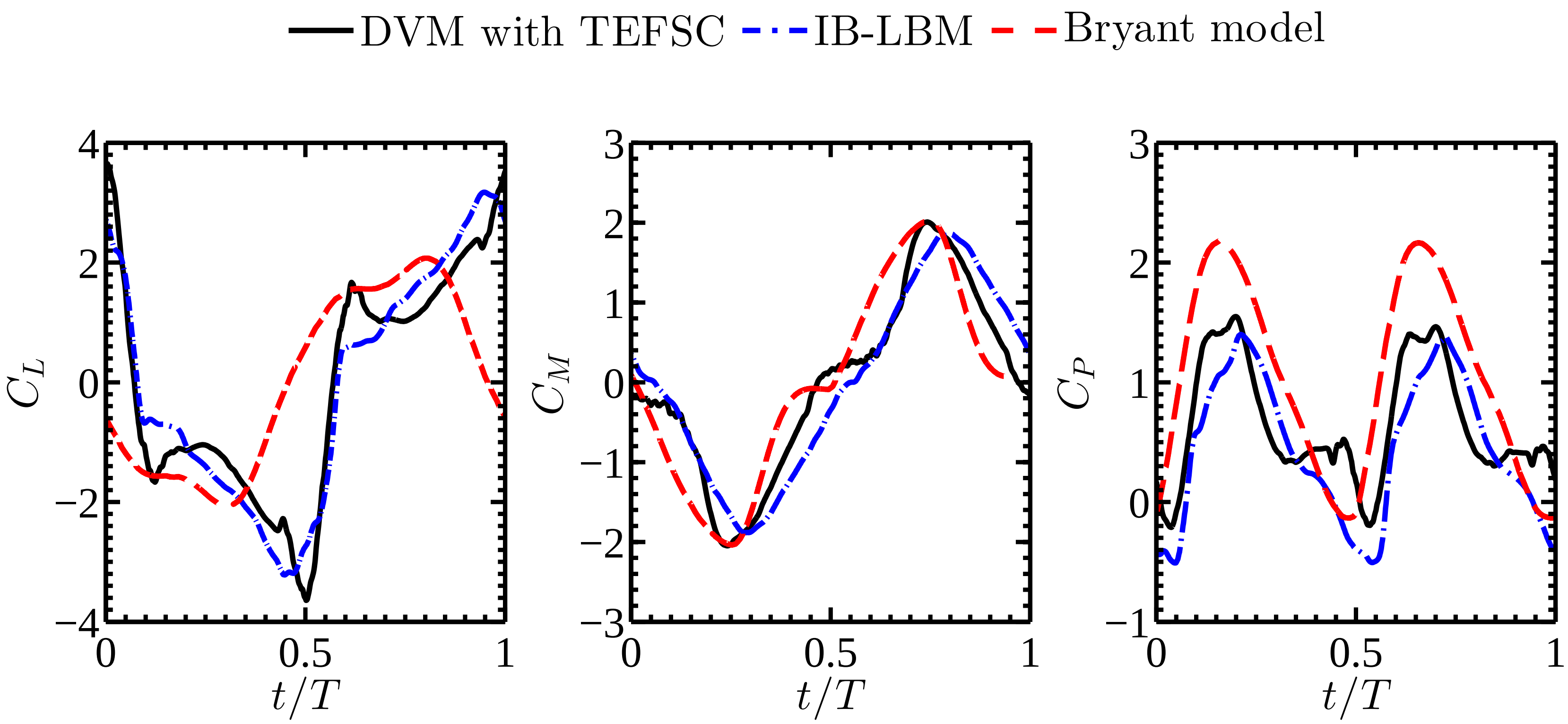

Fig. 4.6: Time histories of C_L, C_M and C_P predicted by the DVM with TEFSC, IB-LBM and Bryant model (Bryant et al. 2013) when $x_{piv} = 0.75$, with $f^* = 0.14$, $\theta_0 = 76.3°$, $h_0 = 1$ and $\varphi = 90°$.

near $t/T = 0.5$ with $x_{piv} = 0.75$ (Fig. 4.6) during the first half cycle which are quite similar to those obtained by the IB-LBM. Furthermore, the peak value of C_L around $t/T = 0.4$ given by the DVM with TEFSC and IB-LBM increases when x_{piv} move aft (Fig. 4.5, 4.3a and 4.6). Even though the trends of C_M obtained by the the Bryant model (Bryant et al. 2013), DVM with TEFSC and IB-LBM are similar for different pivot locations (Fig. 4.5 and 4.6), the peak location (Fig. 4.5) and amplitude (Fig. 4.6) of C_P which contains the contribution of C_L and C_M obtained by the Bryant model (Bryant et al. 2013) are different from those obtained by the DVM with TEFSC and IB-LBM.

Results given by the reduced order models are also compared with the experimental data of Simpson (2009). In this experiment, the NACA0012 foil undergoes a non-sinusoidal plunge motion to keep the angle of attack α sinusoidal at a Reynolds number of 13800. The instantaneous α and θ are given by

$$\theta(t) = \theta_0 \sin(2\pi f t), \tag{4.20}$$

$$\alpha(t) = \alpha_0 \sin(2\pi f t), \tag{4.21}$$

where α_0 is the maximum angle of attack during one cycle. The plunge motion H is obtained by integrating $\dot{H}$

$$H(t) = \int_0^t \dot{H}(t)\,\mathrm{d}t = \int_0^t \tan(\theta(t) - \alpha(t))\,U\mathrm{d}t. \tag{4.22}$$

Since the skin-friction coefficient from the experiment is unavailable, the LESP_0 is determined using RMS errors in the lift coefficient between the experimental data and results of the DVM with TEFSC. The high efficiency case ($f^* = 0.133$, $\alpha_0 = 38.9°$ and $h_0 = 0.75$) is used as the baseline motion for the

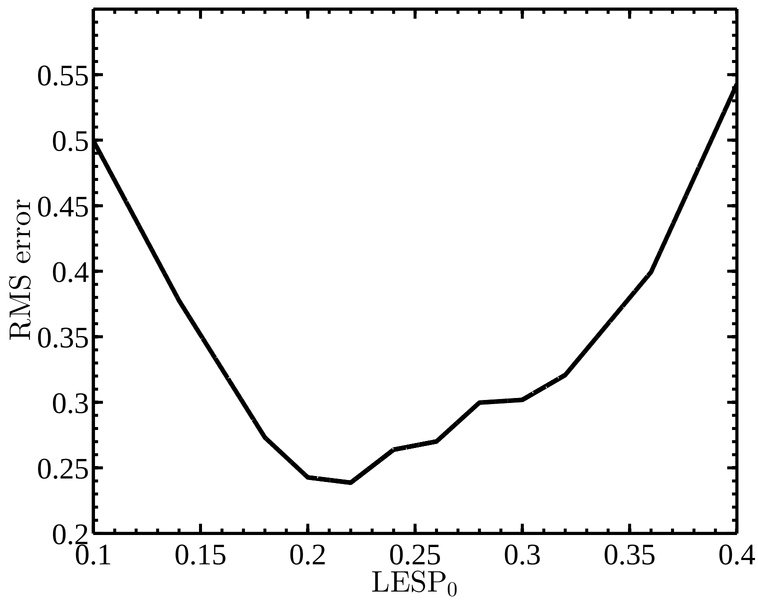

Fig. 4.7: Influence of LESP_0 on the RMS error in C_L between experimental data (Simpson 2009) and results of the DVM with TEFSC.

determination of LESP_0. As shown in Fig. 4.7, the RMS error is minimum at $\mathrm{LESP}_0 = 0.22$. Thus, LESP_0 is taken to be 0.22 here.

Similar to the validation against results of IB-LBM and Bryant model (Bryant et al. 2013) in Fig. 4.3 and Fig. 4.4, two cases of high efficiency ($f^* = 0.133$, $\alpha_0 = 38.9°$) and of low efficiency ($f^* = 0.2$, $\alpha_0 = 53°$) with $h_0 = 0.75$ and $x_{piv} = 0.333$ are selected for comparison of the lift coefficient C_L obtained by the Bryant model (Bryant et al. 2013) and the experimental data of Simpson (2009) with DVM with and without TEFSC in Fig. 4.8. In both cases, the DVM with TEFSC gives better predictions compared to the DVM without TEFSC and Bryant model (Bryant et al. 2013). In particular, when the angle of attack is high ($\alpha_0 = 53°$, Fig. 4.8b), predictions given by the DVM with TEFSC are reasonable while there are significant differences between C_L predicted by the DVM without TEFSC and the experimental data (Simpson 2009). It is also clear from Fig. 4.8b that the Bryant model (Bryant et al. 2013) fails to predict the trend of C_L. The discrepancies between predictions

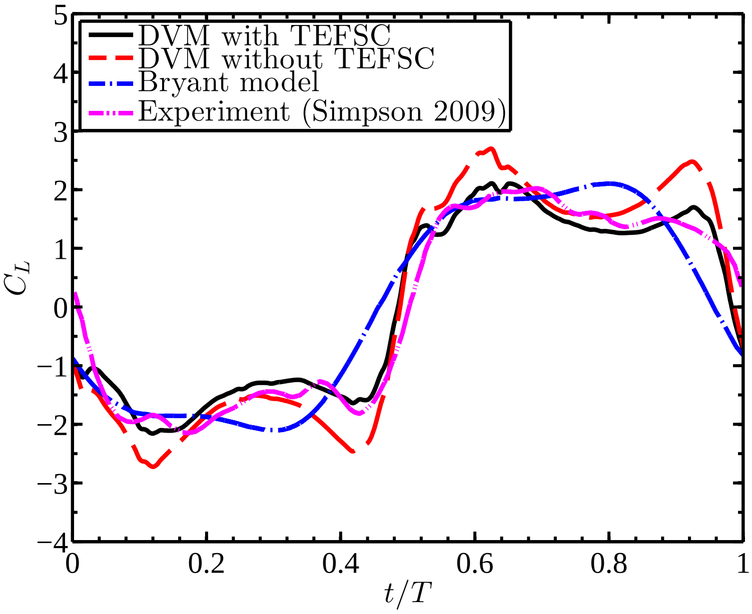

(a) $f^* = 0.133$ and $\alpha_0 = 38.9°$.

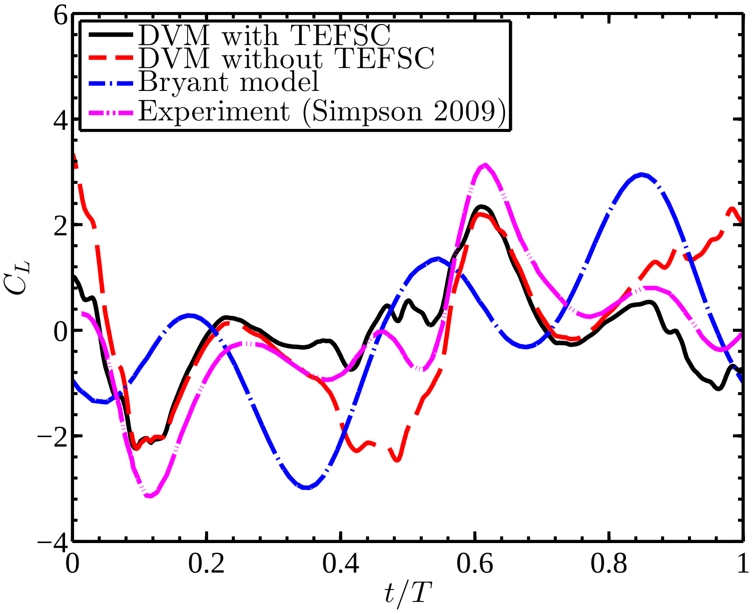

(b) $f^* = 0.2$ and $\alpha_0 = 53°$.

Fig. 4.8: Comparison of C_L predicted by the DVM with and without TEFSC and Bryant model (Bryant et al. 2013) against experimental results of Simpson (2009) at $h_0 = 0.75$, $\varphi = 90°$ and $x_{piv} = 0.333$.

of the Bryant model (Bryant et al. 2013) and DVM without TEFSC and the experimental data could be attributed to the significant effects of the trailing edge flow separation at high α which are neglected in the Bryant model (Bryant et al. 2013) and DVM without TEFSC. These results demonstrate that when compared with the CFD and experimental results, the DVM with TEFSC provides reasonable results for the analysis of a flapping foil power generator, but with substantially less computational resources (2 orders of magnitude less, see Section 4.2.1).

4.2.3 Kinematic parameters

For further validation of the DVM with TEFSC over a set of kinematic parameters, the contours of efficiency are compared with those of Kinsey & Dumas (2014) to examine predictions of the optimal kinematics. The results are also compared with the Bryant model (Bryant et al. 2013).

Fig. 4.9, 4.10 and 4.11 display contours of the efficiency as a function of f^* and θ_0 at $h_0 = 0.75$, $h_0 = 1$ and $h_0 = 1.5$ respectively. Both the DVM with TEFSC and Bryant model (Bryant et al. 2013) predict the trend that the region of positive and high efficiency ($\eta > 30\%$) narrows and θ_0 for high efficiency increases as h_0 is increased from 0.75 to 1.5 . This can be partially explained as the optimal kinematic parameters share a similar maximum angle of attack approximated by the modulus of the quarter-period value $\alpha_{T/4} = |\theta_0 - \arctan(\omega H_0/U))|$ (Kinsey & Dumas 2014). In addition, the optimal f^* around 0.14 regardless of h_0 differences and θ_0 around 75° at $h_0 = 1$ captured by these two reduced order models are the same. However, the optimal θ_0 of around 70° and 90° at $h_0 = 0.75$ and $h_0 = 1.5$ respectively obtained by the Bryant model (Bryant et al. 2013) is different from that of around 75°

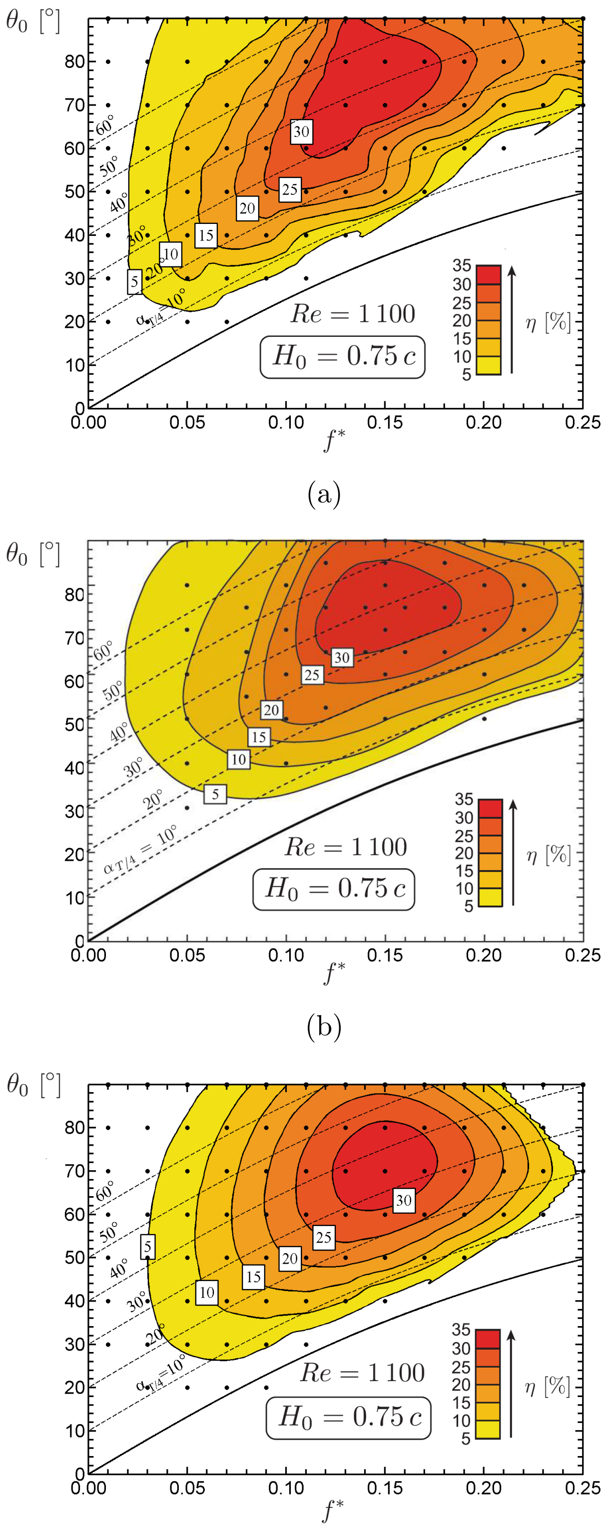

(a)

(b)

(c)

Fig. 4.9: Contours of efficiency given by (a) the DVM with TEFSC (b) Kinsey & Dumas (2014) and (c) the Bryant model (Bryant et al. 2013), with $h_0 = 0.75$, $\varphi = 90°$ and $x_{piv} = 0.333$.

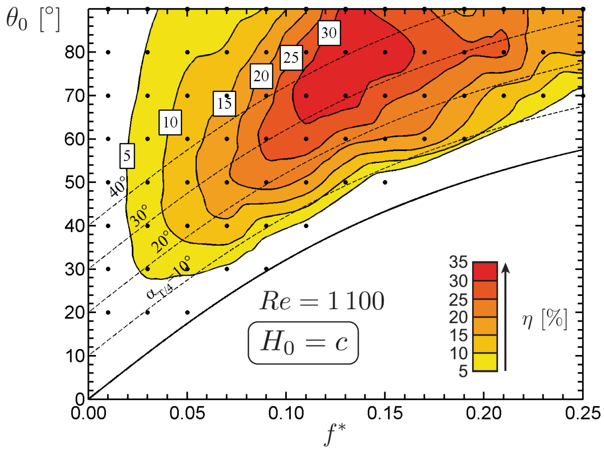

(a)

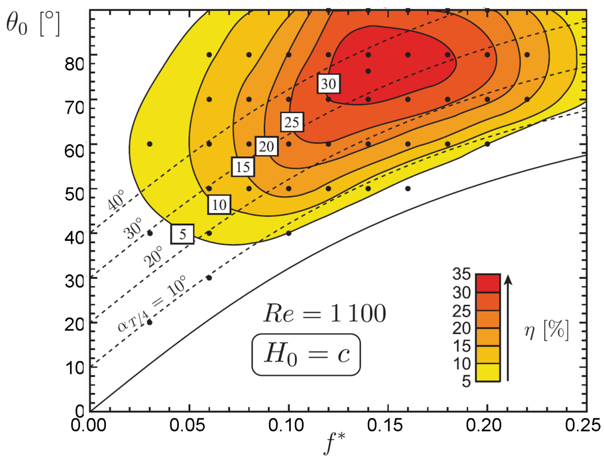

(b)

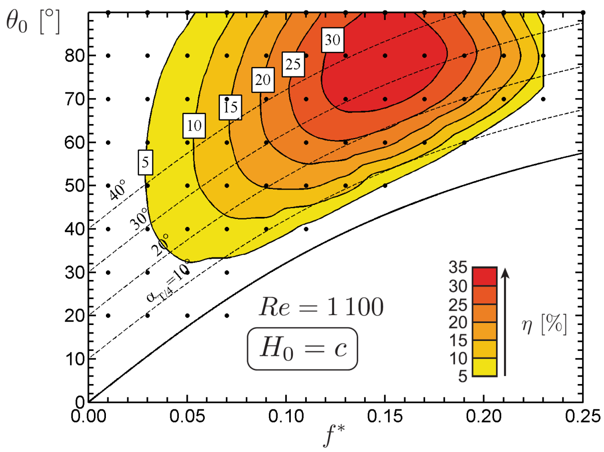

(c)

Fig. 4.10: Contours of efficiency given by (a) the DVM with TEFSC (b) Kinsey & Dumas (2014) and (c) the Bryant model (Bryant et al. 2013), with $h_0 = 1$, $\varphi = 90°$ and $x_{piv} = 0.333$.

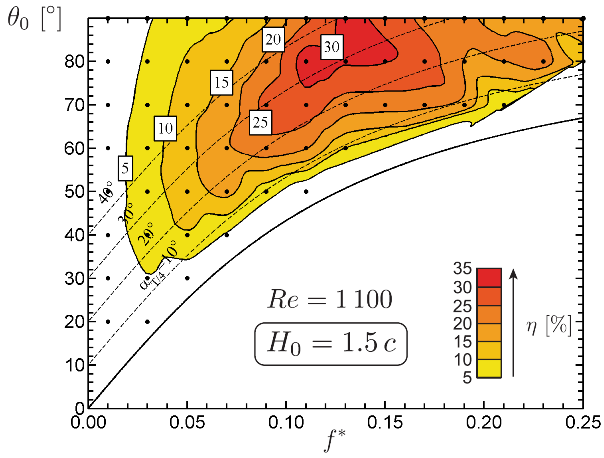

(a)

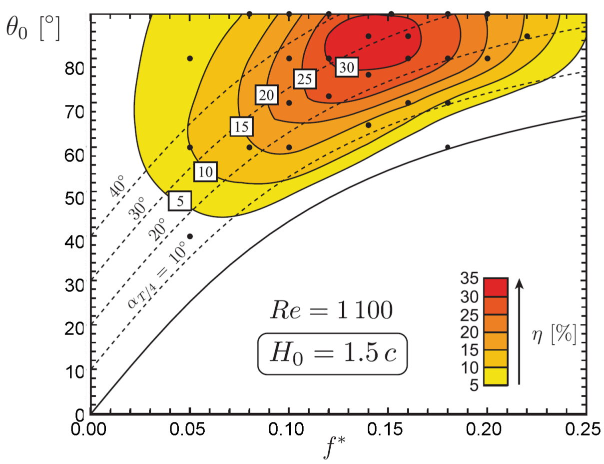

(b)

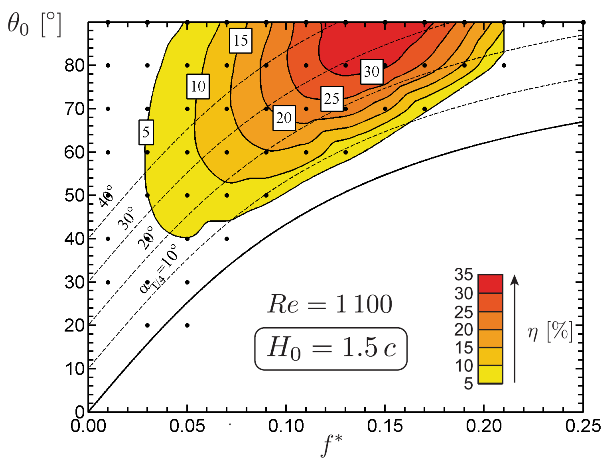

(c)

Fig. 4.11: Contours of efficiency given by (a) the DVM with TEFSC (b) Kinsey & Dumas (2014) and (c) the Bryant model (Bryant et al. 2013), with $h_0 = 1.5$, $\varphi = 90°$ and $x_{piv} = 0.333$.

and 85° obtained by the DVM witph TEFSC and Kinsey & Dumas (2014). The similarity in major features of optimal kinematics captured by the DVM with TEFSC and Kinsey & Dumas (2014) demonstrates the capability of the DVM with TEFSC for kinematics optimization. Furthermore, in the Bryant model (Bryant et al. 2013), constants in the equations accounting for dynamic stall effects and the influence of varying pressure center caused by LEVs transition on the moment are tuned to match the results of Kinsey & Dumas (2008) at $f^* = 0.14$, $\theta_0 = 76.3°$, $h_0 = 1$, $\varphi = 90°$ and $x_{piv} = 0.333$ and tied to the flow condition, foil geometry and, particularly, kinematic parameters. This could partially explain the difference in optimal θ_0 obtained by the Bryant model (Bryant et al. 2013) compared to the results of DVM with TEFSC and Kinsey & Dumas (2014) when h_0 deviates from 1, thus limiting the application of the Bryant model (Bryant et al. 2013) to parameter space validated by CFD simulations or experiments of the flapping foil power generator. On the other hand, empirical constants used in the DVM with TEFSC which govern the LEVs formation (leading edge suction parameter, LESP) and trailing edge flow separation (Kirchhoff flow approximation) only rely on the flow condition ($Re = 1100$, incompressible flow) and the foil profile (NACA0015). These constants can be identified from skin friction analysis regardless of motion kinematics (critical LESP (Ramesh et al. 2014)) and ramp-up motion experiments (constants used in the Kirchhoff flow approximation (Bauchau 2007)).

4.3 Summary

Modelling aerodynamic forces on the flapping foil by reduced order methods based on physical mechanisms is useful in power extraction analysis when a large number of cases are investigated, for instance, for design optimization. In this chapter, a reduced order model based on the discrete vortex method (D-VM) and Leishman-Beddoes dynamic stall model (Leishman & Beddoes 1989) to capture flow separations at both leading and trailing edges of a flapping foil power generator has been presented. This DVM with trailing edge flow separation corrections (TEFSC) takes far less computational time (at least two orders of magnitude) compared to the immersed boundary-lattice Boltzmann method (IB-LBM) which is 15 times faster than the Navier-Stokes solver (Barad et al. 2017). Then, the Bryant reduced order model (Bryant et al. 2013) based on the quasi-steady model and ONERA dynamic stall model and DVM with TEFSC were used for aerodynamic modelling and kinematic analysis of a flapping foil power generator with prescribed pitch and plunge motions.

For kinematic conditions upon which the constants are tuned in the Bryant model (Bryant et al. 2013), the mean power coefficient and efficiency obtained by the Bryant model (Bryant et al. 2013) and the DVM with TEFSC are in good agreement with those of Kinsey & Dumas (2008). However, for kinematic conditions outside the range on which the constants of the Bryant model (Bryant et al. 2013) are based such as changing the pivot location, results here show that the DVM with TEFSC captures the physics of the flow much better than Bryant model (Bryant et al. 2013) compared with CFD simulations based on the IB-LBM. Examination of the influence of the plunge amplitude shows that the optimal frequency and pitch amplitude of a flapping foil power generator obtained by the DVM with TEFSC approximate results of Kinsey & Dumas (2014) better than the Bryant model (Bryant et al. 2013) and demonstrate the capability of the DVM with TEFSC to predict the optimal kinematic parameters for high performance of a flapping foil power generator. In addition, the empirical constants used in the DVM with TEFSC are only dependent on the Reynolds number and foil profile and the low computational cost makes the

DVM with TEFSC an attractive tool for optimization, engineering design and performance analysis of the flapping foil generator.

Chapter 5

Kinematic Parameters Optimizations

In this chapter, the search for combination of kinematic parameters with high energy extraction performance from a flapping foil is discussed. An in-house multi-fidelity evolutionary algorithm (MFEA) code described in Section 3.4 is employed with the Bryant model (Bryant et al. 2013) reproduced in Section 3.2 and the discrete vortex method (DVM) modified in Chapter 4. The convergence performance of EA using single and multi fidelity strategies is first examined through a single objective problem with two variables. Then, five kinematic parameters are optimized using the multi-fidelity strategy for two different cases: (a) maximization of efficiency (single objective problem); and (b) maximization of efficiency and power output (bi-objective). The solutions are further evaluated using the immersed boundary-lattice Boltzmann method (IB-LBM described in Section 3.3) and discussed in detail through

The following paper is based on this chapter:
[1]. Zhengliang Liu, Kalyan Shankar Bhattacharjee, Fang-Bao Tian, John Young, Tapabrata Ray, and Joseph C.S. Lai. Kinematic optimization of a flapping foil power generator using multi-fidelity evolutionary algorithm. *Renewable Energy*, submitted

hydrodynamic loads and flow fields in order to provide insight into the physics underpinning the performance of a flapping foil power generator.

5.1 Parameter settings of the evolutionary algorithm

In the EA code, the probability of crossover and mutation are set to 1 and 0.2 respectively. The distribution indices for crossover (η_c) and mutation (η_m) are set as 20 and 30 respectively, as those in Section 3.4.

As discussed in Chapter 4, the differences in η given by the modified DVM are negligible after seven flapping cycles. Thus, the solution evaluated by the DVM of 7 flapping cycles is considered as the highest fidelity estimate. There are 8 fidelity levels for the solutions of the flapping foil problem. The lowest fidelity estimate (fidelity 1) is based on the Bryant model, while the fidelity 2-8 estimates are based on modified DVM using 1-7 flapping cycles respectively. Because of the substantial computational time required, the IB-LBM is only used for detailed analysis of specific solutions. When the pre-defined budget of computational cost is reached, the optimization process is terminated. An equivalent cost unit is introduced to estimate the budget. A single evaluation using the lowest fidelity level (Bryant model) is assumed to incur 1 unit of computational cost, about 1 second of CPU time on a single Xeon/2.67-GHz processor with 16 GB memory. Since the runtime of the DVM depends on the total number of time steps as well as the number of vortex elements shed from the leading and trailing edge of the foil and the LEV shedding is related to the bounded circulation at the leading edge (Chapter 4), it is hard to identify the cost of DVM at the beginning of the optimization. For convenience, it is assumed that the cost of simulations using DVM is 10 units for each flapping cycle (e.g. a simulation of 7 flapping cycles takes 70 units). Thus, the value of the equivalent time unit is related to the number of simulations and the fidelity levels with which these solutions are evaluated. For example, a budget of 140 units permits 140 evaluations using the Bryant model or 2 evaluations using the DVM of 7 flapping cycles during the optimization process. A simulation at higher fidelity levels can start from the closest check point if the individual has been evaluated by the same model with lower fidelity levels. For instance, if a solution has been evaluated with the DVM of 1, 2 and 5 flapping cycles, the simulation of this solution using the DVM of 7 flapping cycles can be restarted from DVM of 5 flapping cycles.

5.2 Convergence of optimization using single and multi fidelity solutions

At the early stage of the optimization, low fidelity solutions are used extensively to search the entire space of the design variables. Thereafter, the approach evaluates promising solutions at higher levels of fidelity. To investigate the convergence of the approach using single (highest fidelity level) and multi fidelity models, a single objective (power generation efficiency η) problem is studied. The population size μ_{EA} is set to 20 (10 times 2 design variables) and the computational budget B_{EA} is set to 14,000 time units. This corresponds to about 200 simulations using DVM of 7 flapping cycles which is about 100 times the dimension of the search space (for two design variables). The two design variables are f^* and θ_0 in the range of $0.01 - 0.25$ and $0° - 100°$, respectively which are the same as those in the parametric study conducted by

Kinsey & Dumas (2008). $Re = 1100$ and other kinematic parameters $h_0 = 1$, $\varphi = 90°$ and $x_{piv} = 0.333$ are fixed. Since EA includes random processes (e.g., random seeds are used to generate the initial population), to reduce the random influences on the EA performance, 30-100 independent runs with random initial values are generally used in the performance analysis of optimization algorithms (Branke et al. 2017, Deb et al. 2002). However, because of the significant computational resources required for a large number of independent runs, the results in this section are based on the average of five independent optimization runs with random initial values to give an indication of the EA performance.

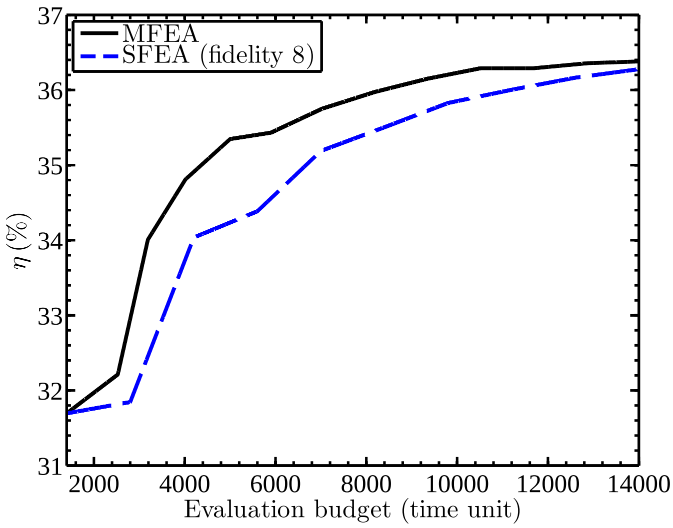

Fig. 5.1: Convergence history of efficiency averaged over five runs with a budget of 14,000 time units.

Optimization using the highest fidelity model (i.e. DVM with 7 flapping cycles) uses up the budget in 10 generations, while MFEA on average evolves over 13.4 generations. At the end of runs, the best solution delivered by MFEA gives a maximum efficiency of 36.4%, while that using single fidelity (highest fidelity in this case) gives an efficiency of 36.3%. The convergence history in Fig. 5.1 shows that the starting point (1,400 time units for initialization of a

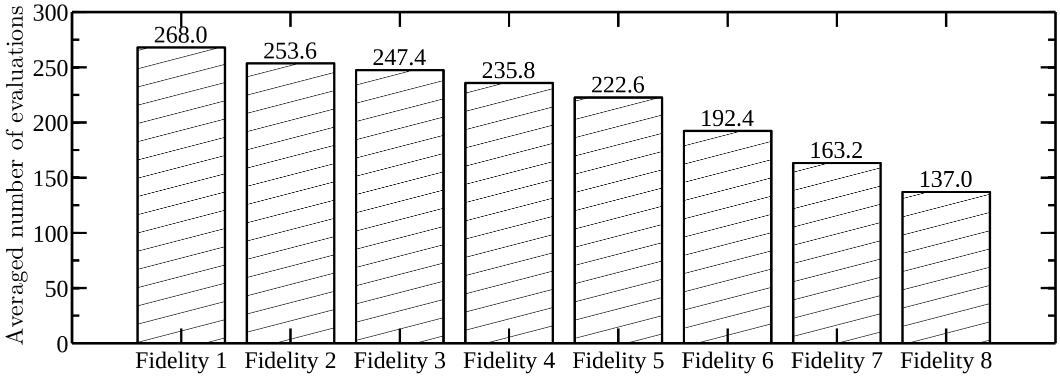

(a) Averaged total number of evaluations with different fidelity levels.

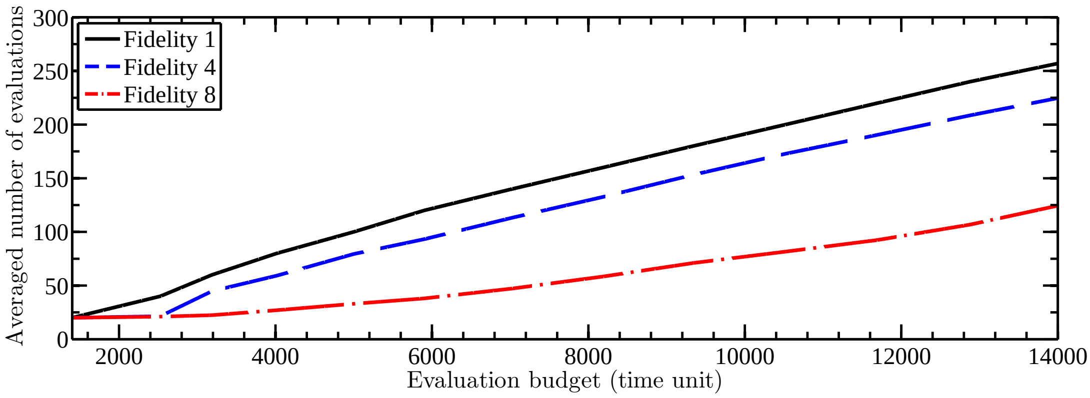

(b) Number of evaluations with the fidelity level of 1, 4 and 8 at different evaluation budget.

Fig. 5.2: Number of evaluations with different fidelity levels in the MFEA optimization process with 1 objective and 2 variables.

population size μ_{EA} of 20 individuals) of the optimization process using the MFEA and SFEA is the same. All the individuals in the initial generation are evaluated with 1-8 fidelity levels by MFEA. The difference in efficiency between each run is less than 1.2% and 0.5% for SFEA and MFEA respectively. As shown in Fig. 5.1, MFEA only uses 71.4% of the available budget (10,000 time units) to achieve the same efficiency $\eta = 36.3\%$ as obtained by SFEA. To gain a better understanding of the performance of MEFA, the number of solutions evaluated with different fidelity levels during the optimization process are investigated. As shown in Fig. 5.2a, the total number of highest fidelity evaluations is about half of that of the lowest ones. In addition, the difference in the number of evaluations between adjacent fidelity levels of 6-8 decreases dramatically compared to that of 1-5 since the difference in the results given by the DVM is insignificant after four flapping cycles. The test problem of two design variables demonstrates the capability of MFEA to reduce the computational cost by only evaluating solutions at higher fidelity levels when there is a need for discrimination. In addition, if solutions at the highest fidelity level are evaluated by the IB-LBM of 12 flapping cycles which generally takes more than 100 hours on a single Xeon/2.67-GHz processor with 16 GB memory (see Chapter 4), the time budget should be at least 12,000,000 time units which corresponds to around 20,000 CPU hours (200 simulations). The MFEA using the DVM of 7 flapping cycles as the highest fidelity model makes it possible to determine high performance solutions using realistic computational resources, around 3 orders of magnitude lower than that using IB-LBM. Since the DVM is a low order model which may not capture the flow physics accurately, the efficiency and power output of the solutions identified by the MFEA are then recalculated using the IB-LBM.

Table 5.1: Optimal cases given by the multi-fidelity evolutionary algorithm when single objective (η) problems with 2 (f^*, θ_0) and 5 ($f^*, \theta_0, h_0, \varphi, x_{piv}$) design variables are considered.

Design variables	f^*	$\theta_0(^\circ)$	h_0	$\varphi(^\circ)$	x_{piv}	η (Bryant)	η (DVM)	η (IB-LBM)
f^*, θ_0	0.125	78.3	1.00	90.0	0.333	33.4%	36.5%	32.7%
$f^*, \theta_0, h_0, \varphi, x_{piv}$	0.175	71.8	0.52	114.6	0.303	14.8%	39.6%	35.6%

5.3 Optimization results

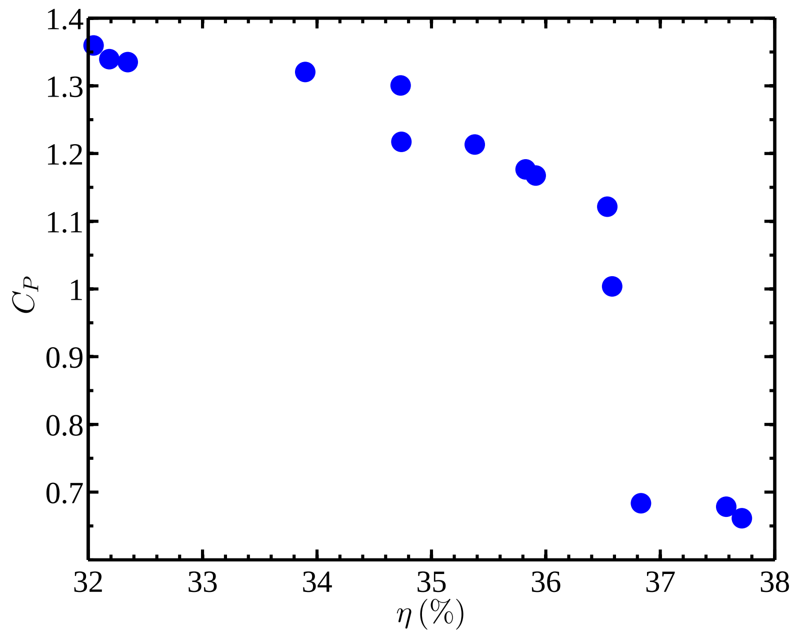

Fig. 5.3: Plot of non-dominated solutions from the bi-objective problem with 5 variables using MFEA. Solutions are evaluated by the DVM using 7 flapping cycles.

In this section, single(η) and bi-objective (η and $\overline{C}_P$) optimization problems involving 5 design variables are considered. Since the aim of this study is to search for some high energy extraction performance solutions which are found within a limited but realistic time budget, results obtained by the MFEA in this section are based on a single run consuming about 50 CPU hours for the single-objective problem and 170 CPU hours for the bi-objective problem with 16 GB memory and a single Xeon/2.67-GHz processor. The ranges of the design variables are $f^* = 0.01 - 0.25, \theta_0 = 0^\circ - 100^\circ, h_0 = 0.5 - 2.0, \varphi =$

Table 5.2: List of the non-dominated solutions given by the bi-objective problem in the last generation.

Case	f^*	$\theta_0(^\circ)$	h_0	$\varphi(^\circ)$	x_{piv}	η (Bryant)	η (DVM)	η (IB-LBM)	$\overline{C}_p$ (Bryant)	$\overline{C}_p$ (DVM)	$\overline{C}_p$ (IB-LBM)
1	0.146	79.7	1.77	81.6	0.253	6.1%	32.1%	18.4%	0.26	1.36	0.84
2	0.112	78.6	1.78	85.4	0.260	20.1%	32.2%	21.8%	0.84	1.34	0.91
3	0.112	81.7	1.77	100.5	0.254	35.0%	34.7%	29.3%	1.31	1.30	1.12
4	0.112	78.3	1.78	86.6	0.260	20.9%	32.3%	22.8%	0.86	1.34	0.95
5	0.119	81.7	1.43	98.4	0.208	34.6%	35.8%	31.7%	1.14	1.18	1.04
6	0.118	78.3	1.50	94.8	0.249	32.0%	35.4%	29.5%	1.10	1.21	1.02
7	0.118	79.7	1.36	98.9	0.273	36.4%	36.5%	33.4%	1.12	1.12	1.02
8	0.118	81.7	1.77	95.5	0.254	32.8%	33.9%	28.5%	1.28	1.32	1.12
9	0.118	81.8	1.43	99.5	0.210	34.4%	35.9%	31.2%	1.12	1.17	1.01
10	0.118	81.8	1.14	103.4	0.175	32.1%	36.6%	32.0%	0.89	1.00	0.88
11	0.118	81.9	1.50	93.2	0.249	31.2%	34.7%	32.5%	1.09	1.22	1.14
12	0.217	78.6	0.76	126.8	0.181	-9.6%	37.6%	25.7%	-0.17	0.68	0.45
13	0.217	75.8	0.74	126.8	0.181	-4.8%	37.7%	27.3%	-0.08	0.66	0.47
14	0.223	79.1	0.79	126.3	0.182	-12.1%	36.8%	22.9%	-0.23	0.68	0.47

$45° - 135°$ and $x_{piv} = 0 - 1$, in which power could be extracted from the flow and many parametric studies on prescribed energy harvesting system are conducted, as summarized in Table A.1. For comparison of single objective problems involving 2 and 5 design variables, the same computational budget of 14,000 units and population size of 20 as those in Section 5.2 are used. The solution providing the highest η among the 5 runs described in Section 5.2 for single objective and 2 design variables and the optimal solution (i.e., the optimal values for the design variables) given by the MFEA (12 generations) considering one objective and 5 variables are listed in Table 5.1, where η is re-calculated by the Bryant model, DVM of 7 flapping cycles and IB-LBM of 12 flapping cycles. The results show that for the same budget, MFEA involving 5 variables lead to an η of 39.6% evaluated by the DVM using 7 flapping cycles (the highest fidelity level used in the MFEA), which is 8.5% higher than that achieved by the MFEA involving two variables. The increase of 8.5% in efficiency achieved by increasing the number of design variables is more than half of 15.8% increment achieved by controlling the camberline deformation (Hoke et al. 2015) when the power consumption of the active control is not taken into account (see Section 2.3.2). In addition, $\eta = 35.6\%$ under the optimal condition given by the MFEA for the single objective case with five variables is similar to the optimal $\eta = 35.5\%$ suggested by Kinsey & Dumas (2008) under a different operating condition $f^* = 0.140, \theta_0 = 76.3°, h_0 = 1.0, \varphi = 90.0°$ and $x_{piv} = 0.333$ (both η are predicted by the IB-LBM).

Then, the energy harvesting system is optimized for high η and $\overline{C}_P$. A computational budget of 42,000 units and a population size of 40 (20 times 2 objectives) is considered for the bi-objective problem with five variables. The budget is equivalent to about 600 simulations with DVM of 7 flapping cycles which is 120 times the dimension of the search space (with 5 variables). After

19 generations, the budget was used up and 14 non-dominated solutions were obtained. The trade-off (Pareto front) of these solutions between η and $\overline{C}_P$ is shown in Fig. 5.3. Each of these 14 solutions was further analysed using the IB-LBM. The results in Table 5.2 show that the solutions evaluated with the DVM of 7 flapping cycles are in the range of $f^* = 0.1-0.25, \theta_0 = 75°-85°, h_0 = 0.7 - 1.8, \varphi = 80° - 130°$ and $x_{piv} = 0.15 - 0.3$. When η is emphasized, f^* is high but h_0 is small, while when power is emphasized, f^* is low but h_0 is large. For all cases, θ_0 is greater than 75°, providing large enough angles of attack for LEV formation. The influence of h_0 on $\overline{C}_P$ dominates when η is similar, since the total available power in the flow increases linearly with the increase of d which relies heavily on h_0 (Eq. 2.13 and 2.14). All the solutions recalculated by the IB-LBM show lower η and $\overline{C}_P$ in comparison with the values obtained by the DVM. Although the Bryant model provides reasonable results in the range of $f^* = 0.1 - 0.12, \varphi = 85° - 105°$, it gives poor results outside this range since the empirical constants used in Bryant model are tuned to match the optimal condition. These results indicate that the DVM is a useful surrogate model to narrow down the search space at the early stage of optimization, while the Bryant model is appropriate for engineering design since it performs well near the optimum if the data used to tune the empirical constants can be obtained from previous studies. However, the non-dominated solutions are not necessarily optimal because the DVM is a low order model but it enables the search for high performance solutions within a limited budget of computing resources. When the budget was increased by 50% from 42,000 to 63,000 units, only one extra non-dominated solution (15 in total) was obtained after 28 generations (19 generations for 42,000 units).

Table 5.3: Performance of a power generator with different kinematic parameters, in descending order by η. H stands for high efficiency, M stands for moderate efficiency, L stands for low efficiency and K stands for the case under the kinematic conditions gvien by Kinsey & Dumas (2008).

Case		f_0^*	$\theta_0(°)$	h_0	$\varphi(°)$	x_{piv}	η	$\overline{C}_P$	d/c	$\alpha_{max}(°)$	$\overline{\lvert C_L \rvert}$	$\overline{C}_{Ph}$	$\overline{C}_{P\theta}$
15	(KH)	0.140	76.3	1.00	90.0	0.333	35.5%	0.91	2.56	35.0	1.40	0.84	0.07
16	(H1)	0.146	83.5	1.36	99.5	0.250	33.8%	1.04	3.10	32.9	1.33	0.94	0.10
7	(H2)	0.118	79.7	1.36	98.9	0.273	33.4%	1.02	3.07	35.0	1.33	0.86	0.16
17	(M1)	0.113	78.3	1.78	81.6	0.253	23.2%	0.96	4.13	26.8	1.18	0.97	-0.01
14	(M2)	0.223	79.1	0.79	126.3	0.182	22.9%	0.43	1.86	46.8	1.32	0.90	-0.47
1	(L1)	0.146	79.7	1.77	81.6	0.253	18.4%	0.80	4.24	21.8	1.78	0.97	-0.17
18	(L2)	0.110	79.7	1.77	81.6	0.276	17.0%	0.74	4.23	29.3	1.30	0.78	-0.04
19	(KL)	0.180	60.0	1.00	90.0	0.333	11.6%	0.28	2.40	11.5	0.62	0.39	-0.11

5.4 Mechanisms for high performance

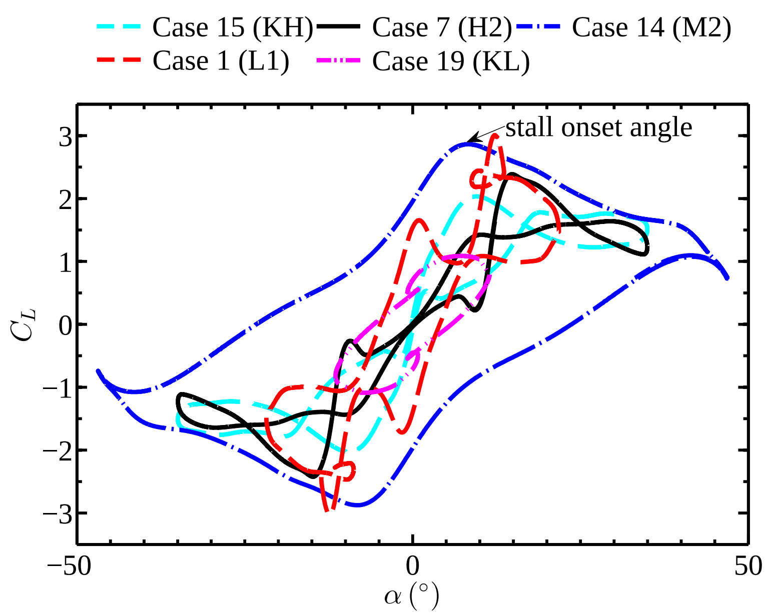

Fig. 5.4: Changes in C_L with α in the 12$^{\text{th}}$ flapping cycle.

Based on η, the simulated cases are classified into high ($\eta > 30\%$), moderate ($20\% < \eta \leq 30\%$) and low ($\eta \leq 20\%$) performance groups. To discuss the physical mechanism for high performance of the flapping foil system, especially the influence of the LEV, Case 15 (KH) under the optimal operating conditions given by Kinsey & Dumas (2008), two cases with similar η of each group showing strong LEVs and Case 19 (KL) of the low performance group where no obvious LEV is observed in the study of Kinsey & Dumas (2008) are examined in detail through time averaged values over the 12^{th} flapping cycle in Table 5.3. Cases 16-18 are not non-dominated solutions but individuals in the final population given by the MFEA. Note that the non-dimensional swept distance d/c determining the maximum potential energy which can be extracted from the flow highly depends on the plunge amplitude h_0. Thus, the flapping foil system with higher h_0 harvests more energy for the same η. As pointed out in the last section, the MFEA does not necessarily identify the true optimum because of the use of the reduced order DVM and a limited but realistic budget of computing resources. Hence the best performing non-dominated solution in Table 5.2, Case 7 (H2), has an efficiency of 33.4%, slightly lower than the 35.5% under the optimal condition (Case 15) found by Kinsey & Dumas (2008) but it does achieve 13% increase in $\overline{C}_P$. For similar reasons, non-dominated solutions such as Case 1 (L1) in Table 5.2 can have very low efficiency while individuals in the final population such as Case 17 (M1) can give moderate efficiency. Nevertheless, results here show that high energy extraction performance solutions can be identified using the MFEA.

During one flapping cycle, Cases 1, 7, 14, 15, 16, 17 and 18 experience angle of attack α much higher than the critical angle of static stall $\alpha_c = 10°$ of NACA0015 aerofoil at $Re = 42,900$ (Jacobs & Sherman 1937), leading to large flow separations. However, α_{max} of Case 19 is 11.5° and only a slight stall is observed in Fig. 5.4. As shown in Fig. 5.4, the maximum lift coefficient C_L of Cases 1, 7, 14, 15 and 19 is at $\alpha = 12.3°$, $14.8°$, $8.4°$, $9.5°$ and $7.3°$ respectively where the rate of change of α is 0.25 rad/s, -0.26 rad/s, 1.26 rad/s, -0.43 rad/s and 0.27 rad/s respectively. Following Jumper et al. (1989), the stall onset angle is considered as the α exceeding the value where the foil experiences a sudden jump in C_L. For Case 19, the difference between the maximum C_L at $\alpha = 7.3°$ and the C_L at α_{max} of 11.5° is only 0.27 (27%) while that of other cases is at least 0.49 (40%); thus the foil of Case 19 is considered to experience shallow stall. Since the maximum C_L is achieved after α reaches the maximum (negative rate of change of α) for Cases 7 and 15, the α at which C_L reaches the maximum is not considered as the stall onset angle. It is noted that Case 14 is the only case for which the onset angle of deep dynamic stall (8.4°) is smaller than the static stall angle $\alpha_c = 10°$ because of two reasons:(a) α_c decreases with the increase of Re (Jacobs & Sherman 1937); and (b) the stall onset angle decreases as the pivot location is moved fore (Jumper et al. 1989) (x_{piv} of Case 14 is the smallest among all cases). Table 5.3 shows that except for Case 19 ($\overline{|C_L|} = 0.62$), $\overline{|C_L|}$ is much higher than the maximum C_L of 0.82 given by the static experimental study (Jacobs & Sherman 1937) because the flapping foil can exploit the LEV to achieve high lift in propulsive systems (Shyy & Liu 2007). As expected, Case 19 gives much lower plunge power coefficient contribution $\overline{C}_{Ph}$, which is the time average of the product of C_L and $\dot{h}$, than other cases. For all cases, the contribution of the pitch motion to the power coefficient ($\overline{C}_{P\theta}$, the time average of the product of C_M and $\dot{\theta}$) is small or even negative. In addition, $\overline{C}_{P\theta}$ of Case 14 is negative (i.e., consuming instead of generating power) and its magnitude is the highest among all cases because: (1) the maximum pitch rate $\dot{\theta}_{max} = 2\pi f^* \theta_0$ of Case 14 is the highest; and (2) the pivot location of Case 14 is near the leading edge of the foil, leading to a long moment arm when the low pressure center resulting from LEV is at the aft foil.

In order to understand the physics underpinning the performance of a flapping foil power generator, five cases are examined in details through time histories of the hydrodynamic loads and their contribution to the power out-

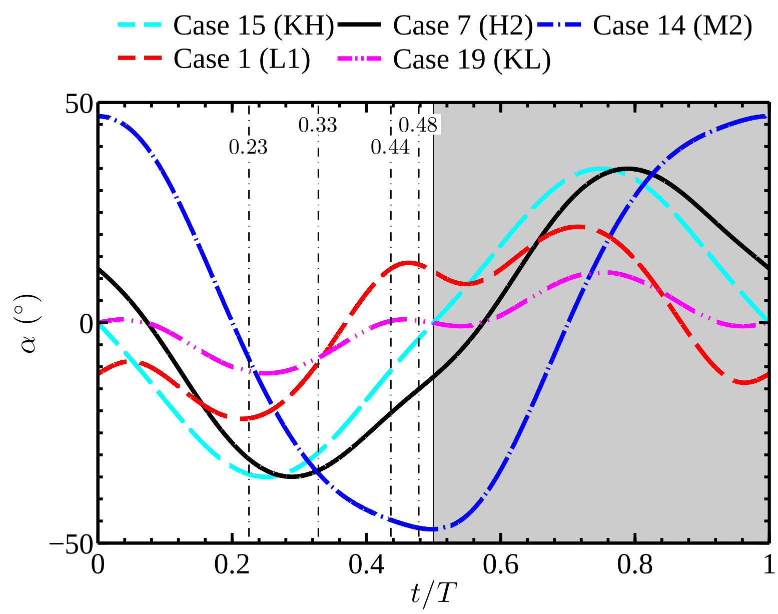

Fig. 5.5: Time histories of α given by Case 1, 7, 14, 15 and 19 listed in Table 6.2. The shaded region is the upstroke. The vertical black dash-dotted lines denote time instants for examination of flow field in Figs. 5.12 and 5.13.

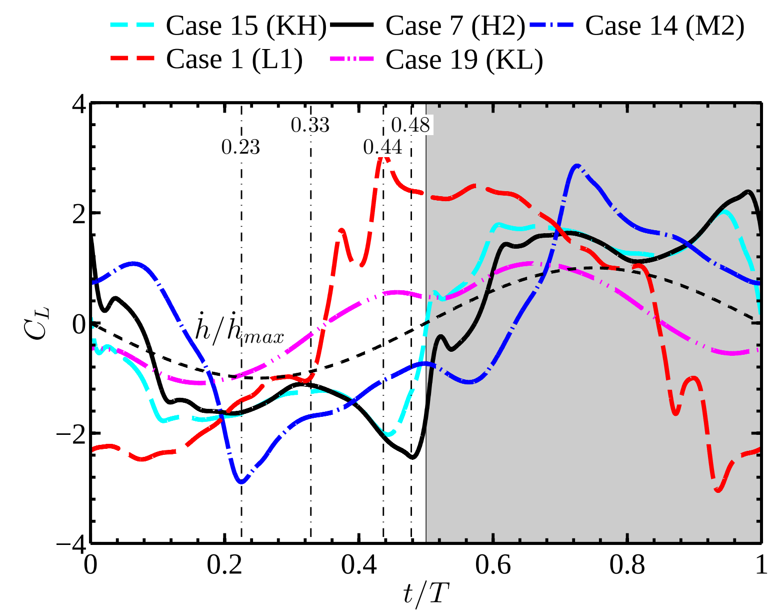

Fig. 5.6: Time histories of C_L given by Case 1, 7, 14, 15 and 19 listed in Table 5.3. The shaded region is the upstroke. The vertical black dash-dotted lines denote time instants for examination of flow field in Figs. 5.12 and 5.13.

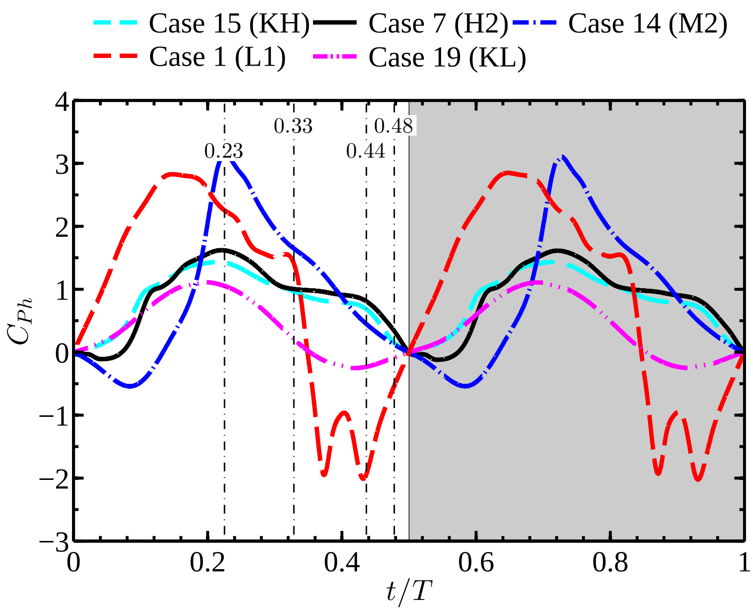

Fig. 5.7: Time histories of C_{Ph} given by Case 1, 7, 14, 15 and 19 listed in Table 5.3. The shaded region is the upstroke. The vertical black dash-dotted lines denote time instants for examination of flow field in Figs. 5.12 and 5.13.

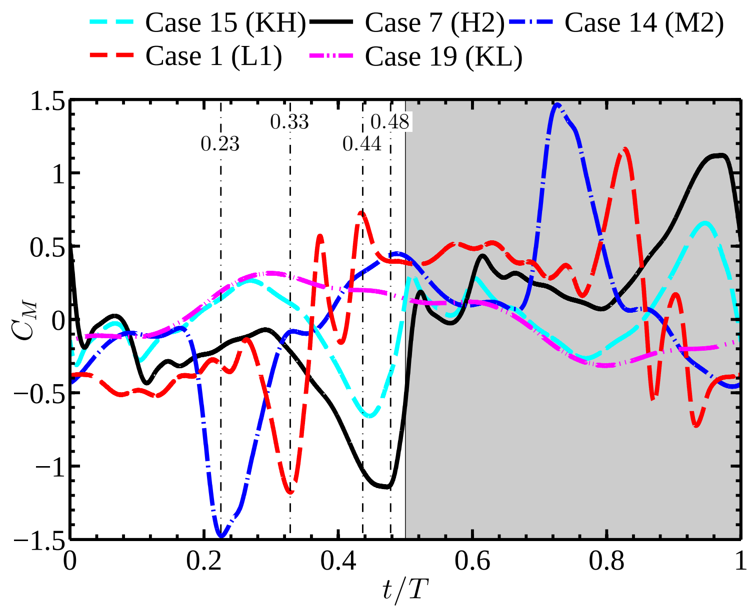

Fig. 5.8: Time histories of C_M given by Case 1, 7, 14, 15 and 19 listed in Table 5.3. The shaded region is the upstroke. The vertical black dash-dotted lines denote time instants for examination of flow field in Figs. 5.12 and 5.13.

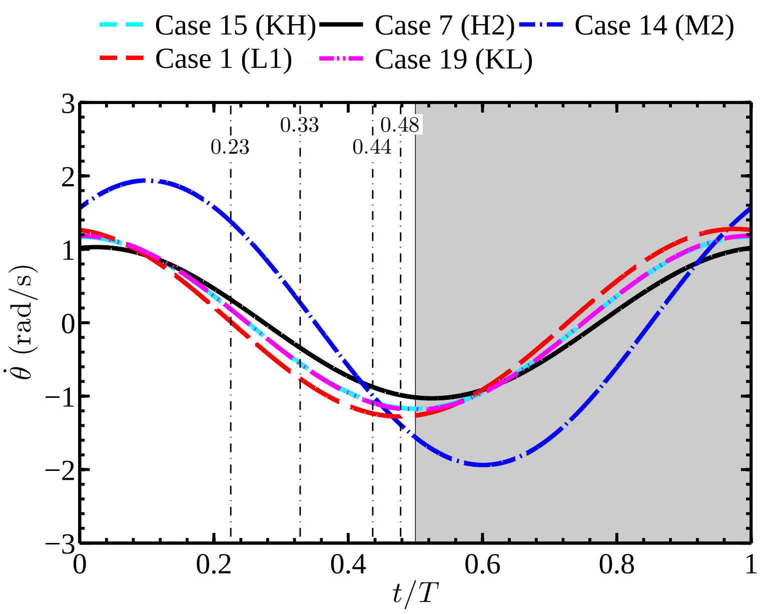

Fig. 5.9: Time histories of $\dot{\theta}$ given by Case 1, 7, 14, 15 and 19 listed in Table 5.3. The shaded region is the upstroke. The vertical black dash-dotted lines denote time instants for examination of flow field in Figs. 5.12 and 5.13.

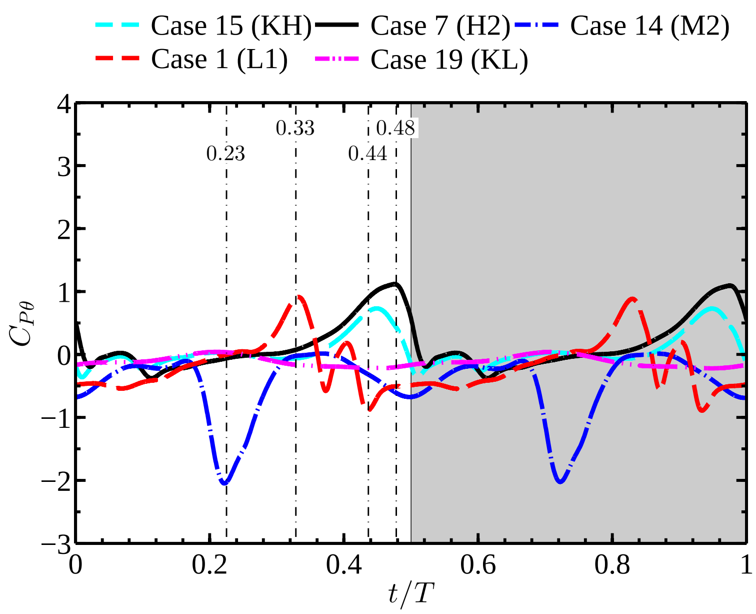

Fig. 5.10: Time histories of $C_{P\theta}$ given by Case 1, 7, 14, 15 and 19 listed in Table 5.3. The shaded region is the upstroke. The vertical black dash-dotted lines denote time instants for examination of flow field in Figs. 5.12 and 5.13.

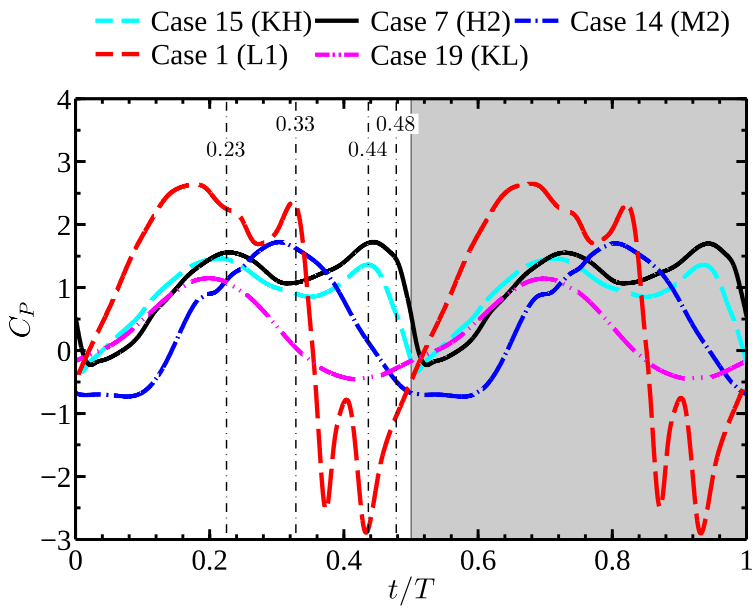

Fig. 5.11: Time histories of C_P given by Case 1, 7, 14, 15 and 19 listed in Table 5.3. The shaded region is the upstroke. The vertical black dash-dotted lines denote time instants for examination of flow field in Figs. 5.12 and 5.13.

put: Case 15 (KH) with optimal kinematic parameters suggested by Kinsey & Dumas (2008), Case 7 (H2) with the highest efficiency among all the non-dominated solutions given by the optimization in Table 5.2, Case 14 (M2) giving the lowest $\overline{C}_{P\theta}$, Case 1 (L1) giving the largest $\overline{|C_L|}$ and Case 19 (KL) with slight dynamic stall. In Figs. 5.5-5.11, $t/T = 0 - 1$ represents the last flapping cycle (the 12$^{\text{th}}$ cycle) and $t/T = 0$ is the instant at the beginning of the down stroke. Thus the normalized plunge velocity $\dot{h}/\dot{h}_{max}$ is the same for all the cases, while there are phase differences in the pitch velocity $\dot{\theta}$ due to the differences in φ (see Fig. 5.9). As shown in Fig. 5.5, the time history of the angle of attack (α) for Case 7 is similar to that of Case 15, except for a small phase shift. In Fig. 5.6, Case 19 (KL) shows a smooth curve of C_L similar to that of α in Fig. 5.5, of which the amplitude is smaller compared to other cases since the influence of flow separation is limited. Cases 7 (H2) and 15 (KH) give similar lift curves with a small phase difference. In addition, C_L of Case 1 (L1) before the stroke reversal $0.36 < t/T < 0.50$ is in the opposite direction of $\dot{h}/\dot{h}_{max}$, resulting in a significant drop of C_{Ph} (Fig. 5.7). In Fig. 5.8, Cases 7 (H2), 14 (M2) and 15 (KH) show troughs of C_M at instants $t/T = 0.48, 0.23$ and 0.45 respectively, the same as where C_L is the minimum in Fig. 5.6. However, due to the influence of the location of pressure center, the minimum C_M of Case 1 (L1) in Fig. 5.8 is at $t/T = 0.33$ where C_L is neither the minimum nor the maximum in Fig. 5.6. Fig. 5.10 illustrates that for Case 14 (M2), power is required to drive the pitch motion during the entire flapping cycle, i.e. $C_{P\theta} \leq 0$, while other cases can harvest energy from the pitch motion at some instants. The combination of C_{Ph} and $C_{P\theta}$ is shown in Fig. 5.11. Cases 1 (L1), 7 (H2), 14 (M2) and 15 (KH) with large flow separations give larger amplitude of C_P compared to Case 19 (KL) where the stall phenomena is slight. In contrast to the rotational turbines on which the impact of flow separation needs to be reduced, the performance improvement of a flapping foil system relies on the extent of benefits from exploiting the flow separation.

To explore the influence of vortex shedding on the hydrodynamic loads, non-dimensional vorticity ($C_v = c\omega_z/U$, where ω_z is the spanwise vorticity) and relative pressure coefficient ($C_p = 2(p - p_\infty)/\rho U^2$) contours are presented respectively in Fig. 5.12 and Fig. 5.13. As the hydrodynamic loads, the pitch motion and power output are symmetric/antisymmetric (Fig. 5.6 to Fig. 5.11), only the flow fields of the downstroke are presented (the upstroke is a mirror image of the upstroke). Flow fields of Case 1 (L1), 7 (H2), 14 (M2), 15 (KH) and 19 (KL) near the flapping foil are investigated in details at four typical non-dimensional time instants $t/T = 0.23$ when Case 14 (M2) with moderate efficiency ($20\% < \eta \leq 30\%$) shows a trough of C_L and C_M in Fig. 5.6 and Fig. 5.8, respectively; $t/T = 0.33$ when Case 1 (L1) with low efficiency

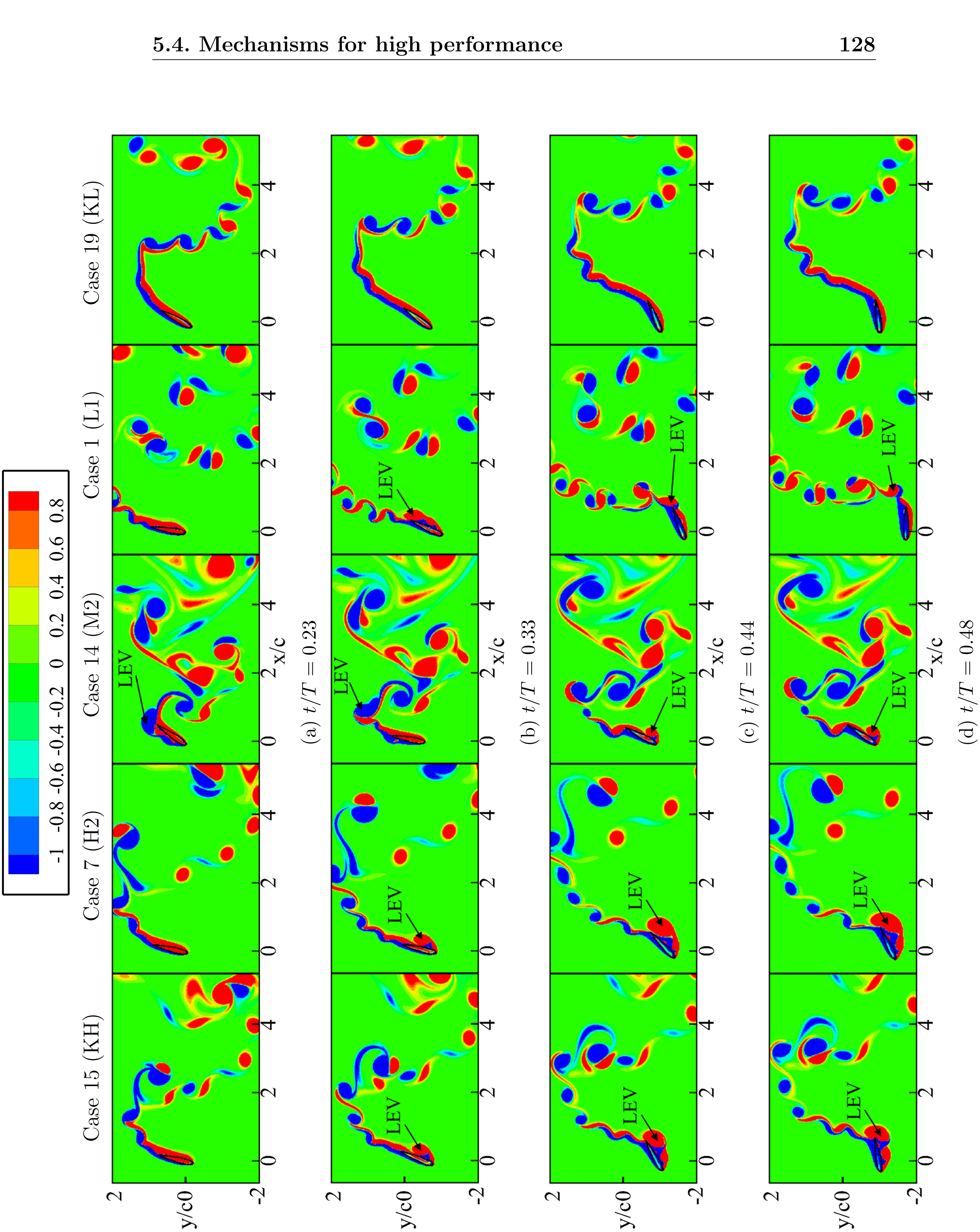

(a) $t/T = 0.23$

(b) $t/T = 0.33$

(c) $t/T = 0.44$

(d) $t/T = 0.48$

Fig. 5.12: Non-dimensional vorticity contours for Cases 1, 7, 14, 15 and 19.

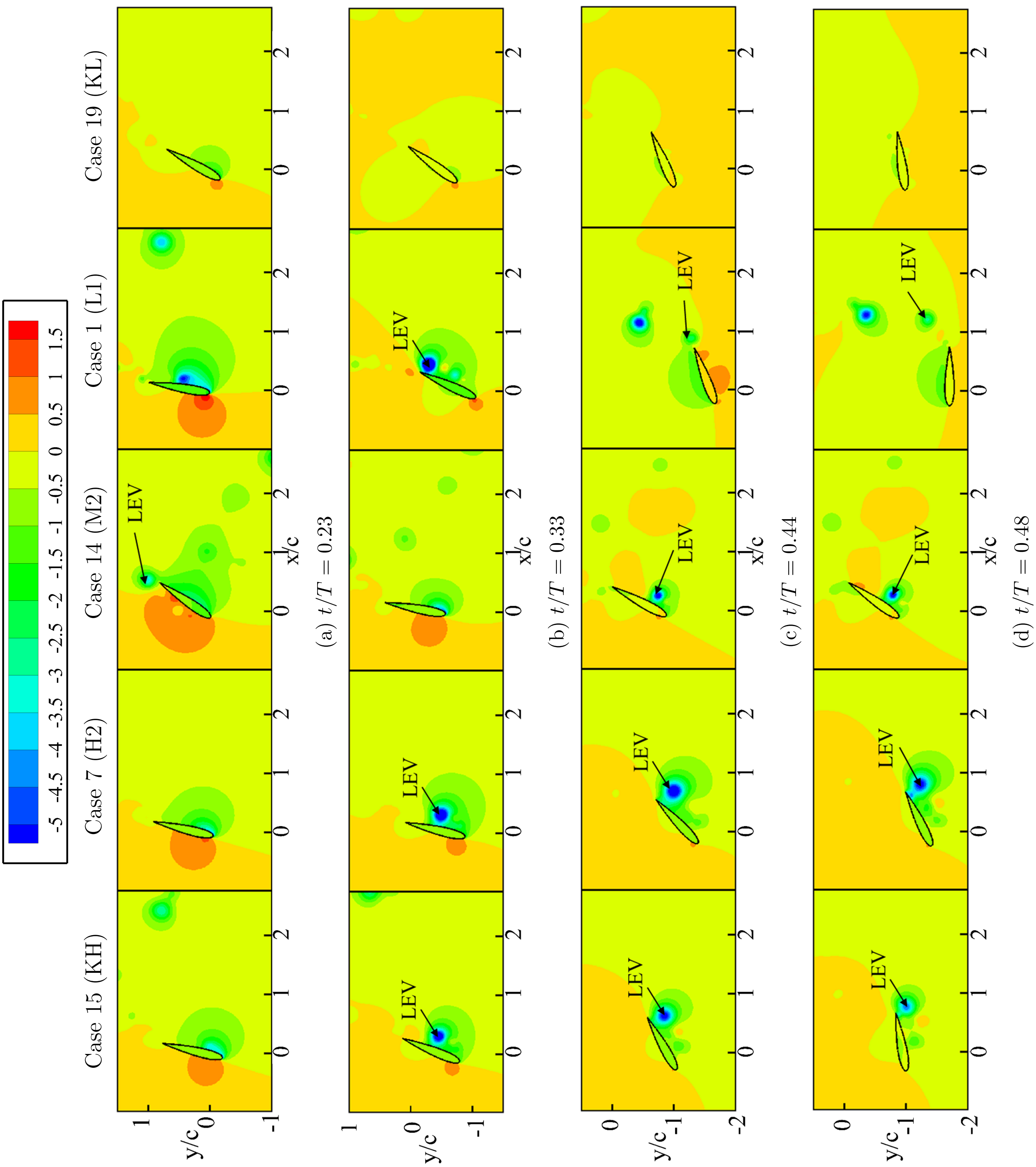

Fig. 5.13: Relative pressure coefficient contours for Cases 1, 7, 14, 15 and 19.

($\eta \leq 20\%$) shows a trough of C_M (Fig. 5.8); $t/T = 0.44$ when Case 1 (L1) shows a trough of C_L (Fig. 5.6); and $t/T = 0.48$ when Case 7 (H2) with high efficiency ($\eta > 30\%$) shows a trough of C_L and C_M in Fig. 5.6 and Fig. 5.8, respectively. For Cases 1 (L1), 7 (H2), 14 (M2) and 15 (KH), vortices form near the leading edge of the foil and shed into the wake at some instants, while for Case 19 (KL) with the lowest η of 11.6%, no LEV is observed during one flapping cycle. In addition, the pressure difference between the upper and lower surface of the foil in Case 19 (KL) is smaller than that for the other four cases in Fig. 5.13, resulting in small $\overline{|C_L|}$ of 0.62 in Table 5.3. For Case 1 (L1) with low efficiency ($\eta = 18.4\%$), even though $|C_L|$ is less than 1/6 of the amplitude of C_L at $t/T = 0.33$ (Fig. 5.6), C_M in Fig. 5.8 reaches the minimum (i.e. $|C_M|$ is maximum) at that instant. This is because the low pressure center is near the trailing edge of the foil at $t/T = 0.33$ (Fig. 5.13b), resulting in a long moment arm. The LEV of Case 1 (L1) sheds into the wake before the stroke reversal ($t/T = 0.44$ in Fig. 5.12c) and the pressure on the lower surface is higher than that on the upper surface (C_L is in the opposite direction to $\dot{h}$ in Fig. 5.6), in contrast to Cases 7 (H2), 14 (M2) and 15 (KH) as shown in Fig. 5.13c. For Case 14 (M2) with moderate efficiency ($\eta = 22.9\%$), the LEV which has formed on the upper surface detaches from the foil near the mid-downstroke where the foil is at the neutral position of the plunge motion (Fig. 5.12a). Case 7 (H2) and Case 15 (KH) with high efficiency show similar timing of LEV formation (Fig. 5.12b) and detachment (Fig. 5.12d). Near the stroke reversal ($t/T = 0.48$), since the low pressure center resulting from the LEV in Case 7 (H2) is near the foil and the pitch angle is small ($\theta = 22°$), the projection of the pressure difference between the upper and lower surface of the foil in the plunge direction (C_L) reaches maximum when α is decreasing(Figs. 5.4-5.6). In addition, the low pressure center of Case 7 (H2) and Case 15 (KH) is after the pivot point, producing positive power through the pitch motion ($C_{P\theta}$ in Fig. 5.10). It is noted that for cases with high efficiency (Case 7 and 15), the LEV detaches from the foil near the stroke reversal, resulting in good synchronization between the hydrodynamic loads (C_L and C_M) and the motions ($\dot{h}$ and $\dot{\theta}$).

Finally, the time-averaged non-dimensional vorticity contours over 4 flapping cycles (13^{th}-16^{th}) of all 8 cases listed in Table 5.3 are examined in Fig. 5.14. All cases show distinct paths of vortices that persist from behind the turbine plane to far downstream, except for Case 19 (KL) which shows much weaker vortex shedding prominent only near the extreme positions of the foil because the foil only experiences slight stall as α remains small during the flapping cycle. In Fig. 5.14a, 5.14b and 5.14c, Case 15 (KL), Case 16 (H1) and Case 7 (H2) with high $\eta > 30\%$ show a vorticity wake pattern of horseshoe shape behind the turbine plane. The LEVs detach from the foil near the stroke reversal and convect downstream towards the neutral position of the plunge motion (y=0). Then the vortices shed near the end of up and down strokes interact at 5 (Case 7), 2.8 (Case 15) and 3.4 (Case 16) chord lengths from the pivot location and continue to move downstream. The path of vortices shedding near the end of the down stroke resembles a horseshoe with a width approximating the swept distance d behind the turbine plane. Cases with moderate efficiencies (Case 14 and Case 17, $20\% < \eta \leq 30\%$) and low efficiencies (Case 1 and Case 18, $\eta \leq 20\%$) in Fig. 5.14d-Fig. 5.14g show significant differences in wake patterns compared to Cases 7, 15 and 16 with high efficiencies ($\eta > 30\%$): the upper and lower branches of the wake path behind the turbine plan are close to each other (Cases 1, 17 and 18 in Fig. 5.14f, Fig. 5.14d and Fig. 5.14g respectively) or break into 4 branches (Case 14 in Fig. 5.14e). Since the time-averaged wake patterns rely on the detach-

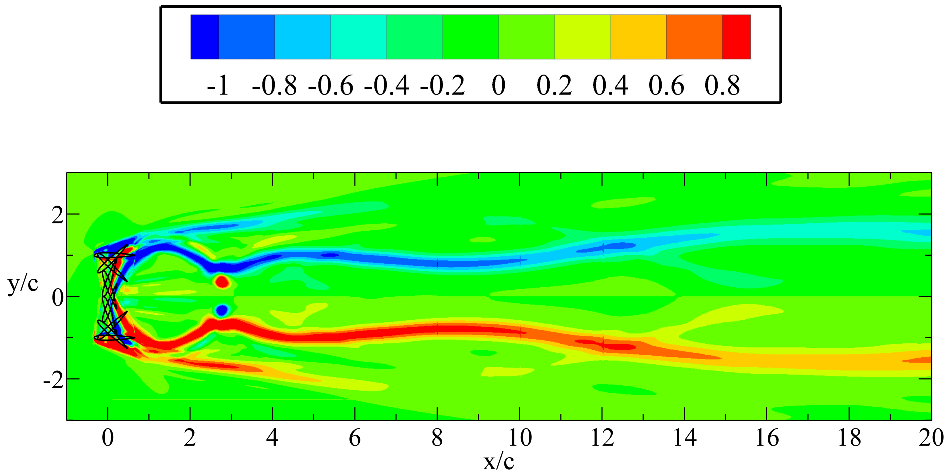

(a) Non-dimensional time-averaged vorticity contours for the power extraction system of high efficiency $\eta = 35.5\%$ (Case 15) with $f^* = 0.140, \theta_0 = 76.3°, h_0 = 1.00, \varphi = 90.0°$ and $x_{piv} = 0.333$.

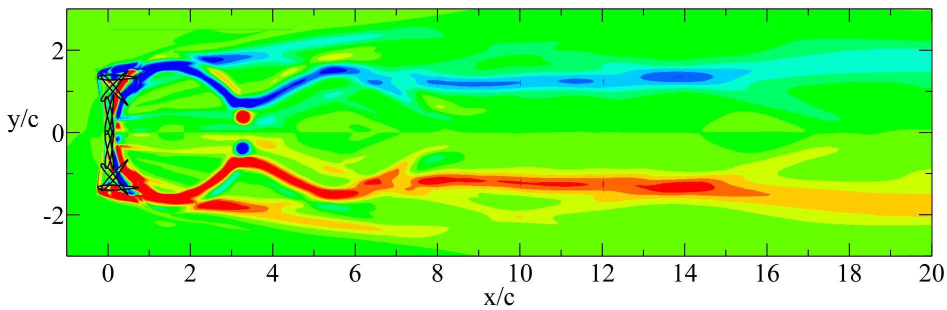

(b) Non-dimensional time-averaged vorticity contours for the power extraction system of high efficiency $\eta = 33.8\%$ (Case 16) with $f^* = 0.146, \theta_0 = 83.5°, h_0 = 1.36, \varphi = 99.5°$ and $x_{piv} = 0.250$.

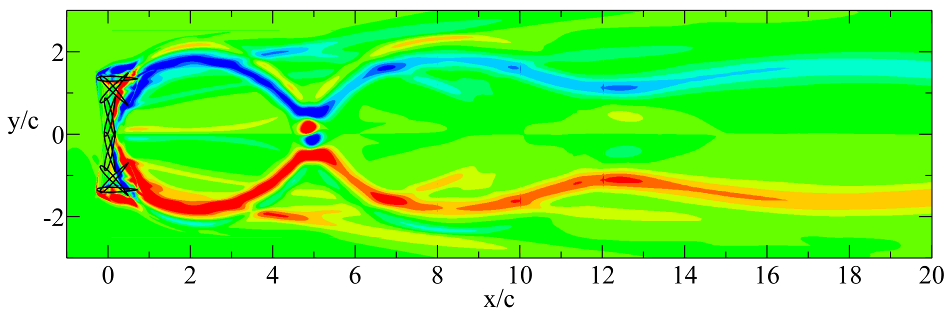

(c) Non-dimensional time-averaged vorticity contours for the power extraction system of high efficiency $\eta = 33.4\%$ (Case 7) with $f^* = 0.118, \theta_0 = 79.7°, h_0 = 1.36, \varphi = 98.9°$ and $x_{piv} = 0.273$.

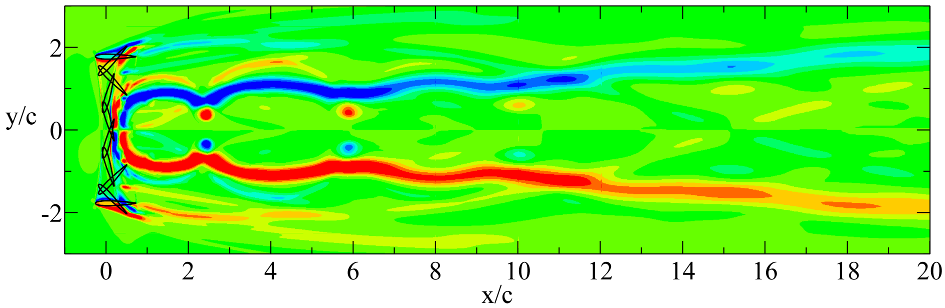

(d) Non-dimensional time-averaged vorticity contours for the power extraction system of moderate efficiency $\eta = 23.2\%$ (Case 17) with $f^* = 0.113, \theta_0 = 78.3°, h_0 = 1.78, \varphi = 86.1°$ and $x_{piv} = 0.259$.

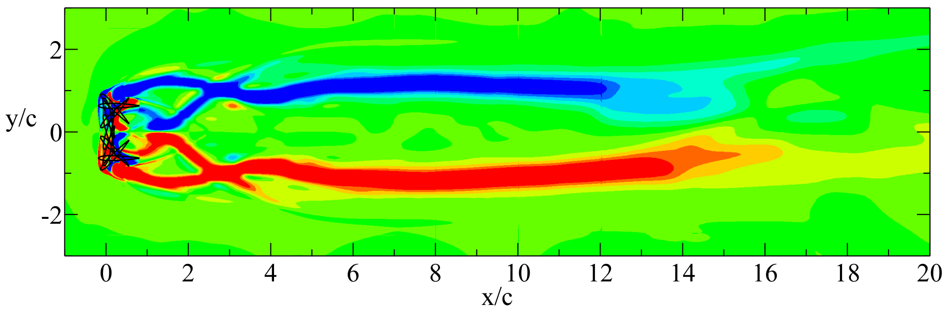

(e) Non-dimensional time-averaged vorticity contours for the power extraction system of moderate efficiency $\eta = 22.9\%$ (Case 14) with $f^* = 0.223, \theta_0 = 79.1°, h_0 = 0.79, \varphi = 126.3°$ and $x_{piv} = 0.182$.

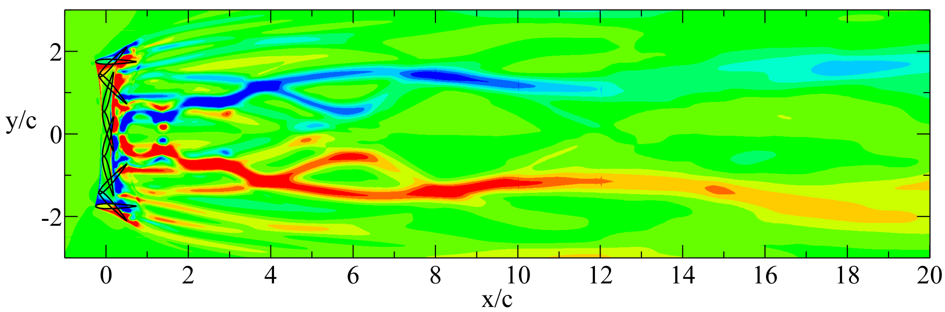

(f) Non-dimensional time-averaged vorticity contours for the power extraction system of low efficiency $\eta = 18.4\%$ (Case 1) with $f^* = 0.146, \theta_0 = 79.7°, h_0 = 1.77, \varphi = 81.6°$ and $x_{piv} = 0.253$.

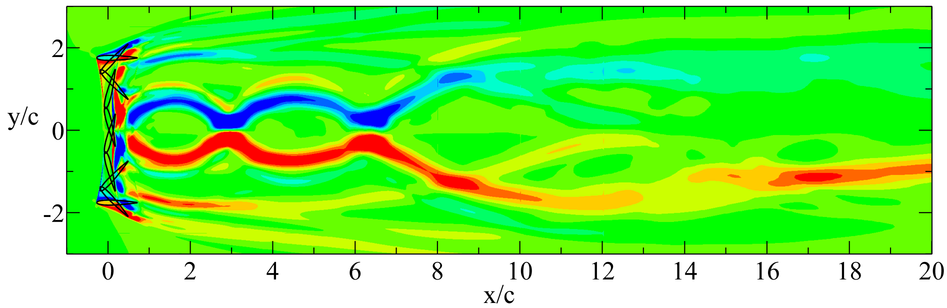

(g) Non-dimensional time-averaged vorticity contours for the power extraction system of low efficiency $\eta = 17.0\%$ (Case 18) with $f^* = 0.110, \theta_0 = 79.7°, h_0 = 1.77, \varphi = 81.6°$ and $x_{piv} = 0.276$.

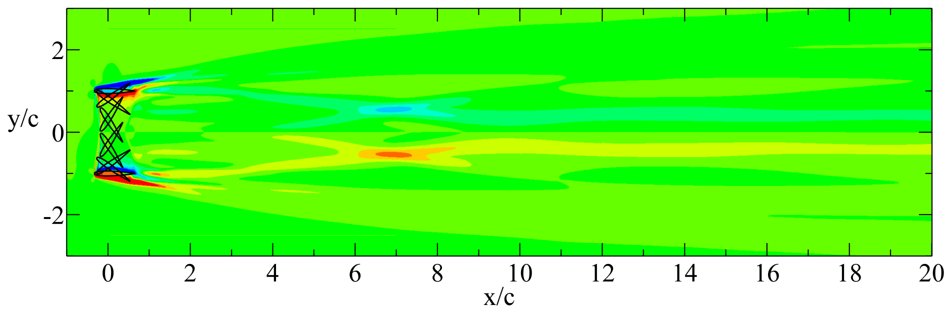

(h) Non-dimensional time-averaged vorticity contours for the power extraction system of low efficiency $\eta = 11.6\%$ (Case 19) with $f^* = 0.18, \theta_0 = 60.0°, h_0 = 1.00, \varphi = 90.0°$ and $x_{piv} = 0.333$.

Fig. 5.14: Non-dimensnioal time-averaged vorticity contours of cases listed in Table 5.3

ment and convection of the vortices, the horseshoe-shaped wake pattern with a width approximating the swept distance d behind the turbine plane illustrates that LEVs are only shed near the stroke reversal. Under this condition, the hydrodynamic loads are in good synchronizations with the prescribed motions, resulting in high efficiency. However, when the horseshoe-shaped wake is broken (Case 14) or two branches of the wake path approach each other behind the turbine plane (Cases 1, 17 and 18), there are LEVs detaching from the foil near the middle of the stroke. Under these situations, the hydrodynamic loads can be in the opposite direction of the motion for a considerable time period, resulting in significant reduction in power output; e.g. the product of C_L and $\dot{h}$ for Case 1 and that of C_M and $\dot{\theta}$ for Case 14 in Figs. 5.6-5.10.

5.5 Summary

The performance of a flapping foil power generator undergoing prescribed pitch and plunge motions at $Re = 1100$ is optimized using a multi-fidelity evolutionary algorithm. Solutions of 1-8 fidelity levels are given by the Bryant model and modified discrete vortex method of 1-7 flapping cycles respectively. The non-dominated solutions identified by the multi-fidelity approach was further assessed using the immersed boundary-lattice Boltzmann method to gain insights to the physics underpinning the performance of a flapping foil power generator through analysis of hydrodynamic loads and flow fields.

The convergence of the evolutionary algorithm using the multi and single fidelity methods is first conducted via a single objective optimization problem (η) involving two variables (f^* and θ_0). The results show that during the multi-fidelity optimization process, the number of the solutions evaluated with the highest fidelity level is roughly half of that evaluated with the lowest fidelity. This indicates that computationally expensive simulations can be stopped at an early stage thereby saving computational time. With the same computational time and initial values, the multi-fidelity evolutionary algorithm delivers better results than that using the single fidelity strategy with solutions evaluated by the highest fidelity level (i.e. DVM of 7 flapping cycles). When $\eta = 36.3\%$ is considered as the termination criterion, the multi-fidelity strategy offers 28.6% savings in computational time compared with a single fidelity approach.

Then the flapping foil system is optimized under two scenarios, i.e a single objective (η) and a bi-objective (η and $\overline{C}_P$) formulation, with the following ranges of parameter values: $f^* = 0.01 - 0.25, \theta_0 = 0° - 100°, h_0 = 0.5 - 2.0, \varphi = 45° - 135°$ and $x_{piv} = 0 - 1$. With the same evaluation budget for the single objective case, the multi fidelity method with five design variables gives an efficiency η that is 8.5% higher than the one obtained using two design variables ($f^* = 0.01 - 0.25, \theta_0 = 0° - 100°$). In the bi-objective optimization problem, the non-dominated solutions show a set of trade-off solutions and solutions with preferred η have low f^* and small h_0. On the contrary, solutions with preferred $\overline{C}_P$ have high values of f^* and h_0. In addition, high performance is achieved in the range of $\theta_0 = 70° - 90°$, $x_{piv} = 0.1 - 0.3$ and $\varphi = 80° - 110°$. Detailed study on hydrodynamic loads and flow fields for typical cases with different efficiencies indicate that the formation of vortices can be exploited for high lift, while the timing of vortex detachment influences the phase between hydrodynamic loads and prescribed motions. When the LEVs detach from the foil near the stroke reversal, the pattern of vorticity wake is horseshoe-shaped with a width approximating the swept distance d behind the turbine plane, resulting in high energy extraction performance. When the timing of vortex detachment from the foil is near the mid stroke, the efficiency and power output decrease significantly.

Chapter 6

Flexibility Enhanced Performance

Besides kinematics discussed in Chapter 5, deformation of the foil also has impact on the energy harvesting performance. In this chapter, the influence of structural flexibility on the performance of a flapping foil power generator under different kinematic conditions is examined. The aero-elastic system containing a spring-connected tail with a length of l_{tail} attached to a rigid foil with a length of $(c-l_{tail})$ is described in Section 3.1. Since reduced order models are not suitable for simulations involving fluid-structure interaction due to their low accuracy, the aero-elastic problem is solved by the immersed boundary-lattice Boltzmann method (IB-LBM). The optimal kinematic parameters of a NACA0015 foil with and without a tail are first identified to ensure that any enhancement in efficiency can be attributed to the flexibility alone. Then,

The following papers have been published from this chapter:
[1]. Zhengliang Liu, Joseph C.S. Lai, John Young, and Fang-Bao Tian. Numerical study on the performance of a flapping foil power generator with a passively flapping flat plate. In *20th Australasian Fluid Mechanics Conference*, Perth, Australia, December 2016.
[2]. Zhengliang Liu, Fang-Bao Tian, John Young, and Joseph C.S. Lai. Flapping foil power generator performance enhanced with a spring-connected tail. *Physics of Fluids*, 29(12):123601, 2017.

the effects of the passive flexibility in terms of the mass density and natural frequency on power-extraction efficiency are discussed in detail by considering time averaged and instantaneous hydrodynamic loads and tail deformations under various kinematic conditions.

6.1 Effects of flexibility on the performance under the rigid-system optimal condition

As described in Section 2.2 and Chapter 5, the performance of a flapping foil power generator relies on a large number of parameters. In McKinney & DeLaurier (1981), θ_0 is only considered up to 20°, resulting in a low efficiency of around 17%. Results given by Davids (1999) indicate that η initially increases then decreases with the increase of f^*, θ_0 and h_0, whereas $\overline{C_p}$ increases linearly with h_0. To reduce the influence of parameters other than flexibility as much as possible, optimal parameters of the rigid case including f^*, h_0, θ_0, φ and x_{piv} are first identified. Studies on power extraction systems with prescribed pitch and plunge motions discussed in Section 2.2.3 suggest a range of parameters ($f^* = 0.11 - 0.18$, $\theta_0 = 60° - 100°$, $h_0 = 0.8 - 1$ and $x_{piv} = 0.25 - 0.5$) with constant $\varphi = 90°$ for the optimal performance. According to the definition of efficiency (Eq. 2.6) and discussions in Section 5.3, $\overline{C}_P$ increases with the increase of d at the same η, θ_0 and x_{piv} (d is determined by θ_0, x_{piv} and h_0). Thus, $h_0 = 1$ is used in this study to produce high power output. Since the optimal x_{piv} is case dependent (Young et al. 2014), $x_{piv} = 0.333$ used here is chosen based on studies for prescribed motion systems (Kinsey & Dumas 2008, Simpson 2009, Xiao et al. 2012, Le et al. 2013). The optimal f^* and θ_0 at $Re = 1100$ are identified from the efficiency contours generated by IB-

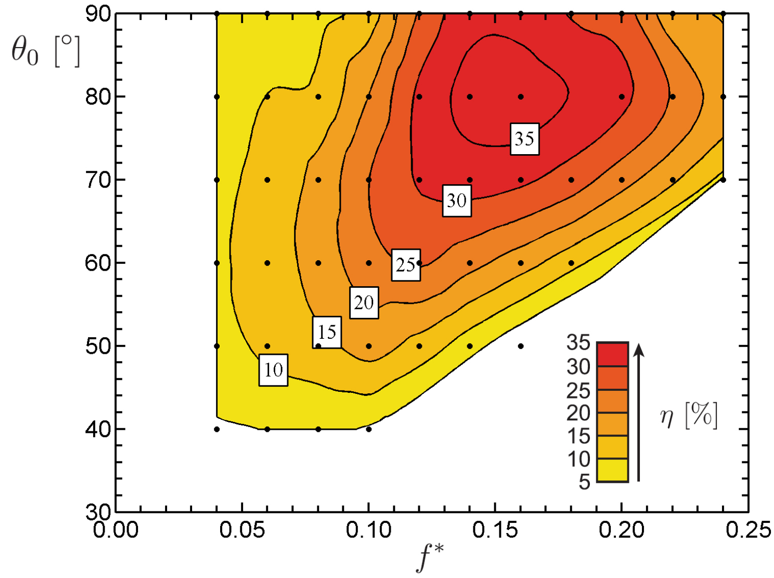

(a) Efficiency of a rigid NACA0015 foil.

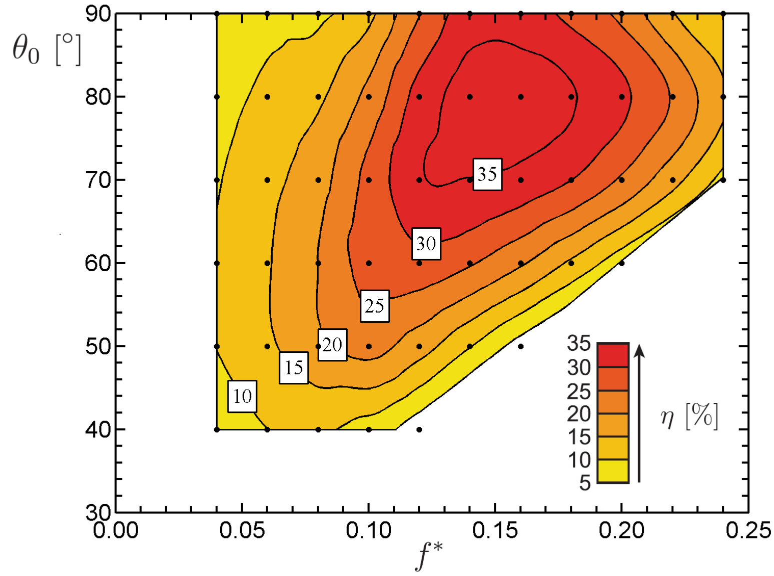

(b) Efficiency of a rigid NACA0015 foil with a fixed 0.3c flat plate tail.

Fig. 6.1: Contours of efficiency at $h_0 = 1$, $\varphi = 90°$ and $x_{piv} = 0.333$.

LBM simulations in Fig. 6.1a, where simulated cases are shown with dots. In the mapping of efficiency, the rigid foil with a fixed flat plate tail of $0.3c$ (Fig. 6.1b) shows higher efficiency compared with its counterpart under the same kinematic conditions. This can be explained as the thickness of the rigid foil with a tail is only 0.7 of that of the rigid foil with the same NACA0015 profile and the same chord length. The peak efficiencies of a rigid foil with and without a tail identified from simulated cases are 37.3% and 36.9% under the same operating condition of $f^* = 0.16$ and $\theta_0 = 80°$, which agrees with the finding of McCroskey et al. (1981) that the impact of the foil profile is insignificant when the vortex-shedding phenomenon dominates.

6.1.1 Parametric study on the effects of flexibility

In this study, the flexibility of this system is governed by the stiffness K_s and linear density of the tail $\rho_l = \rho_{tail} h_s$ which gives two non-dimensional parameters: the non-dimensional natural frequency $f_0^* = f_0 c/U = c\sqrt{K_s/J}/(2\pi U)$ and the structure-to-fluid density ratio $\mu = \rho_l / (\rho c)$, where J is the moment inertia of the tail about the the spring connection point. The length of the tail $l_{tail} = 0.3c$ (same as Wu, Shu, Zhao & Tian 2015), thickness of the tail $h_s = 0.06c$ and spring damping $R = 0$ are constants. It should be noted that simulations have also been conducted for two other tail lengths $l_{tail} = 0.1c$ and $0.5c$ for a range of spring stiffness, giving a maximum efficiency of 38.0% and 37.4% respectively, both lower than the maximum efficiency of 40.0% for $l_{tail} = 0.3c$. Thus only results for $l_{tail} = 0.3c$ are presented and discussed here.

The influence of the spring-connected tail on the energy extraction performance is systematically studied by varying f_0^* from 0.15 to 10 and μ from 0.03 to 2.00. Note that f_0^* , defined as $c\sqrt{(K_s/J)\,/\,(2\pi U)}$, is the ratio of the

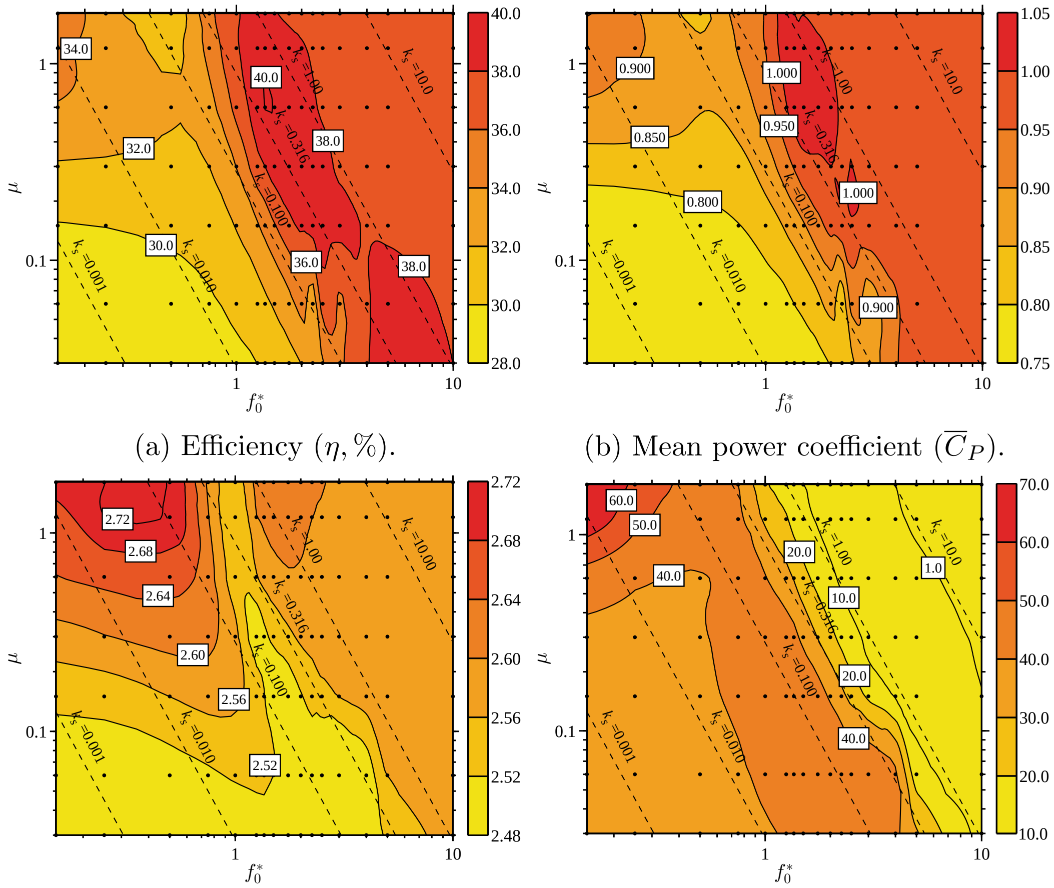

(a) Efficiency ($\eta, \%$).

(b) Mean power coefficient ($\overline{C}_P$).

(c) Maximum non-dimensional swept distance (d/c).

(d) Maximum angular position of the tail in degrees ($\alpha_{Tmax}, ^\circ$).

Fig. 6.2: Contours of a flapping foil power generator with a spring-connected tail.

restoring force to the structure inertia. The definition of the angular position of the tail α_T can be found in Section 3.1. We do not consider cases where the inertia force is much larger than the restoring force (e.g. $f_0^* < 0.15$ and $\mu > 4$) because this would give a large maximum angular position α_{Tmax} (e.g. $\alpha_{Tmax} > 80°$ at $f_0^* <= 0.05$ and $\mu = 4$, see Fig. 6.2d), leading to collision between the foil and the tail. This would give a large α_{Tmax} (e.g. $\alpha_{Tmax} > 80°$ at $f_0^* = 0.050$ and $\mu = 4.00$), leading to a collision between the foil and the tail. Contours of efficiency (η), mean power coefficient ($\overline{C}_P$), maximum swept distance (d) and maximum angular position of the tail (α_{Tmax}) are presented in Fig. 6.2. In Fig. 6.2 (a) and (b), contours of η and $\overline{C}_P$ share several similar features: (a) η and $\overline{C}_P$ initially increase then decrease with the increase of f_0^* at the same μ; (b) η and $\overline{C}_P$ approximate those given by the rigid case ($\eta = 37.3\%$ and $\overline{C}_P = 0.966$) when f_0^* and μ are high; (c) cases with low f_0^* and μ show performance reduction compared to the rigid case; and (d) the peak $\eta = 40.0\%$ and $\overline{C}_P = 1.03$ are achieved at $f_0^* = 1.36$ and $\mu = 2.00$ where the flapping frequency $f^* = 0.16$ is about 12% of $f_0^* = 1.36$. This is similar to the study on propulsion system where the flapping frequency of the dragonfly is about 16.0% of the natural frequency (Chen et al. 2008). The dashed line in Fig. 6.2 is the non-dimensional stiffness defined as $k_s = K_s/\left(\rho U^2 c^3\right)$. Fig. 6.2d shows that in the region of $k_s > 1.0$, α_{Tmax} is smaller than 10°. Moreover, when $k_s > 10.0$, α_{Tmax} is smaller than 1° and the tail can be considered as rigid and the differences in power extracting performance are less than 1% (see Fig. 6.2 (a) and (b)). In addition, performance improvements can be observed in the range of $k_s = 0.316 - 1.00$ (see Fig. 6.2 (a) and (b)). The non-dimensional swept distance d/c referring to the potential power available in the inflow is shown in Fig. 6.2c. When $0.100 < k_s < 0.316$, d/c decreases dramatically with the increase of f_0^*; while for $k_s < 0.100$, d/c highly depends

Table 6.1: Performance of a power generator with a spring-connected tail (Case 1-3) compared to that with a rigid tail (Case 4) at the same optimal kinematic conditions determined for the main rigid foil ($f^* = 0.16$, $\theta_0 = 80°, h_0 = 1, \varphi = 90°, x_{piv} = 0.333$).

Case	f_0^*	μ	k_s	f_r^*	η	$\overline{C}_P$	d/c	$\sqrt{\overline{C_L^2}}$	$\overline{C}_{Ph}$	$\overline{C}_{P\theta}$	$\alpha_{Tmax}(°)$	$\alpha_{effmax}(°)$
1	1.36	0.60	0.393	1.180	40.0%	1.03	2.57	1.64	1.02	0.01	29.5	35.4
2	1.36	0.03	0.020	0.491	30.3%	0.76	2.50	1.13	0.74	0.02	42.9	30.0
3	0.15	0.60	0.005	0.130	33.9%	0.90	2.64	1.59	0.96	-0.06	46.0	33.5
4	-	-	-	-	37.3%	0.97	2.59	1.57	0.95	0.02	0.00	34.8

on μ. However, according to Eq. 2.6, the similarity of Fig. 6.2 (a) and (b) indicates the influence of f_0^* and μ on $\overline{C}_P$ is more significant than on d/c. When $k_s < 0.100$, both d/c and α_{Tmax} increase with the increase of μ. Fig. 6.2d shows that when $k_s > 0.100$, the gradients of α_{Tmax} and k_s are in the opposite directions while the relationship between d/c and k_s is ambiguous in the same region. In addition, the peaks of d/c and α_{Tmax} are achieved at different f_0^*. The differences between maximum swept distance (Fig. 6.2c) and maximum angular position (Fig. 6.2d) indicate that factors other than α_{Tmax} (e.g. the direction of the tail deflection) also impact d/c when h_0, θ_0 and φ are fixed.

6.1.2 Mechanism of performance improvement due to flexibility

To further discuss how the flexibility (i.e. f_0^* and μ) affects the energy harvesting performance, cases with a spring-connected tail of different stiffness values which improve (Case 1) or reduce (Case 2 and Case 3) the performance and the rigid case (Case 4) are examined in detail through the time averaged values (η and $\overline{C}_P$), time histories of the hydrodynamic loads (C_L and C_M) and the passive motion and the flow field at different instants t/T sequentially. In all the figures showing time histories, $t/T = 0 - 1$ represents the last flapping cycle (the 12th cycle). Firstly, stiffness parameters and time averaged values are presented in Table 6.1. Case 1 is the case providing the highest efficiency in Fig. 6.2a. Case 2 is selected with the same f_0^* as Case 1 but with a much lower μ (lighter tail) than Case 1 so that the influence of fluid added mass becomes more important. Case 3 is selected with the same μ (i.e. same mass) as Case 1 but with a much lower k_s (hence f_0^*) so that the influence of lower stiffness is assessed. An efficiency improvement of 7.24% with a similar swept distance compared with the rigid tail (Case 4) is achieved at optimal f_0^* and μ (i.e. Case 1). However, a spring-connected tail with low μ (Case 2) or low f_0^* (Case 3) degrades the performance of a flapping foil power generator at the optimal condition of the rigid case. Since the lift force and prescribed plunge velocity contribute significantly to the power extraction performance (Kinsey & Dumas 2008), the root mean square of lift coefficient $\sqrt{\overline{C_L^2}}$ is the hydrodynamic load of interest since lift and plunge velocity contribute to the power. As shown in Table 6.1, the lowest $\sqrt{\overline{C_L^2}} = 1.13$ given by Case 2 is accompanied with the poorest performance. However, η and $\overline{C}_P$ of Case 1, 3 and 4 which share similar $\sqrt{\overline{C_L^2}}$ of around 1.6 are different. In addition, only Case 3 shows negative $\overline{C}_{P\theta}$ even though $\sqrt{\overline{C_L^2}}$ and $\overline{C}_{Ph}$ are similar to Case 4. These observations indicate that in addition to the magnitude of C_L, there are other factors (e.g., the phase angle between C_L and $\dot{h}$) that influence of the performance of a flapping foil power generator.

To further investigate the impact of C_L on the performance, time histories of C_L are presented in Fig. 6.3a. As expected from $\sqrt{\overline{C_L^2}}$ in Table 6.1, Case 2 shows the smallest amplitude of C_L among the four cases. C_L of Case 1, 3 and 4 are similar during the mid of up (gray region) and down (white region) strokes. Near stroke reversals ($t/T = 0, 0.5$), both Case 1 and Case 3 exhibit peaks while Case 4 shows a smoother curve. After the end of strokes, even

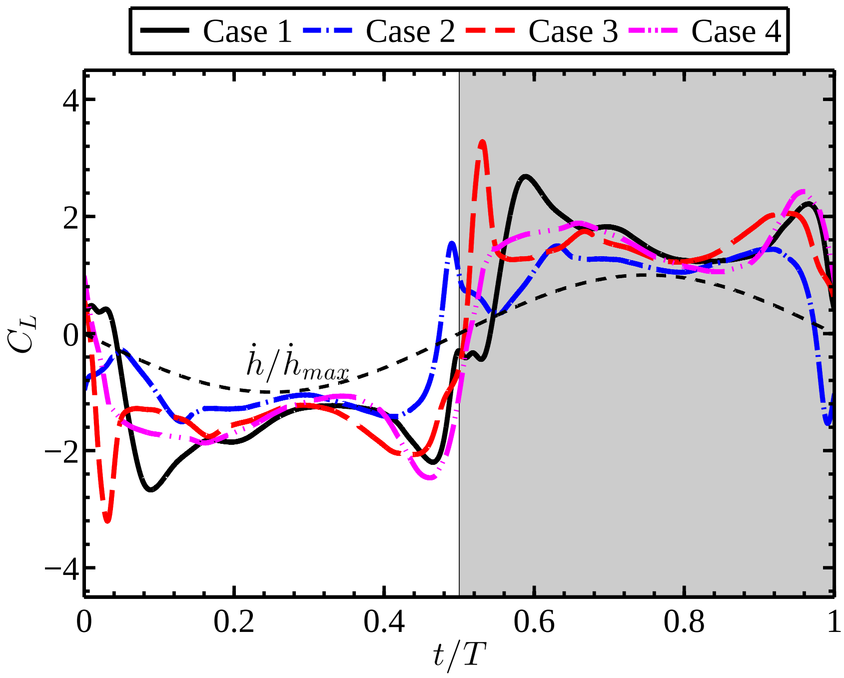

(a) Time history of C_L and $\dot{h}/\dot{h}_{max}$.

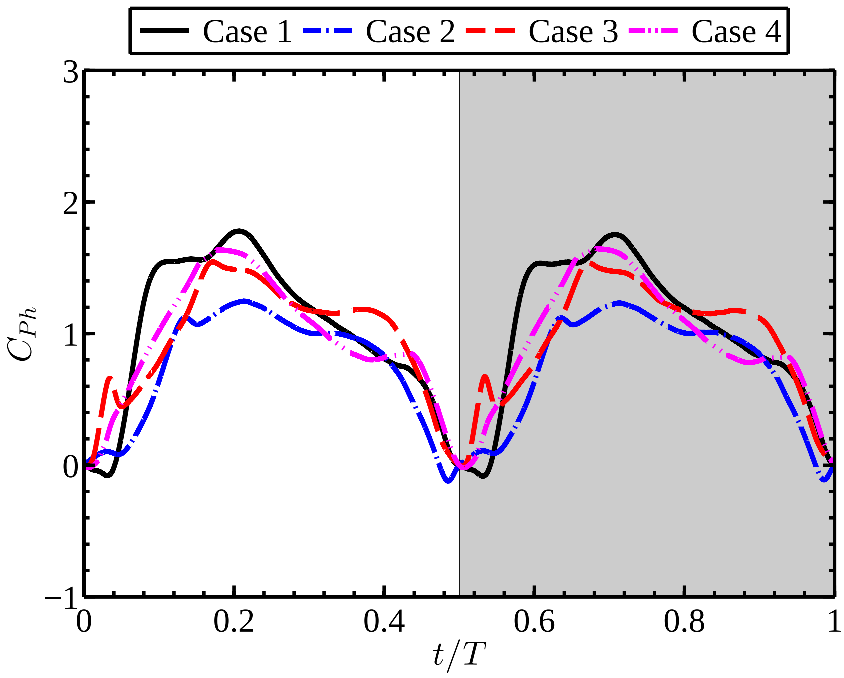

(b) Time history of C_{Ph}.

Fig. 6.3: Comparison of C_L and C_{Ph} of a rigid foil with a spring-connected or a rigid tail at $f^* = 0.16$, $\theta_0 = 80°$, $h_0 = 1$, $\varphi = 90°$ and $x_{piv} = 0.333$.

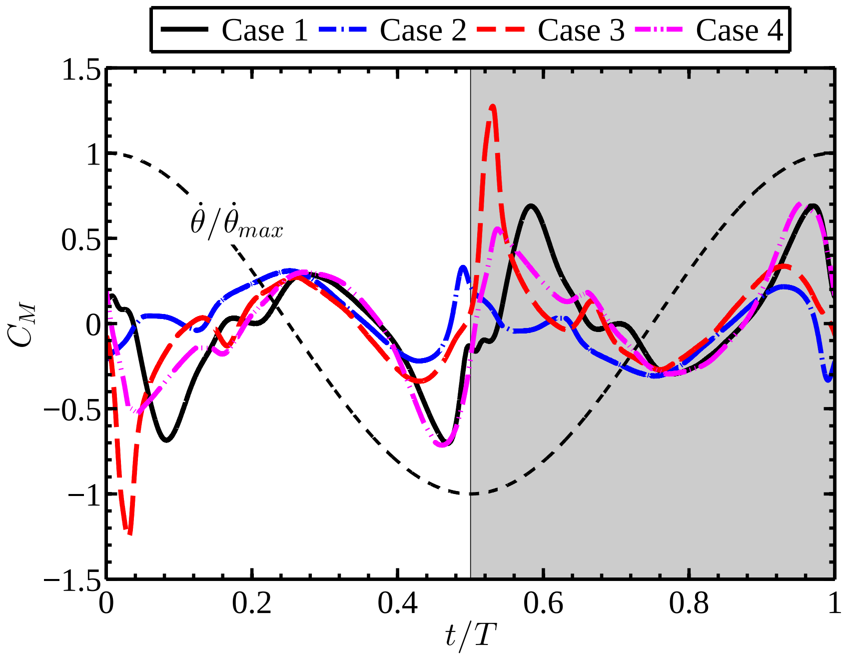

(a) Time history of C_M and $\dot{\theta}/\dot{\theta}_{max}$.

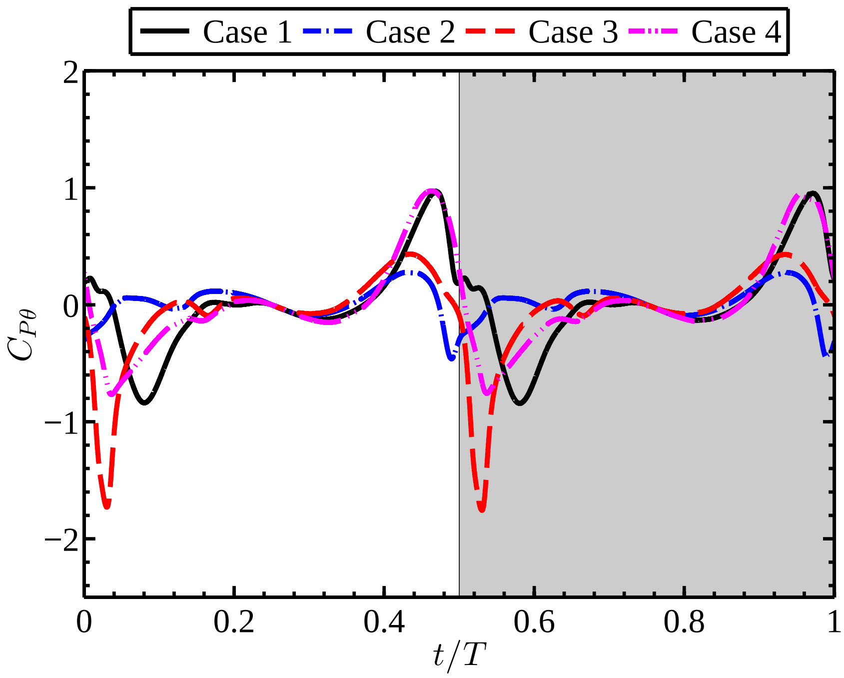

(b) Time history of $C_{P\theta}$.

Fig. 6.4: Comparison of C_M and $C_{P\theta}$ of a rigid foil with a spring-connected or a rigid tail at $f^* = 0.16$, $\theta_0 = 80°$, $h_0 = 1$, $\varphi = 90°$ and $x_{piv} = 0.333$.

though Case 3 gives the highest peak of C_L ($t/T = 0.53$), Case 3 and Case 4 share similar C_{Ph} while Case 1 provides higher C_{Ph} at $t/T = 0.59$ (Fig. 6.3b) because of the delayed peak of C_L where $\dot{h} = \dot{H}/c$ is higher (Fig. 6.3a). This leads to the differences in $\overline{C}_{Ph}$ of Case 1, 3 and 4 sharing similar $\sqrt{\overline{C_L^2}}$ (Table 6.1). Similar to the time histories of C_L in Fig. 6.3a, C_M in Fig. 6.4a shows some differences near stroke reversals. It can be noted that the peaks of C_M for Case 1, 2 and 3 occur at the same time instants t/T where C_L reaches the peaks. However, C_M for Case 4 also shows the peak after the end of strokes where the curve of C_L is smooth. This indicates that the magnitude of the force is the primary factor affecting C_M while the location of the force center also influences C_M. In addition, drops of $C_{P\theta}$ near the end of strokes where $\dot{\theta} = \dot{\theta}_{max}$ in Fig. 6.4b lead to negative C_P in Fig. 6.5a. The sharp drops of $C_{P\theta}$ shown by Case 3 leads to the performance reduction compared to the rigid case with a similar $\overline{C}_{Ph}$ (Table 6.1).

The differences in amplitudes of α_T partially explain the increase of d/c from 2.57 (Case 1) to 2.64 (Case 3), while factors (e.g. the phase between the prescribed motion and α_T) other than α_{Tmax} also influence d/c (Case 1 and Case 2, Table 6.1). To further investigate the influence of α_T on d/c, time histories of the passive pitch angle (α_T, Fig. 3.2) are illustrated in Fig. 6.5b. Even though α_{Tmax} of Case 2 is larger than that of Case 1, α_T of Case 2 is in the opposite direction of θ before the middle of up and down strokes, resulting in a small distance swept by the tail. The frequency components of the passively flapping motion (α_T) are analysed using a Fast Fourier Transform (FFT) decomposition of the time-series data over 10 cycles (37500 points). As shown in Fig. 6.6, the peaks of the 3 cases are at $f_\alpha^* = f_\alpha c/U = 0.160, 0.480, 0.800, 1.12$ and 1.44 which are 1, 3, 5, 7 and 9 times of the reduced flapping frequency f^*. It can be observed that even though f_0^* for Case 1 and Case 2 is the same,

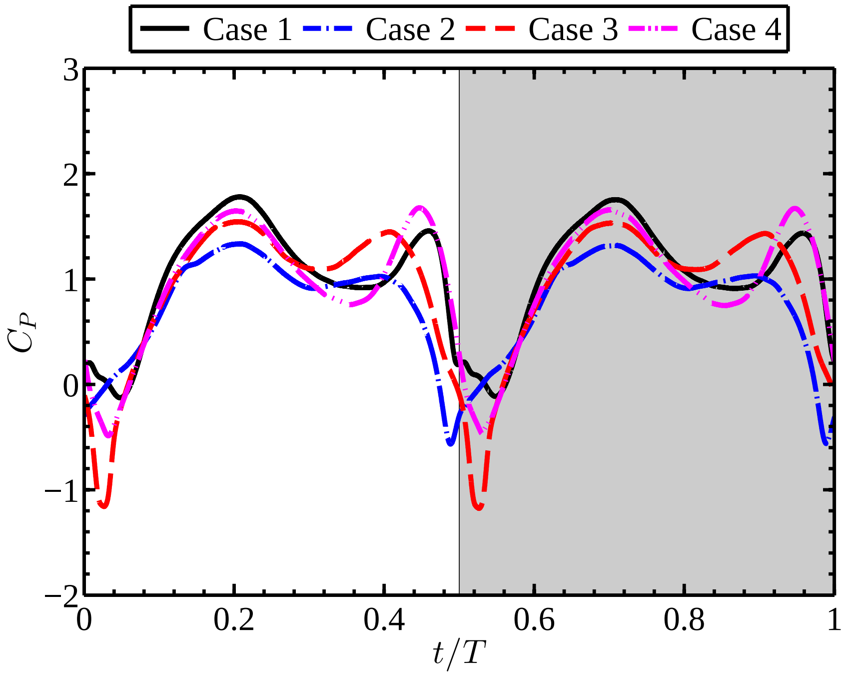

(a) Time histories of C_P.

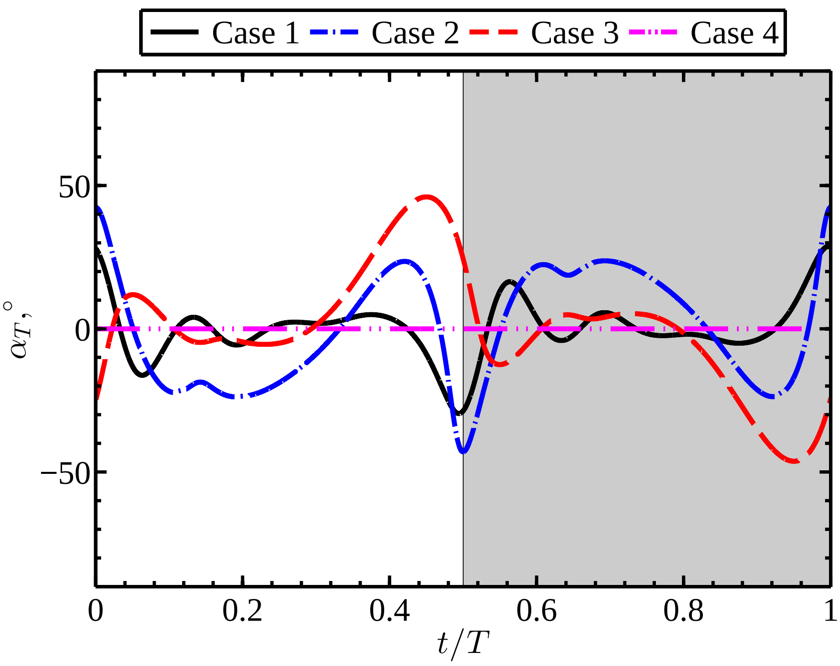

(b) Time histories of α_T.

Fig. 6.5: Comparison of C_P and α_T of a rigid foil with a spring-connected or a rigid tail at $f^* = 0.16$, $\theta_0 = 80°$, $h_0 = 1$, $\varphi = 90°$ and $x_{piv} = 0.333$.

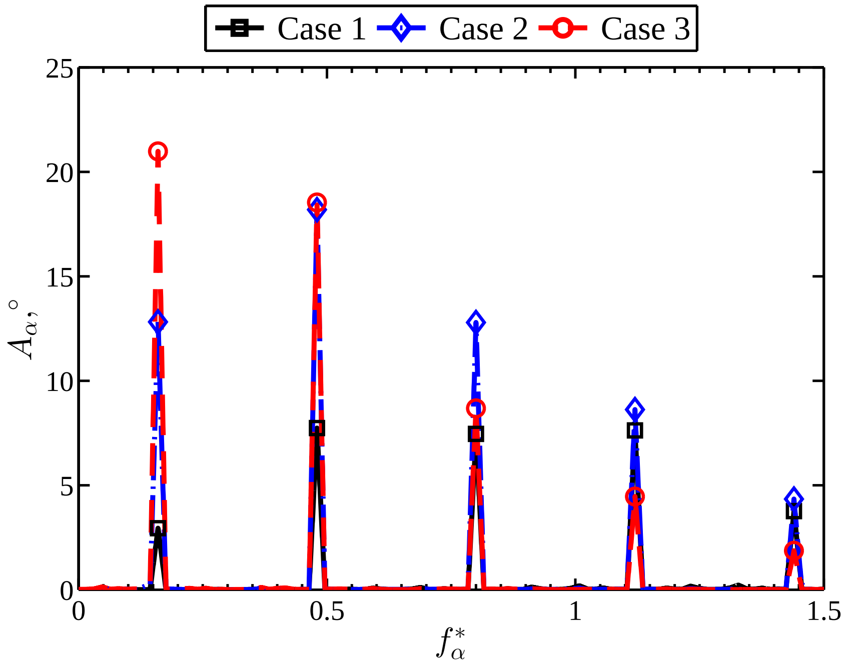

Fig. 6.6: Frequency spectra of the passively flapping motions at $f^* = 0.16$, $\theta_0 = 80°$, $h_0 = 1$, $\varphi = 90°$ and $x_{piv} = 0.333$.

the amplitude of the decomposed motions (A_α) of Case 2 varies from less than 5° when $f^*_\alpha \geq 1.44$ to a maximum of 18.2° at $f^*_\alpha = 0.480$ whereas A_α of Case 1 at $f^*_\alpha = 0.480, 0.800, 1.12$ are similar around 7.60°. Hence, for Case 1, the decomposed motions with similar A_α but with different f^*_α and phase angles lead to suppression in the tail deformation during the mid-strokes as shown in Fig. 6.5b. To account for the energy required to accelerate the fluid around the tail, the resonant frequency f^*_r is introduced as:

$$f^*_r = \frac{c}{2\pi U}\sqrt{\frac{K_s}{J + J_f}}, \tag{6.1}$$

where $J_f = 9\pi\rho l^4_{tail}/128$ is an estimate of the moment of inertia due to fluid acceleration (Brennen 1982). From Fig. 6.6, it is noted that the maximum amplitude of the passive motion of the tail for each case occurs close to the resonant frequency: f^*_r of 1.18 (Case 1), 0.49 (Case 2) and 0.13 (Case 3). This partially explains the difference between Case 1 and Case 2 shown in Fig. 6.6

even though their natural frequencies (f_0^*) are the same.

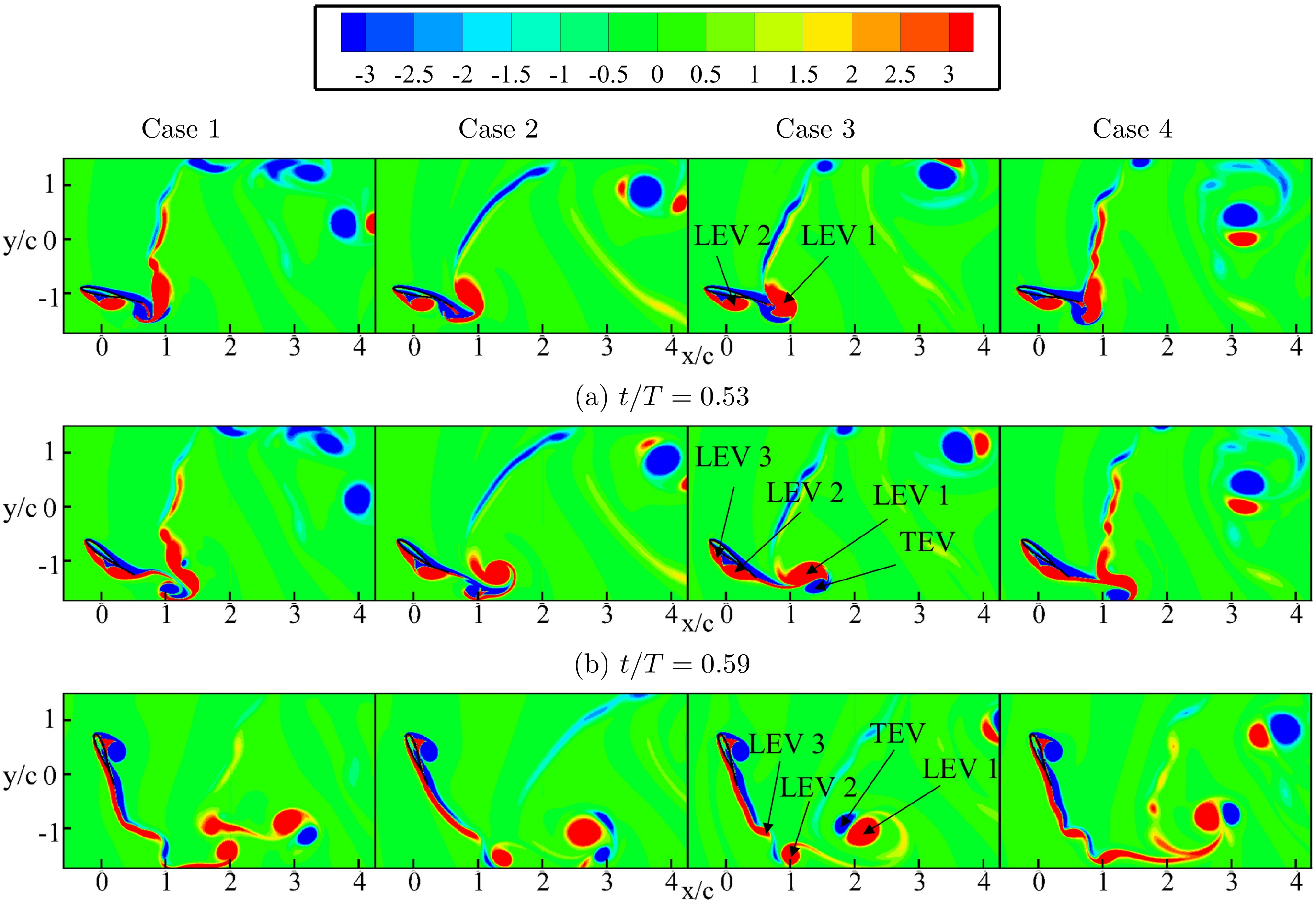

(a) $t/T = 0.53$

(b) $t/T = 0.59$

(c) $t/T = 0.82$

Fig. 6.7: Instantaneous non-dimensional vorticity contours of Case 1-4 with $f^* = 0.16$, $\theta_0 = 80°$, $h_0 = 1$, $\varphi = 90°$ and $x_{piv} = 0.333$ at $t/T = 0.53$, 0.59 and 0.82.

Finally, to investigate effects of the formation and convection of vortices on the hydrodynamic load, non-dimensional vorticity ($C_v = c\omega_z/U$, where ω_z is the spanwise vorticity) and relative pressure coefficient ($C_p = 2(p - p_\infty)/\rho U^2$) contours are presented in Fig. 6.7, Fig. 6.8 and Fig. 6.9. As the hydrodynamic load and tail deflection are symmetric/antisymmetric (Fig. 6.3 to Fig. 6.5), we only present the flow fields of the upstroke (the downstroke is a mirror image of the upstroke). Flow fields of the four cases near the flapping foil are investigated in detail at three typical non-dimensional time instants $t/T = 0.53$

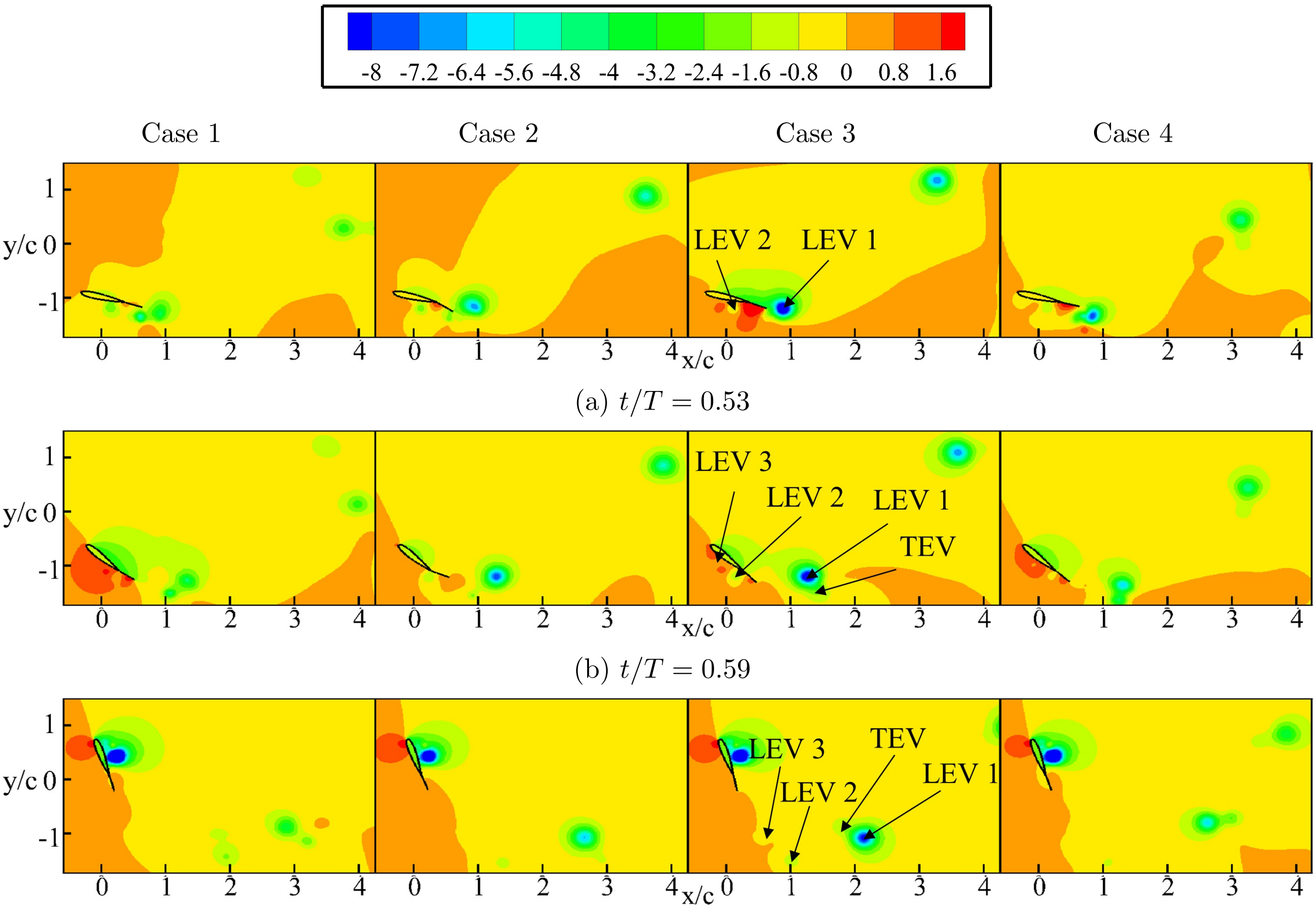

(a) $t/T = 0.53$

(b) $t/T = 0.59$

(c) $t/T = 0.82$

Fig. 6.8: Relative pressure coefficient contours of Case 1-4 with $f^* = 0.16$, $\theta_0 = 80°$, $h_0 = 1$, $\varphi = 90°$ and $x_{piv} = 0.333$ at $t/T = 0.53$, 0.59 and 0.82.

when Case 3 shows a peak of C_L (Fig. 6.3a) and a sharp drop of $C_{P\theta}$ (Fig. 6.4b); $t/T = 0.59$ when Case 1 shows a peak of C_L (Fig. 6.3a); and $t/T = 0.82$ when the four cases share similar hydrodynamic load (Fig. 6.3a to Fig. 6.5). For all the four cases shown in Fig. 6.7, it is noted that three LEVs move downward and shed into the wake during the upstroke. The first LEV and the trailing edge vortex (TEV) constitute a vortex pair of opposite signs while the other two LEVs (2 and 3) detach from the foil separately. After the stroke reversal ($t/T = 0.53$ in Fig. 6.7a), the first LEV is stretched by the interaction with the tail in Case 1 and 4. Near the stroke reversal, the deflection of the tail (Fig. 6.5b) of Case 3 is in the opposite direction of those of Case 1 and 2, resulting in the strong LEV close to upper surface of the tail. The mapping of C_p is shown in Fig. 6.8. In Fig. 6.8a, Case 3 shows a larger low pressure region resulting from the strong LEV compared to the other three cases, leading to high pressure differences between the upper and lower surface of the tail. At $t/T = 0.59$, the second LEV reaches the trailing edge of the rigid foil (Fig. 6.7b), resulting in pressure discontinuity near the trailing edge of the foil for all the cases (Fig. 6.8b). In Fig. 6.8b, it is noted that the influence of the second LEV for Case 1 is the smallest, partially explaining the highest C_L found in Fig. 6.3a. At $t/T = 0.82$ (Fig. 6.7c and Fig. 6.8c), the four cases show similar flow fields around the foil. Case 1 shows some differences in the wake as the first LEV breaks into two vortices and one of them merges with the second LEV which is detached from the tail (Fig. 6.7c). The differences in the flow fields can be explained by the rapid movement of the tail (Fig. 6.5b) that influences the formation and the trajectory of the TEV as well as the detachment of the LEVs, especially near the end of strokes (Fig. 6.7). The deflection of the tail with the appropriate flexibility (Case 1) reduces the low pressure region at the pressure surface around the trailing edge caused by the second LEV, resulting in high C_L at $t/T = 0.59$ where the plunge velocity is $\dot{h}/\dot{h}_{max} = 0.536$, producing a high performance (7.24% and 6.63% improvement in η and $\overline{C}_P$ over the rigid tail). On the other hand, in Case 3 where the tail stiffness is low, the first LEV circumnavigates the tail near the stroke reversal earlier than in other cases, resulting in high hydrodynamic loads (C_L and C_M) at low $\dot{h}/\dot{h}_{max}$ but high $\dot{\theta}/\dot{\theta}_{max}$. As a consequence, the power extracted from the plunge motion is low and more power is required for the pitch motion.

Then, the vortices in the wake (20 chord lengths after the pivot point) are examined at the end of downstroke in Fig. 6.9. For comparison, the vorticity scale in Fig. 6.9 is the same as Fig. 6.7. It is noted that the rotations of the vortex pairs (the first LEV and the TEV) and the first LEV are in the same direction which indicates that the strength of the first LEV is stronger than that of the TEV in each pair. In the downstream region, differences between Case 1 and the other 3 cases in the vortex structures are evident. Different from a propulsive system where a reverse Kármán vortex sheet is observed (Zhang et al. 2010), a Kármán vortex sheet occurs in Case 2, 3 and 4. However, Case 1 gives a different structure in the downstream with multiple sequential vortices of the same sign rather than vortex pairs, but the resulting structure downstream is still a wake. In Case 2, 3 and 4, the second LEV dissipates after advecting 10 chord lengths while that of Case 1 can be found even near 20 chord lengths since the strength of the second LEV is reinforced by the first LEV which breaks into two vortices, as shown in Fig. 6.7b and 6.7c.

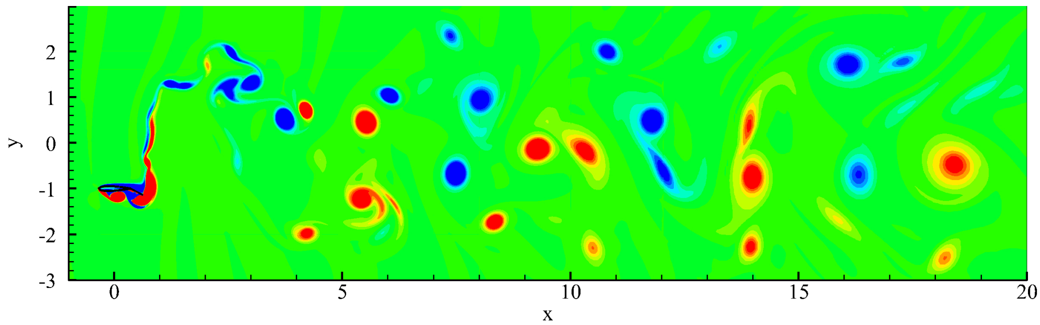

(a) Case 1

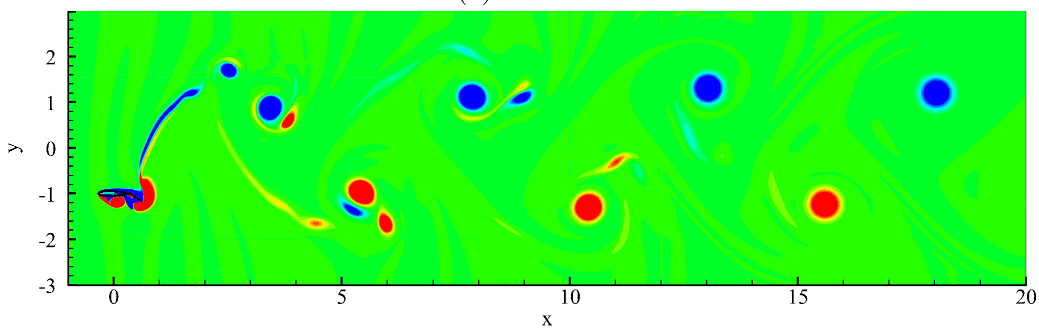

(b) Case 2

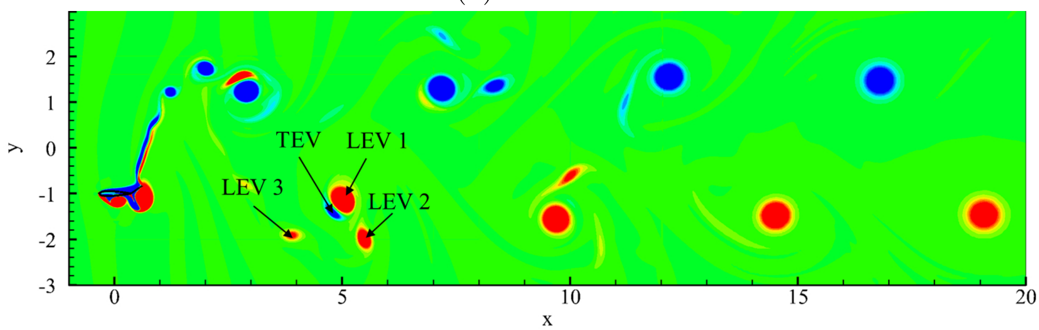

(c) Case 3

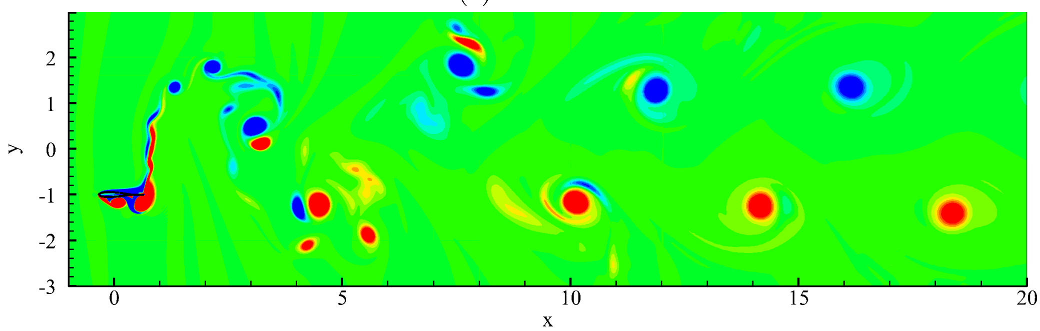

(d) Case 4

Fig. 6.9: Instantaneous non-dimensional vorticity contours of Case 1-4 at $f^* = 0.16$, $\theta_0 = 80°$, $h_0 = 1$, $\varphi = 90°$ and $x_{piv} = 0.333$ and $t/T = 0.5$. Vorticity scale is the same as that in Fig. 6.7.

6.2 Effects of flexibility on the performance under different kinematic conditions

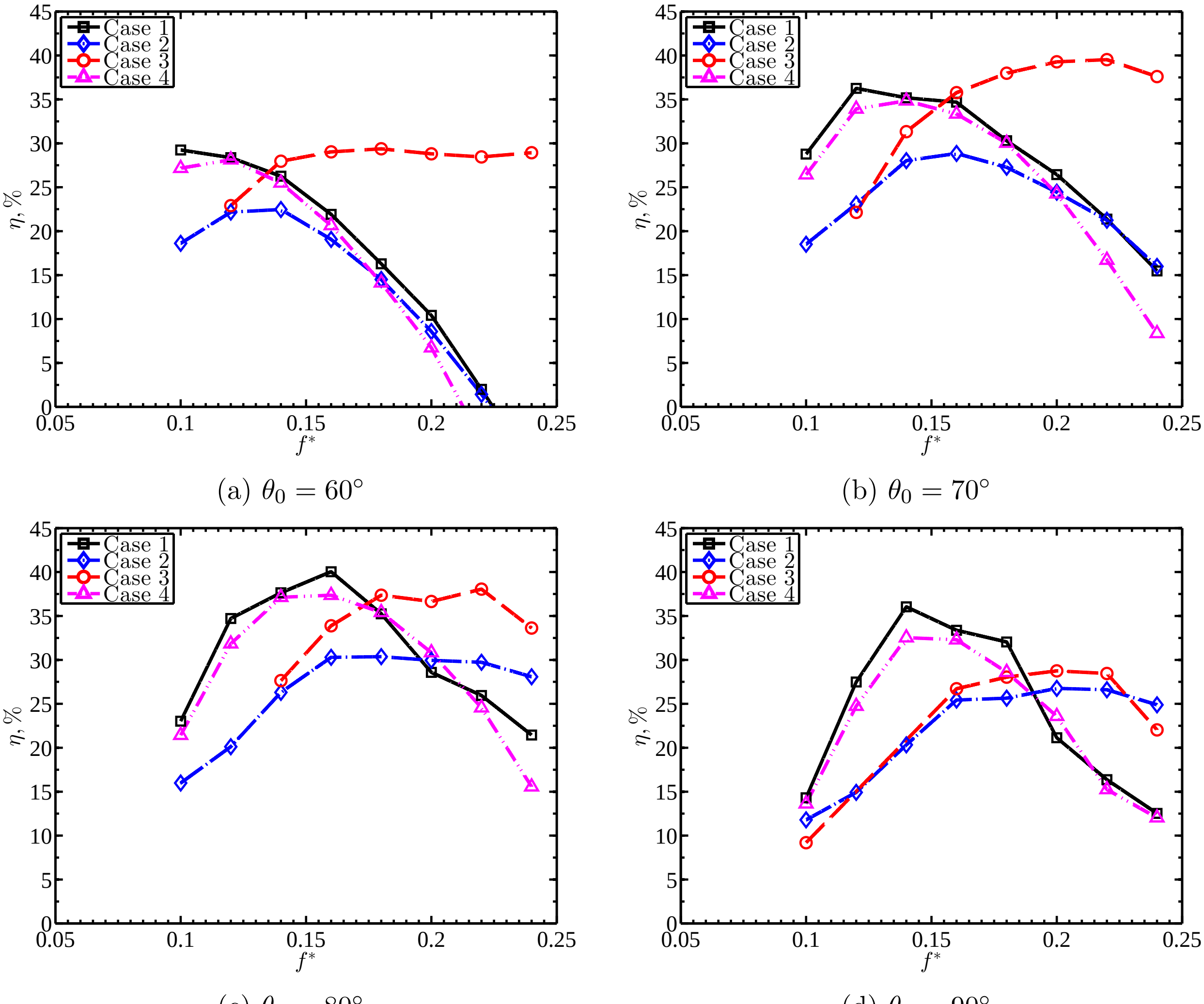

(a) $\theta_0 = 60°$

(b) $\theta_0 = 70°$

(c) $\theta_0 = 80°$

(d) $\theta_0 = 90°$

Fig. 6.10: Comparison of η in the range of $f^* = 0.10 - 0.24$ at $h_0 = 1$, $\varphi = 90°$ and $x_{piv} = 0.333$.

To study the energy harvesting performance of the spring-connected system under different kinematic conditions, 4 cases listed in Table 6.1 are simulated over a range of kinematic parameters ($f^* = 0.10 - 0.24$, $\theta_0 = 60° - 90°$). The efficiency results in Fig. 6.10 show similar trends with f^* at each θ_0 as the power coefficient results in Fig. 6.11. This because efficiency is the product of

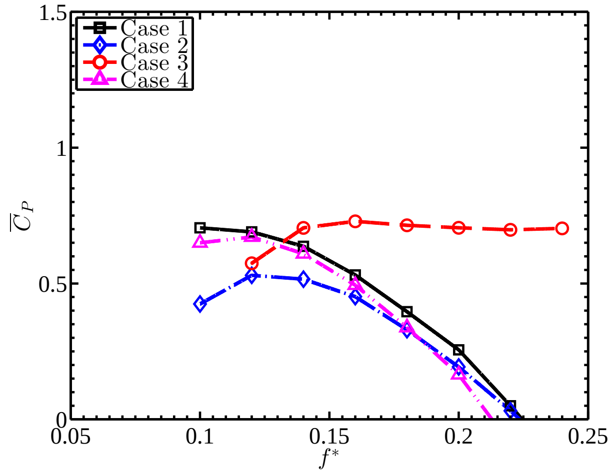

(a) $\theta_0 = 60°$

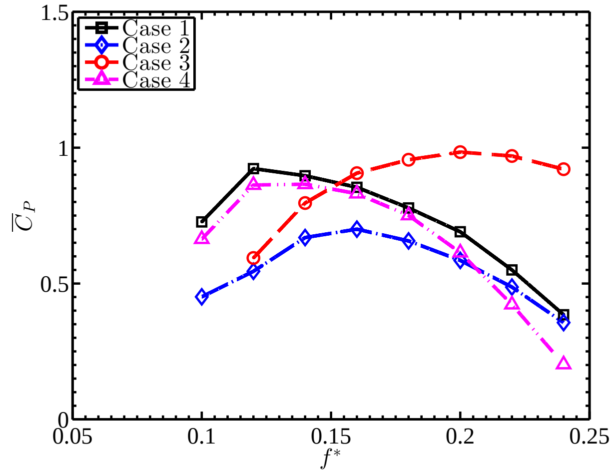

(b) $\theta_0 = 70°$

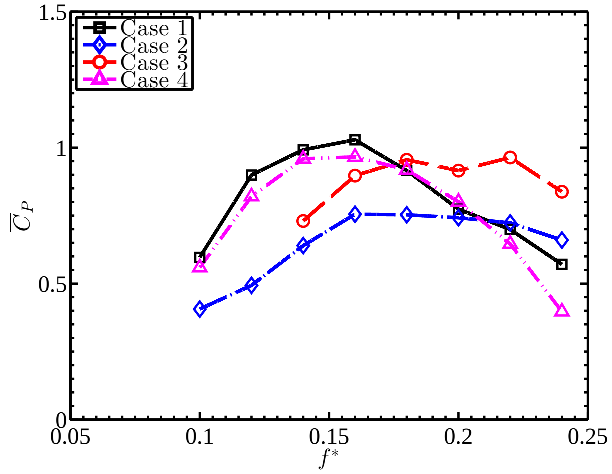

(c) $\theta_0 = 80°$

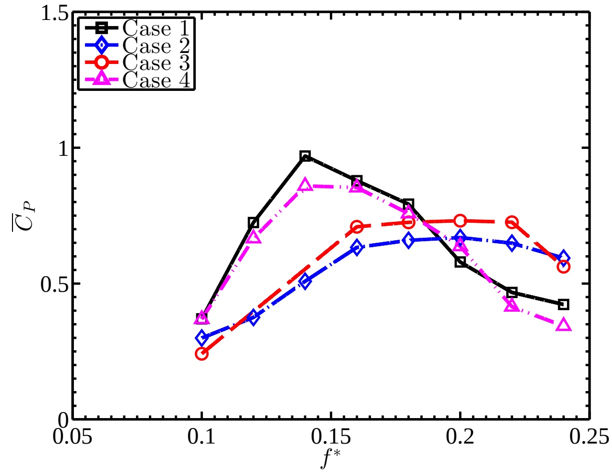

(d) $\theta_0 = 90°$

Fig. 6.11: Comparison of $\overline{C}_P$ in the range of $f^* = 0.10 - 0.24$ at $h_0 = 1$, $\varphi = 90°$ and $x_{piv} = 0.333$.

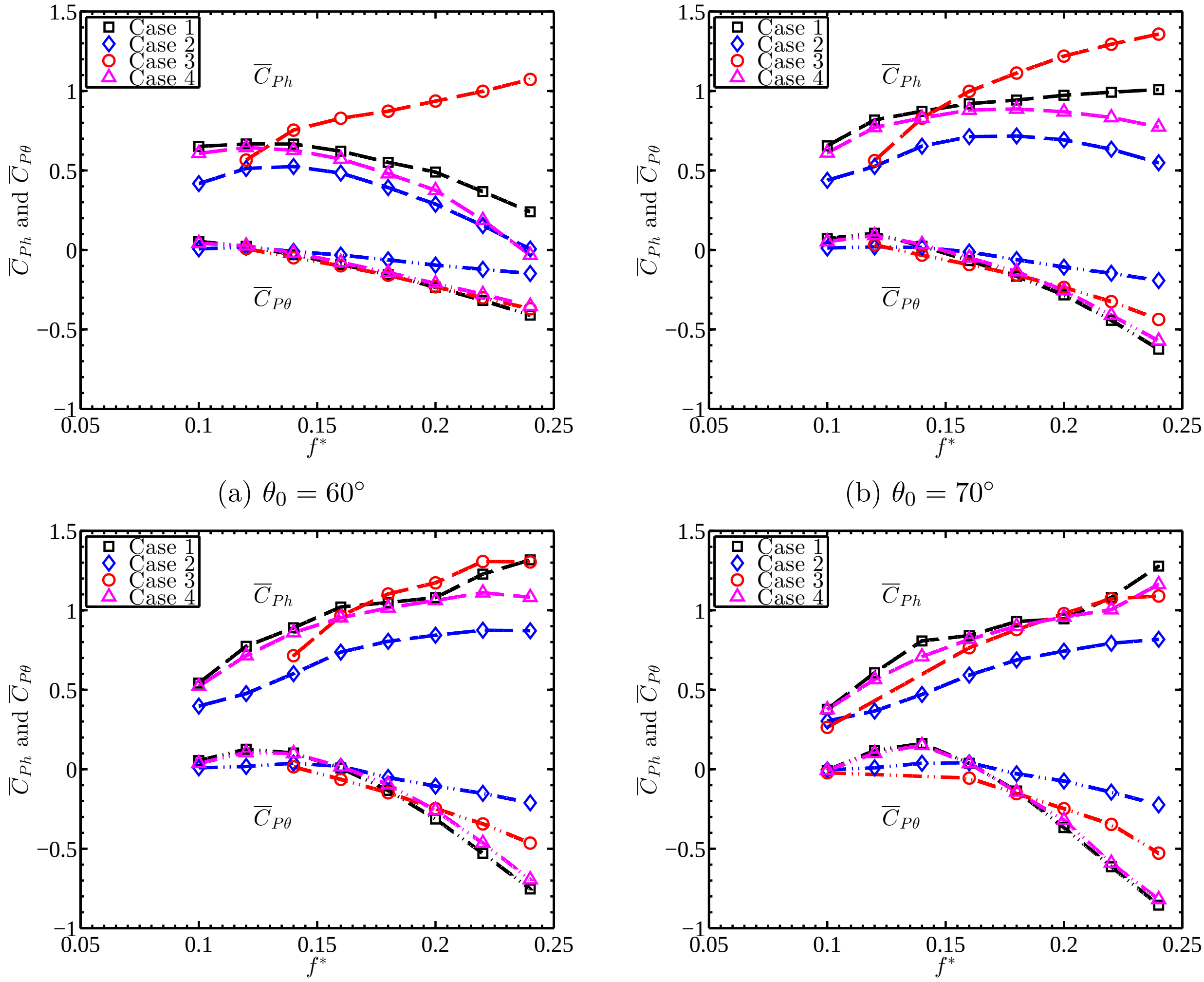

(a) $\theta_0 = 60°$

(b) $\theta_0 = 70°$

(c) $\theta_0 = 80°$

(d) $\theta_0 = 90°$

Fig. 6.12: Comparison of $\overline{C}_{Ph}$ nd $\overline{C}_{P\theta}$ in the range of $f^* = 0.10 - 0.24$ at $h_0 = 1$, $\varphi = 90°$ and $x_{piv} = 0.333$.

the power coefficient and c/d (see Eq. 2.6) but the change of the swept distance d is limited as it is dependent on the plunge amplitude h_0 which is fixed. Case 1 provides performance improvement in the optimal range of flapping frequencies, i.e. $f^* = 0.12 - 0.18, \theta_0 = 80°$ and $90°$. On the other hand, Case 3 gives the highest efficiency and power coefficient in the range of high flapping frequencies $f^* = 0.20 - 0.24$ regardless of θ_0 except at $f^* = 0.24$, $\theta_0 = 90°$. At $f^* = 0.22$, Case 3 where the natural frequency of the tail ($f_0^* = 0.15$) is close to the flapping frequency achieves the highest efficiency among the 4 cases in the range of θ_0 from 60° to 90°, which is consistent with findings of Wu, Shu, Zhao & Tian (2015) that a tail with $f_0^* = 0.20$ gives the highest efficiency around 34% at the same f^* but lower amplitudes for pitch ($\theta_0 = 52.1°$) and plunge ($h_0 = 0.5$). In their study, the performance improvement is attributed to the strengthened LEV resulting from the tail deformation. However, the performance cannot be directly related to just the LEV strength in this study with high $\theta_0 = 80°$ and $h_0 = 1$ where the strong LEV is observed in all the four cases. In Fig. 6.12, $\overline{C}_{Ph}$ of Case 3 increases with f^* in the range of $f^* = 0.10 - 0.22$ at $\theta_0 = 60° - 90°$, while other cases show significant reduction in $\overline{C}_{Ph}$ with increase of f^* at $\theta_0 = 60°$. In addition, $\overline{C}_{P\theta}$ of the four cases is negative except for $f^* < 0.15$ and decreases (i.e. more negative) almost linearly with increase of f^* at high flapping frequencies $f^* > 0.16$ where Case 1 and Case 4 show relatively larger decrease compared to the other cases. Even though $\overline{C}_{Ph}$ of Case 1 and Case 4 increases with f^* at $\theta_0 = 80°$ and $90°$, significant drop in $\overline{C}_{P\theta}$ due to the increase of pitch rate results in mean power output $\overline{C}_P$ reduction at high flapping frequencies. On the other hand, in the range of $f^* = 0.18 - 0.24$, Case 3 gives relatively high $\overline{C}_{Ph}$ at $\theta_0 = 60°$ and 70°, while it gives relatively low $\overline{C}_{P\theta}$ at $\theta_0 = 80°$ and 90°, producing relatively high $\overline{C}_P$ regardless of θ_0 as shown in Fig. 6.11. These results demonstrate that it is feasible to achieve good performance at different flapping frequencies by tuning the natural frequencies of the spring-tail system.

Table 6.2: Performance of a power generator with a spring-connected tail (Case 1-3) compared to that with a rigid tail (Case 4) at $f^* = 0.14$, $\theta_0 = 80°$, $h_0 = 1, \varphi = 90°, x_{piv} = 0.333$.

Case	f_0^*	μ	k_s	f_r^*	η	$\overline{C}_P$	d/c	$\sqrt{\overline{C_L^2}}$	$\overline{C}_{Ph}$	$\overline{C}_{P\theta}$	$\alpha_{Tmax}(°)$	$\alpha_{effmax}(°)$
1	1.36	0.60	0.393	1.180	37.6%	0.99	2.63	1.73	0.89	0.10	38.8	38.3
2	1.36	0.03	0.020	0.491	26.3%	0.64	2.44	1.03	0.60	0.04	88.8	32.6
3	0.15	0.60	0.005	0.130	27.6%	0.73	2.64	1.56	0.71	0.02	68.8	35.3
4	-	-	-	-	37.1%	0.96	2.59	1.64	0.86	0.10	0.00	38.7

Table 6.3: Performance of a power generator with a spring-connected tail (Case 1-3) compared to that with a rigid tail (Case 4) at $f^* = 0.20$, $\theta_0 = 80°$, $h_0 = 1, \varphi = 90°, x_{piv} = 0.333$.

Case	f_0^*	μ	k_s	f_r^*	η	$\overline{C}_P$	d/c	$\sqrt{\overline{C_L^2}}$	$\overline{C}_{Ph}$	$\overline{C}_{P\theta}$	$\alpha_{Tmax}(°)$	$\alpha_{effmax}(°)$
1	1.36	0.60	0.393	1.180	28.6%	0.77	2.70	1.40	1.08	-0.31	20.3	29.0
2	1.36	0.03	0.020	0.491	29.9%	0.74	2.46	1.07	0.84	-0.11	46.6	24.7
3	0.15	0.60	0.005	0.130	36.6%	0.92	2.51	1.69	1.17	-0.25	73.6	31.7
4	-	-	-	-	30.8%	0.80	2.59	1.45	1.06	-0.26	0.00	28.5

Table 6.4: Performance of a power generator with a spring-connected tail (Case 1-3) compared to that with a rigid tail (Case 4) at $f^* = 0.24$, $\theta_0 = 80°$, $h_0 = 1, \varphi = 90°, x_{piv} = 0.333$.

Case	f_0^*	μ	k_s	f_r^*	η	$\overline{C}_P$	d/c	$\sqrt{\overline{C_L^2}}$	$\overline{C}_{Ph}$	$\overline{C}_{P\theta}$	$\alpha_{Tmax}(°)$	$\alpha_{effmax}(°)$
1	1.36	0.60	0.393	1.180	21.4%	0.57	2.65	1.88	1.32	-0.75	13.3	25.1
2	1.36	0.03	0.020	0.491	28.1%	0.66	2.36	0.97	0.87	-0.22	48.9	20.6
3	0.15	0.60	0.005	0.130	33.6%	0.84	2.50	1.59	1.30	-0.46	82.6	28.9
4	-	-	-	-	15.5%	0.40	2.60	1.83	1.08	-0.69	0.00	23.6

To uncover the physics underpinning the performance of power extraction under non-optimal conditions of the rigid case, the four cases at the same $\theta_0 = 80°$ as that used in Section 6.1 but different $f^* = 0.14, 0.20, 0.24$ are further investigated (Table 6.2, 6.3 and 6.4). In Table 6.1-6.4, $\overline{C}_{Ph}$ of the four cases increases monotonically with the increase of f^* since the plunge velocity increases linearly with the increase of f^*. However, $\overline{C}_{P\theta}$ shows an opposite trend, indicating that more power is required for the pitch motion at high flapping frequencies. For all the four cases, $\overline{C}_{P\theta}$ is negligible at the low flapping frequency $f^* = 0.14$, while the absolute value of $\overline{C}_{P\theta}$ ranges from a minimum of 38% of $\overline{C}_P$ for Case 2 to a maximum of 174% of $\overline{C}_P$ for Case 4 at $f^* = 0.24$. In addition, the flapping frequencies where the highest η and C_P of the four cases are achieved are different from those where the highest $\overline{C}_{Ph}$ is observed. These observations illustrate that the contribution of the pitch motion to the performance becomes more important with the increase of f^*. As expected, Case 1 with the highest stiffness ($k_s = 0.393$) gives the smallest α_{Tmax} in Table 6.1-6.4. At the low flapping frequency ($f^* = 0.14$), Case 2 with the lowest density ratio ($\mu = 0.03$) gives the largest α_{Tmax}, while Case 3 gives the largest α_{Tmax} at higher flapping frequencies ($f^* = 0.16 - 0.24$). This can be explained as the ratio between the inertia force and the restoring force of Case 3 with large μ and small f_0^* is the highest and the inertia effect plays an important role in the passive deflection when the acceleration is large at high f^*.

To visualize the prescribed motion combined with the passive deflection of the the tail, the effective angle of attack (α_{eff}) defined as the angle between the relative inflow velocity and the secant connecting the leading edge of the foil and the end of the tail, as shown in Fig. 3.2, is introduced. When the tail is rigid (Case 4), the definition of α_{eff} is the same as Kinsey & Dumas (2008). For all the cases, the maximum of α_{eff} in Table 6.1 to 6.4 decreases with the increase of f_0^*. The time history of α_{eff} in Fig. 6.13 shows that the magnitude of α_{eff} for Case 1 (high stiffness) and Case 4 (rigid tail) before the stroke reversal decreases dramatically at high flapping flapping frequencies (e.g. at

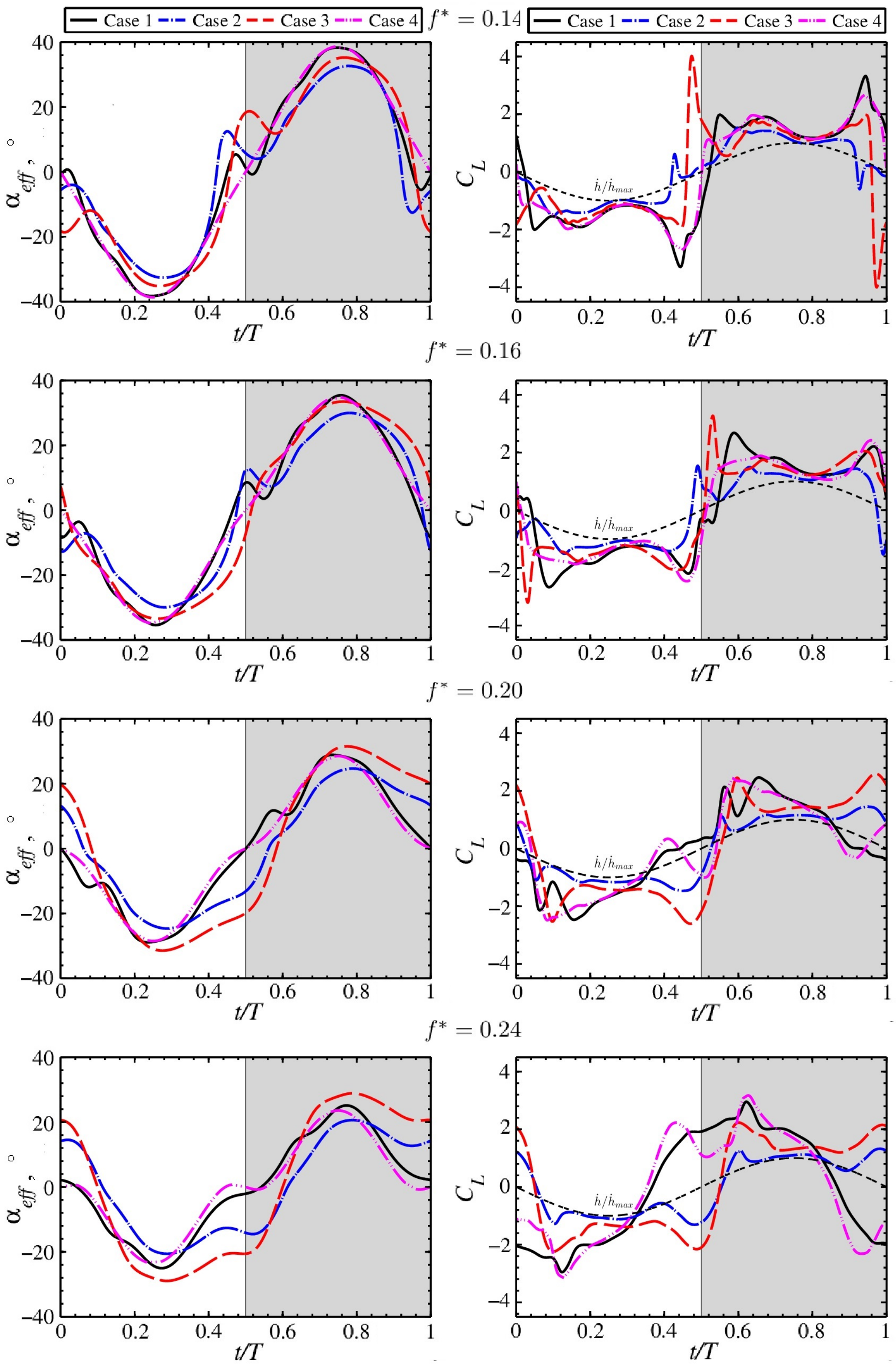

Fig. 6.13: Comparison of α_{eff} and C_L of a rigid foil with a spring-connected or a rigid tail at $f^* = 0.14 - 0.24$, $\theta_0 = 80°$, $h_0 = 1$, $\varphi = 90°$ and $x_{piv} = 0.333$.

$t/T = 0.4$, the magnitude of α_{eff} for Case 4 is respectively $19.7°, 16.4°, 10.6°$ and $5.47°$ at $f^* = 0.14$, 0.16, 0.20 and 0.24). In addition, before the stroke reversal ($t/T = 0.4-0.5$), C_L of Case 1 and Case 4 increases dramatically, even with the opposite sign to the plunge motion, at the high flapping frequencies ($f^* = 0.20, 0.24$) compared to that at the low flapping frequencies ($f^* = 0.14, 0.16$). On the other hand, at the low flapping frequency ($f^* = 0.14$), even though Case 3 shows the largest amplitude of C_L, the peak of C_L is in the opposite direction of the plunge velocity, resulting in a low C_{Ph} in Table 6.2. At the high flapping frequencies ($f^* = 0.20, 0.24$), Case 3 gives relatively high α_{eff} before the stroke reversal ($t/T = 0.4-0.5$) since the large deflection of the tail lags behind the pitch angle due to the inertia effects. At $t/T = 0.2 - 0.5$ during the downstroke and $t/T = 0.75 - 1$ during the upstroke, Case 3 gives reasonable C_L in the the same direction as the plunge motion, resulting in relatively high $\overline{C}_{Ph}$ among the four cases compared to that at the low flapping frequencies. Among the four cases, Case 2 gives the smallest magnitude of α_{eff}, resulting in the smallest magnitude of C_L as well as the lowest $\sqrt{\overline{C_L^2}}$ and C_{Ph} in Table 6.1-6.4.

To further investigate the negative contribution of the pitch motion to the performance which increases with the increase of f^* for all the cases, the time history of C_M and $C_{P\theta}$ is shown in Fig. 6.14. It is noted that for Case 1 and Case 4, C_M with the opposite sign to $\dot{\theta}$ after the mid of the up and down stroke ($t/T = 0.75 - 1$ and $0.25 - 0.5$, respectively) increases with the increase of f^*, resulting in the large amount of power required for the pitch motion at the high flapping frequencies. On the other hand, excluding the delayed peak of C_M at the high flapping frequencies of f^* in Case 3, the change in the magnitude of C_M of Case 2 and Case 3 after the mid of the stroke is insignificant. At $f^* = 0.20$ and 0.24, even though the magnitude of C_L in Case

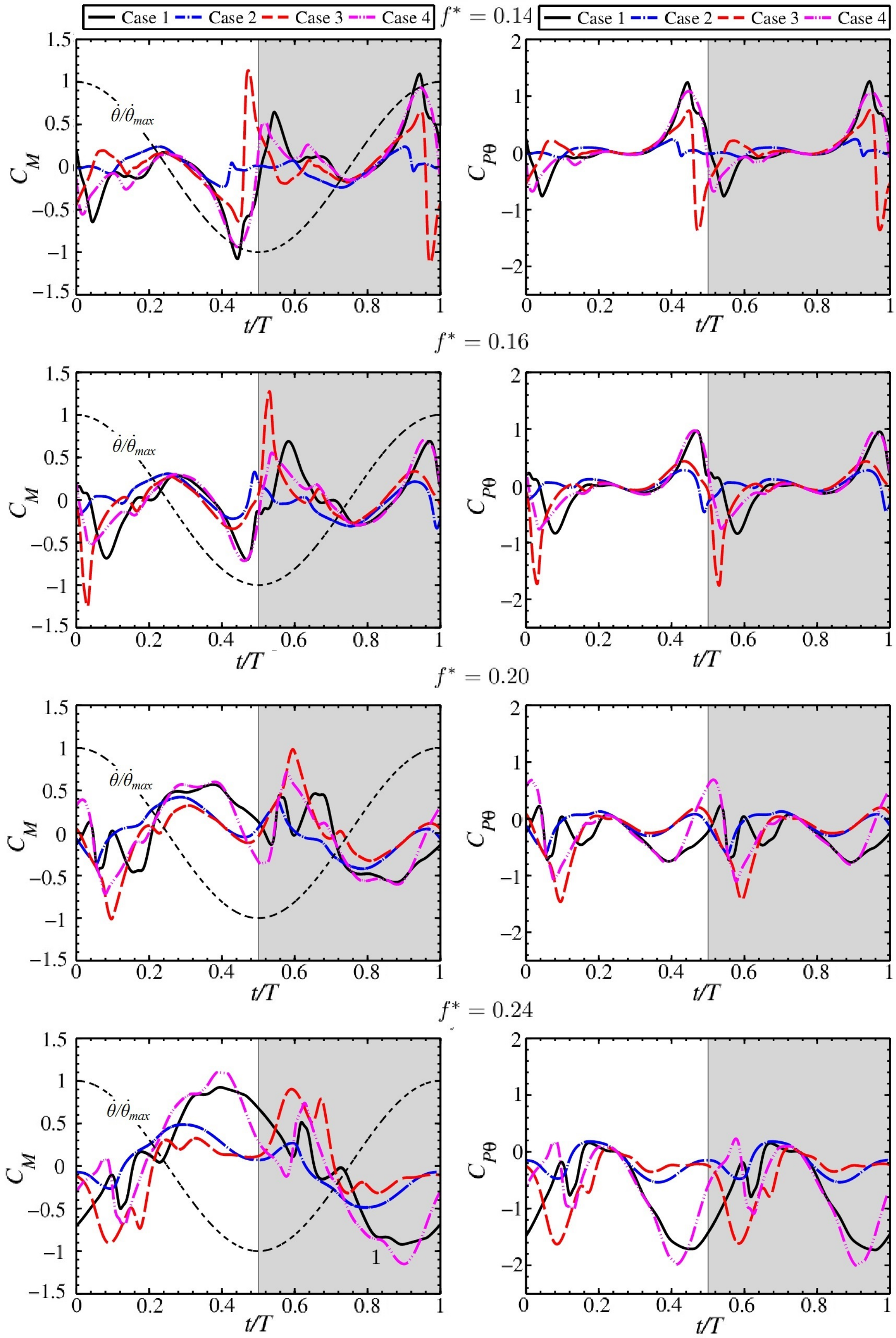

Fig. 6.14: Comparison of C_M and $C_{P\theta}$ of a rigid foil with a spring-connected or a rigid tail at $f^* = 0.14 - 0.24$, $\theta_0 = 80°$, $h_0 = 1$, $\varphi = 90°$ and $x_{piv} = 0.333$.

2 and Case 3 is large before the stroke reversal (Fig. 6.13), the magnitude of C_M approaches 0, which is different from that observed in Case 1 and Case 4 where the magnitudes of both C_L and C_M are large. Furthermore, due to the smaller magnitude of C_M after the mid of the stroke ($t/T = 0.75 - 1$ and $0.25 - 0.5$), Case 2 and Case 3 gives higher $C_{P\theta}$ as shown in the right column of Fig. 6.14, thus higher $\overline{C}_{P\theta}$ in Table 6.3 and 6.4.

The vorticity and pressure distribution of the four cases with $f^* = 0.14$, 0.16, 0.20 and 0.24 at $t/T = 0.9$ where C_L and C_M show major differences between low stiffness cases (Case 2 and Case 3) and high stiffness cases (Case 1 and Case 4) as shown in Fig. 6.15 and 6.16 respectively. The mapping of vorticity shows that at the same t/T, the size and propagation distance of the LEV decrease with the increase of f^*. According to the review on the dynamic stall (Choudhry et al. 2014), the critical angle of attack increases with the increase of the pitch rate. In addition, the angle of attack at the pivot location with the same sign as the plunge motion, which is the same as α_{eff} of Case 4 in Fig. 6.13, at the low f^* is greater than or equal to that at high f^*. Thus at the high f^*, the formation of LEV is delayed. This explains the decrease of the distance travelled by the LEV at the high flapping frequencies. Since the time period of one flapping cycle is related to f^*, the physical time at the same t/T increases with the decrease of f^*. This implies that at the low f^*, the LEV is fed by the vortex filament for a longer time, resulting in the larger LEV compared to that at the high f^*. At $t/T = 0.9$, the strength of the vortex filament shed into the wake at the high f^* is stronger than that at the low f^*. In Fig. 6.15d, it is noted that due to the sharp change in the curvature resulting from the deflection of the tail, the vortex filament in Case 2 and Case 3 detaches from the trailing edge of the foil instead of from the end of the plate in Case 1 and Case 4. The vortex filament in Case 2 and Case 3

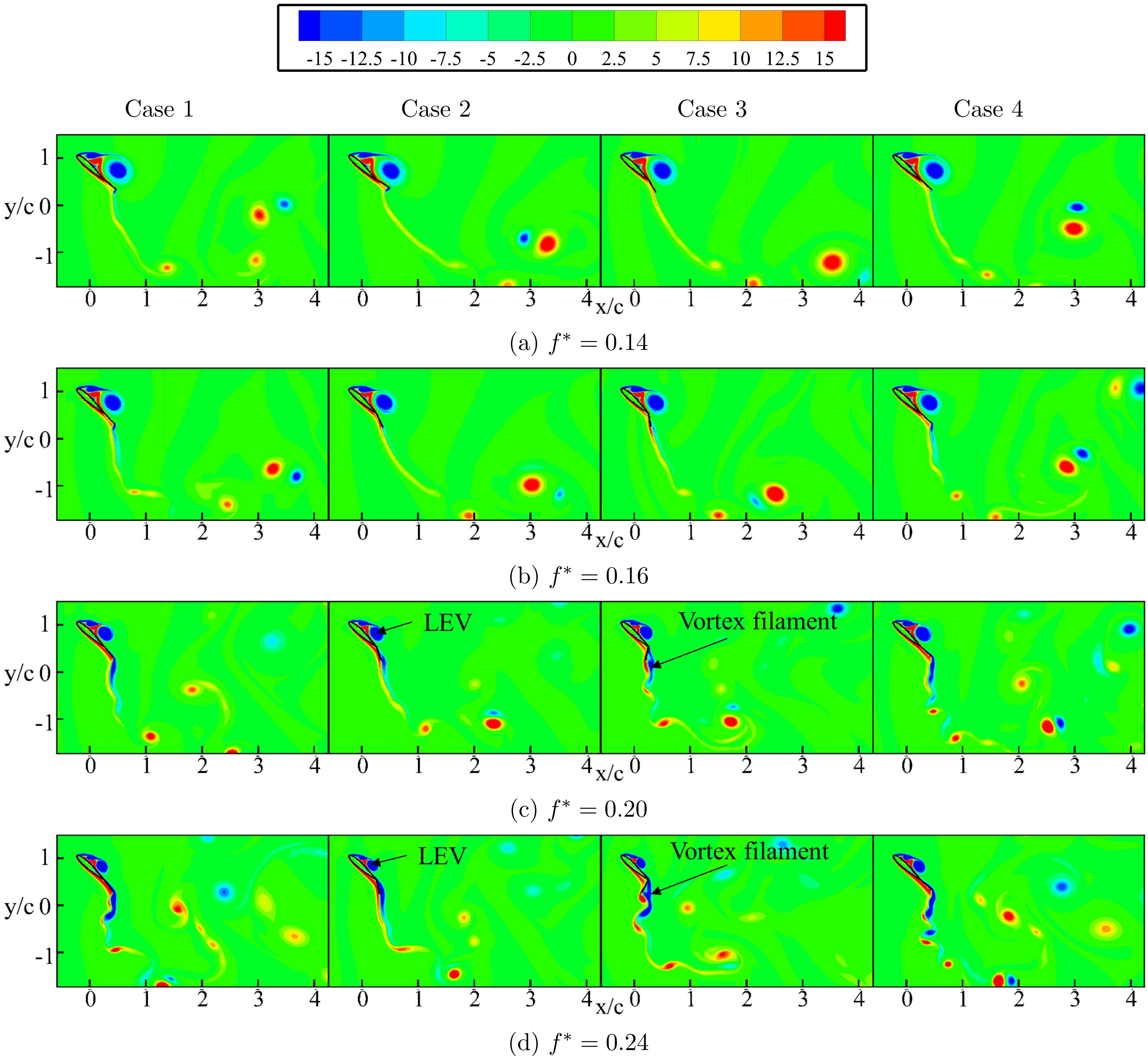

Fig. 6.15: Instantaneous non-dimensional vorticity contours of Case 1-4 at different f^* and $\theta_0 = 80°$, $h_0 = 1$, $\varphi = 90°$ and $x_{piv} = 0.333$ and $t/T = 0.9$.

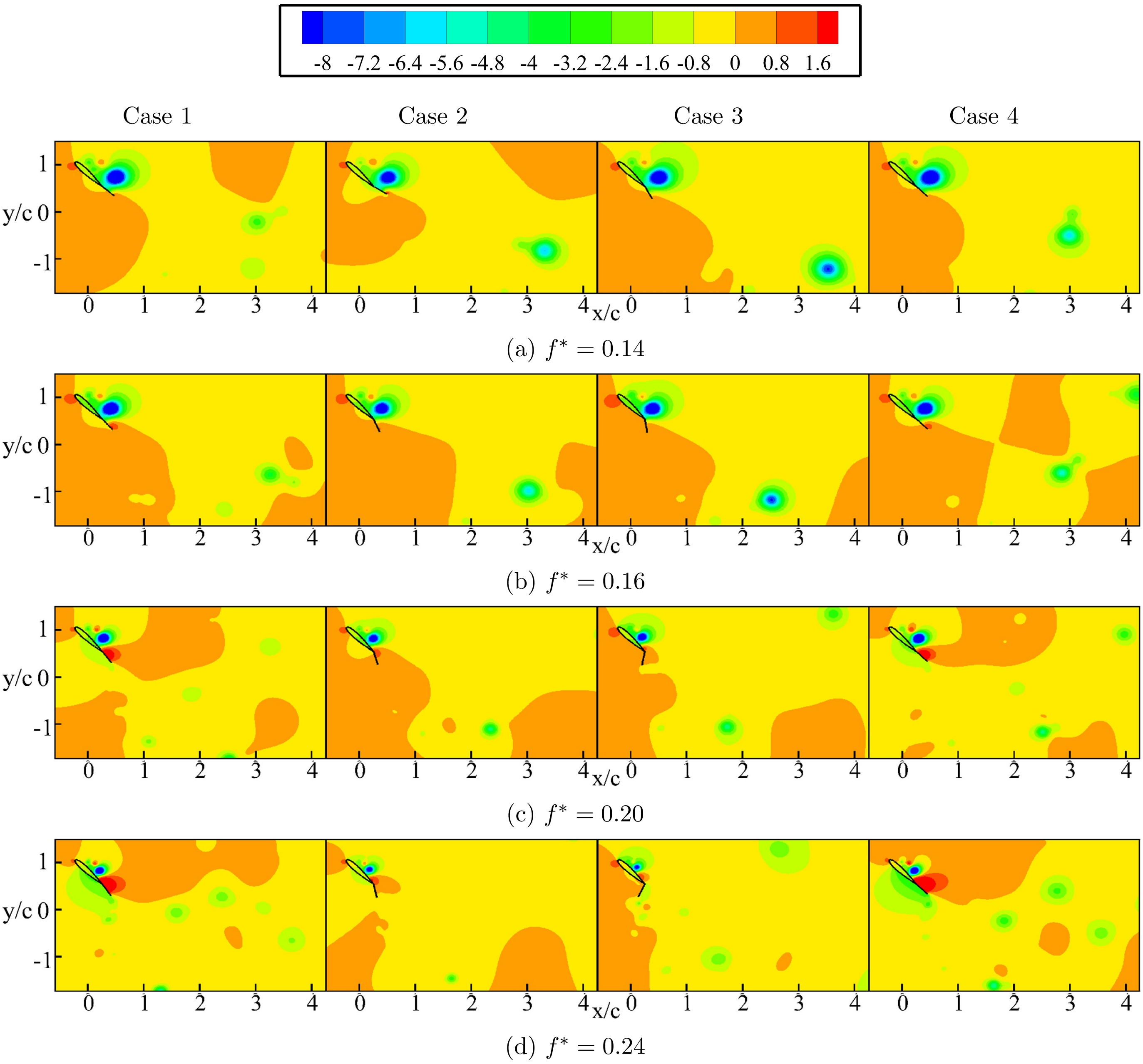

Fig. 6.16: Relative pressure coefficient contours of Case 1-4 at different f^* and $\theta_0 = 80^\circ$, $h_0 = 1$, $\varphi = 90^\circ$ and $x_{piv} = 0.333$ and $t/T = 0.9$.

suppresses the high pressure region on the upper surface of the tail, as shown in Fig. 6.16d. At the high f^*, the center of the low pressure region is near the pivot, causing the small magnitude of C_M (Fig. 6.14) of Case 2 and Case 3 before the stroke reversal where C_L is high (Fig. 6.13). In Case 1 and Case 4, the high pressure region acting on the tail has long moment-arm to the pivot point, resulting in the large magnitude of C_M in Fig. 6.14. In Case 3, the large deflection of the tail alleviates the rapid increase of power required for the pitch motion by eliminating the high pressure region on the suction surface of the tail when f^* is higher than the optimal value of the rigid system.

6.3 Summary

The influence of fluid-structure interactions on the performance of a flapping foil power generator has been numerically studied using the immersed boundary-lattice Boltzmann method (IB-LBM). The flexibility is achieved by using a flat plate pinned to the trailing edge of a rigid NACA0015 foil through a torsional spring. The deformation of the tail is passively determined by the hydrodynamic loading. As discussed in Section 2.3.2, performance improvement is achieved by several studies using active deformation. However, if the power consumption of the active deformation is taken into account, the improvement of the performance is limited. In addition, the simple torsional spring model employed in this chapter only introduces 2 new parameters (natural frequency and density ratio), while more parameters are required to model the complicated passive motion of the attached tail (Fig. 6.5b). Thus the simple torsional spring model is used in this chapter for parametric study.

The optimum kinematic condi6tions of a rigid foil and a rigid foil with a rigid tail are first identified by conducting simulations over a range of values for the flapping frequency f^* and pitch amplitude θ_0, with $h_0 = 1$, $\varphi = 90°$ and $x_{piv} = 0.333$. Peak efficiencies of 36.9% and 37.3% respectively for the rigid foil and the rigid foil with a rigid tail are found to occur at $f^* = 0.16$, $\theta_0 = 80°$. A parametric study on the structure-to-fluid density ratio (μ) and natural frequency (f_0^*) shows that the performance improvement is achieved in the range of stiffness $k_s = 0.316 - 1.00$. In addition, when $k_s > 10$, the spring-connected system tends to be a rigid system. It is noted that a spring-connected tail with appropriate mass density ($\mu = 0.6$) and natural frequency ($f_0^* = 1.36$) enhances the maximum efficiency of a flapping power generator by 7.24% compared to a rigid tail.

The time history of C_L under the rigid-system optimal condition shows that the improvement in performance is due to the increase in the magnitude of the hydrodynamic load and synchronization between the hydrodynamic load and the prescribed motion. Analysis on the tail deformation indicates that the major component of the passive motion relies on the resonant frequency (f_r^*). The movement of the tail influences vortex shedding, especially near stroke reversals. For the case with the highest efficiency ($f_r^* = 1.18$), the deflection of the tail reduces the low pressure region on the pressure surface after the stroke reversal, resulting in high pressure differences between the upper and lower surface of the foil. For the case with low flexibility ($f_r^* = 0.13$), the LEV prematurely circumnavigates the tail near the stroke reversal, leading to a sharp drop in the power coefficient. In the near wake, interactions between the leading edge and trailing edge vortex of case 1 which has the highest efficiency are stronger than those of the other cases.

Finally, these four cases are simulated under different kinematic condition-s. Compared to the rigid case, a tail with $\mu = 0.60$ and $f_0^* = 1.36$ shows performance improvement (up to 15.3%) over a range of operating conditions

($f^* = 0.12 - 0.18, \theta_0 = 60° - 90°$). A spring-connected tail with $\mu = 0.60$ and $f_0^* = 0.150$ achieves good efficiencies $\eta > 33.0\%$ (up to 137% improvement over that with a rigid tail at $f^* = 0.22, \theta_0 = 70°$) in the range of frequencies $f^* = 0.18 - 0.24$ with $\theta_0 = 70°$ and $80°$. Under high flapping frequencies, the deflection of the tail with the low stiffness increases the magnitude of the effective angle of attack and eliminates the high pressure region acting on the suction surface of the tail near the stroke reversal, reducing the power required for the pitch motion. The results indicate that a spring-connected tail with appropriate stiffness can improve the performance of a flapping foil power generator for a reasonable range of operating conditions. In addition, according to the definition of the reduced frequency ($f^* = fc/U$), a spring-connected tail of low stiffness can benefit from low inflow velocity, which potentially expands the exploitable energy resource base.

Chapter 7

Conclusions and Recommendations

7.1 Conclusions

In this study, a novel type of wind/tidal turbines harvesting energy from combined pitch and plunge motions was investigated numerically. In contrast to rotary turbines which rely on attached flow for high performance, power generators making use of flapping foil motions can benefit from the formation and convection of leading edge vortices (LEVs), promising relatively high energy harvesting performance in low speed flows. A review of the literature in Chapter 2 introduced the fundamental concept of the flapping foil power generator and recent advances in this innovative concept of wind turbines, covering parameters governing the kinematics of the system, geometries and deformation of the foil and the system and environmental effects.

The kinematics of the foil are governed by different parameters depending on the activation mechanism of the flapping foil system. By tuning the structure parameters (e.g. damping and stiffness) in the semi-passive system and fully passive system with one degree of freedom, high performance can be achieved under the optimal conditions similar to those found in the fully-prescribed system. Thus, the fully prescribed system is commonly considered in studies on the flapping foil power generator, especially those focusing on the influence of factors other than kinematics (e.g. geometry and environment) and the physical mechanisms for high performance.

Parametric studies on the fully prescribed system generally are focused on two variables with others fixed because of the complex influence of the kinematic parameters on the performance and the high computational cost of CFD methods (such as the Navier-Stokes solver or IB-LBM). These studies suggest operating conditions for high performance in the range of non-dimensional frequency $f^* = 0.11 - 0.18$, pitch amplitude $\theta_0 = 60° - 100°$, plunge amplitude $h_0 = 0.8 - 1.5$, phase difference between the pitch and plunge motions $\varphi = 90° - 110°$ and non-dimensional pivot point location $x_{piv} = 0.25 - 0.5$. In addition, large flow separations are observed near the optimal condition in many studies, of which simulations are beyond the capability of potential flow based methods. Studies using methods based on the potential flow theory generally constrain the maximum angle of attack to avoid the occurrence of large flow separations.

Besides the kinematics, the geometry of the foil, the configuration of the system and the operating environment also affect the performance of the flapping foil power generator. According to results of propulsive system using flapping foils, it is attractive to exploit the deformation of the foil to improve the performance of the flapping foil power generator when a single foil system in the unconstrained flow is considered. Several studies show that active deformation of the foil influences the formation of LEVs and appropriate phase angle between the plunge motion and the deformation can improve power output under optimal and non-optimal conditions of the rigid system. However, the power required to deform the foil is significant but generally neglected in the performance analysis. In addition, recent studies show that the passive deformation can enhance the performance of the flapping foil power generator under the on-optimal conditions of the rigid system, while the improvement in the maximum efficiency is negligible.

This study was, therefore, aimed at achieving high performance of the flapping foil power generator through appropriate combination of kinematic parameters and coupling between the foil deformation and the aerodynamic loads. To achieve this goal, discrete vortex method was modified in Chapter 4 to capture the influence of flow separations for rapid performance estimations; kinematic parameters were optimized using multi-fidelity evolutionary algorithm in Chapter 5; and the influence of the passive motion of a spring connected tail on the performance was examined in Chapter 6.

To remove the impediment for optimization due to the high computational cost of CFD methods, the discrete vortex method based on potential flow theory was developed in Chapter 4. The results given by the modified discrete vortex method showed good agreement with the CFD simulations and the experiment data for both optimal and non-optimal conditions with respect to kinematic parameters and pivot point locations. The influence of the leading edge vortex and trailing edge flow separation was successfully predicted by introducing the leading edge suction parameter and trailing edge flow separation corrections into the potential flow based method. Moreover, the modified discrete vortex method performed well under different kinematic conditions with or without large flow separations, as demonstrated in Chapter 4 and Chapter 5, since the empirical constants in this model were only dependent on the Reynolds number and foil geometry. In addition, it took much less computational time (at least two order of magnitudes) than CFD methods. Thus, the modified discrete vortex method is an attractive tool for engineering design and optimization of the flapping foil with large flow separations.

In Chapter 5, the multi-fidelity evolutionary algorithm implemented with the low order models reproduced in Chapter 3 and developed in Chapter 4 was used to search for values of kinematic parameters that produced high energy extraction performance. The results indicated that the use of multi-fidelity strategy achieves a computational saving of 28.6%. Despite the use of low fidelity models and limited budget of computational resources, the multi-fidelity strategy was capable of finding kinematic conditions suitable for high energy extraction performance from a flapping foil. In addition, detailed flow analysis using immersed boundary-lattice Boltzmann method revealed that high energy extraction performance was associated with the detachment of the LEV near stroke reversal, resulting in a horseshoe-shaped vorticity wake with a width approximating the swept distance of the foil behind the turbine plane. When the LEV detached from the foil near mid stroke, both efficiency and power output suffered.

Investigation in Chapter 6 on the aero-elastic system containing a rigid foil and a spring connected tail showed that under the rigid-system optimal kinematic condition, a tail with appropriate mass density ($\mu = 0.6$) and resonant frequency ($f_r^* = 1.18$) could improve the maximum efficiency by 7.24% accompanied by an increase of 6.63% in power compared to those of a rigid foil with a rigid tail. This was because the deflection of the tail reduced the low pressure region on the pressure surface (i.e. the lower surface during the upstroke or the upper surface during the downstroke) caused by the leading edge vortex after the stroke reversal, resulting in a higher efficiency. In the rigid system, the power required to pitch the foil increased significantly with the increase of the flapping frequency, resulting in low efficiency. At high flapping frequencies, a spring-connected tail ($f_r^* = 0.13$) eliminated the large spike in the pitching moment observed in high stiffness cases, reducing the power required for the pitch motion, resulting in 117% improvement in efficiency over that with a rigid tail at a reduced frequency of 0.24.

7.2 Recommendations for future work

In this thesis study, the influence of the kinematics and passive deformation on the performance of the flapping foil power generator in two-dimensional uniform flow was investigated. Some extended studies would be worthwhile to be conducted in the future to further the understanding of the performance of flapping foil power generators.

First of all, the influence of the foil deformation is not considered in the discrete vortex method (DVM) modified in Chapter 4. According to the DVM, the local velocity normal to the foil corresponding to the change of the chord line curvature is easy to implement, while it remains a challenge to predict the foil deformation in response to the aerodynamic loads. Further modification of the DVM considering fluid-structure interactions is worthwhile for studies on foil deformation in both energy harvesting and propulsive systems using flapping foils. In addition, the DVM assumes that the aspect ratio of the wing is infinite, neglecting three-dimensional effects. The idea of introducing the leading edge suction parameter and trailing edge flow separation corrections considered in this study can be employed in the unsteady penal method developed for three-dimensional potential flow to include the effects of flow separations.

In Chapter 5, the highest fidelity model used in the optimization process is the modified DVM. Even though the modified DVM shows reasonable agreement with the CFD methods and experiment, employing higher fidelity results (e.g. CFD and experiment) in the optimization process may achieve better performance since they contain more information (e.g. the flow field) which might be neglected in low order models. In addition, besides parameters governing the kinematics of the fully prescribed system, geometry and deformation of the foil, configuration of multiple foils and parameters in the semi-passive and fully passive system remain to be optimized for higher performance.

According to the studies using Reynolds averaged Navier Stokes methods reviewed in Chapter 3, the formation of the leading edge vortex is not necessary for high performance when turbulence is considered. Thus, more work should be conducted in the turbulent flow region. In addition, since several turbulence models give different timing and position of flow separations, large eddy simulations or direct numerical simulations of the flapping foil power generator remain to be accomplished.

Reference

Abiru, H. & Yoshitake, A. (2011*a*), Experimental study on a cascade flapping wing hydroelectric power generator, *in* 'ASME Power Conference', Denver, USA, July 12–14, 2011, pp. 537–543.

Abiru, H. & Yoshitake, A. (2011*b*), 'Study on a flapping wing hydroelectric power generation system', *Journal of Environment and Engineering* **6**(1), 178–186.

Ackermann, T. & Söder, L. (2000), 'Wind energy technology and current status: a review', *Renewable and Sustainable Energy Reviews* **4**(4), 315–374.

Akpinar, E. K. & Akpinar, S. (2005), 'An assessment on seasonal analysis of wind energy characteristics and wind turbine characteristics', *Energy Conversion and Management* **46**(11), 1848–1867.

Andersen, A., Pesavento, U. & Wang, Z. J. (2005), 'Unsteady aerodynamics of fluttering and tumbling plates', *Journal of Fluid Mechanics* **541**, 65–90.

Andersson, J. (2001), Multiobjective optimization in engineering design: applications to fluid power systems, PhD thesis, Linköpings universitet.

Antonini, E. G., Bedon, G., De Betta, S., Michelini, L., Raciti Castelli, M. & Benini, E. (2014), 'Innovative discrete-vortex model for dynamic stall simulations', *AIAA Journal* **53**(2), 479–485.

Archer, C. L. & Jacobson, M. Z. (2005), 'Evaluation of global wind power', *Journal of Geophysical Research: Atmospheres* **110**(D12).

Ashraf, M., Young, J., , Lai, J. C. S. & Platzer, M. (2011), 'Numerical analysis of an oscillating-wing wind and hydropower generator', *AIAA Journal* **49**(7), 1374–1386.

Barad, M. F., Kocheemoolayil, J. G. & Kiris, C. C. (2017), Lattice boltzmann and navier-stokes cartesian cfd approaches for airframe noise predictions, *in* 'AIAA Computational Fluid Dynamics Conference', Denver, USA, June 5–9, 2017, pp. 4404 (1–16).

Bauchau, O. A. (2007), *DYMORE users manual*, Georgia Institute of Technology, Atlanta.

Beal, D., Hover, F., Triantafyllou, M., Liao, J. & Lauder, G. (2006), 'Passive propulsion in vortex wakes', *Journal of Fluid Mechanics* **549**, 385–402.

Betz, A. (1919), 'Schraubenpropeller mit geringstem energieverlust. mit einem zusatz von l. prandtl', *Nachrichten von der Gesellschaft der Wissenschaften zu Göttingen, Mathematisch-Physikalische Klasse* **1919**, 193–217.

Bösch, F. & Karlin, I. (2013), 'Exact lattice Boltzmann equation', *Physical Review Letters* **111**(9), 090601.

Box, M. (1965), 'A new method of constrained optimization and a comparison with other methods', *The Computer Journal* **8**(1), 42–52.

Branke, J., Asafuddoula, M., Bhattacharjee, K. S. & Ray, T. (2017), 'Efficient use of partially converged simulations in evolutionary optimization', *IEEE Transactions on Evolutionary Computation* **21**(1), 52–64.

Brennen, C. (1982), A review of added mass and fluid inertial forces, Technical Report ADA110190, Defense Technical Information Center.

Bryant, M., Gomez, J. C. & Garcia, E. (2013), 'Reduced-order aerodynamic modeling of flapping wing energy harvesting at low Reynolds number', *AIAA Journal* **51**(12), 2771–2782.

Campobasso, M. S., Piskopakis, A., Drofelnik, J. & Jackson, A. (2013), 'Turbulent navierstokes analysis of an oscillating wing in a power-extraction regime using the shear stress transport turbulence model', *Computers & Fluids* **88**, 136 – 155.
URL: *http://www.sciencedirect.com/science/article/pii/S0045793013003332*

Chen, J.-S., Chen, J.-Y. & Chou, Y.-F. (2008), 'On the natural frequencies and mode shapes of dragonfly wings', *Journal of Sound and Vibration* **313**(3), 643–654.

Chen, Y., Zhan, J., Wu, J. & Wu, J. (2017), 'A fully-activated flapping foil in wind gust: Energy harvesting performance investigation', *Ocean Engineering* **138**, 112 – 122.
URL: *http://www.sciencedirect.com/science/article/pii/S0029801817302159*

Choudhry, A., Leknys, R., Arjomandi, M. & Kelso, R. (2014), 'An insight into the dynamic stall lift characteristics', *Experimental Thermal and Fluid Science* **58**, 188–208.

Coello, C. C. (2006), 'Evolutionary multi-objective optimization: a historical view of the field', *Computational Intelligence Magazine* **1**(1), 28–36.

Daniele, E. (2013), Numerical and experimental investigation of low Reynolds number wind turbine airfoils under stall and post-stall conditions, PhD thesis, Ingegneria Industriale.

Davids, S. T. (1999), A computational and experimental investigation of a flutter generator, Master's thesis, Monterey, California: Naval Postgraduate School.

Deb, K., Pratap, A., Agarwal, S. & Meyarivan, T. (2002), 'A fast and elitist multiobjective genetic algorithm: NSGA-II', *IEEE Rransactions on Evolutionary Computation* **6**(2), 182–197.

Deng, J., Caulfield, C. & Shao, X. (2014), 'Effect of aspect ratio on the energy extraction efficiency of three-dimensional flapping foils', *Physics of Fluids* **26**(4), 043102.

Deng, J., Teng, L., Pan, D. & Shao, X. (2015), 'Inertial effects of the semi-passive flapping foil on its energy extraction efficiency', *Physics of Fluids* **27**(5), 053103.

Drofelnik, J. & Campobasso, M. S. (2016), 'Comparative turbulent three-dimensional navierstokes hydrodynamic analysis and performance assessment of oscillating wings for renewable energy applications', *International Journal of Marine Energy* **16**, 100 – 115.

URL: *http://www.sciencedirect.com/science/article/pii/S2214166916300431*

Drofelnik, J. & Campobasso, S. (2015), Three-dimensional navier-stokes turbulent hydrodynamic analysis and performance assessment of oscillating wings for power generation, *in* 'International Conference on Fluid Flow Technologies', Budapest, Hungary, September 1–4, 2015, pp. 1–8.

Dyachuk, E., Goude, A. & Bernhoff, H. (2013), 'Dynamic stall modeling for the conditions of vertical axis wind turbines', *AIAA Journal* **52**(1), 72–81.

El-Shahat, A. (2016), 'Bladeless wind turbine as wind energy possible future technology', *Natural Gas & Electricity* **33**(4), 16–20.

Eldredge, J. D., Toomey, J. & Medina, A. (2010), 'On the roles of chord-wise flexibility in a flapping wing with hovering kinematics', *Journal of Fluid Mechanics* **659**, 94–115.

Fan, Y. & Lutze, F. H. (1996), 'Identification of an unsteady aerodynamic model at high angles of attack', *AIAA Paper* pp. 96–3407.

Fenercioglu, I., Zaloglu, B., Young, J., Ashraf, M., Lai, J. C. S. & Platzer, M. (2015), 'Flow structures around an oscillating-wing power generator', *AIAA Journal* .

Fogel, D. B. (1997), The advantages of evolutionary computation, *in* 'Bio-computing and Emergent Computation: Proceedings of BCEC97', Citeseer, Skvde, Sweden, pp. 1–11.

Garrick, I. (1937), Propulsion of a flapping and oscillating airfoil, Technical Report NACA-TR-567, National Advisory Committee for Aeronautics: Langley Aeronautical Lab, Langley Field, VA, United States. Accession Number: 93R20932 Document ID: 19930091642.

Gauthier, E., Kinsey, T. & Dumas, G. (2016), 'Impact of blockage on the hydrodynamic performance of oscillating-foils hydrokinetic turbines', *Journal of Fluids Engineering* **138**(9), 091103.

Giorgio, C., Andrew, H. & Ivan, P. (2015), Wind energy scenarios for 2030, Technical report, European Wind Energy Association.

Goman, M. & Khrabrov, A. (1994), 'State-space representation of aerodynamic characteristics of an aircraft at high angles of attack', *Journal of Aircraft* **31**(5), 1109–1115.

Guo, Z., Zheng, C. & Shi, B. (2002), 'An extrapolation method for boundary conditions in lattice Boltzmann method', *Physics of Fluids* **14**(6), 2007–2010.

Gursul, I., Cleaver, D. & Wang, Z. (2014), 'Control of low Reynolds number flows by means of fluid–structure interactions', *Progress in Aerospace Sciences* **64**, 17–55.

GWEC (2014), Global wind energy outlook, Technical report, Global Wind Energy Council.

Hammer, P., Altman, A. & Eastep, F. (2014), 'Validation of a discrete vortex method for low Reynolds number unsteady flows', *AIAA Journal* **52**(3), 643–649.

Hoke, C. M., Young, J. & Lai, J. C. S. (2015), 'Effects of time-varying camber deformation on flapping foil propulsion and power extraction', *Journal of Fluids and Structures* **56**, 152 – 176.
URL: *http://www.sciencedirect.com/science/article/pii/S0889974615001176*

Hughes, E. (2001), Evolutionary multi-objective ranking with uncertainty and noise, *in* 'Evolutionary Multi-Criterion Optimization', Springer, pp. 329–343.

Huxham, G., Cochard, S. & Patterson, J. (2012), Experimental parametric investigation of an oscillating hydrofoil tidal stream energy converter, *in*

'Australasian Fluid Mechanics Conference', Launceston, Australia, December 3–7, 2012, pp. 1–4.

IEA (2016), CO_2 emissions from fuel combustion, Technical report, International Energy Agency.

Jacobs, E. N. & Sherman, A. (1937), Airfoil section characteristics as affected by variations of the Reynolds number, Technical Report NACA-TR-586, National Advisory Committee for Aeronautics: Langley Aeronautical Lab., Langley Field, VA, United States.

Jacobson, M. Z. (2009), 'Review of solutions to global warming, air pollution, and energy security', *Energy & Environmental Science* **2**(2), 148–173.

Jami, M., Mezrhab, A., Bouzidi, M. & Lallemand, P. (2007), 'Lattice Boltzmann method applied to the laminar natural convection in an enclosure with a heat-generating cylinder conducting body', *International Journal of Thermal Sciences* **46**(1), 38 – 47.
URL: *http://www.sciencedirect.com/science/article/pii/S1290072906000937*

Jeanmonod, G. & Olivier, M. (2017), 'Effects of chordwise flexibility on 2d flapping foils used as an energy extraction device', *Journal of Fluids and Structures* **70**, 327 – 345.
URL: *http://www.sciencedirect.com/science/article/pii/S0889974616303991*

Jiang, W., Zhang, D. & Xie, Y. (2016), 'Numerical investigation into the effects of arm motion and camber on a self-induced oscillating hydrofoil', *Energy* **115**, 1010 – 1021.
URL: *http://www.sciencedirect.com/science/article/pii/S0360544216312968*

Jiang, W., Zhang, D. & Xie, Y. (2017), 'Numerical investigation into energy

extraction from self-induced oscillations of an elliptical plate', *Journal of Fluids and Structures* **69**, 1 – 15.
URL: *http://www.sciencedirect.com/science/article/pii/S0889974616301591*

Jones, K. D., Davids, S. & Platzer, M. F. (1999), Oscillating-wing power generator, *in* 'ASME/JSME Joint Fluids Engineering Conference', San Francisco, USA, July 18–23, 1999, pp. 1–6.

Jones, K. D., Lindsey, K. & Platzer, M. (2003), 'An investigation of the fluid-structure interaction in an oscillating-wing micro-hydropower generator', *Fluid Structure Interaction II* .

Jones, K. & Platzer, M. (1997), 'Numerical computation of flapping-wing propulsion and power extraction', *AIAA Paper* **97**, 826.

Jumper, E., Dimmick, R. & Allaire, A. (1989), 'The effect of pitch location on dynamic stall', *ASME Transactions, Journal of Fluids Engineering* **111**, 256–262.

Karakas, F., Zaloglu, B., Fenercioglu, I., Hoke, C., Young, J., Lai, J. C. S. & Platzer, M. F. (2016), On optimal oscillating-foil power generation in free and constrained flow, *in* 'AIAA Aerospace Sciences Meeting', San Diego, USA, January 4–8, 2016, pp. 2070 (1–13).

Katz, J. (1981), 'A discrete vortex method for the non-steady separated flow over an airfoil', *Journal of Fluid Mechanics* **102**, 315–328.

Katz, J. & Plotkin, A. (2001), *Low-speed aerodynamics*, Vol. 13, Cambridge University Press.

Kim, D., Strom, B., Mandre, S. & Breuer, K. (2017), 'Energy harvesting performance and flow structure of an oscillating hydrofoil with finite span',

Journal of Fluids and Structures **70**, 314 – 326.
URL: *http://www.sciencedirect.com/science/article/pii/S0889974616305114*

Kinsey, T. & Dumas, G. (2008), 'Parametric study of an oscillating airfoil in a power-extraction regime', *AIAA Journal* **46**(6), 1318–1330.

Kinsey, T. & Dumas, G. (2012*a*), 'Computational fluid dynamics analysis of a hydrokinetic turbine based on oscillating hydrofoils', *Journal of Fluids Engineering* **134**(2), 021104.

Kinsey, T. & Dumas, G. (2012*b*), 'Optimal tandem configuration for oscillating-foils hydrokinetic turbine', *Journal of Fluids Engineering* **134**(3), 031103.

Kinsey, T. & Dumas, G. (2012*c*), 'Three-dimensional effects on an oscillating-foil hydrokinetic turbine', *Journal of Fluids Engineering* **134**(7), 071105.

Kinsey, T. & Dumas, G. (2014), 'Optimal operating parameters for an oscillating foil turbine at Reynolds number 500,000', *AIAA Journal* **52**(9), 1885–1895.

Kinsey, T., Dumas, G., Lalande, G., Ruel, J., Mehut, A., Viarouge, P., Lemay, J. & Jean, Y. (2011), 'Prototype testing of a hydrokinetic turbine based on oscillating hydrofoils', *Renewable Energy* **36**(6), 1710–1718.

Kloos, G., Gonzalez, C. & Finnigan, T. (2009), The biostream tidal current energy converter, *in* 'European Wave and Tidal Conference', Uppsala, Sweden, September 7–10, 2009, pp. 426–433.

Krus, P. & Andersson, J. (2003), Optimizing optimization for design optimization, *in* 'International Design Engineering Technical Conferences and Computers and Information in Engineering Conference', Chicago, USA, September 2-6, 2003, pp. 951–960.

Lallemand, P. & Luo, L.-S. (2000), 'Theory of the lattice Boltzmann method: Dispersion, dissipation, isotropy, galilean invariance, and stability', *Physical Review E* **61**(6), 6546.

Le, T. Q., Ko, J. H. & Byun, D. (2013), 'Morphological effect of a scallop shell on a flapping-type tidal stream generator', *Bioinspiration & Biomimetics* **8**(3), 036009.

Lee, T. & Gerontakos, P. (2004), 'Investigation of flow over an oscillating airfoil', *Journal of Fluid Mechanics* **512**, 313–341.

Leifsson, L. & Koziel, S. (2015), 'Aerodynamic shape optimization by variable-fidelity computational fluid dynamics models: A review of recent progress', *Journal of Computational Science* **10**, 45–54.

Leishman, J. & Beddoes, T. (1989), 'A semi-empirical model for dynamic stall', *Journal of the American Helicopter society* **34**(3), 3–17.

Lentink, D. & Dickinson, M. H. (2009), 'Biofluiddynamic scaling of flapping, spinning and translating fins and wings', *Journal of Experimental Biology* **212**(16), 2691–2704.

Lewis, M., Neill, S., Robins, P. & Hashemi, M. (2015), 'Resource assessment for future generations of tidal-stream energy arrays', *Energy* **83**, 403–415.

Lindsey, K. (2002), A feasibility study of oscillating-wing power generators, Technical report, DTIC Document.

Liu, N., Peng, Y., Liang, Y. & Lu, X. (2012), 'Flow over a traveling wavy foil with a passively flapping flat plate', *Physical Review E* **85**(5), 056316.

Liu, W. (2017), 'A case study on tandem configured oscillating foils in shallow water', *Ocean Engineering* **144**, 351 – 361.
URL: *http://www.sciencedirect.com/science/article/pii/S0029801817305784*

Liu, W., Xiao, Q. & Cheng, F. (2013), 'A bio-inspired study on tidal energy extraction with flexible flapping wings', *Bioinspiration & Biomimetics* **8**(3), 036011.

Liu, Z., Lai, J. C. S., Young, J. & Tian, F.-B. (2016), 'Discrete vortex method with flow separation corrections for flapping-foil power generators', *AIAA Journal* pp. 1–9.

Loshchilov, I. G. (2013), Surrogate-assisted evolutionary algorithms, PhD thesis, Citeseer.

Lu, K., Xie, Y. & Zhang, D. (2014), 'Nonsinusoidal motion effects on energy extraction performance of a flapping foil', *Renewable Energy* **64**, 283 – 293.
URL: *http://www.sciencedirect.com/science/article/pii/S0960148113006319*

Lu, K., Xie, Y., Zhang, D. & Xie, G. (2015), 'Systematic investigation of the flow evolution and energy extraction performance of a flapping-airfoil power generator', *Energy* **89**, 138 – 147.
URL: *http://www.sciencedirect.com/science/article/pii/S0360544215009482*

Make, M. & Vaz, G. (2015), 'Analyzing scaling effects on offshore wind turbines using cfd', *Renewable Energy* **83**, 1326–1340.

Maldonado, V., Farnsworth, J., Gressick, W. & Amitay, M. (2010), 'Active control of flow separation and structural vibrations of wind turbine blades', *Wind Energy* **13**(2-3), 221–237.

Marsh, G. (2009), 'Wave and tidal poweran emerging new market for composites', *Reinforced Plastics* **53**(5), 20–24.

Masters, G. M. (2013), *Renewable and Efficient Electric Power Systems*, John Wiley & Sons.

McAlister, K. W., Lambert, O. & Petot, D. (1984), Application of the onera model of dynamic stall, Technical report, DTIC Document.

McCroskey, W. (1981), The phenomenon of dynamic stall, Technical report, DTIC Document.

McCroskey, W. J., McAlister, K., Carr, L., Pucci, S., Lambert, O. & Indergrand, R. (1981), 'Dynamic stall on advanced airfoil sections', *Journal of the American Helicopter Society* **26**(3), 40–50.

McKinney, W. & DeLaurier, J. (1981), 'Wingmill: an oscillating-wing windmill', *Journal of Energy* **5**(2), 109–115.

Mohamad, A. A. (2011), *Lattice Boltzmann method: fundamentals and engineering applications with computer codes*, Springer Science & Business Media.

Ong, Y. S., Nair, P. B. & Keane, A. J. (2003), 'Evolutionary optimization of computationally expensive problems via surrogate modeling', *AIAA Journal* **41**(4), 687–696.

Pan, Y., Dong, X., Zhu, Q. & Yue, D. K. (2012), 'Boundary-element method for the prediction of performance of flapping foils with leading-edge separation', *Journal of Fluid Mechanics* **698**, 446–467.

Panwar, N., Kaushik, S. & Kothari, S. (2011), 'Role of renewable energy sources in environmental protection: a review', *Renewable and Sustainable Energy Reviews* **15**(3), 1513–1524.

Pelc, R. & Fujita, R. M. (2002), 'Renewable energy from the ocean', *Marine Policy* **26**(6), 471–479.

Peng, Y. & Luo, L.-S. (2008), 'A comparative study of immersed-boundary and interpolated bounce-back methods in lbe', *Progress in Computational Fluid Dynamics, an International Journal* **8**(1-4), 156–167.

Peng, Z. & Zhu, Q. (2009), 'Energy harvesting through flow-induced oscillations of a foil', *Physics of Fluids* **21**(12), 123602.

Platzer, M. F., Jones, K. D., Young, J. & Lai, J. C. S. (2008), 'Flapping-wing aerodynamics: progress and challenges', *AIAA Journal* **46**(9), 2136.

Pryor, S. & Barthelmie, R. (2010), 'Climate change impacts on wind energy: A review', *Renewable and Sustainable Energy Reviews* **14**(1), 430–437.

Ragheb, M. & Ragheb, A. M. (2011), Wind turbines theory-the betz equation and optimal rotor tip speed ratio, *in* 'Fundamental and Advanced Topics in Wind Power', InTech.

Ramesh, K., Gopalarathnam, A., Granlund, K., Ol, M. V. & Edwards, J. R. (2014), 'Discrete-vortex method with novel shedding criterion for unsteady aerofoil flows with intermittent leading-edge vortex shedding', *Journal of Fluid Mechanics* **751**, 500–538.

REN21 (2017), Renewables 2017 global status report, Technical Report ISBN 978-3-9818107-6-9, Renewable Energy Policy Network for the 21st Century.

Rostami, A. B. & Armandei, M. (2017), 'Renewable energy harvesting by vortex-induced motions: review and benchmarking of technologies', *Renewable and Sustainable Energy Reviews* **70**, 193–214.

Rourke, F. O., Boyle, F. & Reynolds, A. (2010), 'Tidal energy update 2009', *Applied Energy* **87**(2), 398–409.

Sane, S. P. & Dickinson, M. H. (2002), 'The aerodynamic effects of wing rotation and a revised quasi-steady model of flapping flight', *Journal of Experimental Biology* **205**(8), 1087–1096.

Schubel, P. J. & Crossley, R. J. (2012), 'Wind turbine blade design', *Energies* **5**(9), 3425–3449.

Send, W. (2016), Stroke-wing engine with dual wings for extracting power from an airstream, *in* 'New Results in Numerical and Experimental Fluid Mechanics X', Springer, pp. 883–894.

Shimizu, E. (2004), Multi-objective design study of a flapping wing generator, *in* 'International Congress of the Aeronautical Sciences', Yokohama, Japan, August 29 – September 3, 2004, pp. 1–8.

Shimizu, E., Isogai, K. & Obayashi, S. (2008), 'Multiobjective design study of a flapping wing power generator', *Journal of Fluids Engineering* **130**(2), 021104.

Shyy, W., Aono, H., Chimakurthi, S., Trizila, P., Kang, C.-K., Cesnik, C. & Liu, H. (2010), 'Recent progress in flapping wing aerodynamics and aeroelasticity', *Progress in Aerospace Sciences* **46**(7), 284 – 327.
URL: *http://www.sciencedirect.com/science/article/pii/S0376042110000023*

Shyy, W. & Liu, H. (2007), 'Flapping wings and aerodynamic lift: the role of leading-edge vortices', *AIAA Journal* **45**(12), 2817–2819.

Simpson, B. J. (2009), Experimental studies of flapping foils for energy extraction, PhD thesis, Massachusetts Institute of Technology.

Simpson, B. J., Hover, F. S., Triantafyllou, M. S. et al. (2008), Experiments in direct energy extraction through flapping foils, *in* 'International Offshore and Polar Engineering Conference', Vancouver, Canada, July 6–11, 2008, pp. 370–376.

Sotiropoulos, F. & Yang, X. (2014), 'Immersed boundary methods for simulating fluid–structure interaction', *Progress in Aerospace Sciences* **65**, 1–21.

Sun, X., Zhang, L., Huang, D. & Zheng, Z. (2017), 'New insights into aerodynamic characteristics of oscillating wings and performance as wind power generator', *International Journal of Energy Research* .

Teng, L., Deng, J., Pan, D. & Shao, X. (2016), 'Effects of non-sinusoidal pitching motion on energy extraction performance of a semi-active flapping foil', *Renewable Energy* **85**, 810 – 818.
URL: *http://www.sciencedirect.com/science/article/pii/S0960148115301336*

Theodorsen, T. (1979), General theory of aerodynamic instability and the mechanism of flutter, Technical Report NACA-TR-496, National Advisory Committee for Aeronautics. Langley Aeronautical Lab., Langley Field, VA, United States.

Tian, F.-B., Luo, H., Song, J. & Lu, X.-Y. (2013), 'Force production and asymmetric deformation of a flexible flapping wing in forward flight', *Journal of Fluids and Structures* **36**, 149–161.

Tian, F.-B., Luo, H., Zhu, L., Liao, J. C. & Lu, X.-Y. (2011), 'An efficient immersed boundary-lattice Boltzmann method for the hydrodynamic interaction of elastic filaments', *Journal of Computational Physics* **230**(19), 7266–7283.

Tian, F.-B., Luo, H., Zhu, L. & Lu, X.-Y. (2011), 'Coupling modes of three filaments in side-by-side arrangement', *Physics of Fluids* **23**(11), 111903.

Tian, F.-B., Young, J. & Lai, J. C. S. (2014), 'Improving power-extraction efficiency of a flapping plate: From passive deformation to active control', *Journal of Fluids and Structures* **51**, 384–392.

Toomey, J. & Eldredge, J. D. (2008), 'Numerical and experimental study of the fluid dynamics of a flapping wing with low order flexibility', *Physics of Fluids* **20**(7), 073603.

Triantafyllou, M. S., Techet, A. H. & Hover, F. S. (2004), 'Review of experimental work in biomimetic foils', *IEEE Journal of Oceanic Engineering* **29**(3), 585–594.

Veilleux, J.-C. & Dumas, G. (2013), Numerical simulations of experimentally observed high-amplitude self-sustained pitch-heave oscillations of a NACA0012 airfoil, *in* 'Annual conference of the CFD Society of Canada', Sherbrooke, Canada, May 6–9, 2013, pp. 1–12.

Veilleux, J.-C. & Dumas, G. (2017), 'Numerical optimization of a fully-passive flapping-airfoil turbine', *Journal of Fluids and Structures* **70**, 102 – 130.
URL: *http://www.sciencedirect.com/science/article/pii/S0889974616303917*

Vennell, R. (2013), 'Exceeding the betz limit with tidal turbines', *Renewable*

Energy **55**, 277 – 285.

URL: *http://www.sciencedirect.com/science/article/pii/S096014811200780X*

Wang, G., Lewalle, J., Glauser, M. & Walczak, J. (2013), 'Investigation of the benefits of unsteady blowing actuation on a 2d wind turbine blade', *Journal of Turbulence* **14**(1), 165–189.

Wang, Y., Huang, D., Han, W., YangOu, C. & Zheng, Z. (2017), 'Research on the mechanism of power extraction performance for flapping hydrofoils', *Ocean Engineering* **129**, 626 – 636.

URL: *http://www.sciencedirect.com/science/article/pii/S0029801816304607*

Wang, Z., Du, L., Zhao, J. & Sun, X. (2017), 'Structural response and energy extraction of a fully passive flapping foil', *Journal of Fluids and Structures* **72**, 96 – 113.

URL: *http://www.sciencedirect.com/science/article/pii/S0889974617300312*

Wright, A. & Wood, D. (2004), 'The starting and low wind speed behaviour of a small horizontal axis wind turbine', *Journal of Wind Engineering and Industrial Aerodynamics* **92**(14), 1265–1279.

Wu, J., Chen, Y. & Zhao, N. (2015), 'Role of induced vortex interaction in a semi-active flapping foil based energy harvester', *Physics of Fluids* **27**(9), 093601.

Wu, J., Chen, Y., Zhao, N. & Wang, T. (2016), 'Influence of stroke deviation on the power extraction performance of a fully-active flapping foil', *Renewable Energy* **94**, 440 – 451.

URL: *http://www.sciencedirect.com/science/article/pii/S0960148116302841*

Wu, J., Shu, C., Zhao, N. & Tian, F.-B. (2015), 'Numerical study on the power extraction performance of a flapping foil with a flexible tail', *Physics of Fluids* **27**(1), 013602.

Wu, J., Wu, J., Tian, F.-B., Zhao, N. & Li, Y.-D. (2015), 'How a flexible tail improves the power extraction efficiency of a semi-activated flapping foil system: A numerical study', *Journal of Fluids and Structures* **54**, 886–899.

Wu, J., Yang, S., Shu, C., Zhao, N. & Yan, W. (2015), 'Ground effect on the power extraction performance of a flapping wing biomimetic energy generator', *Journal of Fluids and Structures* **54**, 247 – 262.
URL: *http://www.sciencedirect.com/science/article/pii/S0889974614002497*

Wu, J., Zhan, J., Wang, X. & Zhao, N. (2015), 'Power extraction efficiency improvement of a fully-activated flapping foil: With the help of an auxiliary rotating foil', *Journal of Fluids and Structures* **57**, 219 – 228.
URL: *http://www.sciencedirect.com/science/article/pii/S0889974615001528*

Xiao, Q., Hu, J. & Liu, H. (2014), 'Effect of torsional stiffness and inertia on the dynamics of low aspect ratio flapping wings', *Bioinspiration & Biomimetics* **9**(1), 016008.

Xiao, Q., Liao, W., Yang, S. & Peng, Y. (2012), 'How motion trajectory affects energy extraction performance of a biomimic energy generator with an oscillating foil?', *Renewable Energy* **37**(1), 61–75.

Xiao, Q. & Zhu, Q. (2014), 'A review on flow energy harvesters based on flapping foils', *Journal of Fluids and Structures* **46**, 174–191.

Xie, Y., Lu, K. & Zhang, D. (2014), 'Investigation on energy extraction performance of an oscillating foil with modified flapping motion', *Renewable*

Energy **63**, 550 – 557.

URL: *http://www.sciencedirect.com/science/article/pii/S0960148113005600*

Xu, J., Sun, H. & Tan, S. (2016), 'Wake vortex interaction effects on energy extraction performance of tandem oscillating hydrofoils', *Journal of Mechanical Science and Technology* **30**(9), 4227–4237.

Yen, J. & Ahmed, N. A. (2013), 'Enhancing vertical axis wind turbine by dynamic stall control using synthetic jets', *Journal of Wind Engineering and Industrial Aerodynamics* **114**, 12–17.

Young, J., Ashraf, M. A., Lai, J. C. S. & Platzer, M. F. (2013), 'Numerical simulation of fully passive flapping foil power generation', *AIAA Journal* **51**(11), 2727–2739.

Young, J., Lai, J. C. S. & Platzer, M. F. (2014), 'A review of progress and challenges in flapping foil power generation', *Progress in Aerospace Sciences* **67**, 2–28.

Yu, D., Mei, R. & Shyy, W. (2002), 'A multi-block lattice Boltzmann method for viscous fluid flows', *International Journal for Numerical Methods in Fluids* **39**(2), 99–120.

Zhang, J., Liu, N.-S. & Lu, X.-Y. (2010), 'Locomotion of a passively flapping flat plate', *Journal of Fluid Mechanics* **659**, 43–68.

Zhou, Z., Ong, Y. S., Nair, P. B., Keane, A. J. & Lum, K. Y. (2007), 'Combining global and local surrogate models to accelerate evolutionary optimization', *IEEE Transactions on Systems, Man, and Cybernetics, Part C (Applications and Reviews)* **37**(1), 66–76.

Zhu, B., Han, W., Sun, X., Wang, Y., Cao, Y., Wu, G., Huang, D. & Zheng, Z. C. (2015), 'Research on energy extraction characteristics of an adaptive deformation oscillating-wing', *Renewable and Sustainable Energy* **7**(2), 023101.

Zhu, Q. (2011), 'Optimal frequency for flow energy harvesting of a flapping foil', *Journal of Fluid Mechanics* **675**, 495–517.

Zhu, Q. (2012), 'Energy harvesting by a purely passive flapping foil from shear flows', *Journal of Fluids and Structures* **34**, 157–169.

Zhu, Q., Haase, M. & Wu, C. H. (2009), 'Modeling the capacity of a novel flow-energy harvester', *Applied Mathematical Modelling* **33**(5), 2207–2217.

Zhu, Q. & Peng, Z. (2009), 'Mode coupling and flow energy harvesting by a flapping foil', *Physics of Fluids* **21**(3), 033601.

Appendix A

Summary of the literature

Table A.1: Summary of studies on flapping foil power generators with prescribed pitch and plunge motions. η_m is the maximum efficiency achieved in the literature using the definition in Eq. 2.6 and $\overline{C}_{Pm}$ is the power coefficient corresponding to the maximum efficiency. AR stands for aspect ratio and NST stands for not stated.

Authors	**Year**	**Re**	f^*	$\theta_0(^\circ)$	h_0	$\varphi(^\circ)$	x_{piv}	$\overline{C}_{Pm}$	η_m	**Information**
					Numerical studies					

Authors	**Year**	**Re**	f^*	$\theta_0(^\circ)$	h_0	$\varphi(^\circ)$	x_{piv}	$\overline{C}_{Pm}$	η_m	**Information**
Jones & Platzer	1999	∞	0.01-0.40[a]	15-78[b]	0.2-4.0[c]	90	0.5	0.52	26%	NACA0012 foil. Simulations using panel method.
Davids	1999	∞	0.02-0.24[a]	8-76[b]	0.3-5.0	65-125	-0.3-1.3	0.82	35%[d]	NACA0012 foil. Simulations using panel method.
Lindsey	2002	∞, 2.0×10^4, 1.0×10^6	0.01-0.80[a]	10-105[b]	0.0-5.0	80-110	0.13-0.8	1.00	32%	NACA0014 foil. The highest efficiency was achieved at $Re = 10^6$ using a NS solver.
Jones et al.	2003	∞, 2.0×10^4, 1.0×10^6	0.01-0.32[a]	0-99[b]	0.0-5.0	80-110	0.25	1.25	40%	NACA0014 foil. The highest efficiency was achieved at $Re = 10^6$ using a NS solver.

[a]Original reduced frequency was defined as $k = 2\pi fc/U$. The non-dimensional frequency f^* is calculated using $f^* = fc/U$.

[b]Calculated according to the amplitude of the angle of attack α_0, plunge amplitude h_0 and non-dimensional frequency f^*.

[c]Calculated according to the maximum non-dimensional plunge velocity kh_0 and reduced frequency k.

[d]Davids (1999) stated a peak efficiency of 30.0% in Table 1 on page 41. Here the efficiency of 34.9% listed in Appendix 2 on page 78 is considered.

Authors	**Year**	**Re**	$\boldsymbol{f^*}$	$\boldsymbol{\theta_0(^\circ)}$	$\boldsymbol{h_0}$	$\boldsymbol{\varphi(^\circ)}$	$\boldsymbol{x_{piv}}$	$\boldsymbol{\overline{C}_{Pm}}$	$\boldsymbol{\eta_m}$	**Information**
Kinsey & Dumas	2008	1100	0.01-0.25	0-90	1.0	90	0.25, 0.333, 0.5	0.86	33.7%	NACA0015 foil. The influence of foil thickness is insignificant, while that of the pivot location is significant.
Ashraf et al.	2011	2.0×10^4	0.04-0.32	40, 73	0.5, 1.05	70-130	0.5	0.89 1.44[e]	34% 54%[f]	NACA0014 foil. Non-sinusoidal pitch and plunge motions. Single foil and two foils in tandem.
Zhu	2011	1000	0.05-0.25	30-90	0.3-2.0	60-130	0.2, 0.35, 0.5	0.81[g]	31%	Joukowski foil. Peak efficiency was achieved when the most unstable frequency in the wake coincided with the flapping frequency.

[e]Total power coefficient of multiple foils.

[f]Total efficiency of multiple foils.

[g]Calculated according to the efficiency and swept distance computed from Eq. 2.13 and 2.14.

Authors	**Year**	**Re**	f^*	$\theta_0(^\circ)$	h_0	$\varphi(^\circ)$	x_{piv}	$\overline{C}_{Pm}$	η_m	**Information**
Kinsey & Dumas	2012*a*	5.0×10^5	0.04-0.20	60, 75	1	90	0.333	1.02	40%	NACA0015 foil. Single foil and foils in tandem. Comparison of predictions given by 2D and 3D URANS using different turbulence models.
Kinsey & Dumas	2012*b*	5.0×10^5	0.04-0.20	62-75	0.75, 1.00	90	0.333	1.64[e]	64%[f]	NACA0015 foil. Two foils in tandem.
Kinsey & Dumas	2012*c*	5.0×10^5	0.14	75	1.00	90	0.333	0.99[e]	39%[f]	NACA0015 foil. AR=5-10.
Xiao et al.	2012	1.0×10^4	0.01-0.25[h]	15-75	0.5, 1.0	90	0.333	0.98	39%[i]	NACA0012 foil. Non-sinusoidal pitch motion.

[h] Original frequency is given by the Strouhal number $St = 2fh_0/U$. The non-dimensional frequency f^* is calculated using $f^* = fc/U$

[i] The definition of efficiency in Xiao et al. (2012) was the same as Eq. 2.8. Since the curve of power coefficient (Fig.5) and that of efficiency (Fig. 6) were different, definition in Eq. 2.6 is considered here.

Authors	**Year**	**Re**	f^*	$\theta_0(^\circ)$	h_0	$\varphi(^\circ)$	x_{piv}	$\overline{C}_{Pm}$	η_m	**Information**
Campobasso et al.	2013	1100, 1.5×10^6	0.14, 0.18	76, 60	1.0	90	0.333	1.01	40%	NACA0015 foil. Good synchronization between the plunge motion and LEVs was not required for high performance in the turbulent flow.
Le et al.	2013	9.0×10^4	0.1, 0.125, 0.15	55, 60, 65	0.7-1.1	90	0.333	0.68[g]	39%	NACA 0008, cambered NACA0012 and corrugation foil.
Liu et al.	2013	1.0×10^6	0.05-0.25	9-58[j]	0.5, 1.0	90	0.333	0.75	32%	NACA0012 foil. High efficiency was achieved at low angle of attack $\alpha_0 \leq 20^\circ$ with active foil deformation. Single foil and two foils in parallel.
Deng et al.	2014	1100	0.16	60-82	1.23	90	0.333	1.11[g]	36%	NACA0015 foil. AR=1-8. 3D effects were stronger when non-sinusoidal motion was imposed.

[j]Calculated according to the amplitude of the angle of attack α_0, plunge amplitude h_0 and non-dimensional frequency f^*.

Authors	**Year**	**Re**	f^*	$\theta_0(°)$	h_0	$\varphi(°)$	x_{piv}	$\overline{C}_{Pm}$	η_m	**Information**
Kinsey & Dumas	2014	5.0×10^5	0.02-0.28	35-105	1.0-3.0	90	0.333	1.5	45%	NACA0015 foil. LEVs were not observed in most of the optimal turbulent cases.
Lu et al.	2014	1.0×10^4	0.03-0.25[h]	24-67	0.8	90	0.333	0.46	21%[k]	NACA0012 foil. Non-sinusoidal pitch and plunge motions.
Xie et al.	2014	1.0×10^4	0.06-0.44	0-35	1.0	90	0.5	0.90	30%	Elliptical foil. Pitch motion is given by $\theta = \frac{\pi}{2} + \theta_0 \sin(\omega t + \varphi)$.
Tian et al.	2014	1100	0.14	76	1.0	90	0.333	0.98	38%	Flat plate. Passive and active deformation
Drofelnik & Campobasso	2015	1.5×10^6	0.14	76	1.0	90	0.333	1.00	39%[l]	NACA0015 foil with and without end plates. AR=10. Loss due to finite span was caused by tip vortices and LEV suppression.

[k] Original efficiency was given by Eq. 2.8. Recalculated the efficiency using the definition in Eq. 2.6.

[l] Calculated according to the power coefficient and swept distance computed from Eq. 2.13 and 2.14.

Authors	**Year**	**Re**	f^*	$\theta_0(^\circ)$	h_0	$\varphi(^\circ)$	x_{piv}	$\overline{C}_{Pm}$	η_m	**Information**
Hoke et al.	2015	1100	0.14	76	1.0	90	0.333	0.97	38%	NACA0015. Active deformation
Wu et al.	2015	1100	0.12-0.24[a]	36-67[j]	0.5	90	0.333	0.56	35%	NACA0015 foil. A auxiliary foil of 0.5 chord length below the flapping foil.
Wu et al.	2015	1100	0.05-0.25[a]	19-58[j]	0.5	90	0.333	0.56	33%	NACA0015 foil. A flexible flat plate modelled by the Euler-Bernoulli beam theory was attached to a rigid foil.
Wu et al.	2015	500-4000	0.05-0.25[a]	19-78[j]	0.5	90	0.333	0.36	24%	NACA0015 foil. The foil was placed 1-5 chord length from the ground.
Zhu et al.	2015	1.0×10^4, 1.4×10^4	0.14, 0.16	51-91[j]	1.00, 1.23	90	0.333	1.05	41%	NACA0002 and NACA0015 foils. Active deformation.
Drofelnik & Campobasso	2016	1.5×10^6	0.14	76	1.0	90	0.333	1.00	39%	NACA0015 foil.
Gauthier et al.	2016	3.0×10^6	0.08-0.22	80	1.0	90	0.4	1.91[m]	77%[k]	NACA0025 foil. AR=10. Constrained flow.

[m] Calculated from the ratio between power extracted from constrained flow and unconstrained flow defined in Gauthier et al. (2016).

Authors	**Year**	**Re**	f^*	$\theta_0(^\circ)$	h_0	$\varphi(^\circ)$	x_{piv}	$\overline{C}_{Pm}$	η_m	**Information**
Wu et al.	2016	1100	0.1-0.2	75	1.0	90	0.333	0.91[g]	36%	NACA15 foil. Combined pitch, plunge and surge motions.
Xu et al.	22016	4.4×10^4	0.08-0.22	70	1.0	90	NST	NST	54%	NACA0015 foil. Two foils in tandem.
Chen et al.	2017	1100	0.08-0.20	60	1.0	90	0.333	0.93	37%	NACA0015 foil. Study on the influence of the wind gust.
Jeanmonod & Olivier	2017	1100	0.08-0.18	60-90	1.0	90	0.333	0.88	NST	Flat plate. Passive deformation.
Liu	2017	5.0×10^5	14	70	1.0	90	0.333	1.5[l,e]	60% [f]	NACA0015 foil. Two foils in tandem. Efficiency reduced in shallow water.
Sun et al.	2017	6.0×10^5	0.05-0.28	50-110	1.0	90	0.333	1.49[l]	54%	NACA 4 digit foil with different thickness.
Wang et al.	2017	1.4×10^4	0.06-0.22[h]	61-107	0.5-2.0	90	0.333	0.90	30%	NACA0012 foil.

Authors	**Year**	**Re**	f^*	$\theta_0(^\circ)$	h_0	$\varphi(^\circ)$	x_{piv}	$\overline{C}_{Pm}$	η_m	**Information**
					Experimental studies					
Simpson et al.	2008	1.4×10^4	0.08-0.24[h]	43-119[j]	1.23	90	NST	1.06	<43%[n]	NACA0012 foil. AR=4.1, 5.9 and 7.9.
Fenercioglu et al.	2015	1100	0.13[a]	73	1.05	90, 110	0.25, 0.5	0.86	33%	NACA0012 foil with end plates. AR=6. Non-sinusoidal pitch and plunge motions.
Karakas et al.	2016	1.0×10^4	0.13[a]	73	1.05	90, 110	0.40	0.43	17%	Flat plate with end plates. AR=3. Non-sinusoidal pitch and plunge motions. Constrained flow.
Kim et al.	2017	5.0×10^4	0.08-0.20	45-85	0.5-1.0	90	0.50	0.74[g]	38%	Elliptical and rectangle foils with end plates of different sizes. AR=2.5, 3.5 and 4.5.

[n]Original efficiency was given by Eq. 2.8. Cannot recalculate the efficiency using the definition in Eq. 2.6 without pivot location x_{piv}.

Table A.2: Summary of studies on flapping foil power generators with prescribed pitch and passive plunge motions. η_m is the maximum efficiency achieved in the literature using the definition in Eq. 2.6 and $\overline{C}_{Pm}$ is the power coefficient corresponding to the maximum efficiency. AR stands for aspect ratio and NST stands for not stated.

Authors	**Year**	**Re**	f^*	$\theta_0(^\circ)$	h_0	$\varphi(^\circ)$	x_{piv}	$\overline{C}_{Pm}$	η_m	**Information**
				Numerical studies						
Shimizu	2004	∞	0.0-0.10[a]	50	0.5-2.0	100-150	0.0-1.0	0.34[b]	29%[c]	NACA0012 foil. Optimization using evolutionary algorithms with solutions evaluated by the Theodorsen's theory.
Shimizu et al.	2008	∞, 4.6×10^5	0.0-0.10[a]	50	0.5-2.0	100-150	0.0-1.0	0.54[b]	35%[c]	NACA0012 foil. 8 non-dominated solutions were evaluated using a Navier-Stokes solver.

[a] Original reduced frequency was defined as $k = \pi fc/U$. The non-dimensional frequency f^* is calculated using $f^* = fc/U$.

[b] The power coefficient is computed from the dimensional power given by Shimizu (2004) and Shimizu et al. (2008) with an assumed air density of 1.225 kg/m^3.

[c] Original efficiency was given by Eq. 2.10. Recalculated the efficiency using the definition in Eq. 2.6.

Authors	Year	Re	f^*	$\theta_0(^\circ)$	h_0	$\varphi(^\circ)$	x_{piv}	$\overline{C}_{Pm}$	η_m	Information
Zhu et al.	2009	∞	0.03-0.64[a]	10-30	0-0.4	NST	0.0-1.0	0.08[d]	<13%[e]	Flat plate, NACA0005 and NACA0025 foils. Inertia of the foil was neglected. 2D and 3D inviscid flow.
Zhu & Peng	2009	1000	0.03-0.41[a]	5-60	NST	NST	0.0-1.0	0.34[d]	27%	Joukowski foil. $R_h/(\rho c U) = \pi$. Inertia of the foil was neglected.
Deng et al.	2015	1000	0.08-0.22	60-90	NST	75-125	0.333	0.57[f]	33%	NACA0015 foil. $R_h = \pi$. Mass ratio was examined.
Wu et al.	2015	1100	0.16-0.24[a]	15, 30, 45	0-0.5	NST	0.333	NST	43%[g]	NACA0015 foil. Two auxiliary foils of 0.5c in parallel. $R_h/\left(\frac{1}{2}\rho c U\right) = \pi$, $K_h/\left(\frac{1}{2}\rho U^2\right) = 1$, $m_{foil}/\left(\frac{1}{2}\rho c^2\right) = 1$.

[d] The power coefficient is computed from the ratio between the power output and the maximum net power generation capacity $(\pi/8)\,\theta_0^2$ and non-dimensionalized by $1/2\rho U^3 c$.

[e] Original efficiency was given by Eq. 2.8. Cannot recalculate the efficiency using the definition in Eq. 2.6 without additional information.

[f] In Deng et al. (2015), $\overline{C}_{Pm}$ is 0.42. Here $\overline{C}_{Pm} = 0.57$ is considered after communicated with the authors.

[g] Total efficiency of multiple foils.

Authors	**Year**	**Re**	$\boldsymbol{f^*}$	$\boldsymbol{\theta_0(^\circ)}$	$\boldsymbol{h_0}$	$\boldsymbol{\varphi(^\circ)}$	$\boldsymbol{x_{piv}}$	$\boldsymbol{\overline{C}_{Pm}}$	$\boldsymbol{\eta_m}$	**Information**
Wu et al.	2015	1100	0.1-0.3[a]	20, 40	NST	NST	0.333	0.40	20%	NACA0015 foil with a flexible tail of $0.3c$. $R_h/\left(\frac{1}{2}\rho c U\right)=\pi$, $K_h/\left(\frac{1}{2}\rho U^2\right)=1$, $m_{foil}/\left(\frac{1}{2}\rho c^2\right)=5$.
Teng et al.	2016	1000	0.08-0.22	45-90	NST	NST	NST	NST	32%	NACA0015 foil. $R_h/(\rho c U)=\pi$, $\rho_{foil}/\rho = 4.7$. Non-sinusoidal pitch motion.
					Experimental studies					
Abiru & Yoshitake	2011*a*	1.0×10^5	0.10[a]	30-50	NST	90	0.5	0.58[h,i]	46%[c,g]	NACA0015 foil. Two foils in tandem. AR=3.
Abiru & Yoshitake	2011*b*	0.6×10^5-1.2×10^5	0.08-0.16[a]	30-50	0.15-0.7	90	0.5	0.30[h]	22%[c]	NACA0015 foil. AR=3.
Huxham et al.	2012	4.5×10^4	0.03-0.20	0-60	0.0-1.0	NST	0.25	0.29[j]	24%	NACA0012 foil. AR=3.4.

[h]The power coefficient is computed from the dimensional power given by Abiru & Yoshitake (2011*a*) and Abiru & Yoshitake (2011*b*) with an assumed water density of 998 kg/m^3.

[i]Total power coefficient of multiple foils.

[j]Calculated from the input and output power coefficient and non-dimensionalized by $1/2\rho U^3 c$.

Authors	Year	Re	f^*	$\theta_0(^\circ)$	h_0	$\varphi(^\circ)$	x_{piv}	$\overline{C}_{Pm}$	η_m	Information
Lu et al.	2015	3500	0.13[a]	40, 50	1.67 2.5 3.33	90, 110	0.75	0.45[k]	14%[k]	NACA0012 foil. AR=2.5. Prescribed sinusoidal plunge motion and self-motivated pitch motion.

[k]Definition was not stated in Lu et al. (2015). This value was given by numerical simluations and is extracted directly from Fig. 10 in Lu et al. (2015).

Table A.3: Summary of studies on flapping foil power generators with passive pitch and plunge motions. η_m is the maximum efficiency achieved in the literature using the definition in Eq. 2.6 and $\overline{C}_{Pm}$ is the power coefficient corresponding to the maximum efficiency. AR stands for aspect ratio, DFO stands for degree of freedom and NST stands for not stated.

Authors	**Year**	**Re**	f^*	$\theta_0(^\circ)$	h_0	$\varphi(^\circ)$	x_{piv}	$\overline{C}_{Pm}$	η_m	**Information**
				Numerical studies						
Peng & Zhu	2009	1000	0.08-0.15	20-90	NST	NST	0.4-0.9	0.28[a]	20%	Joukowski foil. 2 DOF. $R_h/(\rho c U) = \pi$.
Zhu	2012	1000	0.16-0.31	25-100	0.02-0.06	NST	0.3-0.6	0.34[a]	31%	Joukowski foil. 2 DOF. Small shear expanded the response region for energy harvesting. $R_h/(\rho c U) = \pi$.
Young et al.	2013	1100, 1.1×10^6	0.0-0.3[b]	30-90	1.0	90	0.0-1.0	NST	41%	NACA0012 foil. 1 DOF. High efficiency was achieved via the angle of attack control.
Jiang et al.	2016	1100	0.16-0.31	100-180	NST	NST	NST	0.8	29%	Cambered elliptical foil. 2 DOF.

[a]The power coefficient is twice of that in Peng & Zhu (2009) when non-dimensionalized by $1/2\rho U^3 c$.

[b]Original frequency is given by the Strouhal number $St = 2fh_0/U$. The non-dimensional frequency f^* is calculated using $f^* = fc/U$

Authors	Year	Re	f^*	$\theta_0(^\circ)$	h_0	$\varphi(^\circ)$	x_{piv}	$\overline{C}_{Pm}$	η_m	Information
Jiang et al.	2017	1.0×10^4	NST	NST	NST	NST	0.50	0.32	20%	Elliptical foil. 2 DOF.
Veilleux & Dumas	2017	5.0×10^5	NST	NST	NST	NST	0.333	1.08	34%	NACA0015 foil. 2 DOF. Optimization using gradient-like method.
Wang et al.	2017	400	NST	0-100	0-1.6	NST	0.0-1.0	0.95	32%	NACA0012 foil. 2 DOF.
Experimental studies										
McKinney & DeLaurier	1981	8.5×10^4, 1.1×10^5	0.08-0.20	25, 30	0.3	60-135	0.5[c]	0.17[d]	17%[e]	NACA0012 foil. 1 DOF. AR=5.25.
Davids	1999	Not Stated	0.13-0.19[f]	35-60[g]	0.5-0.9	80-110	0.41, 0.51	0.19	16%	NACA0012 foil. 1 DOF. AR=5.6.

[c] Deducing from Eq. 16 in McKinney & DeLaurier (1981)

[d] Calculated according to the efficiency and swept distance computed from Eq. 2.13 and 2.14.

[e] Original efficiency was given by Eq. 2.10. Recalculated the efficiency using the definition in Eq. 2.6.

[f] Original reduced frequency was defined as $k = 2\pi fc/U$. The non-dimensional frequency f^* is calculated using $f^* = fc/U$.

[g] Calculated according to the amplitude of the angle of attack α_0, plunge amplitude h_0 and rnon-dimensional frequency f^* .

Authors	**Year**	**Re**	f^*	$\theta_0(^\circ)$	h_0	$\varphi(^\circ)$	x_{piv}	$\overline{C}_{Pm}$	η_m	**Information**
Lindsey	2002	2.2×10^4	0.03-0.16[f]	45-73	1.1, 1.3	NST	NST	0.25	<12%[h]	NACA0014 foil. 1 DOF. AR=5.6. Tow foils in tandem.
Jones et al.	2003	2.2×10^4	0.10-0.16[f]	73[i]	1.3[i]	90	0.25[i]	0.25	8%[j]	NACA0014 foil. 1 DOF. AR=5.6. Tow foils in tandem.
Kinsey et al.	2011	4.8×10^5	0-0.2[f]	75	1	90	0.333	0.77[k] 1.02[l]	30% 40%[m]	NACA0015 foil. 1 DOF. AR=7. Tow foils in tandem.

[h]The original efficiency in Lindsey (2002) was 23%. Since the plunge amplitude was 1.05 and power coefficient was 0.25, the efficiency less than 12% is considered here.

[i]Deducing from Section 2.2 in Jones et al. (2003).

[j]Calculated according to the power coefficient and swept distance computed from Eq. 2.13 and 2.14.

[k]Calculated according to the efficiency and swept distance of 2.55 chord length.

[l]Total efficiency of multiple foils. Calculated according to the efficiency and swept distance of 2.55 chord length.

[m]Total efficiency of multiple foils.

Appendix B

Flowchart and Matlab code of the improved discrete vortex method

B.1 Flowchart

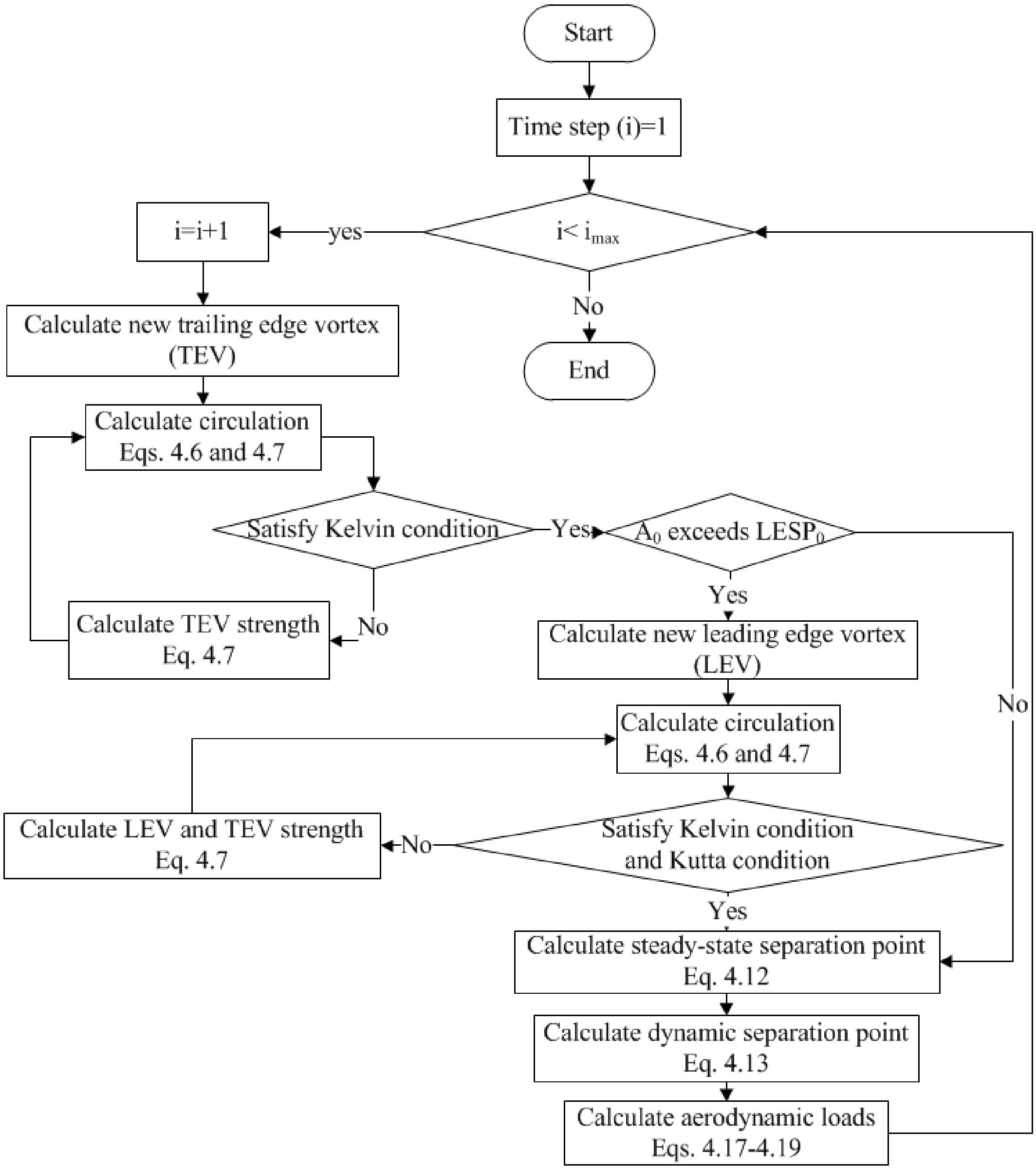

Fig. B.1: Flowchart of the improved discrete vortex method. The predefined number of time step i_{max} is related to the number of flapping cycles and the time spacing Δt.

B.2 Matlab Code

```
% Discrete Vortex Method
%%%%%%%%%%%%%%%%%%%%%%%%%%%%%%%%%%%%%%%%%%%
% NOTICE                                  %
% Righthand and Upward is positive        %
%%%%%%%%%%%%%%%%%%%%%%%%%%%%%%%%%%%%%%%%%%%
clear;
clc;

%Input
%Constant Value
tstep=200;
global ro
ro=1;
global phn
phn=1;
global lplate
lplate=1;
bplate=lplate/2;
global U0
U0=1;            % Freestream velocity

%Kinetic Parameters
h0=1*lplate;                                % Heave amplitude
fstar=0.14;                               % Non-dimensional
    frequency
```

```
omega=2*pi*fstar*U0/lplate;                                  % Pitching velocity
phi=pi/2;                               % Phase angle
theta1=0/180*pi;                        % mean amplitude
theta0=-76.3/180*pi;                       % Pitch amplitude
aplate=1/2;

%Program variables
global wmid
global umid
global v_core
v_core=0.02 ;  %Non-dimensional core radius of point vortices
anmax=40;     %Number of fourier terms used to compute vorticity at a location on chord
dismax=100;
eps=0.00001;
lesp0=0.19;

%TE separation
alpha1=15.25/180*pi;
deltaalpha1=2.1*pi/180;
S1=3.0*pi/180;
S2=2.3*pi/180;
tstar=lplate/2/U0;
t1=1.04*tstar;
```

```
t2=9*tstar;
deltait=2*pi/omega/tstep*phn;
itacc=0.97;
df=0.66/S2;
falphad2(1)=1;
deltaalpha1n(1)=0;

for i=1:tstep
    apiv(i)=(1+aplate)/2;
    t(i)=(i)*2*pi/omega/(tstep)*phn;
    theta(i)=theta1+theta0*sin(omega*t(i));
    dtheta(i)=theta0*omega*cos(omega*t(i));
    d2theta(i)=0-theta0*omega^2*sin(omega*t(i));

    h(i)=h0*sin(omega*t(i)+phi);
    dh(i)=h0*omega*cos(omega*t(i)+phi);
    d2h(i)=0-h0*omega^2*sin(omega*t(i)+phi);

    Ueff(i)=sqrt(U0^2+dh(i)^2);
    alpha(i)=theta(i)+atan(dh(i)/U0);
    dalpha(i)=dtheta(i)+d2h(i)/U0/(1+(dh(i)/U0)^2);
    dalphanon(i)=alpha(i)*lplate/2/U0;

end
% plot(it,alpha)
% hold on
```

```
% plot(it,dalpha)
% grid on
% hold off

global jstep
jstep=50;      %points on the foil
xtheta=zeros(1,jstep);
x=zeros(1,jstep);
ditadx=zeros(1,jstep);
inteA1=zeros(1,jstep);
inteA2=zeros(1,jstep);
inteA0=zeros(1,jstep);
x_bound=zeros(1,jstep);
z_bound=zeros(1,jstep);
downwash_bound=zeros(1,jstep);
gamma=zeros(1,jstep);

n_tev=0;
n_lev=0;
lev_strength=[];
xdist_lev_bound=[];
zdist_lev_bound=[];
levflag=0;
Tau_enf=0;
dist_wind=0;
tev_iter(1)=0;
```

```
tev_iter(2)=-0.01;
kelv_enf=0;
kelv(1)=0;

A0=0;
A1=0;
A2=0;
A3=0;
A0_pre=0;
A1_pre=0;
A2_pre=0;
A3_pre=0;

deltat=2*pi/omega/(tstep)*phn;
dxtheta=pi/(jstep-1);
for j=1:jstep
    xtheta(j)=(j-1)*pi/(jstep-1);
    x(j)=bplate*(1-cos(xtheta(j)));
end

for i=2:tstep
    %Calculate bound vortex positions at this time step
    dist_wind=dist_wind+U0*(t(i)-t(i-1));
    for j=1:jstep
        x_bound(j)=lplate*(apiv(i)-1)*cos(theta(i))+(x(j
            )-apiv(i)*lplate)*cos(theta(i))+dist_wind;
```

```
        z_bound(j)=(apiv(i)*lplate-x(j))*sin(theta(i))-lplate*(apiv(i)-1)*sin(theta(i))+h(i);
        downwash_bound(j)=(U0*cos(theta(i))+dh(i)*sin(theta(i)))-U0*sin(theta(i))-dtheta(i)*(x(j)-apiv(i)*lplate)+dh(i)*cos(theta(i));
    end

    %Distance travelled by LEV
    n_tev=n_tev+1;

    if n_tev==1
        x_tev(n_tev)=x_bound(jstep)+(0.5*U0*(t(i)-t(i-1)));
        z_tev(n_tev)=z_bound(jstep);
    else
        x_tev(n_tev)=x_bound(jstep)+1/3*(x_tev(n_tev-1)-x_bound(jstep));
        z_tev(n_tev)=z_bound(jstep)+1/3*(z_tev(n_tev-1)-z_bound(jstep));
    end

    %Distance between vortices and points on the foil
    for j=1:jstep
        for i_lev=1:n_lev
            xdist_lev_bound(j,i_lev)=x_lev(i_lev)-x_bound(j);
```

```
            zdist_lev_bound(j,i_lev)=z_lev(i_lev)-z_bound(j);
        end
    end
    for j=1:jstep
        for i_tev=1:n_tev
            xdist_tev_bound(j,i_tev)=x_tev(i_tev)-x_bound(j);
            zdist_tev_bound(j,i_tev)=z_tev(i_tev)-z_bound(j);
        end
    end
    %Distance between vortices
    for i_lev=1:n_lev
        for j_lev=1:n_lev
            xdist_lev_lev(i_lev,j_lev)=x_lev(j_lev)-x_lev(i_lev);
            zdist_lev_lev(i_lev,j_lev)=z_lev(j_lev)-z_lev(i_lev);
        end
    end
    for i_tev=1:n_tev
        for j_tev=1:n_tev
            xdist_tev_tev(i_tev,j_tev)=x_tev(j_tev)-x_tev(i_tev);
            zdist_tev_tev(i_tev,j_tev)=z_tev(j_tev)-
```

```
                z_tev(i_tev);
        end
    end
    for i_tev=1:n_tev
        for j_lev=1:n_lev
            xdist_lev_tev(i_tev,j_lev)=x_lev(j_lev)-
                x_tev(i_tev);
            zdist_lev_tev(i_tev,j_lev)=z_lev(j_lev)-
                z_tev(i_tev);
        end
    end


   %Iterate to find A0 when there's no LEV
   iter=1;
   flagerro=1;
   tev_iter(1)=0;
   tev_iter(2)=-0.01;
   while ( iter<1000 && flagerro>eps )
       iter=iter+1;
       tev_strength(n_tev)=tev_iter(iter);
       thetamid=theta(i);
       downwash=f_downwash(n_lev,lev_strength,
           xdist_lev_bound,zdist_lev_bound,n_tev,
           tev_strength,xdist_tev_bound,zdist_tev_bound,
           theta(i),downwash_bound);
```

```

    for j=1:jstep
        inteA0(j)=downwash(j)/U0;
        inteA1(j)=downwash(j)/U0*cos(xtheta(j));
        inteA2(j)=downwash(j)/U0*cos(2*xtheta(j));
        inteA3(j)=downwash(j)/U0*cos(3*xtheta(j));
    end
    A0=-1/pi*trapz(xtheta,inteA0);
    A1=2/pi*trapz(xtheta,inteA1);
    Tau_bound=U0*lplate*pi*(A0+A1/2);

    kelv(iter)=kelv_enf;
    for i_lev=1:n_lev
        kelv(iter)=kelv(iter)+lev_strength(i_lev);
    end
    for i_tev=1:n_tev
        kelv(iter)=kelv(iter)+tev_strength(i_tev);
    end
    kelv(iter)=kelv(iter)+Tau_bound;
    flagerro=abs( kelv(iter));
    if flagerro>eps
       dkelv=(kelv(iter)-kelv(iter-1))/(tev_iter(iter
           )-tev_iter(iter-1));
       tev_iter(iter+1)=tev_iter(iter)-(kelv(iter)/
           dkelv);
    end
```

```
end
lesp=A0;
levx=U0-dtheta(i)*sin(theta(i))*apiv(i)+umid(1);
levy=-(dtheta(i)*cos(alpha(i))*apiv(i))-dh(i)+wmid(1)
    ;

if (abs(lesp)>lesp0)
        n_lev=n_lev+1;
        tev_iter(1)=0;
        tev_iter(2)=-0.01;
        lev_iter(1)=0.;
        lev_iter(2)=0.01;
        if (levflag==0)
              x_lev(n_lev)=x_bound(1)+(0.5*levx*(t(i)-t(i
                  -1)));
              z_lev(n_lev)=z_bound(1)+(0.5*levy*(t(i)-t(i
                  -1)));
        else
              x_lev(n_lev)=x_bound(1)+(1/3*(x_lev(n_lev-1)
                  -x_bound(1)));
              z_lev(n_lev)=z_bound(1)+(1/3*(z_lev(n_lev-1)
                  -y_bound(1)));
        end
        levflag=1;

        for j=1:jstep
```

```
            xdist_lev_bound(j,n_lev)=x_lev(n_lev)-
                x_bound(j);
            zdist_lev_bound(j,n_lev)=z_lev(n_lev)-
                z_bound(j);
        end
        for i_lev=1:n_lev
            xdist_lev_lev(i_lev,n_lev)=x_lev(n_lev)-
                x_lev(i_lev);
            zdist_lev_lev(i_lev,n_lev)=z_lev(n_lev)-
                z_lev(i_lev);
        end
        for i_lev=1:n_lev
            xdist_lev_lev(n_lev,i_lev)=x_lev(i_lev)-
                x_lev(n_lev);
            zdist_lev_lev(n_lev,i_lev)=z_lev(i_lev)-
                z_lev(n_lev);
        end
        for i_tev=1:n_tev
            xdist_lev_tev(i_tev,n_lev)=x_lev(n_lev)-
                x_tev(i_tev);
            zdist_lev_tev(i_tev,n_lev)=z_lev(n_lev)-
                z_tev(i_tev);
        end

        flagerro=1;
        iter=1;
```

```
        clear kelv
        kelv(1)=0;
        kutta(1)=0;
        while(iter<1000 && flagerro>eps)
            iter=iter+1;
            lev_strength(n_lev)=lev_iter(iter-1);
            tev_strength(n_tev)=tev_iter(iter);
            downwash=f_downwash(n_lev,lev_strength,
               xdist_lev_bound,zdist_lev_bound,n_tev,
               tev_strength,xdist_tev_bound,
               zdist_tev_bound,theta(i),downwash_bound);
            kelv_tev=kelv_enf;
            for i_lev=1:n_lev
               kelv_tev=kelv_tev+tev_strength(i_lev);
            end
            for i_tev=1:n_tev
               kelv_tev=kelv_tev+tev_strength(i_tev);
            end
            for j=1:jstep
                inteA0(j)=downwash(j)/U0;
                inteA1(j)=downwash(j)/U0*cos(xtheta(j));
                inteA2(j)=downwash(j)/U0*cos(2*xtheta(j)
                   );
                inteA3(j)=downwash(j)/U0*cos(3*xtheta(j)
                   );
            end
```

```
            A0=-1/pi*trapz(xtheta(2:jstep),inteA0(2:jstep));
            A1=2/pi*trapz(xtheta(2:jstep),inteA1(2:jstep));
            Tau_bound=U0*lplate*pi*(A0+A1/2);
            kelv_tev=kelv_tev+Tau_bound;
            kutta_tev=A0-sign(lesp)*lesp0;
            dkelv_tev=(kelv_tev-kelv(iter-1))/(tev_iter(iter)-tev_iter(iter-1));
            dkutta_tev=(kutta_tev-kutta(iter-1))/(tev_iter(iter)-tev_iter(iter-1));

            lev_strength(n_lev)=lev_iter(iter);
            tev_strength(n_tev)=tev_iter(iter-1);
            downwash=f_downwash(n_lev,lev_strength,xdist_lev_bound,zdist_lev_bound,n_tev,tev_strength,xdist_tev_bound,zdist_tev_bound,theta(i),downwash_bound);
            kelv_lev=kelv_enf;
            for i_lev=1:n_lev
                kelv_lev=kelv_lev+lev_strength(i_lev,1);
            end
            for i_tev=1:n_tev
                kelv_lev=kelv_lev+tev_strength(i_tev,1);
            end
            for j=1:jstep
```

```
            inteA0(j)=downwash(j)/U0;
            inteA1(j)=downwash(j)/U0*cos(xtheta(j));
            inteA2(j)=downwash(j)/U0*cos(2*xtheta(j));
            inteA3(j)=downwash(j)/U0*cos(3*xtheta(j));
        end
        A0=-1/pi*trapz(xtheta(2:jstep),inteA0(2:jstep));
        A1=2/pi*trapz(xtheta(2:jstep),inteA1(2:jstep));
        Tau_bound=U0*lplate*pi*(A0+A1/2);
        kelv_lev=kelv_lev+Tau_bound;
        kutta_lev=A0-sign(lesp)*lesp0;
        dkelv_lev=(kelv_lev-kelv(iter-1))/(lev_iter(iter)-lev_iter(iter-1));
        dkutta_lev=(kutta_lev-kutta(iter-1))/(lev_iter(iter)-lev_iter(iter-1));

        lev_strength(n_lev)=lev_iter(iter);
        tev_strength(n_tev)=tev_iter(iter);
        downwash=f_downwash(n_lev,lev_strength,xdist_lev_bound,zdist_lev_bound,n_tev,tev_strength,xdist_tev_bound,zdist_tev_bound,theta(i),downwash_bound);
        kelv(iter)=kelv_enf;
```

```
            for i_lev=1:n_lev
                kelv(iter)=kelv(iter)+lev_strength(i_lev
                    );
            end
            for i_tev=1:n_tev
                kelv(iter)=kelv(iter)+tev_strength(i_tev
                    );
            end

            for j=1:jstep
                inteA0(j)=downwash(j)/U0;
                inteA1(j)=downwash(j)/U0*cos(xtheta(j));
                inteA2(j)=downwash(j)/U0*cos(2*xtheta(j)
                    );
                inteA3(j)=downwash(j)/U0*cos(3*xtheta(j)
                    );
            end
            A0=-1/pi*trapz(xtheta,inteA0);
            A1=2/pi*trapz(xtheta,inteA1);
            Tau_bound=U0*lplate*pi*(A0+A1/2);
            kelv(iter)=kelv(iter)+Tau_bound;
            kutta(iter)=A0-sign(lesp)*lesp0;

            tev_iter(iter+1)=tev_iter(iter)-((1/(
               dkelv_tev*dkutta_lev-dkelv_lev*dkutta_tev
               ))*((dkutta_lev*kelv(iter))-(dkelv_lev*
```

```
                    kutta(iter))));
                lev_iter(iter+1)=lev_iter(iter)-((1/(dkelv_tev*dkutta_lev-dkelv_lev*dkutta_tev))*((-dkutta_tev*kelv(iter))+(dkelv_tev*kutta(iter))));

                flagerro=max(abs(kelv(iter)),abs(kutta(iter)));
            end
    else
        levflag=0;
    end
    for j=1:jstep
            inteA2(j)=downwash(j)/U0*cos(2*xtheta(j));
            inteA3(j)=downwash(j)/U0*cos(3*xtheta(j));
    end
    A2=2/pi*trapz(xtheta,inteA2);
    A3=2/pi*trapz(xtheta,inteA3);
    dAn(1)=(A0-A0_pre)/(t(i)-t(i-1));
    dAn(2)=(A1-A1_pre)/(t(i)-t(i-1));
    dAn(3)=(A2-A2_pre)/(t(i)-t(i-1));
    dAn(4)=(A3-A3_pre)/(t(i)-t(i-1));


    if (i==2)
        tev_strength(1)=0;
```

```
    end

    An(5:anmax)=0;
    An(1)= A0;
    An(2)= A1;
    An(3)= A2;
    An(4)= A3;
    for iAn=5:anmax
        for j=2:jstep
            An(iAn)=An(iAn)+((((downwash(j)*cos((iAn-1)*
                xtheta(j)))...
                  +(downwash(j-1)*cos((iAn-1)*xtheta(j-1))))
                    /2)*dxtheta);
        end
        An(iAn)=(2./pi)*An(iAn);
    end
    A0_pre= A0;
    A1_pre= A1;
    A2_pre= A2;
    A3_pre= A3;

    %Calculate bound vortex strengths
    for j=1:jstep
        gamma(j)=(A0*(1+cos(xtheta(j))));
        for iAn=1:anmax
            gamma(j)=gamma(j)+(An(iAn)*sin(iAn*xtheta(j))*
```

```
                sin(xtheta(j)));
        end
        gamma(j)=gamma(j)*lplate;
    end

    for j=2:jstep
        bound_mid_strength(j)=((gamma(j)+gamma(j-1))/2)*
            dxtheta;
        x_bound_mid(j)=(x_bound(j)+x_bound(j-1))/2;
        z_bound_mid(j)=(z_bound(j)+z_bound(j-1))/2;
    end

    %Move speed of vitices
    uind_tev(1:n_tev)=0;
    wind_tev(1:n_tev)=0;
    for i_tev=1:n_tev
        for j_tev=1:n_tev
            if (i_tev ~= j_tev)
                dist=xdist_tev_tev(i_tev,j_tev)^2+
                    zdist_tev_tev(i_tev,j_tev)^2;
                uind_tev(i_tev)=uind_tev(i_tev)+...
                        ((tev_strength(j_tev)*(-zdist_tev_tev(
                            i_tev,j_tev)))/(2*pi*sqrt(v_core^4+
                            dist^2)));
                wind_tev(i_tev)=wind_tev(i_tev)+...
                        ((-tev_strength(j_tev)*(-xdist_tev_tev(
```

```
i_tev,j_tev)))/(2*pi*sqrt(v_core^4+dist^2)));
            end
        end
        for j=2:jstep
            xdist_bound_mid_tev=x_tev(i_tev)-x_bound_mid(j);
            zdist_bound_mid_tev=z_tev(i_tev)-z_bound_mid(j);
            dist=xdist_bound_mid_tev^2+zdist_bound_mid_tev^2;
            uind_tev(i_tev)=uind_tev(i_tev)+((bound_mid_strength(j)*xdist_bound_mid_tev)/(2*pi*sqrt(v_core^4+dist^2)));
            wind_tev(i_tev)=wind_tev(i_tev)+((-bound_mid_strength(j)*xdist_bound_mid_tev)/(2*pi*sqrt(v_core^4+dist^2)));
        end
    end
    uind_lev(1:n_lev)=0;
    wind_lev(1:n_lev)=0;
    for i_lev=1:n_lev
        for j_lev=1:n_lev
            if (i_lev ~= j_lev)
                dist=xdist_lev_lev(i_lev,j_lev)^2+zdist_lev_lev(i_lev,j_lev)^2;
```

```
                uind_lev(i_lev)=uind_lev(i_lev)+...
                    ((lev_strength(j_lev)*(-zdist_lev_lev(i_lev,j_lev)))/(2*pi*sqrt(v_core^4+dist^2)));
                wind_lev(i_lev)=wind_lev(i_lev)+...
                    ((-lev_strength(j_lev)*(-xdist_lev_lev(i_lev,j_lev)))/(2*pi*sqrt(v_core^4+dist^2)));
            end
        end
        for j=2:jstep
            xdist_bound_mid_lev=x_lev(i_lev)-x_bound_mid(j);
            zdist_bound_mid_lev=z_lev(i_lev)-z_bound_mid(j);
            dist=xdist_bound_mid_lev^2+zdist_bound_mid_lev^2;
            uind_lev(i_lev)=uind_lev(i_lev)+((bound_mid_strength(j)*xdist_bound_mid_lev)/(2*pi*sqrt(v_core^4+dist^2)));
            wind_lev(i_lev)=wind_lev(i_lev)+((-bound_mid_strength(j)*xdist_bound_mid_lev)/(2*pi*sqrt(v_core^4+dist^2)));
        end
    end
%Update the location of votices
```

```
for i_tev=1:n_tev
    x_tev(i_tev)=x_tev(i_tev)+(deltat*uind_tev(i_tev))
        ;
    z_tev(i_tev)=z_tev(i_tev)+(deltat*wind_tev(i_tev))
        ;
end
for i_lev=1:n_lev
    x_lev(i_lev)=x_lev(i_lev)+(deltat*uind_lev(i_lev))
        ;
    z_lev(i_lev)=z_lev(i_lev)+(deltat*wind_lev(i_lev))
        ;
end
%Remove TEVs and LEVs that have crossed a certain
    distance and update Kelvin condition
if (x_tev(1)-x_bound(jstep)>dismax)
    for i_tev=1:n_tev-1
        tev_strength(i_tev)=tev_strength(i_tev+1);
        x_tev(i_tev)=x_tev(i_tev+1);
        z_tev(i_tev)=z_tev(i_tev+1);
    end
    n_tev=n_tev-1;
    kelv_enf=kelv_enf+tev_strength(1);
end
if (x_lev(1)-x_bound(jstep)>dismax)
    for i_lev=1:n_lev-1
        lev_strength(i_lev)=lev_strength(i_lev+1);
```

```
            x_lev(i_lev)=x_lev(i_lev+1);
            z_lev(i_lev)=z_lev(i_lev+1);
        end
        n_lev=n_lev-1;
        kelv_enf=kelv_enf+lev_strength(1);
    end
    CC=2*pi*A0^2;
    CNcir1(i)=2*pi*(U0*cos(theta(i))+dh(i)*sin(theta(i))*(A0+A1/2))/U0;
    CNcir2(i)=sum((umid*cos(theta(i))-wmid*sin(theta(i))).*bound_mid_strength)*2/(U0^2*lplate);
    CMcir2(i)=sum((umid*cos(theta(i))-wmid*sin(theta(i))).*x.*bound_mid_strength)*2/(U0^2*lplate^2);
    CNmass(i)=(2*pi*((3*lplate*dAn(1)/(4*U0))+(lplate*dAn(2)/(4*U0))+...
        (lplate*dAn(3)/(8*U0))))/U0;


    if (alpha(i)-t2*dalphanon(i)*U0/bplate)*sign(alpha(i))<0
        Calphat2(i)=0;
    else
        Calphat2(i)=abs(alpha(i)-t2*dalphanon(i)*U0/bplate)*sign(alpha(i));
    end

```

```
if i==1
        Salpha(i)=0;
else
        Salpha(i)=abs(alpha(i))-abs(alpha(i));
end

if (abs(alpha(i))<alpha1)
        falpha(i)=1-0.3*exp((abs(alpha(i))-alpha1)/S1);
else
        falpha(i)=0.04+0.66*exp((alpha1-abs(alpha(i)))/S2);
end

if ((Salpha(i)>0))
        deltaalpha1n(i)=0;
else
        deltaalpha1n(i)=(abs(1-falphad2(i-1))^0.25*deltaalpha1);
end
alpha1n(i)=alpha1-deltaalpha1n(i);

if (abs(Calphat2(i))<=alpha1n(i))
      fx0(i)=1-0.3*exp((abs(Calphat2(i))-alpha1n(i))/S1);
else
      fx0(i)=0.04+0.66*exp((alpha1n(i)-abs(Calphat2(i))
```

```
        )/S2);
    end
    falphad2(i)=((2*t1-deltait)*falphad2(i-1)+2*deltait*(
        fx0(i)))/(2*t1+deltait);

    if (i==1)
        deltafmax(i)=0;
    else
        if (abs(dalphanon(i))>0.01)
            deltafmax(i)=0.01D0*df*(t(i)-t(i-1))*U0/
                bplate;
        else
            deltafmax(i)=dalphanon(i)*df*(t(i)-t(i-1))*
                U0/bplate;
        end
    end

    if (i==1)
        falphad2(i)=1;
    else
        if (abs(falphad2(i)-falphad2(i-1))>abs(deltafmax(
            i)))
            falphad2(i)=falphad2(i-1)+abs(deltafmax(i))*
                sign(falphad2(i)-falphad2(i-1)) ;
        end
    end
```

```
    KNn(i)=((1+sqrt(falphad2(i)))/2.D0)^2;
    CL(i)=((CNcir1(i)+CNcir2(i))*KNn(i)+CNmass(i))*cos(
        theta(i))+itacc*CC*sqrt(falphad2(i));
    CN(i)=(CNcir1(i)+CNcir2(i))*KNn(i);
    Pivoffset=(-0.135*(1-falphad2(i))+0.04*sin(pi*(
        falphad2(i)^2)));
    CMadd(i)=(CN(i))*(apiv(i)+Pivoffset)+CNmass(i)*apiv(i
        )-(2*pi*(((cos(theta(i)))+(dh(i)*sin(theta(i))/U0)
        )*((A0/4)+(A1/4)-(A2/8))*KNn(i)+(lplate/U0)*((7*
        dAn(1)/16)+(3*dAn(2)/16)+(dAn(3)/16)-(dAn(4)/64)))
        )-CMcir2(i)*KNn(i);
end
```